POLITECNICO DI TORINO

MASTER's Degree in AEROSPACE ENGINEERING

MASTER's Degree Thesis

PARTICLE SWARM OPTIMIZATION APPLIED TO TRAJECTORY DESIGN FOR EARTH TO MARS MISSIONS USING REFUELING ISRU CANDIDATE ASTEROIDS

Supervisors

Prof. Lorenzo CASALINO

Dr. Davide CONTE

Candidate

Francesco LOPEZ

JULY 2023

Summary

The colonization of Mars is an ambitious goal, but the low-cost transfer of resources between Earth and Mars remains a major challenge. To address this, utilizing asteroids as refueling points could significantly reduce ΔV requirements for Earth-Mars journeys. Therefore, refueling with In-Situ Resource Utilization on asteroids can help decrease the launch mass of spacecraft since they wouldn't need to carry as much propellant from Earth, which could in turn minimize the size and cost of the launch vehicles required.

Ideally, asteroids with an abundant amount of water and volatile compounds would be preferred. These resources could be used for propellant production or even for onboard consumption. Selecting suitable asteroids requires that exploration missions evaluate their physical properties and resources. In this thesis, we estimate the mass and composition of asteroids, including how many and what resources will be found on the asteroids needed to proceed with our orbital study.

This thesis focuses on trajectories from Earth to a list of candidate asteroids and, from it, to Mars. Additionally, we select the best asteroid among these candidates such that the total ΔV from the Earth to the asteroid and the time of flight (TOF) from Earth to Mars are minimized, and to maximize the number of resupplies on the asteroid.

For this mission, a double arc trajectory is studied. The first arc intercepts one of the candidate asteroids. Then, insertion into a Sun-asteroid Distant Retrograde Orbit (DRO) and a landing trajectory on the asteroid are performed. Along the second arc, the spacecraft leaves the candidate asteroid to be captured at Martian periareion using the propellant obtained from the asteroid.

The two conics for each arc are obtained by solving Lambert's problem, which is computed for different TOF from Earth to the asteroid, from the asteroid to Mars and for different waiting times on the asteroid to minimize the total TOF and the ΔV from the Earth to the asteroid.

Modeling the dynamics of Sun-asteroid systems is done with the CR3BP with the Sun and asteroid as the primary masses. It is then possible to compute periodic orbits in the vicinity of the asteroid, such as DROs. DROs are marginally stable periodic CR3BP orbits that are adequately distant from the asteroid surface that can be used as parking orbits around asteroids.

The initial conditions (ICs) of a proposed Sun-asteroid DRO are obtained with Particle Swarm Optimization (PSO). PSO is a heuristic algorithm within the computational swarm intelligence technique which combines social, cognitive and inertial factors of bird flocks to find the local optimal solution. PSO is also used to compute some parameters to determine a suitable landing trajectory on the asteroid from DROs and to compute the ΔV-optimal maneuvers to land at the asteroid to then perform ISRU.

After using PSO to solve the problem of trajectory design, deterministic gradient-based methods are used to understand if it can find more accurate solutions. A Differential Correction (DC) method combined with dynamical system theory is used to determine the ICs of a Sun-asteroid DRO, discovering that PSO can find accurate solutions without the use of it.

The final results show that using 2009-OS5 as the asteroid for refueling gives an Earth-Asteroid ΔV (4.4800 km/s) 27% lower than the minimum direct Earth-Mars ΔV possible (6.1696 km/s), a TOF (386 days) for the entire mission higher than 4 months respect of an actual Mars mission (252 days) and it has been estimated the possibility to refuel about 83 times on it.

Acknowledgements

I would like to express my genuine gratitude to all those who have been instrumental in the successful completion of my master's degree. Their unwavering support, guidance, and encouragement have made this achievement possible, and for that, I am truly grateful.

First and foremost, I extend my deepest appreciation to Doctor Davide Conte, whose mentorship during my time abroad at Embry-Riddle Aeronautical University in Arizona, Prescott has been invaluable. His comprehensive technical guidance and expertise in the field of astrodynamics have played a pivotal role in significantly expanding my knowledge within a short span of time. Doctor Conte's dedication and support throughout the thesis writing process have been truly indispensable.

I would also like to express my sincere gratitude to Embry-Riddle Aeronautical University for providing me with an enriching experience that has allowed me to grow not only academically but also as an individual. The opportunity to immerse myself in a different culture and embark on new adventures has broadened my horizons and shaped my perspective in profound ways.

Furthermore, I extend my heartfelt thanks to my home university, Politecnico di Torino, for nurturing and shaping me over the course of six years. The world-class engineering education I received has equipped me with a solid foundation and enviable skills that are recognized worldwide. The invaluable lessons and experiences gained from my time at Politecnico di Torino have undoubtedly been instrumental in my academic and personal growth.

I am grateful to Professor Lorenzo Casalino for his guidance and expertise which have not only enhanced my understanding of the subject but have also instilled in me a passion for continuous learning and improvement.

I would also like to express my heartfelt gratitude to my family for their unwavering support throughout my academic journey. Their love, encouragement,

and belief in my abilities have been a constant source of motivation and strength. I am truly grateful for their understanding during the challenging moments, their words of wisdom, and the sacrifices they have made to ensure my success.

Their support extends beyond the emotional realm, as they have also provided invaluable financial assistance that has allowed me to pursue my education and participate in various opportunities that have shaped my academic and personal growth. Their belief in the value of education and their willingness to invest in my future have been instrumental in my achievements, and for that, I am deeply thankful.

I would like to express my overwhelming thanks to the Ente Regionale per il Diritto allo Studio Universitario del Piemonte (EDISU) for their tremendous support throughout my academic journey. Winning numerous scholarships from EDISU has been instrumental in alleviating the financial burden associated with pursuing higher education.

Their assistance has not only eased my financial worries but has also provided me with the opportunity to focus wholeheartedly on my studies and personal growth. The provision of a free accommodation has been especially invaluable, as it has allowed me to create a conducive and comfortable living environment while pursuing my academic endeavors. I will be forever grateful.

In addition, I want to express my appreciation to all my friends, professors, and individuals I have encountered throughout my university journey. Their friendship, support, and intellectual exchanges have enriched my educational experience and contributed to my personal and professional development.

To each and every person and institution mentioned above, and to all those who have supported me along the way, I extend my deepest gratitude. Your impact on my academic and personal growth is immeasurable, and I am truly honored to have had the privilege of learning from and alongside such exceptional individuals.

"Vita facile est, si quis velit facere difficile"
"La vita è facile, se uno vuole fare cose difficili"
Orazio

Table of Contents

List of Tables

List of Figures

Acronyms

3BP
: Three-Body Problem

ABC
: Artificial Bee Colony

ACE
: Advanced Composition Explorer

ACO
: Ant Colony Optimization

CR3BP
: Circular Restricted Three-Body Problem

DST
: Dynamical Systems Theory

EOMs
: Equations Of Motion

FWA
: Fireworks Algorithm

IAU MPC
: International Astronomical Union's Minor Planet Center

ICs
: Initial Conditions

ISEE-3
International Sun/Earth Explorer 3

ISRU
In-Situ Resource Utilization

JWST
James Webb Space Telescope

KR2BP
Keplerian Restricted 2 Body Problem

LEO
Low Earth Orbit

LMO
Low Mars Orbit

LOA
Line Of Apsides

MAP
Microwave Anisotrophy Probe

PSO
Particle Swarm Optimization

R3BP
Restricted Three-Body Problem

SI
Swarm Intelligence

SMA
Semi-Major Axis

SOHO
Solar and Heliospheric Observatory

STM

State Transition Matrix

TOF

Time Of Flight

Introduction

The exploration of Mars has long captured the imagination of scientists, space enthusiasts, and dreamers alike. As Earth's closest neighbor in the vast expanse of the solar system, Mars has beckoned humanity with its mystique and potential for uncovering answers to fundamental questions about our own origins and the possibility of life beyond our home planet. Mars, often referred to as the "Earth's Twin", possesses remarkable similarities to our own planet. With a thin atmosphere, polar ice caps, and a diverse terrain featuring towering volcanoes, deep canyons, and ancient riverbeds, Mars serves as a tantalizing scientific laboratory. Through the efforts of numerous robotic missions, including orbiters, landers, and rovers, we have gained unprecedented insights into Mars' geological history, climate patterns, and the potential for habitability in the past.

In recent years, the exploration of Mars has taken on renewed momentum, fueled by the ambitious plans of space agencies and private enterprises. Mars is viewed as a potential destination for human colonization, with scientists and engineers envisioning the establishment of permanent habitats and the development of self-sustaining ecosystems. The journey to Mars presents formidable challenges, including the long-duration space travel, exposure to cosmic radiation, and the need for innovative life support systems. However, the allure of discovering whether life exists beyond Earth and the prospect of becoming a multi-planetary species provide the impetus for overcoming these hurdles.

As mentioned above, Mars exploration faces a number of significant challenges. One among all is the immense cost associated with interplanetary travel. The journey to Mars demands substantial financial resources due to the complexities of designing and launching spacecraft capable of enduring the long-duration voyage and sustaining human life in a harsh extraterrestrial environment. The high costs arise from the need for advanced technologies, extensive fuel requirements, and the development of robust life support systems to ensure the safety and well-being of astronauts throughout their mission.

In light of the significant costs involved in Mars missions, innovative approaches are being explored to mitigate financial barriers and enhance mission sustainability. One such approach is to leverage the exploration of asteroids, which are rich in resources, as a means of refueling and resupplying spacecraft en route to Mars. By mining and utilizing the resources available on asteroids, it becomes possible to reduce the payload and fuel requirements for Mars missions, thereby decreasing the overall costs associated with interplanetary travel.

Asteroids, the remnants of the early solar system, are rich in valuable resources that can be extracted and utilized for space exploration purposes. These celestial bodies contain abundant water ice, metals, and organic compounds. By harnessing the resources present on asteroids, we can envision a future where spacecraft bound for Mars can refuel, resupply, and potentially even manufacture necessary materials using locally available resources.

In-situ resource utilization (ISRU) on asteroids offers several advantages for Mars missions. Firstly, it reduces the need to transport large amounts of fuel and supplies from Earth, thereby significantly decreasing the costs associated with interplanetary travel. Instead, spacecraft can utilize the resources found on asteroids to produce propellants like liquid oxygen and liquid hydrogen, which are essential for spacecraft propulsion. This approach not only minimizes the payload but also enables longer-duration missions and greater flexibility in mission planning.

Moreover, ISRU on asteroids opens up possibilities for the production of other essential materials required for Mars exploration and colonization. For instance, asteroids can provide a source of raw materials for construction, such as metals and minerals, which can be processed and transformed into habitats, infrastructure, and tools. By utilizing asteroid resources, we can reduce reliance on Earth's limited supplies and create a sustainable infrastructure in space.

This thesis aims to investigate the potential of utilizing asteroids as a means to diminish the costs and enhance the feasibility of Mars missions focusing on trajectory design and optimization techniques for spacecraft traveling between Earth, asteroids, and Mars. More specifically, optimal Earth-asteroid and asteroid-Mars trajectories will be analyzed in order to find asteroids that result in fuel savings for Earth-Mars missions. The research is structured into several chapters, each delving into specific aspects of the mission design process.

Chapter 1 provides a comprehensive understanding of the the Circular Restricted Three-Body Problem (CR3BP), which will later be useful for designing periodic orbits around the asteroid.

Chapter 2 focuses on the Lambert's problem, which deals with determining the trajectory between two points in space under the influence of gravitational forces. The Lambert's problem is one of many methods used in interplanetary mission planning, and this chapter explores two different solutions to solve it.

Chapter 3 mentions heuristic algorithms, with a specific emphasis on the Particle Swarm Optimization (PSO) technique. PSO is an intelligent optimization algorithm inspired by the social behavior of bird flocks, and it has shown remarkable success in solving complex optimization problems.

Chapter 4 uses Lambert's problem to find trajectories between Earth and a series of asteroids, and from them to Mars. ΔVs for different launch windows will also be calculated and the best asteroids (lowest ΔV) will be proposed.

In Chapter 5, the focus shifts to the insertion of spacecraft into a Distant Retrograde Orbit (DRO), which is a periodic orbit within the CR3BP. This chapter employs the PSO algorithm to determine the initial conditions for achieving DROs.

Chapter 6 examines potential landing trajectories for spacecraft, utilizing the PSO algorithm for trajectory optimization.

Through the study of the Circular Restricted Three-Body Problem, the solving of the Lambert's problem and the application of heuristic algorithms such as PSO, this thesis aims to contribute to the field of interplanetary mission design and optimization, and more specifically to the realization of efficient missions to Mars.

Chapter 1

The Circular Restricted Three-Body Problem

In astrodynamics, according to the theory of universal gravitation formulated by Isaac Newton, in *Philosophiae Naturalis Principia Mathematica* [1], two bodies with mass exert an attractive force proportional to the product of their masses and inversely proportional to the square of the distance between them. Mathematically, the gravitational force of one body onto another is:

$$\vec{F}_g = -\frac{GMm}{r^2}\frac{\vec{r}}{r} \tag{1.1}$$

where G is the Universal Gravitational Constant equal to $6.6743 \times 10^{-11} \frac{m^3}{kg \cdot s^2}$, M is the mass of the primary body, m is the mass of the secondary mass and r is the distance between them. In the Three-Body Problem (3BP) we consider three bodies that gravitationally influence themselves. In the Restricted Three-Body Problem (R3BP) there is a negligible mass, m, with respect to the primaries, m_1 and m_2, that represents a spacecraft and that does not influence the motions of m_1 and m_2. In the Circular Restricted Three-Body Problem (CR3BP), the two primaries describe a circular orbit around their barycenter of the system (synodic system). The system described is shown in Fig. 1.1.

1.1 Equations of Motion

To describe the equations of motion, we start by defining the total mass of the system, M, and the mass ratio, μ, as

$$M = m_1 + m_2 \tag{1.2}$$

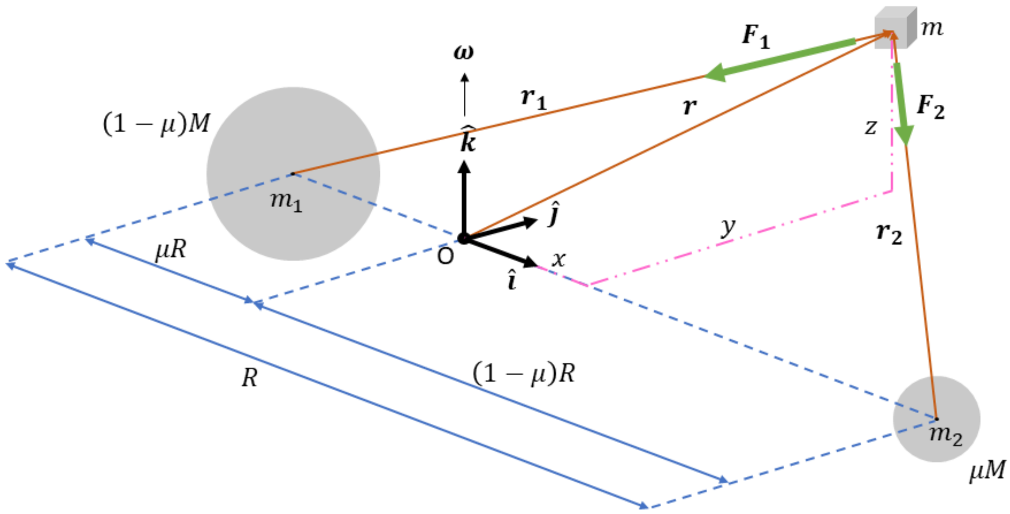

Figure 1.1: Geometric schematization of the CR3BP

$$\mu = \frac{m_2}{M} \tag{1.3}$$

in this way the primary bodies' masses, m_1 and m_2, become:

$$\begin{gathered} m_1 = (1-\mu)M \\ m_2 = \mu M \end{gathered} \tag{1.4}$$

since the distance between the primary bodies is R, in the synodic system, m_1 is placed at

$$\vec{X}_{m_1} = \begin{Bmatrix} -\mu R \\ 0 \\ 0 \end{Bmatrix} \tag{1.5}$$

while m_2 is placed at

$$\vec{X}_{m_2} = \begin{Bmatrix} (1-\mu)\,R \\ 0 \\ 0 \end{Bmatrix} \tag{1.6}$$

and the spacecraft, m, has the following general coordinates

$$\vec{X}_{sc} = \begin{Bmatrix} x \\ y \\ z \end{Bmatrix} \tag{1.7}$$

The synodic reference frame $\left(\hat{i}\hat{j}\hat{k}\right)$ rotates with a constant angular velocity

$$\vec{\omega} = \sqrt{\frac{GM}{R^3}}\hat{k} \tag{1.8}$$

Also, the synodic period is equal to $\tau = \frac{2\pi}{\omega}$, which, when combined with Eq.(1.8), gives

$$\tau = 2\pi\sqrt{\frac{R^3}{GM}} \tag{1.9}$$

Since ω is constant, it is possible to write the equation of motion of the spacecraft with mass m in the synodic reference frame using the following dynamical principles

$$\ddot{\vec{r}} + \vec{\omega} \times (\vec{\omega} \times \vec{r}) + 2\vec{\omega} \times \dot{\vec{r}} = \frac{1}{m}\left(\vec{F}_1 + \vec{F}_2\right) \tag{1.10}$$

where the first term is the relative acceleration in the synodic frame, the second is the centripetal acceleration and the third is the Coriolis acceleration. The right-hand side of the equation is the accelerations due to the gravitational forces of m_1 and m_2 on m. To obtain Eq.(1.10) in each of the three coordinates, we have to decompose the vectors into the three coordinates. It is possible to write the first term of the left-hand side $\ddot{\vec{r}}$ and $\dot{\vec{r}}$, $\vec{r}$ and $\vec{\omega}$ as

$$\ddot{\vec{r}} = \begin{Bmatrix} \ddot{x} \\ \ddot{y} \\ \ddot{z} \end{Bmatrix} \quad \dot{\vec{r}} = \begin{Bmatrix} \dot{x} \\ \dot{y} \\ \dot{z} \end{Bmatrix} \quad \vec{r} = \begin{Bmatrix} x \\ y \\ z \end{Bmatrix} \quad \vec{\omega} = \begin{Bmatrix} 0 \\ 0 \\ \omega \end{Bmatrix} \tag{1.11}$$

while the second term $\vec{\omega} \times (\vec{\omega} \times \vec{r})$ of Eq.(1.10) is obtained in two steps as

$$\vec{\omega} \times \vec{r} = \begin{vmatrix} \hat{i} & \hat{j} & \hat{k} \\ 0 & 0 & \omega \\ x & y & z \end{vmatrix} = \begin{Bmatrix} -\omega y \\ \omega x \\ 0 \end{Bmatrix} \tag{1.12}$$

$$\vec{\omega} \times (\vec{\omega} \times \vec{r}) = \begin{vmatrix} \hat{i} & \hat{j} & \hat{k} \\ 0 & 0 & \omega \\ -\omega y & \omega x & 0 \end{vmatrix} = \begin{Bmatrix} -\omega^2 x \\ -\omega^2 y \\ 0 \end{Bmatrix} \tag{1.13}$$

Similarly, we compute the third term $2\vec{\omega} \times \dot{\vec{r}}$ as

$$2\vec{\omega} \times \dot{\vec{r}} = \begin{vmatrix} \hat{i} & \hat{j} & \hat{k} \\ 0 & 0 & 2\omega \\ \dot{x} & \dot{y} & \dot{z} \end{vmatrix} = \begin{Bmatrix} -2\omega\dot{y} \\ 2\omega\dot{x} \\ 0 \end{Bmatrix} \tag{1.14}$$

Using Eq.(1.4), the gravitational forces of m_1 on m and m_2 on m, $\vec{F_1}$ and $\vec{F_2}$, become

$$\vec{F_1} = -\frac{Gm_1 m}{r_1^2}\frac{\vec{r_1}}{r_1} = -G\left(1-\mu\right)Mm\frac{\vec{r_1}}{r_1^3} \tag{1.15}$$

$$\vec{F_2} = -\frac{Gm_2 m}{r_2^2}\frac{\vec{r_2}}{r_2} = -G\mu Mm\frac{\vec{r_2}}{r_2^3} \tag{1.16}$$

where $\vec{r_1}$ and $\vec{r_2}$ are defined as

$$\vec{r_1} = \left\{\begin{array}{c} x+\mu R \\ y \\ z \end{array}\right\} \quad \vec{r_2} = \left\{\begin{array}{c} x-\left(1-\mu\right)R \\ y \\ z \end{array}\right\} \tag{1.17}$$

and consequently their magnitudes are equal to

$$\begin{aligned} r_1 &= \sqrt{\left(x+\mu R\right)^2 + y^2 + z^2} \\ r_2 &= \sqrt{\left(x-\left(1-\mu\right)R\right)^2 + y^2 + z^2} \end{aligned} \tag{1.18}$$

Collecting all terms, we obtain

$$\left\{\begin{array}{l} \ddot{x} - 2\omega\dot{y} - \omega^2 x = -G\left(1-\mu\right)M\frac{x+\mu R}{r_1^3} - G\mu M\frac{x-(1-\mu)R}{r_2^3} \\ \ddot{y} + 2\omega\dot{x} - \omega^2 y = -G\left(1-\mu\right)M\frac{y}{r_1^3} - G\mu M\frac{y}{r_2^3} \\ \ddot{z} = -G\left(1-\mu\right)M\frac{z}{r_1^3} - G\mu M\frac{z}{r_2^3} \end{array}\right. \tag{1.19}$$

We can recast Eq.(1.19) in non-dimensional form. This allows us to identify the characteristics of the system in a unit-independent manner, facilitating further analysis. First, we define the dimensionless position vector, $\vec{\rho}$, and the dimensionless time, τ, as

$$\vec{\rho} = \left\{\begin{array}{c} \xi \\ \eta \\ \zeta \end{array}\right\} = \frac{\vec{r}}{R} \tag{1.20}$$

$$\tau = \omega t \tag{1.21}$$

and, using the chain rule, we can write any time derivative as

$$\dot{\left(\cdot\right)} = \frac{d\left(\cdot\right)}{dt} = \omega\frac{d\left(\cdot\right)}{d\tau} = \omega\left(\cdot\right)' \tag{1.22}$$

Thus, the set of Eq.(1.19) becomes:

$$\left\{\begin{array}{l} R\omega^2\xi'' - 2R\omega^2\eta' - R\omega^2\xi = -G\left(1-\mu\right)M\frac{R\xi+\mu R}{R^3\rho_1^3} - G\mu M\frac{\xi-(1-\mu)R}{R^3\rho_2^3} \\ R\omega^2\eta'' + 2R\omega^2\xi' - R\omega^2\eta = -G\left(1-\mu\right)M\frac{R\eta}{R^3\rho_1^3} - G\mu M\frac{R\eta}{R^3\rho_2^3} \\ R\omega^2\zeta'' = -G\left(1-\mu\right)M\frac{R\zeta}{R^3\rho_1^3} - G\mu M\frac{R\zeta}{R^3\rho_2^3} \end{array}\right. \tag{1.23}$$

From Eq.(1.8), $\omega^2 = \frac{GM}{R^3}$, so Eq.(1.23) becomes:

$$\begin{cases} \xi'' - 2\eta' - \xi = -\left(1-\mu\right)\frac{\xi+\mu}{\rho_1^3} - \mu\frac{\xi-(1-\mu)}{\rho_2^3} \\ \eta'' + 2\xi' - \eta = -\left(1-\mu\right)\frac{\eta}{\rho_1^3} - \mu\frac{\eta}{\rho_2^3} \\ \zeta'' = -\left(1-\mu\right)\frac{\zeta}{\rho_1^3} - \mu\frac{\zeta}{\rho_2^3} \end{cases} \tag{1.24}$$

where

$$\begin{aligned} \rho_1 &= \sqrt{\left(\xi+\mu\right)^2 + \eta^2 + \zeta^2} \\ \rho_2 &= \sqrt{\left(\xi-\left(1-\mu\right)\right)^2 + \eta^2 + \zeta^2} \end{aligned} \tag{1.25}$$

1.2 Jacobi Integral

The CR3BP has one conservation law called the Jacobi integral, also known as Jacobi constant. We start by defining a three-body potential

$$\mathcal{U} = \frac{1}{2}\left(\xi^2 + \eta^2\right) + \frac{1-\mu}{\rho_1} + \frac{\mu}{\rho_2} \tag{1.26}$$

where the first term on the right hand side is the centrifugal force, while the second and third terms are the gravitational potentials of masses m_1 and m_2. We can compute the partial derivatives of $\mathcal{U}$ with respect to ξ, η and ζ as

$$\frac{\partial \mathcal{U}}{\partial \xi} = \xi - \frac{1-\mu}{\rho_1^2}\frac{\partial \rho_1}{\partial \xi} - \frac{\mu}{\rho_2^2}\frac{\partial \rho_2}{\partial \xi} \tag{1.27}$$

$$\frac{\partial \mathcal{U}}{\partial \eta} = \eta - \frac{1-\mu}{\rho_1^2}\frac{\partial \rho_1}{\partial \eta} - \frac{\mu}{\rho_2^2}\frac{\partial \rho_2}{\partial \eta} \tag{1.28}$$

$$\frac{\partial \mathcal{U}}{\partial \zeta} = \zeta - \frac{1-\mu}{\rho_1^2}\frac{\partial \rho_1}{\partial \zeta} - \frac{\mu}{\rho_2^2}\frac{\partial \rho_2}{\partial \zeta} \tag{1.29}$$

Starting from the definition of ρ_1

$$\rho_1^2 = \left(\xi+\mu\right)^2 + \eta^2 + \zeta^2 \tag{1.30}$$

it is possible to write

$$2\rho_1\frac{\partial \rho_1}{\partial \xi} = 2\left(\xi+\mu\right) \tag{1.31}$$

so that

$$\frac{\partial \rho_1}{\partial \xi} = \frac{\xi+\mu}{\rho_1} \tag{1.32}$$

With the same procedure, we obtain

$$\frac{\partial \rho_2}{\partial \xi} = \frac{\xi - (1-\mu)}{\rho_2} \tag{1.33}$$

In this way, Eq.(1.27) becomes

$$\frac{\partial \mathcal{U}}{\partial \xi} = \xi - \frac{1-\mu}{\rho_1^2}\frac{\xi + \mu}{\rho_1} - \frac{\mu}{\rho_2^2}\frac{\xi - (1-\mu)}{\rho_2} \tag{1.34}$$

Similarly, $\frac{\partial \mathcal{U}}{\partial \eta}$ and $\frac{\partial \mathcal{U}}{\partial \zeta}$ become

$$\frac{\partial \mathcal{U}}{\partial \eta} = \eta - \frac{1-\mu}{\rho_1^2}\frac{\eta}{\rho_1} - \frac{\mu}{\rho_2^2}\frac{\eta}{\rho_2} \tag{1.35}$$

$$\frac{\partial \mathcal{U}}{\partial \zeta} = \zeta - \frac{1-\mu}{\rho_1^2}\frac{\zeta}{\rho_1} - \frac{\mu}{\rho_2^2}\frac{\zeta}{\rho_2} \tag{1.36}$$

The set of Eq.(1.24) becomes

$$\begin{cases} \xi'' - 2\eta' = \frac{\partial \mathcal{U}}{\partial \xi} \\ \eta'' + 2\xi' = \frac{\partial \mathcal{U}}{\partial \eta} \\ \zeta'' = \frac{\partial \mathcal{U}}{\partial \zeta} \end{cases} \tag{1.37}$$

Multiplying the first equation of Eq.(1.37) by ξ', the second by η' the third by ζ' and adding them together, we obtain

$$\xi'\xi'' + \eta'\eta'' + \zeta'\zeta'' = \frac{\partial \mathcal{U}}{\partial \xi}\frac{\partial \xi}{\partial \tau} + \frac{\partial \mathcal{U}}{\partial \eta}\frac{\partial \eta}{\partial \tau} + \frac{\partial \mathcal{U}}{\partial \zeta}\frac{\partial \zeta}{\partial \tau} \tag{1.38}$$

which can be rewritten as

$$\frac{1}{2}\frac{d}{d\tau}\left(\xi'^2 + \eta'^2 + \zeta'^2\right) = \frac{d\mathcal{U}}{d\tau} \tag{1.39}$$

Considering the magnitude of the non dimensional relative velocity of the mass m equal to $V = \sqrt{\xi'^2 + \eta'^2 + \zeta'^2}$ and integrating the previous equation, we obtain

$$V^2 = 2\mathcal{U} - C \tag{1.40}$$

where C is a constant of integration known as the Jacobi constant, or Jacobi integral. Fig. 1.2 shows the potential $\mathcal{U}$ as a function of ξ, η, ζ, while Fig. 1.3 shows contour lines of $\mathcal{U}$, which suggest us that there are five points at the local minima of $\mathcal{U}$. These points are called Lagrange points and will be discussed in the following section.

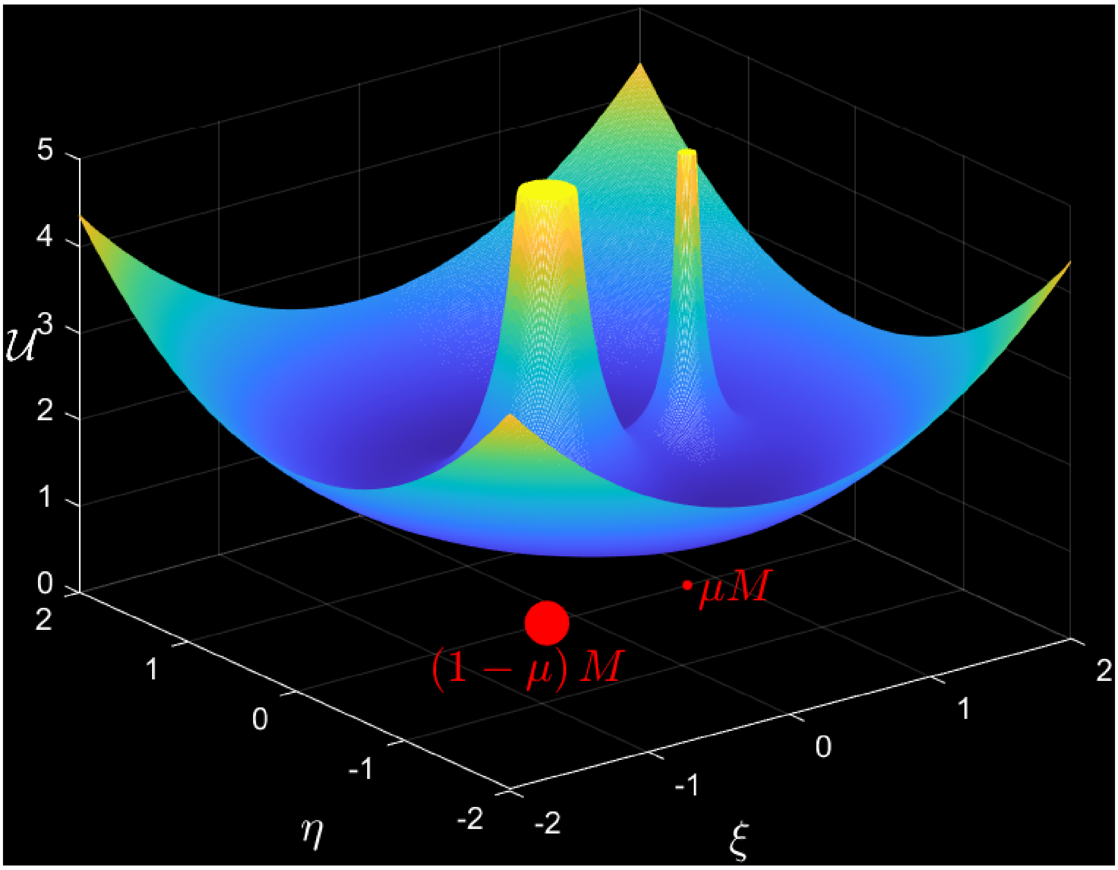

Figure 1.2: Three-body Potential $\mathcal{U}$

1.3 Lagrange Points

In the CR3BP, the Lagrange points are equilibrium points where the gravitational forces of two large bodies equal the centrifugal force felt by the smaller third body. There are five such points in which the velocities and accelerations of the third body must be equal to zero

$$\xi'' = \xi' = \eta'' = \eta' = \zeta'' = \zeta' = 0 \tag{1.41}$$

which means that

$$\begin{cases} \frac{\partial \mathcal{U}}{\partial \xi} = 0 \\ \frac{\partial \mathcal{U}}{\partial \eta} = 0 \\ \frac{\partial \mathcal{U}}{\partial \zeta} = 0 = -\left(1-\mu\right)\frac{\zeta}{\rho_1^3} - \mu\frac{\zeta}{\rho_2^3} \end{cases} \tag{1.42}$$

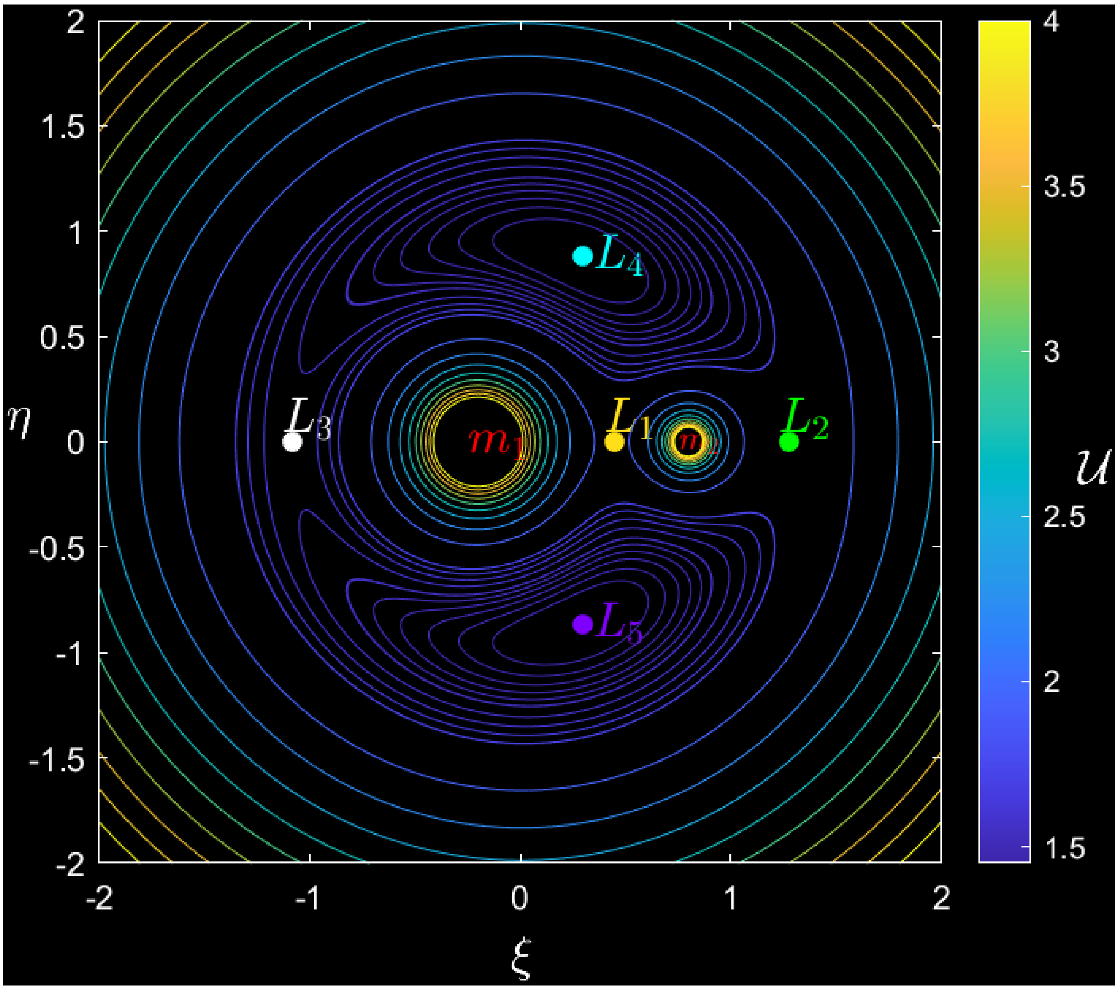

Figure 1.3: Contour lines of $\mathcal{U}$

The third equation of Eq.(1.42) suggests us that the only possible solution is $\zeta = 0$. This means that all five equilibrium points lie on the $\xi - \eta$ plane, which is the plane of motion of the primary bodies.

1.3.1 Collinear Points

Using the definition of $\mathcal{U}$, Eq.(1.42) can be rewritten as

$$\begin{cases} \xi = (1-\mu)\,\frac{\xi+\mu}{\rho_1^3} + \mu\frac{\xi-(1-\mu)}{\rho_2^3} \\ \eta = (1-\mu)\,\frac{\eta}{\rho_1^3} + \mu\frac{\eta}{\rho_2^3} \\ \zeta = 0 \end{cases} \tag{1.43}$$

From the second equation of Eq.(1.43), we can find that the first group of equilibrium points must satisfy $\eta = 0$ is a solution of the second equation, they are positioned along the ξ-axis. Since $\eta = 0$ we have

$$\begin{aligned} \rho_1 &= \xi + \mu \\ \rho_2 &= \xi - (1-\mu) \end{aligned} \tag{1.44}$$

Replacing ρ_1 and ρ_2 in Eq.(1.43) we obtain

$$\begin{cases} \xi = (1-\mu)\frac{\xi+\mu}{|\xi+\mu|^3} + \mu\frac{\xi-(1-\mu)}{|\xi-(1-\mu)|^3} \\ \eta = 0 \\ \zeta = 0 \end{cases} \tag{1.45}$$

where the absolute values are utilized to ensure that the terms in the denominators, representing physical distances, are always positive. The solution to this cubic set of equations gives three real roots which are the adimensional x-coordinates of the libration points L_1, L_2 and L_3.

1.3.2 Equilateral Points

There are two more equilibrium points, called equilateral points, which are the vertices of an equilateral triangle such that $\rho_1 = \rho_2 = 1$. Using this information, we get

$$\sqrt{(\xi+\mu)^2 + \eta^2} = \sqrt{(\xi-(1-\mu))^2 + \eta^2} \tag{1.46}$$

Solving for ξ we have

$$\xi = \frac{1}{2} - \mu \tag{1.47}$$

So ρ_1 becomes

$$\rho_1 = \sqrt{\left(\frac{1}{2} - \mu + \mu\right)^2 + \eta^2} = 1 \tag{1.48}$$

and consequently we obtain

$$\eta = \pm\frac{\sqrt{3}}{2} \tag{1.49}$$

L_4 and L_5 have the following nondimensional coordinates

$$\vec{\chi}_{L_4} = \begin{Bmatrix} \frac{1}{2} - \mu \\ \frac{\sqrt{3}}{2} \\ 0 \end{Bmatrix} \quad \vec{\chi}_{L_5} = \begin{Bmatrix} \frac{1}{2} - \mu \\ -\frac{\sqrt{3}}{2} \\ 0 \end{Bmatrix} \tag{1.50}$$

In the CR3BP, a mass placed exactly at one of these five Lagrange points will theoretically stay there forever. However, in reality we have to consider the effects of perturbations such as solar radiation pressure, non-homogeneous gravitational fields and other perturbations. Periodic orbits around the Lagrange points exist and will be discussed in Sec. 1.4 and Sec. 1.5. In Fig. 1.4, the positions of the Lagrange points with respect to the primary masses are shown.

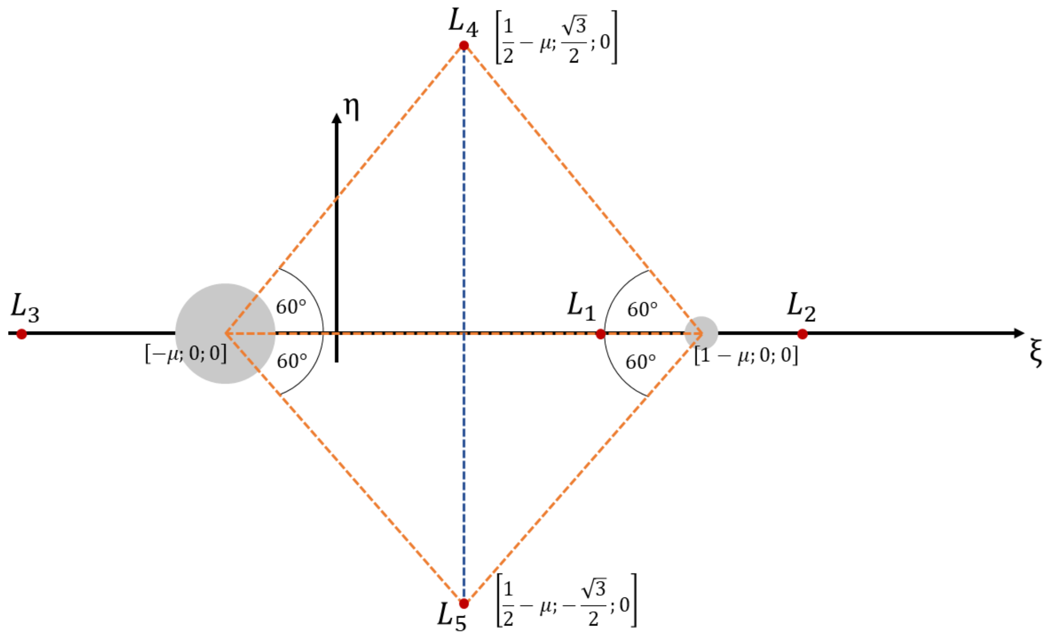

Figure 1.4: Position of the Lagrange Point

1.3.3 Stability of Lagrange Points

The question that needs to be addressed with regards to the Lagrange points, also known as libration points, is whether or not they are stable. The stability of an equilibrium point is determined by the ability of a particle to return to equilibrium if slightly perturbed. To evaluate the stability of the libration points, we slightly perturb the exact solution at each Lagrange point as

$$\begin{cases} \xi = \xi_e + \delta\xi \\ \eta = \eta_e + \delta\eta \\ \zeta = \zeta_e + \delta\zeta = \delta\zeta \end{cases} \tag{1.51}$$

where ξ_e, η_e and ζ_e are the coordinates of Lagrange points and $\delta\xi$, $\delta\eta$ and $\delta\zeta$ are small perturbations in the ξ, η and ζ directions, respectively. Now we can substitute

Eq.(1.51) into Eq.(1.24) and we obtain

$$\left\{\begin{array}{l} \delta\ddot{\xi} - 2\delta\dot{\eta} - \xi_e - \delta\xi = -\left(1-\mu\right)\frac{\xi_e+\delta\xi+\mu}{\rho_1^3} - \mu\frac{\xi_e+\delta\xi-(1-\mu)}{\rho_2^3} \\ \delta\ddot{\eta} + 2\delta\dot{\xi} - \eta_e - \delta\eta = -\left(1-\mu\right)\frac{\eta_e+\delta\eta}{\rho_1^3} - \mu\frac{\eta_e+\delta\eta}{\rho_2^3} \\ \delta\ddot{\zeta} = -\left(1-\mu\right)\frac{\delta\zeta}{\rho_1^3} - \mu\frac{\delta\zeta}{\rho_2^3} \end{array}\right. \tag{1.52}$$

where ρ_1 and ρ_2 become

$$\begin{aligned} \rho_1 &= \sqrt{\left(\xi_e + \delta\xi + \mu\right)^2 + \left(\eta_e + \delta\eta\right)^2 + \delta\zeta^2} \\ \rho_2 &= \sqrt{\left(\xi_e + \delta\xi - \left(1-\mu\right)\right)^2 + \left(\eta_e + \delta\eta\right)^2 + \delta\zeta^2} \end{aligned} \tag{1.53}$$

To solve Eq.(1.52) in $\delta\xi$, $\delta\eta$ and $\delta\zeta$ we collect like terms. We simplify ρ_1^{-3} and ρ_2^{-3} as

$$\begin{aligned} \rho_1^{-3} &= \left[\left(\xi_e + \delta\xi + \mu\right)^2 + \left(\eta_e + \delta\eta\right)^2 + \delta\zeta^2\right]^{-\frac{3}{2}} = \\ &= \left[\left(\xi_e + \mu\right)^2 + \eta_e^2 + 2\left(\xi_e + \mu\right)\delta\xi + 2\eta_e\delta\eta + \delta\xi^2 + \delta\eta^2 + \delta\zeta^2\right]^{-\frac{3}{2}} \end{aligned} \tag{1.54}$$

$$\begin{aligned} \rho_2^{-3} &= \left[\left(\xi_e + \delta\xi - \left(1-\mu\right)\right)^2 + \left(\eta_e + \delta\eta\right)^2 + \delta\zeta^2\right]^{-\frac{3}{2}} = \\ &= \left[\left(\xi_e - \left(1-\mu\right)\right)^2 + \eta_e^2 + 2\left(\xi_e - \left(1-\mu\right)\right)\delta\xi + 2\eta_e\delta\eta + \delta\xi^2 + \delta\eta^2 + \delta\zeta^2\right]^{-\frac{3}{2}} \end{aligned} \tag{1.55}$$

Neglecting the higher-order terms $\delta\xi^2, \delta\eta^2, \delta\zeta^2$ and applying Taylor series expansions, we obtain

$$\begin{aligned} \rho_1^{-3} &\approx \left[\rho_{1e}^2 + 2\left(\xi_e + \mu\right)\delta\xi + 2\eta_e\delta\eta\right]^{-\frac{3}{2}} \approx \\ &\approx \rho_{1e}^{-3}\left[1 - 3\rho_{1e}^{-2}\left(\left(\xi_e + \mu\right)\delta\xi + \eta_e\delta\eta\right)\right] \\ \rho_2^{-3} &\approx \left[\rho_{2e}^2 + 2\left(\xi_e - \left(1-\mu\right)\right)\delta\xi + 2\eta_e\delta\eta\right]^{-\frac{3}{2}} \approx \\ &\approx \rho_{2e}^{-3}\left[1 - 3\rho_{2e}^{-2}\left(\left(\xi_e - \left(1-\mu\right)\right)\delta\xi + \eta_e\delta\eta\right)\right] \end{aligned} \tag{1.56}$$

Thus Eq.(1.52) simplifies to

$$\left\{\begin{array}{l} \delta\ddot{\xi} - 2\delta\dot{\eta} - \left(1-A\right)\delta\xi - B\delta\eta = 0 \\ \delta\ddot{\eta} + 2\delta\dot{\xi} - B\delta\xi - \left(1-C\right)\delta\eta = 0 \\ \delta\ddot{\zeta} + D\delta\zeta = 0 \end{array}\right. \tag{1.57}$$

where A, B, C and D are real constants such that

$$\begin{array}{l} A = \left(1-\mu\right)\left[\frac{1}{\rho_{1e}^3} - 3\frac{\left(\xi_e+\mu\right)^2}{\rho_{1e}^5}\right] + \mu\left[\frac{1}{\rho_{2e}^3} - 3\frac{\left(\xi_e-(1-\mu)\right)^2}{\rho_{2e}^5}\right] \\ B = 3\left(1-\mu\right)\eta_e\left[\frac{\left(\xi_e+\mu\right)}{\rho_{1e}^5} + \frac{\left(\xi_e-(1-\mu)\right)}{\rho_{2e}^5}\right] \\ C = \left(1-\mu\right)\left[\frac{1}{\rho_{1e}^3} - 3\frac{\eta_e^2}{\rho_{1e}^5}\right] + \mu\left[\frac{1}{\rho_{2e}^3} - 3\frac{\eta_e^2}{\rho_{2e}^5}\right] \\ D = \frac{1-\mu}{\rho_{1e}^3} + \frac{\mu}{\rho_{2e}^3} \end{array} \tag{1.58}$$

We assume that Eq.(1.57) have a solution in the form of $\delta x = ce^{\lambda t}$, so we obtain

$$\begin{bmatrix} \lambda^2 - (1-A) & -B-2\lambda & 0 \\ -B+2\lambda & \lambda^2-(1-C) & 0 \\ 0 & 0 & \lambda^2+D \end{bmatrix} \begin{Bmatrix} \delta\xi \\ \delta\eta \\ \delta\zeta \end{Bmatrix} = \begin{Bmatrix} 0 \\ 0 \\ 0 \end{Bmatrix} \tag{1.59}$$

where

$$\delta x = \begin{Bmatrix} \delta\xi \\ \delta\eta \\ \delta\zeta \end{Bmatrix} \tag{1.60}$$

When the matrix of Eq.(1.59) is singular, this eigenvalue problem provides us with non-trivial solutions of the system. Thus, we derive and compute the roots of the characteristic equation of this eigenvalue problem

$$\begin{aligned} \lambda^6 + \lambda^4(2+C+A+D) + \lambda^2(3+AC-B^2+D) + \\ +(1-C-A+AC-B^2+D) = 0 \end{aligned} \tag{1.61}$$

which give us information regarding the stability of the system. If each value of λ is purely imaginary and/or has negative real roots, the system is stable.
Furthermore, it should be acknowledged that although it can be proven that collinear points are consistently unstable, eigenvalue analysis reveals that equilateral points remain stable only when the mass ratio μ is less than approximately $\mu^* = 0.0385209$ [2]. Given that $\mu < \mu^*$ holds true for any combination of the Sun with a planet in our Solar System, L_4 and L_5 points are invariably stable.

1.4 Introduction to Dynamical System Theory

Dynamical Systems Theory (DST) is a mathematical formulation used to understand and predict the behavior of complex systems. In astrodynamics, N-body systems are highly sensitive to initial conditions, which is why these systems are considered to be chaotic. DST provides a systematic way to discover and classify sets of orbits that can be used in space missions. This is a more modern approach than older methods, such as patched conics and Lambert's problem. However, one of the major disadvantages of DST is that it requires significant computational power. With the advancement of technology, this limitation is becoming less of a concern. The Genesis mission was the first one to have its orbits entirely planned through dynamical systems theory, utilizing a Sun-Earth/Moon L_1 orbit [3].

1.4.1 The State Transition Matrix

Given the initial state of the system, a state transition matrix can be used to calculate the state of the system at any future time. A state transition matrix can be used to describe the linearized dynamics of the CR3BP. Thanks to *Dynamical Systems Theory*, the state transition matrix can be used to study periodic orbits of a system. Specifically, the state transition matrix can be used to calculate the stability of the system. For example, if a periodic trajectory is stable, small perturbations in the initial state will not result in large changes in the final state. This can be determined by analyzing the eigenvalues of the monodromy matrix, which is defined as the state transition matrix evaluated at exactly one orbital period. If all the eigenvalues have a magnitude less than 1, the orbit is stable. If, among those, the largest eigenvalue has a magnitude equal to 1, the orbit is marginally stable, and in case at least one eigenvalue has a magnitude greater than 1, the orbit is unstable. The state transition matrix can also be used to study the *invariant manifolds* and so to determine trajectories that leave from or arrive at a given periodic orbit.

Let's recall the three-body potential given by Eq.(1.26) and dimensionless equations of motion, Eq.(1.37). A Taylor series expansions of the three-body potential, $\mathcal{U}$, can be written as

$$\begin{aligned} \frac{\partial \mathcal{U}}{\partial \xi} &= \frac{\partial}{\partial \xi}\left(\frac{\partial \mathcal{U}}{\partial \xi}\right)\xi + \frac{\partial}{\partial \eta}\left(\frac{\partial \mathcal{U}}{\partial \xi}\right)\eta + \frac{\partial}{\partial \zeta}\left(\frac{\partial \mathcal{U}}{\partial \xi}\right)\zeta + \\ &+ \frac{\partial}{\partial \dot{\xi}}\left(\frac{\partial \mathcal{U}}{\partial \xi}\right)\left(\frac{d\xi}{dt}\right) + \frac{\partial}{\partial \dot{\eta}}\left(\frac{\partial \mathcal{U}}{\partial \xi}\right)\left(\frac{d\eta}{dt}\right) + \frac{\partial}{\partial \dot{\zeta}}\left(\frac{\partial \mathcal{U}}{\partial \xi}\right)\left(\frac{d\zeta}{dt}\right) \end{aligned} \tag{1.62}$$

Since $\mathcal{U}$ is only a function of ξ, η and ζ, Eq.(1.62) becomes

$$\begin{aligned} \frac{\partial \mathcal{U}}{\partial \xi} &= \frac{\partial}{\partial \xi}\left(\frac{\partial \mathcal{U}}{\partial \xi}\right)\xi + \frac{\partial}{\partial \eta}\left(\frac{\partial \mathcal{U}}{\partial \xi}\right)\eta + \frac{\partial}{\partial \zeta}\left(\frac{\partial \mathcal{U}}{\partial \xi}\right)\zeta = \\ &= \left(\frac{\partial^2 \mathcal{U}}{\partial \xi^2}\right)\xi + \left(\frac{\partial^2 \mathcal{U}}{\partial \xi \partial \eta}\right)\eta + \left(\frac{\partial^2 \mathcal{U}}{\partial \xi \partial \zeta}\right)\zeta \end{aligned} \tag{1.63}$$

Similarly, we get

$$\frac{\partial \mathcal{U}}{\partial \eta} = \left(\frac{\partial^2 \mathcal{U}}{\partial \xi \partial \eta}\right)\xi + \left(\frac{\partial^2 \mathcal{U}}{\partial \eta^2}\right)\eta + \left(\frac{\partial^2 \mathcal{U}}{\partial \eta \partial \zeta}\right)\zeta \tag{1.64}$$

and

$$\frac{\partial \mathcal{U}}{\partial \zeta} = \left(\frac{\partial^2 \mathcal{U}}{\partial \xi \partial \zeta}\right)\xi + \left(\frac{\partial^2 \mathcal{U}}{\partial \eta \partial \zeta}\right)\eta + \left(\frac{\partial^2 \mathcal{U}}{\partial \zeta^2}\right)\zeta \tag{1.65}$$

Finally, the dimensionless equations of motion (1.37) become

$$\left\{ \begin{aligned} \xi'' - 2\eta' &= \left(\frac{\partial^2 \mathcal{U}}{\partial \xi^2}\right)\xi + \left(\frac{\partial^2 \mathcal{U}}{\partial \xi \partial \eta}\right)\eta + \left(\frac{\partial^2 \mathcal{U}}{\partial \xi \partial \zeta}\right)\zeta \\ \eta'' + 2\xi' &= \left(\frac{\partial^2 \mathcal{U}}{\partial \xi \partial \eta}\right)\xi + \left(\frac{\partial^2 \mathcal{U}}{\partial \eta^2}\right)\eta + \left(\frac{\partial^2 \mathcal{U}}{\partial \eta \partial \zeta}\right)\zeta \\ \zeta'' &= \left(\frac{\partial^2 \mathcal{U}}{\partial \xi \partial \zeta}\right)\xi + \left(\frac{\partial^2 \mathcal{U}}{\partial \eta \partial \zeta}\right)\eta + \left(\frac{\partial^2 \mathcal{U}}{\partial \zeta^2}\right)\zeta \end{aligned} \right. \tag{1.66}$$

We define a six element state vector, $\vec{q}$, as $\vec{q} = \left\{\xi, \eta, \zeta, \dot{\xi}, \dot{\eta}, \dot{\zeta}\right\}^T$ and the first-order variational equations are derived and result in the following vector differential equation:

$$\dot{\vec{q}} = A(\tau)\,\vec{q} \tag{1.67}$$

The 6x6 matrix $A(\tau)$ is typically not constant when the reference solution is an arbitrary trajectory. However, when the reference solution is periodic, $A(\tau)$ also exhibits periodicity. $A(\tau)$ can be broken down into four 3x3 sub-matrices:

$$A(\tau) = \begin{bmatrix} 0_{3\times3} & \mathbb{I}_{3\times3} \\ U & \Omega \end{bmatrix} \tag{1.68}$$

where $0_{3\times3}$ is the 3x3 zero matrix, $\mathbb{I}_{3\times3}$ is the 3x3 identity matrix, and U and Ω are defined as

$$U = \begin{bmatrix} \frac{\partial^2\mathcal{U}}{\partial\xi^2} & \frac{\partial^2\mathcal{U}}{\partial\xi\partial\eta} & \frac{\partial^2\mathcal{U}}{\partial\xi\partial\zeta} \\ \frac{\partial^2\mathcal{U}}{\partial\xi\partial\eta} & \frac{\partial^2\mathcal{U}}{\partial\eta^2} & \frac{\partial^2\mathcal{U}}{\partial\eta\partial\zeta} \\ \frac{\partial^2\mathcal{U}}{\partial\xi\partial\zeta} & \frac{\partial^2\mathcal{U}}{\partial\eta\partial\zeta} & \frac{\partial^2\mathcal{U}}{\partial\zeta^2} \end{bmatrix} \tag{1.69}$$

$$\Omega = \begin{bmatrix} 0 & 2 & 0 \\ -2 & 0 & 0 \\ 0 & 0 & 0 \end{bmatrix} \tag{1.70}$$

so the extended form of matrix $A(\tau)$ is

$$A(\tau) = \begin{bmatrix} 0 & 0 & 0 & 1 & 0 & 0 \\ 0 & 0 & 0 & 0 & 1 & 0 \\ 0 & 0 & 0 & 0 & 0 & 1 \\ \frac{\partial^2\mathcal{U}}{\partial\xi^2} & \frac{\partial^2\mathcal{U}}{\partial\xi\partial\eta} & \frac{\partial^2\mathcal{U}}{\partial\xi\partial\zeta} & 0 & 2 & 0 \\ \frac{\partial^2\mathcal{U}}{\partial\xi\partial\eta} & \frac{\partial^2\mathcal{U}}{\partial\eta^2} & \frac{\partial^2\mathcal{U}}{\partial\eta\partial\zeta} & -2 & 0 & 0 \\ \frac{\partial^2\mathcal{U}}{\partial\xi\partial\zeta} & \frac{\partial^2\mathcal{U}}{\partial\eta\partial\zeta} & \frac{\partial^2\mathcal{U}}{\partial\zeta^2} & 0 & 0 & 0 \end{bmatrix} \tag{1.71}$$

where

$$\begin{aligned} \frac{\partial^2\mathcal{U}}{\partial\xi^2} &= 1 - \frac{1-\mu}{\rho_1^3} - \frac{\mu}{\rho_2^3} + \frac{3(1-\mu)(\xi+\mu)^2}{\rho_1^5} + \frac{3\mu(\xi-1+\mu)^2}{\rho_2^5} \\ \frac{\partial^2\mathcal{U}}{\partial\xi\partial\eta} &= \frac{3(1-\mu)(\xi+\mu)\eta}{\rho_1^5} + \frac{3\mu(\xi-1+\mu)\eta}{\rho_2^5} \\ \frac{\partial^2\mathcal{U}}{\partial\xi\partial\zeta} &= \frac{3(1-\mu)(\xi+\mu)\zeta}{\rho_1^5} + \frac{3\mu(\xi-1+\mu)\zeta}{\rho_2^5} \\ \frac{\partial^2\mathcal{U}}{\partial\eta^2} &= 1 - \frac{1-\mu}{\rho_1^3} - \frac{\mu}{\rho_2^3} + \frac{3(1-\mu)\eta^2}{\rho_1^5} + \frac{3\mu\eta^2}{\rho_2^5} \\ \frac{\partial^2\mathcal{U}}{\partial\eta\partial\zeta} &= \frac{3(1-\mu)\eta\zeta}{\rho_1^5} + \frac{3\mu\eta\zeta}{\rho_2^5} \\ \frac{\partial^2\mathcal{U}}{\partial\zeta^2} &= -\frac{1-\mu}{\rho_1^3} - \frac{\mu}{\rho_2^3} + \frac{3(1-\mu)\zeta^2}{\rho_1^5} + \frac{3\mu\zeta^2}{\rho_2^5} \end{aligned} \tag{1.72}$$

Using a *differential correction* method in *dynamical systems theory* is useful to calculate the initial conditions for a periodic orbit. However, we must also include the differential equations for the state transition matrix

$$\dot{\Phi}\,(\tau,0) = A\,(\tau)\,\Phi\,(\tau,0) \tag{1.73}$$

where $A\,(\tau)$ is given by Eq.(1.71) and the 6x6 state transition matrix results in the following partial derivatives

$$\Phi\,(\tau,0) = \begin{bmatrix} \frac{\partial\xi}{\partial\xi_0} & \frac{\partial\xi}{\partial\eta_0} & \frac{\partial\xi}{\partial\zeta_0} & \frac{\partial\xi}{\partial\dot{\xi}_0} & \frac{\partial\xi}{\partial\dot{\eta}_0} & \frac{\partial\xi}{\partial\dot{\zeta}_0} \\ \frac{\partial\eta}{\partial\xi_0} & \frac{\partial\eta}{\partial\eta_0} & \frac{\partial\eta}{\partial\zeta_0} & \frac{\partial\eta}{\partial\dot{\xi}_0} & \frac{\partial\eta}{\partial\dot{\eta}_0} & \frac{\partial\eta}{\partial\dot{\zeta}_0} \\ \frac{\partial\zeta}{\partial\xi_0} & \frac{\partial\zeta}{\partial\eta_0} & \frac{\partial\zeta}{\partial\zeta_0} & \frac{\partial\zeta}{\partial\dot{\xi}_0} & \frac{\partial\zeta}{\partial\dot{\eta}_0} & \frac{\partial\zeta}{\partial\dot{\zeta}_0} \\ \frac{\partial\dot{\xi}}{\partial\xi_0} & \frac{\partial\dot{\xi}}{\partial\eta_0} & \frac{\partial\dot{\xi}}{\partial\zeta_0} & \frac{\partial\dot{\xi}}{\partial\dot{\xi}_0} & \frac{\partial\dot{\xi}}{\partial\dot{\eta}_0} & \frac{\partial\dot{\xi}}{\partial\dot{\zeta}_0} \\ \frac{\partial\dot{\eta}}{\partial\xi_0} & \frac{\partial\dot{\eta}}{\partial\eta_0} & \frac{\partial\dot{\eta}}{\partial\zeta_0} & \frac{\partial\dot{\eta}}{\partial\dot{\xi}_0} & \frac{\partial\dot{\eta}}{\partial\dot{\eta}_0} & \frac{\partial\dot{\eta}}{\partial\dot{\zeta}_0} \\ \frac{\partial\dot{\zeta}}{\partial\xi_0} & \frac{\partial\dot{\zeta}}{\partial\eta_0} & \frac{\partial\dot{\zeta}}{\partial\zeta_0} & \frac{\partial\dot{\zeta}}{\partial\dot{\xi}_0} & \frac{\partial\dot{\zeta}}{\partial\dot{\eta}_0} & \frac{\partial\dot{\zeta}}{\partial\dot{\zeta}_0} \end{bmatrix} \tag{1.74}$$

with initial conditions

$$\Phi\,(0,0) = \mathbb{I}_{6\times 6} \tag{1.75}$$

Thus, for a set of initial conditions, it is then possible to numerically integrate the trajectory and the STM for any given span of time-

1.4.2 Differential Correction

In the CR3BP, there are different types of periodic orbits that can be classified based on their symmetry, such as axis-symmetric, doubly-symmetric, and planar. These periodic orbits will be described in Sec. 1.5. However, it is difficult to find these periodic orbits without using a suitable numerical method. In this section, a differential correction method is considered. Initially, we consider an estimate for the initial conditions, $\vec{q}_0$, which typically does not result in a periodic orbit. The objective is to identify a set of initial conditions that, when integrated using the equations of the CR3BP, will produce a periodic orbit over a given period of time τ with a final state $\vec{q}_f$, that is the same to that of the initial conditions [4]. This means that

$$\vec{q}_f = \vec{q}(\tau) = \vec{q}_0 \tag{1.76}$$

Expanding the equations of motion of the CR3BP, *i.e.* Eq.(1.24), to the first order about $(\vec{q}_0, \tau)$, we obtain

$$\delta\vec{q}_f = \Phi\,(\tau,0)\,\delta\vec{q}_0 + \frac{\partial\vec{q}_f}{\partial t}\delta\tau \tag{1.77}$$

where Φ is the state transition matrix and $\delta\,(\cdot)$ represents the incremental change of the quantity $(\cdot)$. The design of a halo orbit is presented in Subsec. 1.4.3 to better explain the Differential Corrections method.

1.4.3 Halo Orbit Design with Differential Correction

Numerical algorithms for the CR3BP that utilize the differential correction scheme make use of the properties of halo orbits to create periodic trajectories. Halo orbits are periodic three dimensional orbit which come from L_1, L_2 or L_3. They will be discussed better in Sec. 1.5. These characteristics include the fact that halo orbits pierce the $\xi - \zeta$ plane at right angles (occurring at a specific initial time t_0). Then, at half the period, the orbit must cross the $\xi - \zeta$ plane orthogonally again. As a result, the state vectors at t_0 and at half the period $t_{\frac{\tau}{2}}$ are:

$$\begin{aligned} \vec{q}(t_0) &= [\xi_0, 0, \zeta_0, 0, \dot{\eta}_0, 0] \\ \vec{q}\left(t_{\frac{\tau}{2}}\right) &= \left[\xi_{\frac{\tau}{2}}, 0, \zeta_{\frac{\tau}{2}}, 0, \dot{\eta}_{\frac{\tau}{2}}, 0\right] \end{aligned} \tag{1.78}$$

The algorithm begins with initial conditions obtained from the third order solution proposed in [5], at the time t_0. The trajectory is then propagated until it crosses the $\xi - \zeta$ again at half the period. $\dot{\xi}$ and $\dot{\zeta}$ are computed at this second crossing. Typically, these velocity components will not be zero. The goal of the algorithm is to iteratively adjust the initial conditions until the deviations in these velocity components are reduced to zero, resulting in a periodic orbit. In order to reduce the deviations in the velocity components at the second crossing of the $\xi - \zeta$ plane to zero, the algorithm utilizes the state transition matrix. The STM is initially set to the identity matrix, and is updated over time through numerical integration of 36 differential equations and together with the 6 state equations, for a total number of equations of 42. It's worth noting that the state of the orbit also changes at half period as a result of changes in the initial conditions.
In the process of reducing the deviations in the velocity components, three of the six terminal conditions $\xi_{\frac{\tau}{2}}, \zeta_{\frac{\tau}{2}}, \dot{\eta}_{\frac{\tau}{2}}$ are free, and the $\eta_{\frac{\tau}{2}}$ becomes zero as a result of the termination criteria of the trajectory propagation. This leaves only two variables to be reduced to zero. Indeed, expanding the second element of Eq.(1.77) we have

$$\begin{Bmatrix} \delta\xi_f \\ \delta\eta_f \\ \delta\zeta_f \\ \delta\dot{\xi}_f \\ \delta\dot{\eta}_f \\ \delta\dot{\zeta}_f \end{Bmatrix} = \begin{bmatrix} \Phi_{11} & \Phi_{12} & \Phi_{13} & \Phi_{14} & \Phi_{15} & \Phi_{16} \\ \Phi_{21} & \Phi_{22} & \Phi_{23} & \Phi_{24} & \Phi_{25} & \Phi_{26} \\ \Phi_{31} & \Phi_{32} & \Phi_{33} & \Phi_{34} & \Phi_{35} & \Phi_{36} \\ \Phi_{41} & \Phi_{42} & \Phi_{43} & \Phi_{44} & \Phi_{45} & \Phi_{46} \\ \Phi_{51} & \Phi_{52} & \Phi_{53} & \Phi_{54} & \Phi_{55} & \Phi_{56} \\ \Phi_{61} & \Phi_{62} & \Phi_{63} & \Phi_{64} & \Phi_{65} & \Phi_{66} \end{bmatrix} \begin{Bmatrix} \delta\xi_0 \\ \delta\eta_0 \\ \delta\zeta_0 \\ \delta\dot{\xi}_0 \\ \delta\dot{\eta}_0 \\ \delta\dot{\zeta}_0 \end{Bmatrix} + \begin{Bmatrix} \dot{\xi}_f \\ \dot{\eta}_f \\ \dot{\zeta}_f \\ \ddot{\xi}_f \\ \ddot{\eta}_f \\ \ddot{\zeta}_f \end{Bmatrix} \delta\tau \tag{1.79}$$

which, when simplified, becomes

$$\delta\eta_f = \Phi_{21}\delta\xi_0 + \Phi_{23}\delta\zeta_0 + \Phi_{25}\delta\dot{\eta}_0 + \dot{\eta}_f\delta\tau = 0 \tag{1.80}$$

and solving for $\delta\tau$ we obtain

$$\delta\tau = -\frac{1}{\delta\dot{\eta}_f}\left(\Phi_{21}\delta\xi_0 + \Phi_{23}\delta\zeta_0 + \Phi_{25}\delta\dot{\eta}_0\right) \tag{1.81}$$

where the subscript "f" denotes the final conditions after the integration. In this case it corresponds to half period.
However, there are three unknowns at the initial time. To solve this underdetermined system with two equations and three unknowns, one of the three unknowns is kept fixed. In this particular study, the initial ζ-coordinate is kept unchanged, since it is possible to classify the halo orbit by the maximum value on ζ-axis, the so called *ζ-amplitude*, A_ζ (halo orbits are also classified according to Jacobi constant). A similar approach can be used by keeping the initial ξ-coordinate constant instead. Since ζ_0 is fixed, we can compute the incremental changes needed for ξ_0 and $\dot{\eta}_0$

$$\begin{Bmatrix} \cancel{\delta\xi_f} \\ \cancel{\delta\eta_f} \\ \cancel{\delta\zeta_f} \\ \delta\dot{\xi}_f \\ \cancel{\delta\dot{\eta}_f} \\ \delta\dot{\zeta}_f \end{Bmatrix} = \begin{bmatrix} \cancel{\Phi_{11}} & \cancel{\Phi_{12}} & \cancel{\Phi_{13}} & \cancel{\Phi_{14}} & \cancel{\Phi_{15}} & \cancel{\Phi_{16}} \\ \cancel{\Phi_{21}} & \cancel{\Phi_{22}} & \cancel{\Phi_{23}} & \cancel{\Phi_{24}} & \cancel{\Phi_{25}} & \cancel{\Phi_{26}} \\ \cancel{\Phi_{31}} & \cancel{\Phi_{32}} & \cancel{\Phi_{33}} & \cancel{\Phi_{34}} & \cancel{\Phi_{35}} & \cancel{\Phi_{36}} \\ \Phi_{41} & \cancel{\Phi_{42}} & \cancel{\Phi_{43}} & \cancel{\Phi_{44}} & \Phi_{45} & \cancel{\Phi_{46}} \\ \cancel{\Phi_{51}} & \cancel{\Phi_{52}} & \cancel{\Phi_{53}} & \cancel{\Phi_{54}} & \cancel{\Phi_{55}} & \cancel{\Phi_{56}} \\ \Phi_{61} & \cancel{\Phi_{62}} & \cancel{\Phi_{63}} & \cancel{\Phi_{64}} & \Phi_{65} & \cancel{\Phi_{66}} \end{bmatrix} \begin{Bmatrix} \delta\xi_0 \\ \cancel{\delta\eta_0} \\ \cancel{\delta\zeta_0} \\ \cancel{\delta\dot{\xi}_0} \\ \delta\dot{\eta}_0 \\ \cancel{\delta\dot{\zeta}_0} \end{Bmatrix} + \begin{Bmatrix} \cancel{\dot{\xi}_f} \\ \cancel{\dot{\eta}_f} \\ \cancel{\dot{\zeta}_f} \\ \ddot{\xi}_f \\ \cancel{\ddot{\eta}_f} \\ \ddot{\zeta}_f \end{Bmatrix} \delta\tau \tag{1.82}$$

so that replacing Eq.(1.81) in Eq.(1.82), and setting $\delta\zeta_0 = 0$, we obtain

$$\begin{Bmatrix} \delta\dot{\xi}_f \\ \delta\dot{\zeta}_f \end{Bmatrix} = \begin{bmatrix} \Phi_{41} & \Phi_{45} \\ \Phi_{61} & \Phi_{65} \end{bmatrix} \begin{Bmatrix} \delta\xi_0 \\ \delta\dot{\eta}_0 \end{Bmatrix} - \begin{Bmatrix} \delta\ddot{\xi}_f \\ \delta\ddot{\zeta}_f \end{Bmatrix} \frac{1}{\delta\dot{\eta}_f} \left(\Phi_{21}\delta\xi_0 + \Phi_{25}\delta\dot{\eta}_0\right) \tag{1.83}$$

Solving for $\delta\xi_0$ and $\delta\dot{\eta}_0$, we get

$$\begin{Bmatrix} \delta\xi_0 \\ \delta\dot{\eta}_0 \end{Bmatrix} = \left[\begin{bmatrix} \Phi_{41} & \Phi_{45} \\ \Phi_{61} & \Phi_{65} \end{bmatrix} - \frac{1}{\delta\dot{\eta}_f} \begin{Bmatrix} \delta\ddot{\xi}_f \\ \delta\ddot{\zeta}_f \end{Bmatrix} \begin{bmatrix} \Phi_{21} & \Phi_{25} \end{bmatrix}\right]^{-1} \begin{Bmatrix} \delta\dot{\xi}_f \\ \delta\dot{\zeta}_f \end{Bmatrix} \tag{1.84}$$

The revised initial conditions $\xi_0 + \delta\xi_0$ and $\dot{\eta}_0 + \delta\dot{\eta}_0$ are used to begin the next iteration and this process is continued until $\dot{\xi}_f = \dot{\zeta}_f = 0$ within some acceptable tolerance. We have a set of 42 coupled, differential equations to solve simultaneously: the first 36 equations come from Eq.(1.73) and the last 6 equations come from Eq.(1.67).
In Fig. 1.5, a flowchart of the differential correction algorithm to find halo orbit with ζ_0 fixed is shown. For example, for the Earth-Moon system, $\mu = 0.01215058561$ and starting with initial conditions equal to $[0.83, 0, 0.1, 0.23, 0]^T$ and fixing ζ_0 we find the corresponding halo in a few iterations. As shown in Fig. 1.6, after the first fluctuation, $\dot{\xi}_f$ and $\dot{\zeta}_f$ asymptotically reach zero. In Fig. 1.7 we can see better the behavior of $\left|\dot{\xi}_f\right|$ and $\left|\dot{\zeta}_f\right|$, they reach a value less than tolerance (set to 10^{-14}) in 6 iterations. In Fig. 1.9 and Fig. 1.8 are shown the ICs evolution and the half period evolution. Finally, Fig. 1.10 shows the periodic orbit obtained from using this differential corrector method.

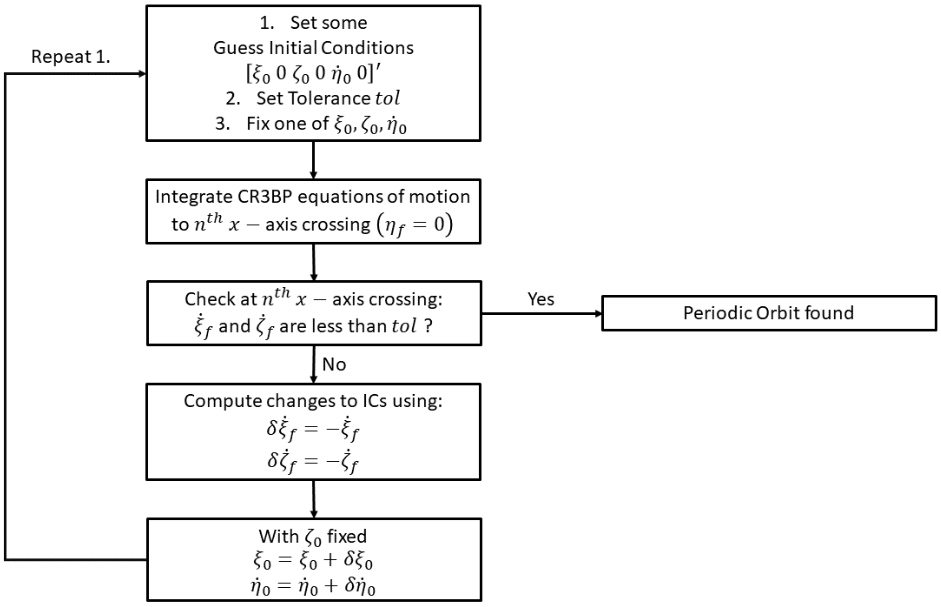

Figure 1.5: Differential Correction flowchart for orbits that are symmetric about the $\xi - \zeta$ plane

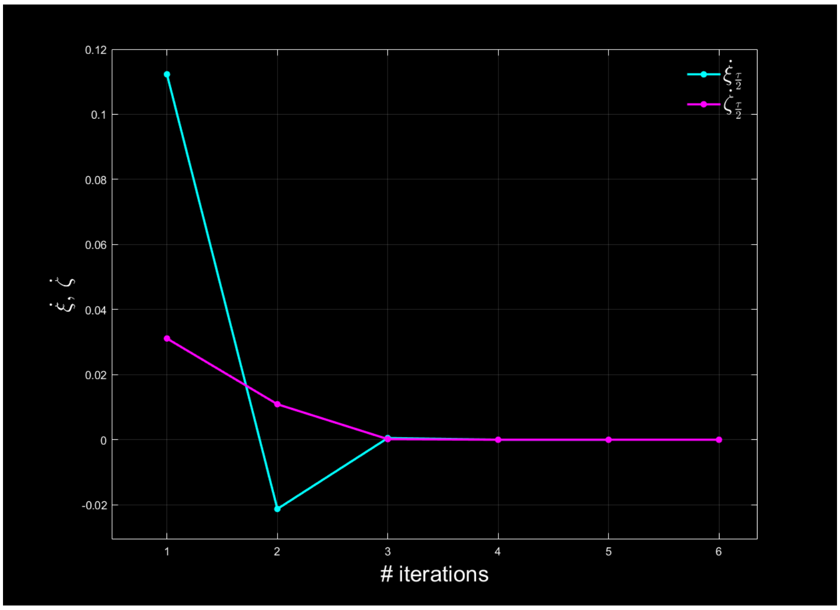

Figure 1.6: $\dot{\xi}_f$ and $\dot{\zeta}_f$ evolution

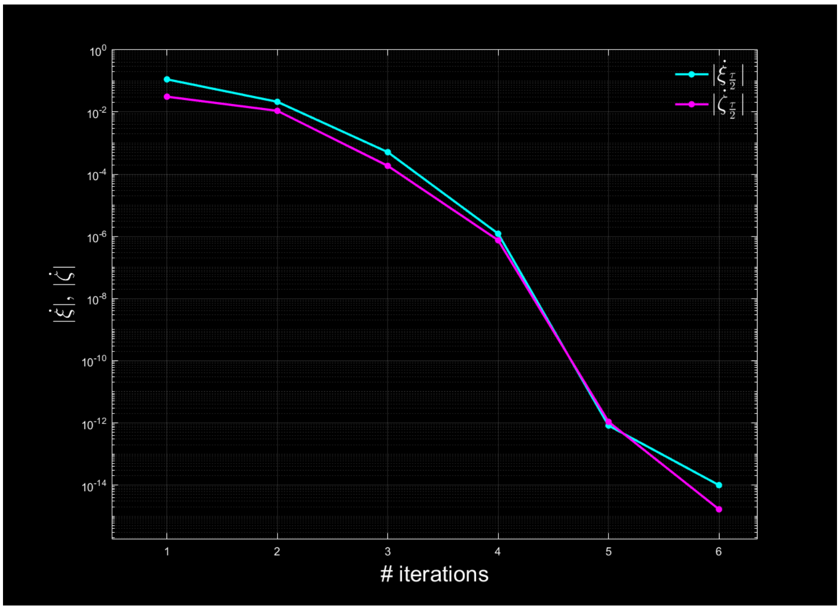

Figure 1.7: $\left|\dot{\xi}_f\right|$ and $\left|\dot{\zeta}_f\right|$ evolution

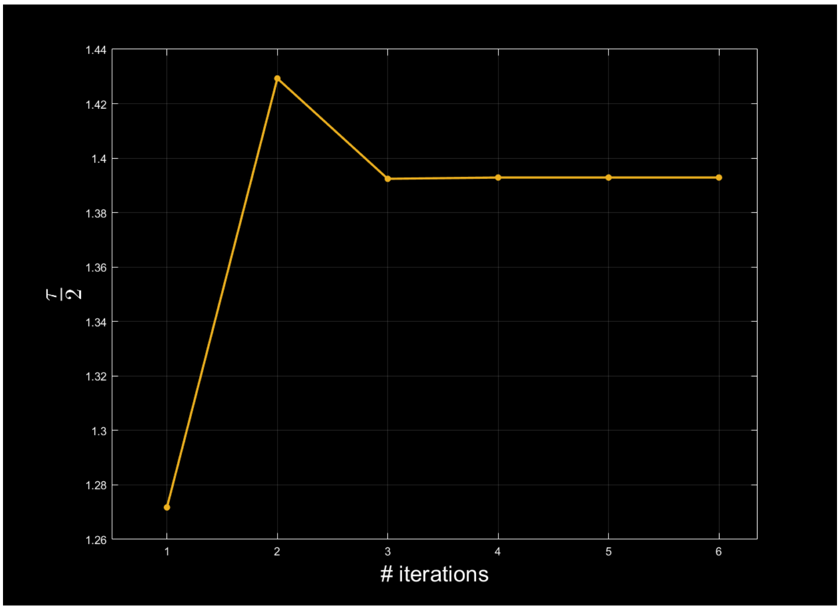

Figure 1.8: $\frac{\tau}{2}$ evolution

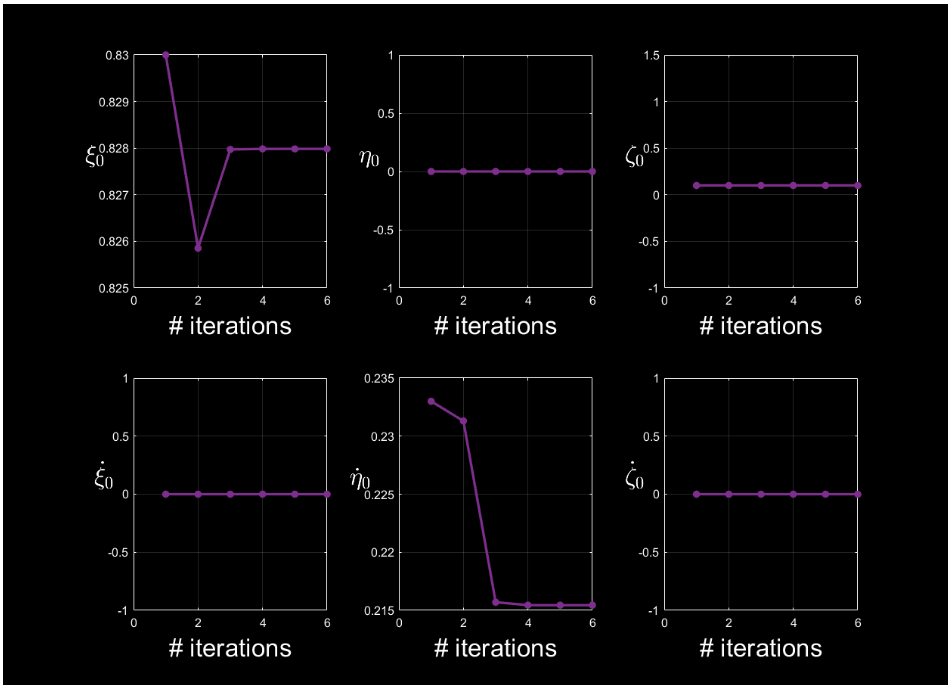

Figure 1.9: $\vec{X}_0$ evolution

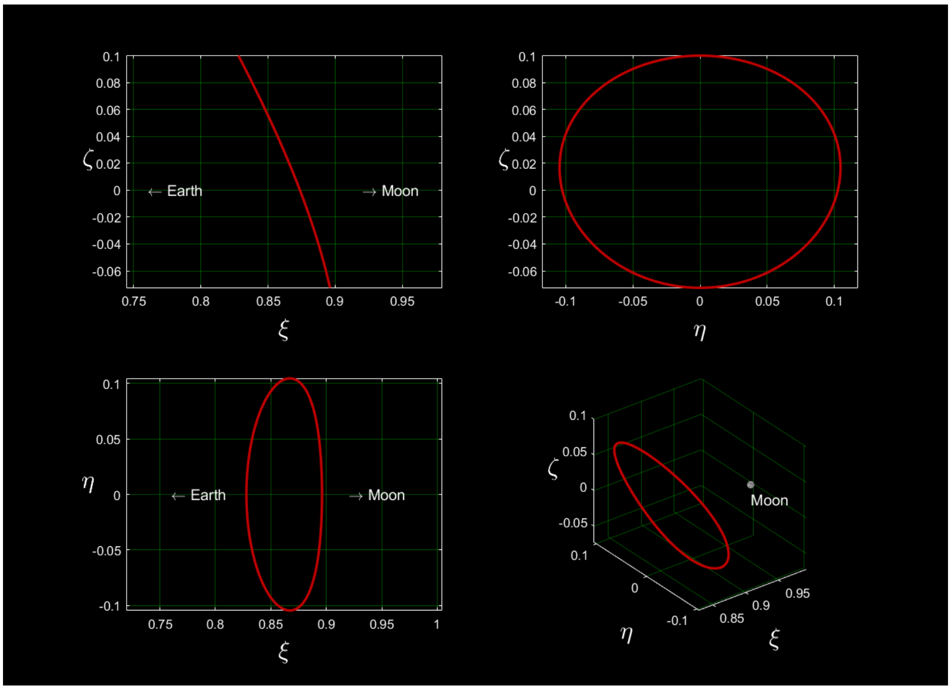

Figure 1.10: Northern Halo L_1 orbit with $A_\zeta = 0.1$ in the Earth-Moon system

The example proposed here gives an example of a 3D orbit. This method will be used to generate DRO in Chapter 5.

1.4.4 Poincaré Maps and Poincaré Sections

Poincaré maps are classical techniques for examining the stability of periodic orbits in the N-body problem (and many other dynamical systems). By selecting an initial state $\vec{x}_0$ of an orbit, we can create a hyper-plane Σ, transverse to the orbit that intersects the orbit at $\vec{x}_0$. The first intersection of Σ by the trajectory propagated from $\vec{x}_0$ is the Poincaré point $P_\Sigma\left(\vec{x}_0\right)$ as shown in Fig. 1.11. Multiple iterations of the Poincaré point are then computed by compounding the map, so we have $P_\Sigma^p\left(\vec{x}_0\right)$ for p returns. A periodic state, $\vec{x}^*$, returns to the same state through a Poincaré map for which $P_\Sigma^p\left(\vec{x}^*\right) = \vec{x}^*$.

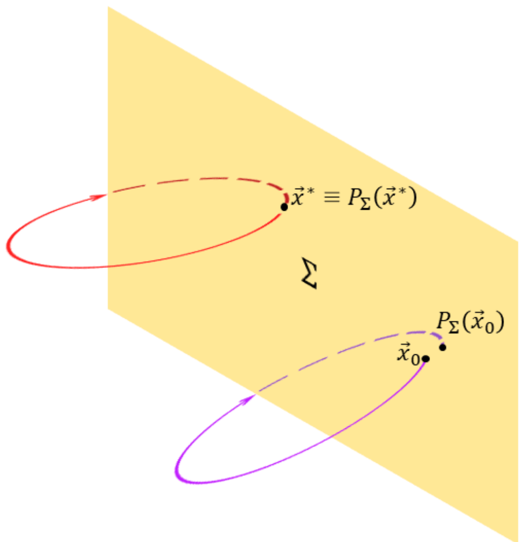

Figure 1.11: Example of a Poincaré map

The dynamical system therefore defines a mapping onto this section Σ, and a periodic orbit corresponds to the *fixed points* of this mapping. Such points can be either *centers* or *saddles*. Stable and unstable manifolds indicate the dynamical flow into and out of periodic orbits, respectively, emerging from saddle points in the Poincaré map. The connection between saddle points is a fundamental feature of Poincaré map topology, where stable and unstable manifolds intersect an infinite number of times, resulting in chaotic tangles, as shown in Fig. 1.12. The matrix corresponding to this mapping is referred to as the monodromy matrix, Π. Π is defined as the state-transition matrix evaluated at exactly one orbital period, or

$$\Pi = \Phi\left(\tau\right) \tag{1.85}$$

The stability of the orbit is determined by the 6 eigenvalues λ_i of the 6x6 monodromy matrix, Π. If one or more eigenvalues have a magnitude greater than 1, the orbit is unstable. If the magnitude of the largest eigenvalue is exactly 1, the orbit is considered neutrally stable. And if all eigenvalues have magnitudes less than 1, the orbit is considered stable. For instance, as demonstrated in [6], a generic halo orbit's monodromy matrix has the following eigenvalue set:

$$\begin{aligned} &\lambda_1 > 1 \\ &\lambda_2 = \frac{1}{\lambda_1} \\ &\lambda_3 = \lambda_4 = 1 \\ &|\lambda_5| = |\lambda_6| = 1 \end{aligned} \tag{1.86}$$

this means that halo orbits are generally unstable.

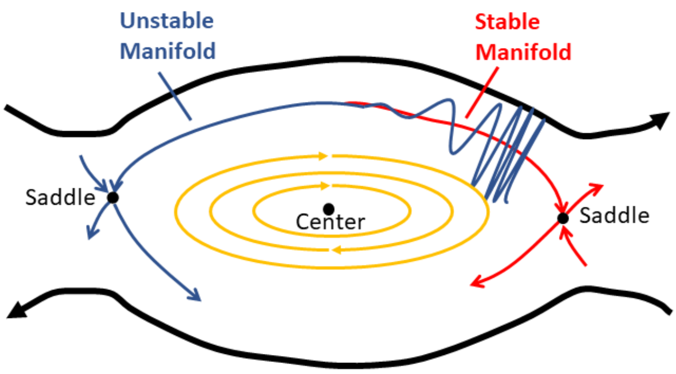

Figure 1.12: Poincaré map topology

1.4.5 Invariant Manifolds

The stability of periodic orbits can be determined by the eigenvalues of the monodromy matrix as described in Subsec. 1.4.1. The local behavior near these orbits is represented by these eigenspaces, which consist of eigenvalues and eigenvectors. Invariant manifolds are time-invariant hyper-surfaces of the dynamical model, the CR3BP in our case. Once a spacecraft is put onto an invariant manifold, assuming no external perturbations are present, it will never depart from it as it follows the natural progression of the dynamic system. The approximation of an unstable (or stable) asymptotic solution, $\vec{x}_{perturbed}$, can be obtained by slightly adjusting an initial state $\vec{x}_0$ on the periodic orbit using a small value, ϵ, in the direction of the unstable (or stable) eigenvectors, which are the unstable (or stable) eigenvectors,

$\vec{\lambda}$, of the monodromy matrix Π, such that

$$\vec{x}_{perturbed} = \vec{x}_0 \pm \epsilon\vec{\lambda} \tag{1.87}$$

This perturbed state, $\vec{x}_{perturbed}$, can be integrated forwards in time to generate trajectories that leave the periodic orbit, or backwards in time to compute trajectories that arrive at the periodic orbit generated from the initial state $\vec{x}_0$. Numerical integration of the CR3BP EOMs from different initial values $\vec{x}_0$ that lie on the same periodic orbit produce a family of approximate asymptotic solution trajectories, forming an *invariant manifold tube*. Stable and unstable manifolds, which are areas in the phase space that converge towards specific periodic orbits of interest, are crucial for orbital transfers. A spacecraft located on a stable manifold, even if it's far from a periodic orbit, will gradually move towards the orbit and can be easily inserted into it with minimal change in velocity. It is important to note that these invariant manifold tubes are formed by an infinite number of real trajectories that solve the equations of motion of the CR3BP.

1.5 CR3BP Orbit Families Overview

Periodic orbit families in the CR3BP represent a group of orbits that share similar properties, such as shape, size, and/or stability. Each periodic orbit family has unique characteristics and applications in the CR3BP. For example, halo orbits are often used as parking orbits for satellites, while Lyapunov orbits can be used to transfer a spacecraft from one orbit to another. The stable and unstable manifolds of these periodic orbits also play a crucial role in determining the feasibility of certain orbital transfers. The following figures show some periodic orbit families in the Earth-Moon system. The Moon shown in these figures is five times bigger than reality to better show its location. In Fig. 1.13 Lyapunov Orbits are displayed around the L_1 point and it is possible to obtain this family in all the collinear points. Halo orbits are divided in Northern and Southern; in Fig. 1.14 Northern Halo Orbits are shown about the L_1 point. It is possible to generate Vertical and Axial Orbits in all Lagrangian points; in Fig. 1.15 and Fig. 1.17 Vertical and Axial Orbit Families about the L_1 point are shown. Butterfly and Dragonfly orbits are subdivided in Northern and Southern and are displayed respectively in Fig. 1.16 and Fig. 1.19. The Distant Retrograde Orbits and Low Prograde Orbits are centered about the second body and they are shown respectively in Fig. 1.20, Fig. 1.18 and Fig. 1.21; the last family can be Western or Eastern. The last families presented are the Short Period and Long Period Orbits, which are placed around the Equilateral points, L_4 and L_5, and they are displayed respectively in Fig. 1.22 and Fig. 1.23.

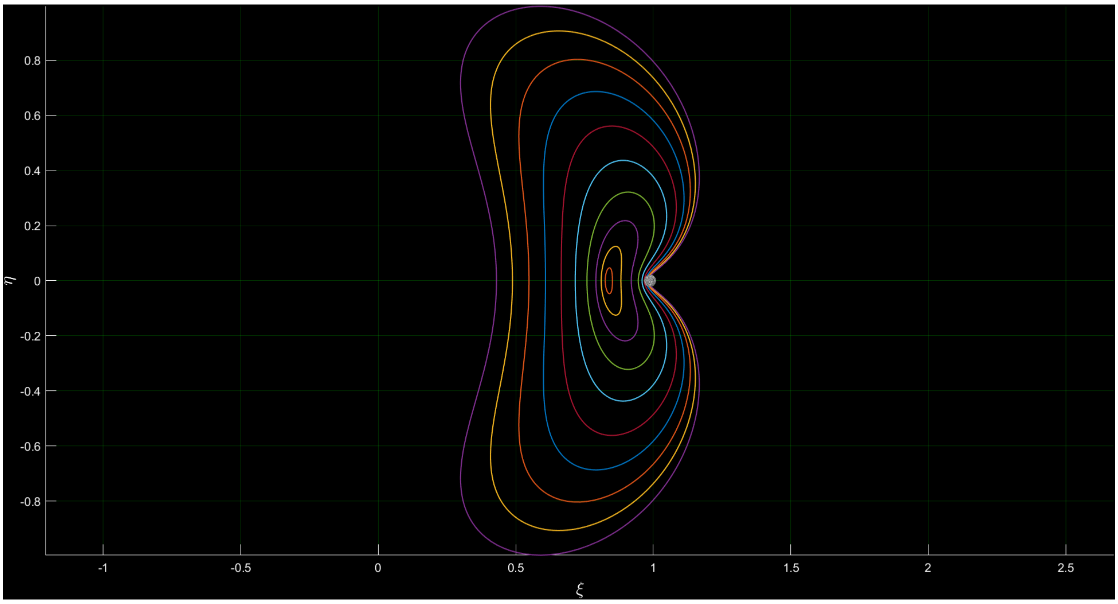

Figure 1.13: L_1 Lyapunov Orbits

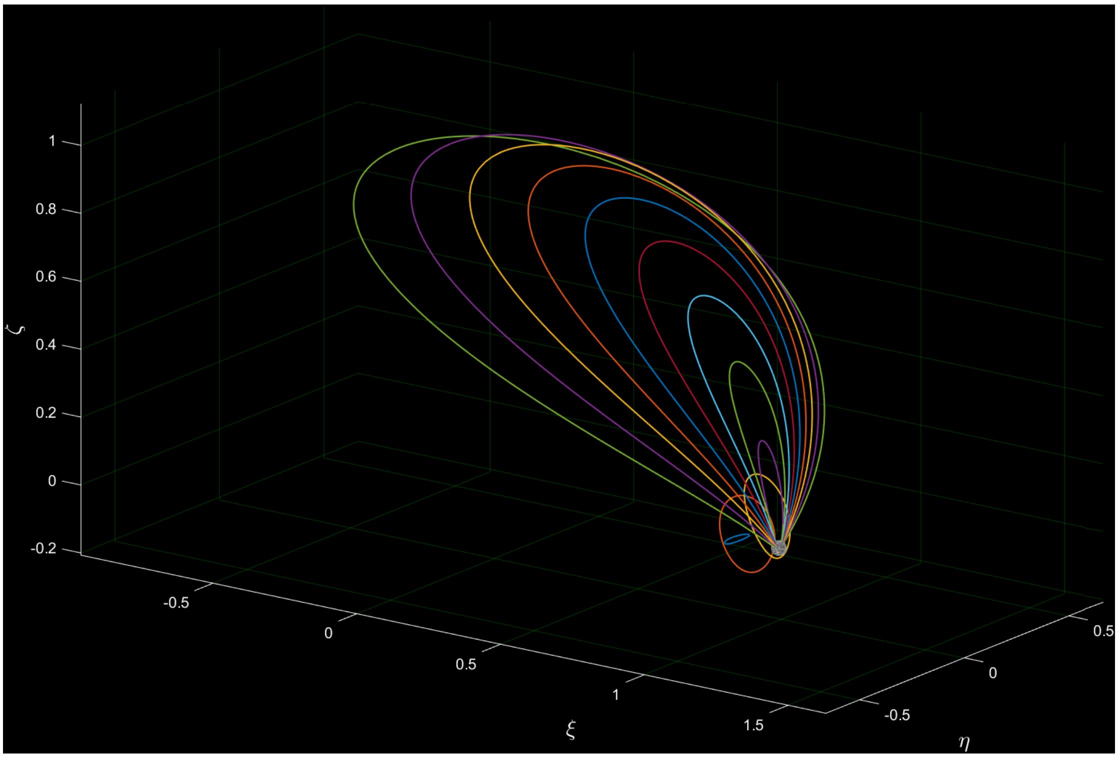

Figure 1.14: L_1 Halo Northern Orbits

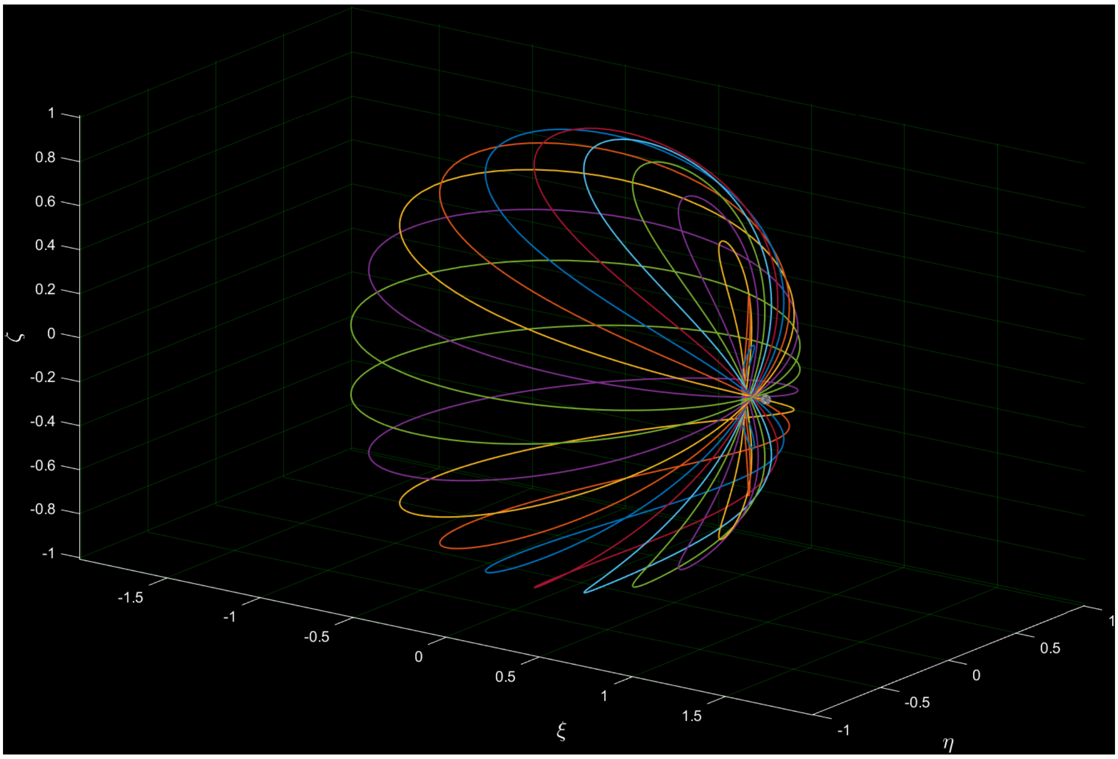

Figure 1.15: L_1 Vertical Orbits

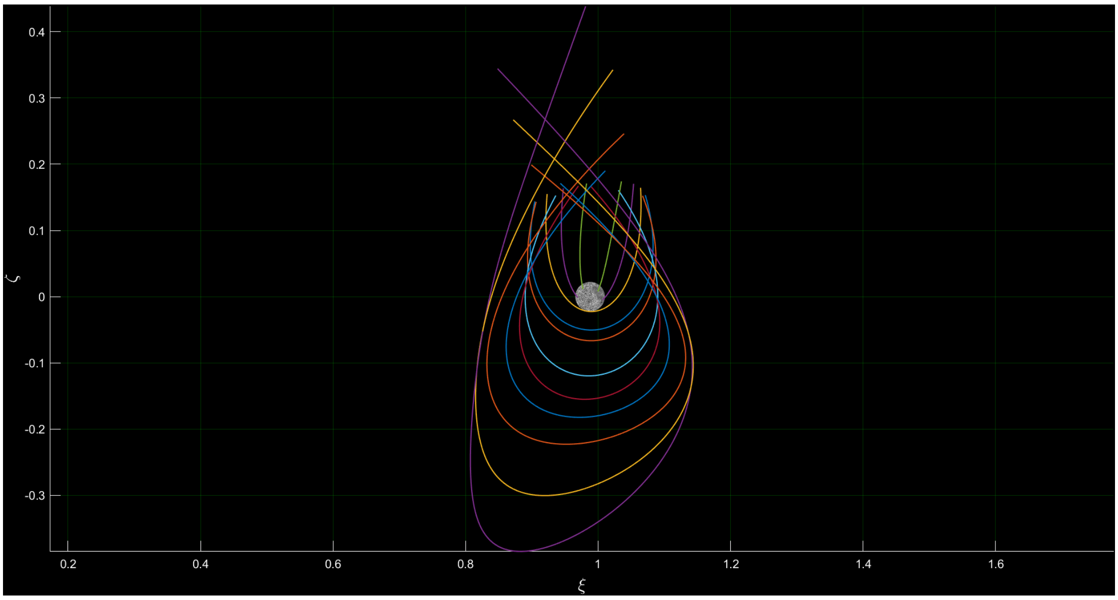

Figure 1.16: Northern Butterfly Orbits

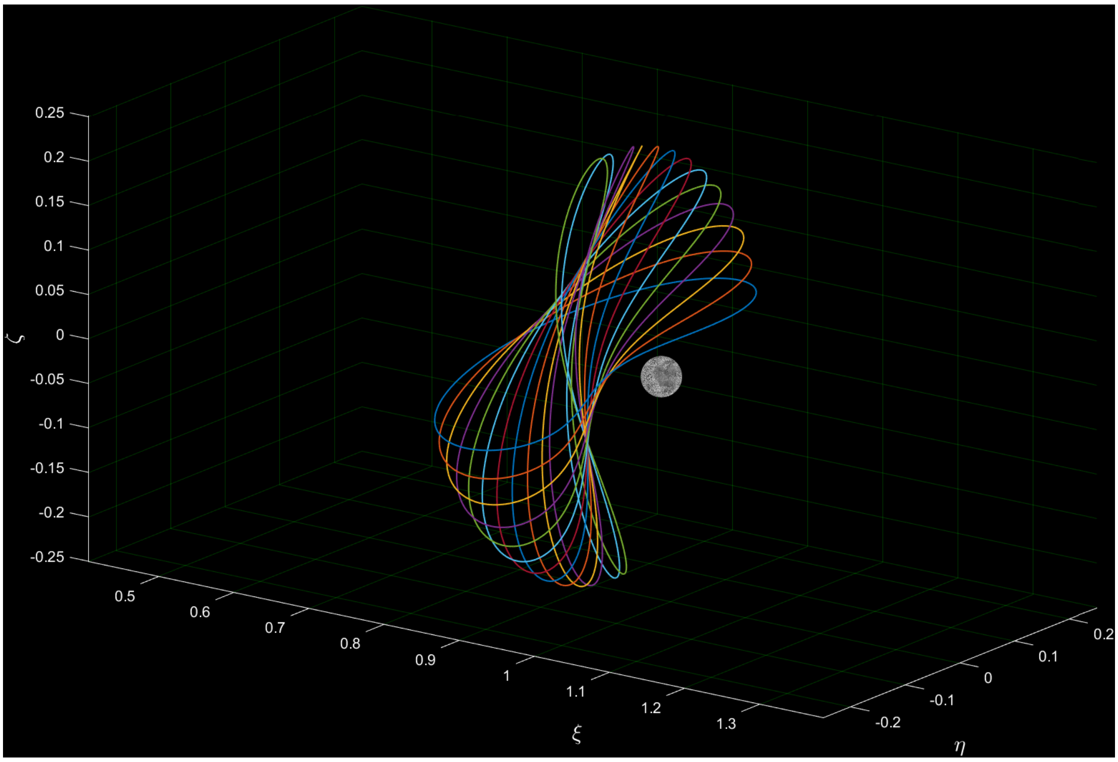

Figure 1.17: L_1 Axial Orbits

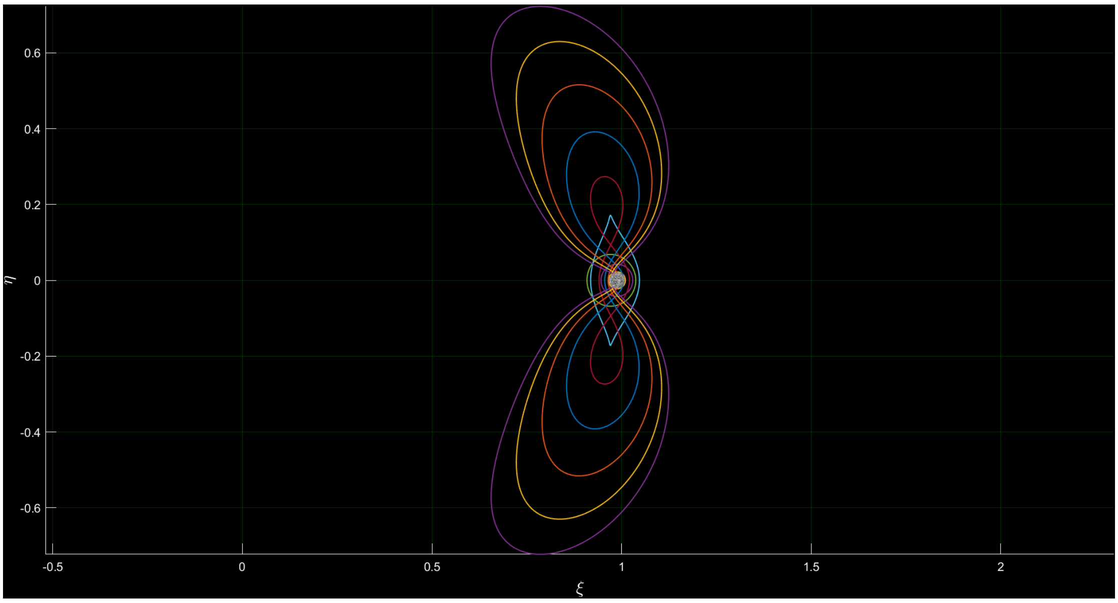

Figure 1.18: Distant Prograde Orbits

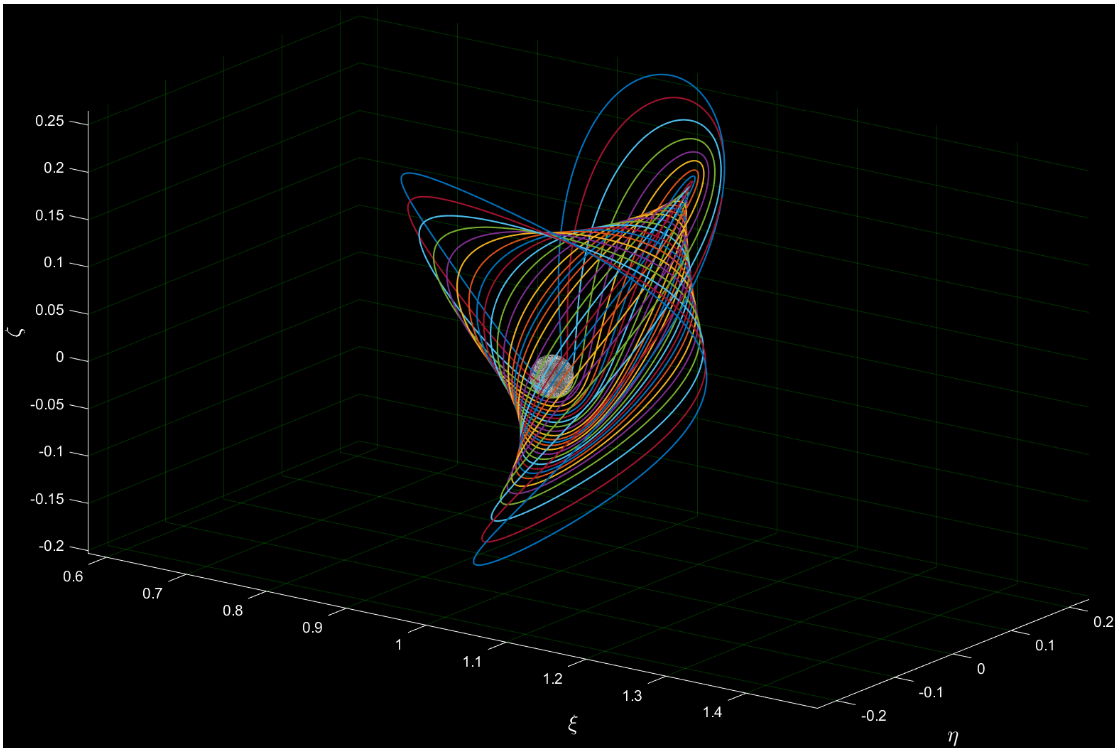

Figure 1.19: Northern Dragonfly Orbits

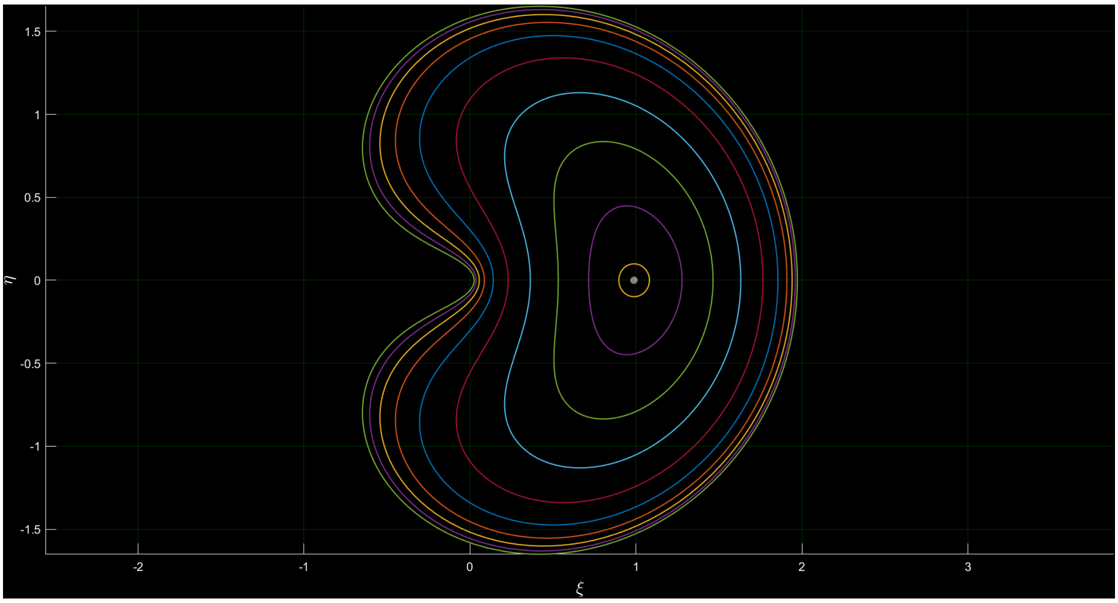

Figure 1.20: Distant Retrograde Orbits

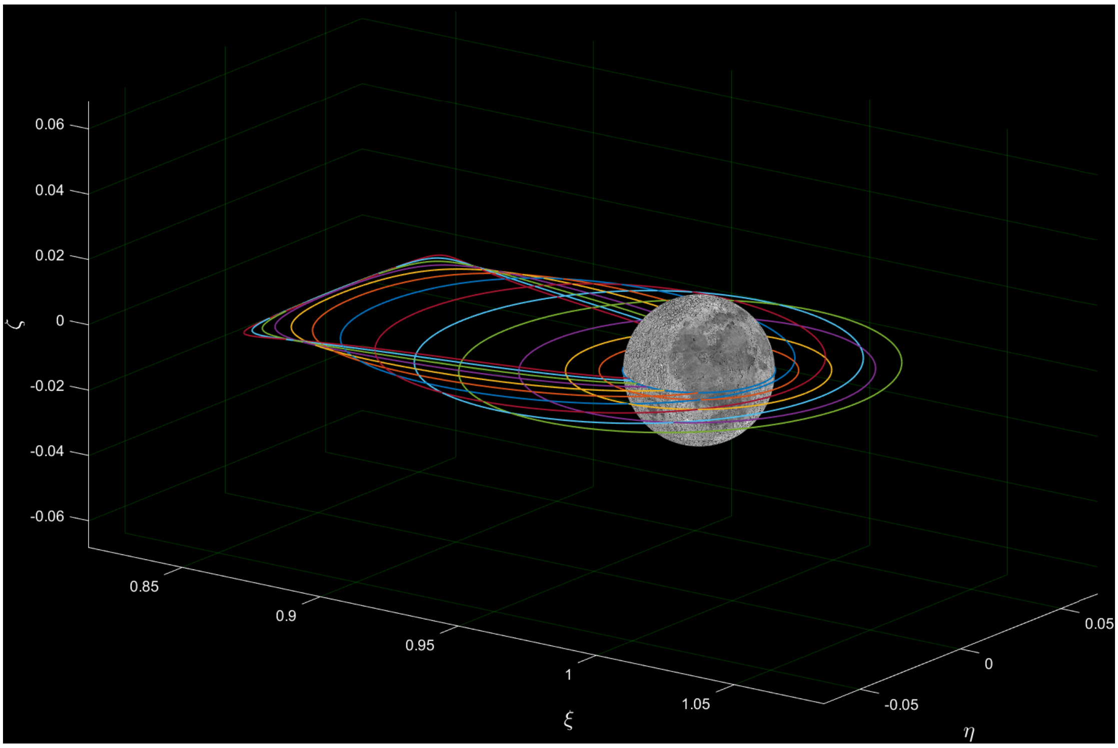

Figure 1.21: Western Low Prograde Orbits

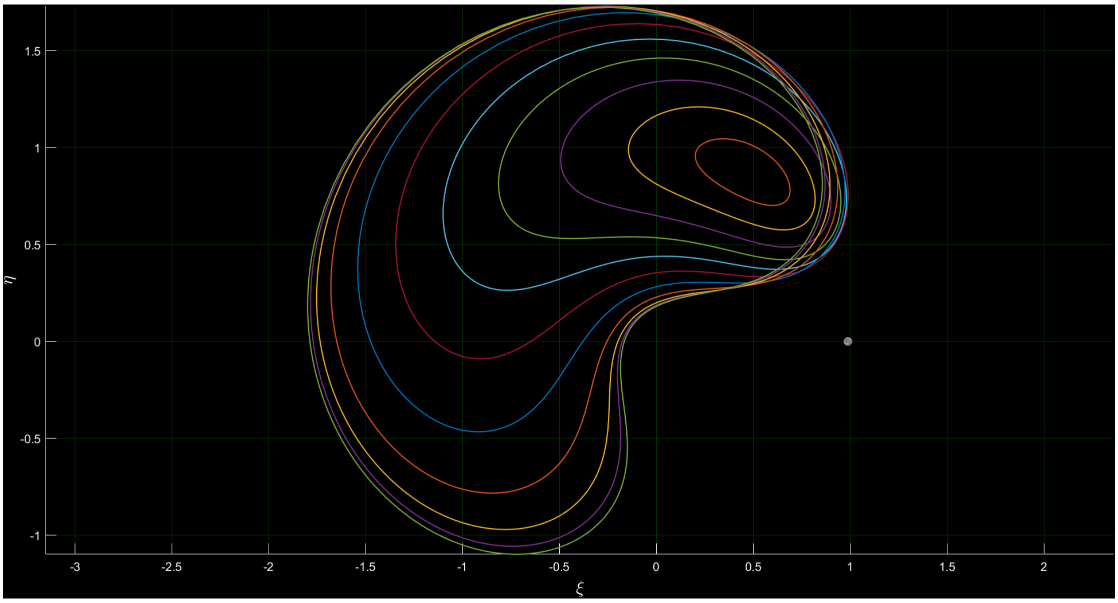

Figure 1.22: L_4 Short Period Orbits

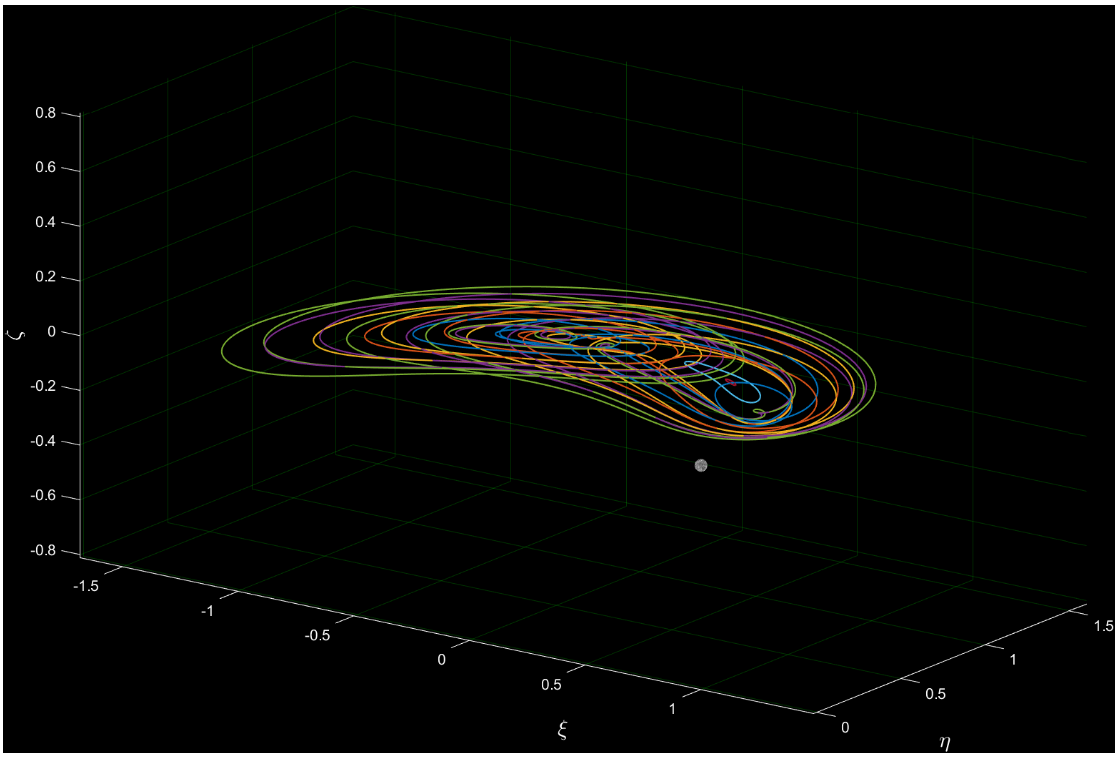

Figure 1.23: L_4 Long Period Orbits

1.5.1 CR3BP Orbit Applications

International Sun/Earth Explorer 3 (*ISEE-3*), launched in 1978, was the first spacecraft to be placed in a libration point orbit. Its mission was to study the Earth's magnetosphere, the region around the Earth that is influenced by its magnetic field. *ISEE-3* was placed in an orbit around the Sun-Earth L_1 point. *WIND*, launched in 1994, was a spacecraft that studied the solar wind, the stream of charged particles emitted by the Sun. *WIND* was placed in a Lissajous orbit around the Sun-Earth L_1 orbit, where it studied the interaction between the solar wind and the Earth's magnetosphere. *Solar and Heliospheric Observatory* (*SOHO*), launched in 1995, was a spacecraft that studied the Sun's structure, from its core to the extensive outer corona, including the solar wind that blows across the Solar System. *SOHO* was placed in a halo orbit around the L_1 point, which allowed it to continuously observe the Sun without being blocked by the Earth. *Advanced Composition Explorer* (*ACE*), launched in 1997, was another spacecraft that collected and analyzed particles of solar, interplanetary, interstellar and galactic origins. *ACE* was placed into a Lissajous orbit around the Sun-Earth L_1, and provided important data on the composition and behavior of the solar wind. *Microwave Anisotrophy Probe* (*MAP*), launched in 2001, was a spacecraft designed to study the cosmic microwave background radiation, which is the afterglow of the Big Bang. *MAP* was placed in an orbit around the Sun-Earth L_2 point. *Genesis*, launched in 2004, was a mission to collect samples of solar wind particles and bring them back to Earth for study. Genesis was also placed in a Sun-Earth L_1 halo orbit. The *James Webb Space Telescope* (*JWST*) is a telescope launched in 2021. It is designed to study the early universe, galaxies, and stars, and was placed in an orbit around the Sun-Earth/Moon L_2 point. Fig. 1.24 shows the position of the JWST which orbits the sun at the second Lagrange point. The *Artemis I* mission, launched in 2022. As the first of a series of progressively intricate missions, *Artemis I* was an unmanned space flight aimed at establishing a basis for human deep space exploration, showcasing our commitment and proficiency in expanding human presence to the Moon and beyond.

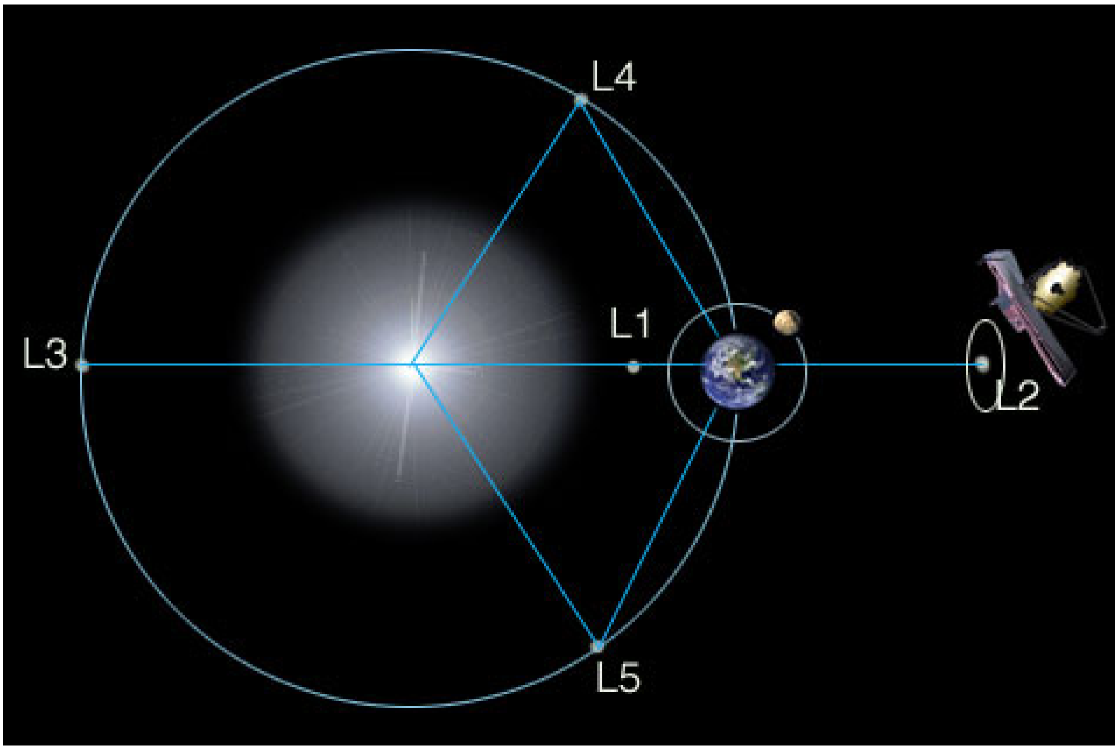

Figure 1.24: JWST in Sun-Earth/Moon System. Credit: `webb.nasa.gov`

In the next chapter, Lambert's problem is discussed which will be applied in Chapter 4 to find trajectories that will reach one of the periodic orbits discussed in this chapter.

Chapter 2

Lambert's Problem

Lambert's problem is a classic problem in orbital mechanics that involves determining the trajectory of a spacecraft that travels between two points in space, subject to a gravitational force for a fixed time-of-flight (TOF). In mathematical terms, Lambert's problem is formulated as a two-point boundary-value problem, where the initial and final positions, are given, and the goal is to determine the trajectory that satisfies these constraints for a given TOF. The solution to Lambert's problem can be found using various numerical iterative methods. In this chapter, the *Classical Solution* proposed by Lagrange in 1778 [7] and the *Universal Variable Solution* proposed by Battin [8] in 1987 are used to analyze Lambert's Problem.
Lambert's Problem will be used in Chapter 4 to find trajectories from Earth to a series of candidate asteroids and from them to Mars.

2.1 Lambert's Problem Definition

Lambert's theorem states that the TOF along an elliptical arc between two points P_1 and P_2, as depicted in Fig. 2.1 is solely dependent on the semi-major axis (SMA), a, of the ellipse and the segments $\bar{FP_1}$, and $\bar{FP_2}$ [9]. It is important to note that the eccentricity, e, does not appear in the formulation. Mathematically, this can be expressed as

$$\sqrt{\mu}TOF = f\left(a, r_1 + r_2, c\right) \tag{2.1}$$

where c is the chord connecting P_1 and P_2, while r_1 and r_2 are the lengths of $\bar{FP_1}$ and $\bar{FP_2}$ respectively. As seen from the Fig. 2.1, the difference in true anomalies between points P_1 and P_2 is

$$\cos \Delta\theta = \frac{\vec{r_1} \cdot \vec{r_2}}{r_1 r_2} \tag{2.2}$$

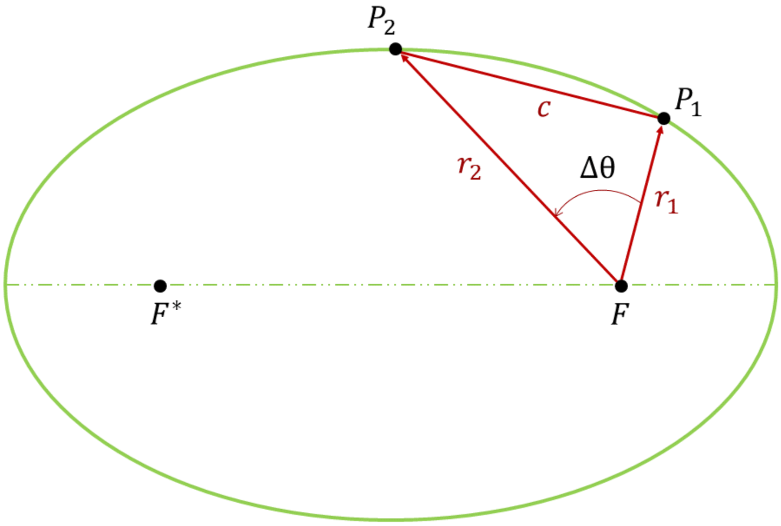

Figure 2.1: Lambert's Problem Geometry

Given the nature of the cosine function we have two solutions, $\Delta\theta$ and $2\pi - \Delta\theta$. To eliminate the confusion caused by the quadrant ambiguity, a relationship that involves the sine of the angular change must be established. Let's begin by analyzing the Z component of the cross product of $(\vec{r_1} \times \vec{r_2})$,

$$(\vec{r_1} \times \vec{r_2})_z = \hat{k} \cdot (\vec{r_1} \times \vec{r_2}) = \hat{k} \cdot r_1 r_2 \sin \Delta\theta \hat{w} \tag{2.3}$$

where the inclination of the orbit, i, can be related with the unit vectors $\hat{k}$ and $\hat{w}$ to get

$$\cos i = \hat{k} \cdot \hat{w} \tag{2.4}$$

so that

$$\sin \Delta\theta = \frac{\hat{k} \cdot (\vec{r_1} \times \vec{r_2})}{r_1 r_2 \hat{k} \cdot \hat{w}} = \frac{\hat{k} \cdot (\vec{r_1} \times \vec{r_2})}{r_1 r_2 \cos i} \tag{2.5}$$

$(\vec{r_1} \times \vec{r_2})_z$ and $\sin \Delta\theta$ will split the problem in four different cases:

$$\begin{cases} \sin \Delta\theta \geqslant 0, & (\vec{r_1} \times \vec{r_2})_z \geqslant 0 \rightarrow & \text{short way, prograde orbit} \\ \sin \Delta\theta \geqslant 0, & (\vec{r_1} \times \vec{r_2})_z < 0 \rightarrow & \text{short way, retrograde orbit} \\ \sin \Delta\theta < 0, & (\vec{r_1} \times \vec{r_2})_z \geqslant 0 \rightarrow & \text{long way, prograde orbit} \\ \sin \Delta\theta < 0, & (\vec{r_1} \times \vec{r_2})_z < 0 \rightarrow & \text{long way, retrograde orbit} \end{cases} \tag{2.6}$$

Transfers can be executed using any of the various conic sections, including ellipses, parabolas, and hyperbolas. As Eq.(2.6) shows, selected the direction of the orbit (prograde or retrograde), there are two alternate paths for each trajectory, the *short way* and the *long way* as shown in Fig. 2.2. These two routes have the same TOF and usually, one is most efficient in terms of required ΔV to transfer since it moves in the same direction of the original trajectory.

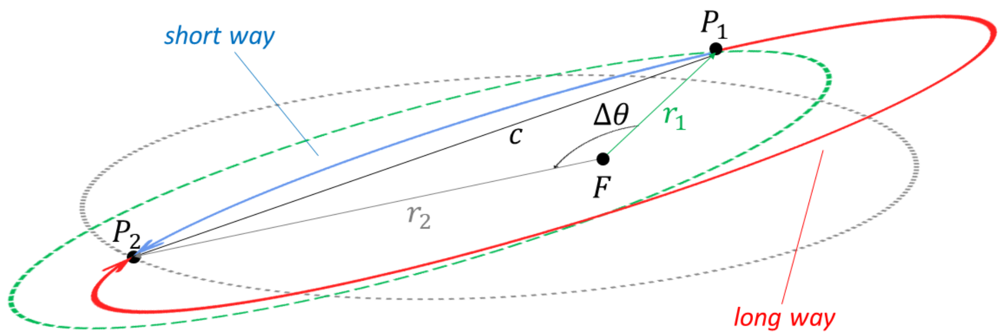

Figure 2.2: Short and Long way

Using eccentric anomaly, E, and recall the time equation in the Kepler's problem, we have

$$\sqrt{\mu}TOF = a^{\frac{3}{2}}\left[E_2 - E_1 - e\left(\sin E_2 - \sin E_1\right)\right] \tag{2.7}$$

where E_1 and E_2 are the eccentric anomaly of the points P_1 and P_2 respectively. Eq.(2.7) can be manipulated into Lambert's equation, where there is no eccentricity term in order to get an equation such as Eq.(2.1). Let's start defining two new variables, E_{mean} as

$$E_{mean} = \frac{1}{2}\left(E_2 + E_1\right) \tag{2.8}$$

and E_{middle} as

$$E_{middle} = \frac{1}{2}\left(E_2 - E_1\right) \tag{2.9}$$

from the formulation of the orbit equation in terms of eccentric anomaly, we know that

$$r = a\left(1 - e\cos E\right) \tag{2.10}$$

so that the sum of two positions, r_1 and r_2, can be obtained as

$$r_1 + r_2 = a\left[2 - e\left(\cos E_2 + \cos E_1\right)\right] \tag{2.11}$$

Applying the trigonometric identity

$$\cos E_2 + \cos E_1 = 2\cos\frac{E_2 + E_1}{2}\cos\frac{E_2 - E_1}{2} \tag{2.12}$$

Eq.(2.11) becomes

$$r_1 + r_2 = 2a\left[1 - e\cos E_{mean}\cos E_{middle}\right] \tag{2.13}$$

Let's define the chord c as

$$c = \sqrt{(x_2 - x_1)^2 + (y_2 - y_1)^2} \tag{2.14}$$

where x and y are the Cartesian coordinates relative to the center of ellipse as

$$\begin{array}{ll} x_1 = a\cos E_1 & y_1 = b\sin E_1 = a\sqrt{1-e^2}\sin E_1 \\ x_2 = a\cos E_2 & y_2 = b\sin E_2 = a\sqrt{1-e^2}\sin E_2 \end{array} \tag{2.15}$$

so using Prostapheresis formula, Eq.(2.14) becomes

$$\begin{aligned} c &= \sqrt{a^2\left(\cos E_2 - \cos E_1\right)^2 + a^2\left(1-e^2\right)\left(\sin E_2 - \sin E_1\right)^2} \\ &= \sqrt{a^2\left(-2\sin E_{mean}\sin E_{middle}\right)^2 + a^2\left(1-e^2\right)\left(2\cos E_{mean}\sin E_{middle}\right)^2} \\ &= \sqrt{4a^2\sin^2 E_{middle}\left[\sin^2 E_{mean} + \cos^2 E_{mean} - e^2\cos^2 E_{mean}\right]} \\ &= \sqrt{4a^2\sin^2 E_{middle}\left[1 - e^2\cos^2 E_{mean}\right]} \\ &= 2a\sin E_{middle}\sqrt{1 - e^2\cos^2 E_{mean}} \end{aligned} \tag{2.16}$$

If we consider another auxiliary variable, Ξ, defined as $\cos\Xi = e\cos E_{mean}$, Eq.(2.14) becomes

$$c = 2a\sin E_{middle}\sin\Xi \tag{2.17}$$

and Eq.(2.13) changes into

$$r_1 + r_2 = 2a\left[1 - \cos E_{middle}\cos\Xi\right] \tag{2.18}$$

The last two auxiliary variables are α and β, which we define as

$$\alpha = \Xi + E_{middle} \tag{2.19}$$

and

$$\beta = \Xi - E_{middle} \tag{2.20}$$

By expressing the relationships between r_1, r_1, and c in terms of the SMA, α, and β, we determine that

$$\begin{aligned} r_1 + r_2 + c &= 2a\left(1 - \cos E_{middle}\cos\Xi + \sin E_{middle}\sin\Xi\right) \\ &= 2a\left[1 - \frac{1}{2}\left(\cos\alpha + \cos\beta\right) - \frac{1}{2}\left(\cos\alpha - \cos\beta\right)\right] \\ &= 2a\left(1 - \cos\alpha\right) = 4a\sin^2\frac{\alpha}{2} \end{aligned} \tag{2.21}$$

and

$$\begin{aligned} r_1 + r_2 - c &= 2a\left(1 - \cos E_{middle}\cos\Xi - \sin E_{middle}\sin\Xi\right) \\ &= 2a\left[1 - \frac{1}{2}\left(\cos\alpha + \cos\beta\right) + \frac{1}{2}\left(\cos\alpha - \cos\beta\right)\right] \\ &= 2a\left(1 - \cos\beta\right) = 4a\sin^2\frac{\beta}{2} \end{aligned} \tag{2.22}$$

Solving Eq.(2.21) and Eq.(2.22) for α and β, respectively, and defining the perimeter of the triangle P_1FP_2 as $s = r_1 + r_2 + c$, we obtain

$$\sin\frac{\alpha}{2} = \sqrt{\frac{s}{2a}} \tag{2.23}$$

and

$$\sin\frac{\beta}{2} = \sqrt{\frac{s-c}{2a}} \tag{2.24}$$

Thus, Eq.(2.7) becomes

$$\begin{aligned} \sqrt{\mu}TOF &= a^{\frac{3}{2}}\left[2E_{middle} - 2e\cos E_{mean}\sin E_{middle}\right] \\ &= 2a^{\frac{3}{2}}\left[E_{middle} - \cos\Xi\sin E_{middle}\right] \end{aligned} \tag{2.25}$$

From Eq.(2.19) and Eq.(2.20) we obtain that $\Xi = \frac{\alpha+\beta}{2}$ and $E_{middle} = \frac{\alpha-\beta}{2}$, so Eq.(2.25) becomes

$$\begin{aligned} \sqrt{\mu}TOF &= a^{\frac{3}{2}}\left[\alpha - \beta - 2\cos\frac{\alpha+\beta}{2}\sin\frac{\alpha-\beta}{2}\right] \\ &= a^{\frac{3}{2}}\left[\alpha - \beta - \left(\sin\alpha - \sin\beta\right)\right] \end{aligned} \tag{2.26}$$

Eq.(2.26), also known as Lambert's equation, depends only on a, α and β, the angles α and β are dependent solely on the SMA, the sum of r_1 and r_2, and c. This demonstrates Lambert's theorem, i.e. that Kepler's equation can be converted into Lambert's equation.

2.2 Classical Solution

The classical solution to solving Lambert's problem, which was developed by Lagrange [7], involves utilizing the geometry of the minimum energy transfer, as depicted in Fig. 2.3, and the specified TOF to determine the type of conic section the transfer must follow. Not all methods for solving Lambert's problem require determining the conic section beforehand, such as the universal variable solution, which will be discussed in the Sec. 2.3. The basic structure of the minimum energy transfer is established with points P_1 and P_2 being the center of circles whose intersection is the vacant focus, F^*, that arises from the minimum energy ellipse. The transfer arc is represented in blue in the Fig. 2.3, along with its line of apsides, LOA. Let's start by defining the minimum energy ellipse which has the smallest

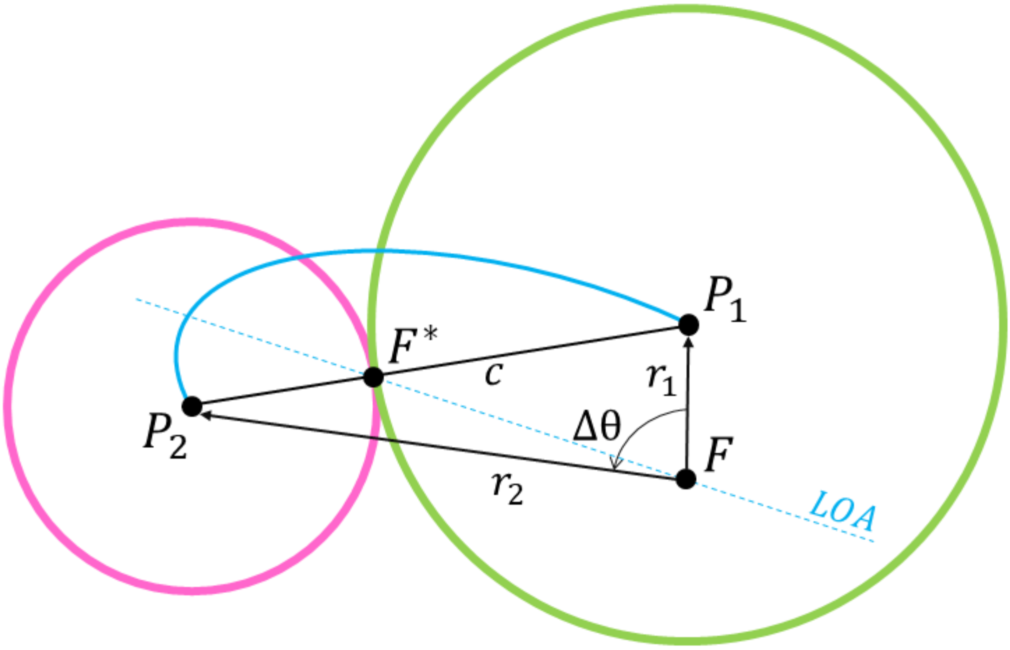

Figure 2.3: Geometry of the Minimum Energy Solution

SMA that connects P_1 and P_2, a_m. The chord, c, is equal to

$$c = \overline{P_1F^*} + \overline{P_2F^*} \tag{2.27}$$

applying the properties of ellipses, we have

$$c = 2a_m - r_1 + 2a_m - r_2 = 4a_m - (r_1 + r_2) \tag{2.28}$$

We define the semi-perimeter of the triangle P_1FP_2, s, as

$$s = \frac{1}{2}\left(r_1 + r_2 + c\right) \tag{2.29}$$

Solving Eq.(2.28) and Eq.(2.29) for a_m, we obtain

$$a_m = \frac{1}{2}s \tag{2.30}$$

After calculating the SMA of the minimum energy ellipse for given P_1, P_2 and $\Delta\theta$, α and β corresponding to the minimum energy ellipse can also be calculated by substituting Eq.(2.30) into Eq.(2.23) and Eq.(2.24), to get

$$\alpha_m = \pi \tag{2.31}$$

and

$$\beta_m = 2sgn\left(\sin\Delta\theta\right)\arcsin\sqrt{\frac{s-c}{s}} \tag{2.32}$$

where *sgn* is the *signum* function, such that

$$sgn\left(x\right) = \begin{cases} 1 & \text{if } x > 0 \\ 0 & \text{if } x = 0 \\ -1 & \text{if } x < 0 \end{cases} \tag{2.33}$$

Replacing α_m and β_m in Eq.(2.26) it is possible to compute the TOF corresponding to the minimum energy ellipse, t_m, as

$$\begin{aligned} \sqrt{\mu}t_m &= a_m^{\frac{3}{2}}\left[\alpha_m - \beta_m - \left(\sin\alpha_m - \sin\beta_m\right)\right] \\ &= \left(\frac{s}{2}\right)^{\frac{3}{2}}\left(\pi - \beta_m + \sin\beta_m\right) \end{aligned} \tag{2.34}$$

Solving for t_m, we obtain

$$t_m = \sqrt{\frac{s^3}{8\mu}}\left(\pi - \beta_m + \sin\beta_m\right) \tag{2.35}$$

To determine the type of orbit, we need to compare the given TOF with the the parabolic time of flight, t_p. This is computed by taking the limit as the SMA goes to infinity using Eq.(2.26)

$$\begin{aligned} t_p &= \lim_{a\to\infty} TOF = \frac{a^{\frac{3}{2}}}{\sqrt{\mu}}\left[\alpha - \beta - \left(\sin\alpha - \sin\beta\right)\right] \\ &= \lim_{a\to\infty} TOF = \frac{a^{\frac{3}{2}}}{\sqrt{\mu}}\left[2\arcsin\sqrt{\frac{s}{2a}} - sgn\left(\sin\Delta\theta\right)2\arcsin\sqrt{\frac{s-c}{2a}} + \right. \\ &\left. - \left(\sin 2\arcsin\sqrt{\frac{s}{2a}} - sgn\left(\sin\Delta\theta\right)\sin 2\arcsin\sqrt{\frac{s-c}{2a}}\right)\right] \end{aligned} \tag{2.36}$$

Since $a \to \infty$, we can make a substitution such that, ε, becomes

$$\varepsilon = \frac{1}{a} \to 0 \tag{2.37}$$

to get

$$\begin{aligned} t_p = \lim_{\varepsilon \to 0} TOF = \frac{\varepsilon^{-\frac{3}{2}}}{\sqrt{\mu}} \Bigg[& 2 \arcsin \sqrt{\frac{s\varepsilon}{2}} - sgn\left(\sin \Delta\theta\right) 2 \arcsin \sqrt{\frac{(s-c)\,\varepsilon}{2}} + \\ & - \left(\sin 2 \arcsin \sqrt{\frac{s\varepsilon}{2}} - sgn\left(\sin \Delta\theta\right) \sin 2 \arcsin \sqrt{\frac{(s-c)\,\varepsilon}{2}} \right) \Bigg] \end{aligned} \tag{2.38}$$

Using Taylor series expansions we obtain

$$\begin{aligned} t_p = \lim_{\varepsilon \to 0} TOF = \frac{\varepsilon^{-\frac{3}{2}}}{\sqrt{\mu}} \Bigg\{ & 2\sqrt{\frac{s\varepsilon}{2}} + \frac{2}{6}\sqrt{\frac{s^3\varepsilon^3}{8}} - sgn\left(\sin \Delta\theta\right) \Bigg(2\sqrt{\frac{(s-c)\,\varepsilon}{2}} + \\ & + \frac{2}{6}\sqrt{\frac{(s-c)^3\,\varepsilon^3}{8}} \Bigg) - \Bigg[2\sqrt{\frac{s\varepsilon}{2}} + \frac{2}{6}\sqrt{\frac{s^3\varepsilon^3}{8}} - \frac{8}{6}\sqrt{\frac{s^3\varepsilon^3}{8}} + \\ & - sgn\left(\sin \Delta\theta\right) \Bigg(2\sqrt{\frac{(s-c)\,\varepsilon}{2}} + \frac{2}{6}\sqrt{\frac{(s-c)^3\,\varepsilon^3}{8}} - \frac{8}{6}\sqrt{\frac{(s-c)^3\,\varepsilon^3}{8}} \Bigg) \Bigg] \Bigg\} \end{aligned} \tag{2.39}$$

simplifying we get

$$\begin{aligned} t_p = \lim_{\varepsilon \to 0} TOF &= \frac{\varepsilon^{-\frac{3}{2}}}{\sqrt{\mu}} \left[\frac{\sqrt{2}}{3} s^{\frac{3}{2}} - sgn\left(\sin \Delta\theta\right) \frac{\sqrt{2}}{3} \left(s-c\right)^{\frac{3}{2}} \right] \varepsilon^{\frac{3}{2}} \\ &= \frac{\sqrt{2}}{3\sqrt{\mu}} \left[s^{\frac{3}{2}} - sgn\left(\sin \Delta\theta\right) \left(s-c\right)^{\frac{3}{2}} \right] \end{aligned} \tag{2.40}$$

Knowing the orbit type (prograde or retrograde, short way or long way) allows us to split the problem into three chategories:

$$\begin{aligned} &TOF > t_p \to \text{elliptical orbit} \\ &TOF = t_p \to \text{parabolic orbit} \\ &TOF < t_p \to \text{hyperbolic orbit} \end{aligned} \tag{2.41}$$

The parabolic case is the simplest, since we know that in that case $a \to \infty$ and $e = 1$, so we don't need to solve the Eq.(2.26). Elliptical and hyperbolic cases need to be further studied in order to find the corresponding SMA that solves Eq. (2.26).

2.2.1 Elliptical Case

Let's fist consider the elliptical case of Lambert's problem where $TOF > t_p$. The values of α and β are based on the TOF and $\Delta\theta$ values as follows

$$\alpha_E = \begin{cases} \alpha & \text{if } TOF \leqslant t_m \\ 2\pi - \alpha & \text{if } TOF > t_m \end{cases} \tag{2.42}$$

and

$$\beta_E = \begin{cases} \beta & \text{if } 0 \leqslant \Delta\theta < \pi \\ -\beta & \text{if } \pi \leqslant \Delta\theta < 2\pi \end{cases} \tag{2.43}$$

where α and β are computed from Eq.(2.23) and Eq.(2.24), respectively. So the Lambert's equation becomes

$$a^{\frac{3}{2}} \left[\alpha_E(a) - \beta_E(a) - (\sin\alpha_E(a) - \sin\beta_E(a))\right] - \sqrt{\mu}TOF = 0 \tag{2.44}$$

Eq.(2.44) guarantees the existence of one and only one solution. After using one of the numerical methods existing in the literature, such as the *secant method*, we can solve for a and then find other orbital parameters, such as, the semilatus rectum, $\wp$, and consequentially the eccentricity, e, as

$$\wp = \frac{4a(s-r_1)(s-r_2)}{c^2} \sin^2 \frac{\alpha_E + \beta_E}{2} \tag{2.45}$$

and

$$e = \sqrt{1 - \frac{\wp}{a}} \tag{2.46}$$

To know the velocities at the points P_1 and P_2, we need to introduce the versors,

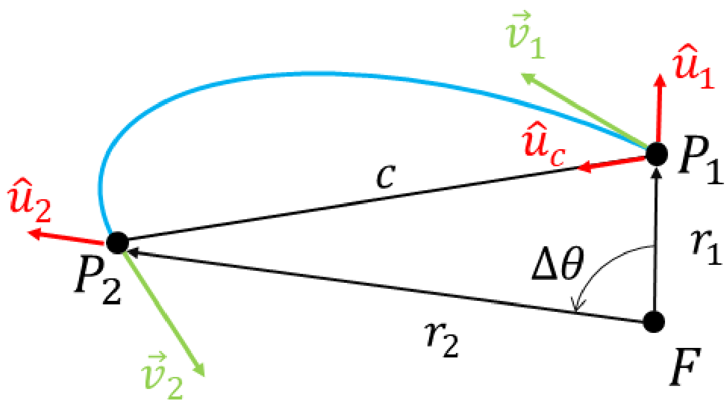

Figure 2.4: Velocity vectors

depicted in Fig. 2.4, as

$$\hat{u}_1 = \tfrac{\vec{r_1}}{r_1} \quad \hat{u}_2 = \tfrac{\vec{r_2}}{r_2} \quad \hat{u}_c = \tfrac{\vec{r_2}-\vec{r_1}}{c} \tag{2.47}$$

Thus, the velocities at the points P_1 and P_2 can be written as

$$\vec{v}_1 = (A + B)\,\hat{u}_c + (B - A)\,\hat{u}_1 \tag{2.48}$$

and

$$\vec{v}_2 = (A + B)\,\hat{u}_c - (B - A)\,\hat{u}_2 \tag{2.49}$$

where

$$\begin{aligned} A &= \sqrt{\tfrac{\mu}{4a}}\cot\tfrac{\alpha_E}{2} \\ B &= \sqrt{\tfrac{\mu}{4a}}\cot\tfrac{\beta_E}{2} \end{aligned} \tag{2.50}$$

2.2.2 Hyperbolic Case

Let's now consider the hyperbolic case of Lambert's problem where $TOF < t_p$. The orbit that links P_1 and P_2 is classified as hyperbolic and Lambert's equation becomes

$$(-a)^{\frac{3}{2}}\left[\sinh\alpha_H - \alpha_H - sgn\,(\sin\Delta\theta)\,(\sinh\beta_H - \beta_H)\right] - \sqrt{\mu}TOF = 0 \tag{2.51}$$

where α_H and β_H are computed according to the Eq.(2.52) and the Eq.(2.53) respectively, where hyperbolic trigonometric functions are used and $a < 0$.

$$\sinh\frac{\alpha_H}{2} = \sqrt{\frac{s}{-2a}} \tag{2.52}$$

$$\sinh\frac{\beta_H}{2} = \sqrt{\frac{s-c}{-2a}} \tag{2.53}$$

Like the elliptical case, the hyperbolic case guarantees the existence of one and only one solution for SMA, a. After finding a using Eq.(2.51) using, e.g., the secant method, we can find the semilatus rectum, $\wp$, as

$$\wp = \frac{-4a\,(s-r_1)\,(s-r_2)}{c^2}\sinh^2\frac{\alpha_H + \beta_H}{2} \tag{2.54}$$

and the eccentricity, e, with Eq.(2.46). To find the velocities at the points P_1 and P_2 in the computed hyperbolic transfer orbit, we use the same versors introduced in Eq.(2.47), and the same velocities of Eq.(2.48) and Eq.(2.49), but with different values of A and B, which are

$$\begin{aligned} A &= \sqrt{\tfrac{\mu}{-4a}}\coth\tfrac{\alpha_H}{2} \\ B &= \sqrt{\tfrac{\mu}{-4a}}\coth\tfrac{\beta_H}{2} \end{aligned} \tag{2.55}$$

2.3 Universal Variable Solution

Battin developed a condensed and computationally effective solution to Lambert's problem [8]. This version employs a universal time of flight equation, which accommodates elliptic, parabolic, and hyperbolic orbits and functions smoothly as a single, independent variable. Let's start by recalling the *vis-viva* equation

$$\epsilon = \frac{v^2}{2} - \frac{\mu}{r} = -\frac{\mu}{2a} \tag{2.56}$$

Solving for a we obtain

$$a = \frac{1}{\frac{2}{r} - \frac{V^2}{\mu}} \tag{2.57}$$

We define a new variable, α, not to be confused with α used in the classical solution, as

$$\alpha = \frac{1}{a} \tag{2.58}$$

This replacement removes the parabolic discontinuity since as $a \to \infty$, $\alpha \to 0$. Also, define χ as the universal anomaly and the dimensionless universal variable, z, as

$$z = \alpha\chi^2 \tag{2.59}$$

For t_0 and t, the variable χ can be related to the classical anomalies by:

$$\chi = \begin{cases} \sqrt{a}\,(E - E_0) & \text{for } \alpha > 0 \\ \sqrt{\wp}\left(\tan\frac{\nu}{2} - \tan\frac{\nu_0}{2}\right) & \text{for } \alpha = 0 \\ \sqrt{-a}\,(H - H_0) & \text{for } \alpha < 0 \end{cases} \tag{2.60}$$

where E, ν and H are, the elliptic eccentric anomaly, the true anomaly and the hyperbolic eccentric anomaly respectively. Let's introduce Lagrange coefficients $f, g, \dot{f}, \dot{g}$ such that

$$\begin{Bmatrix} \vec{r_2} \\ \vec{v_2} \end{Bmatrix} = \begin{bmatrix} f & g \\ \dot{f} & \dot{g} \end{bmatrix} \begin{Bmatrix} \vec{r_1} \\ \vec{v_1} \end{Bmatrix} \tag{2.61}$$

where

$$f = 1 - \frac{\mu r_2}{h^2}(1 - \cos\Delta\theta) \tag{2.62}$$

$$g = \frac{r_1 r_2}{h}\sin\Delta\theta \tag{2.63}$$

$$\dot{f} = \frac{\mu}{h}\left(\frac{1 - \cos\Delta\theta}{\sin\Delta\theta}\right)\left[\frac{\mu}{h^2}(1 - \cos\Delta\theta) - \frac{1}{r_1} - \frac{1}{r_2}\right] \tag{2.64}$$

$$\dot{g} = 1 - \frac{\mu r_1}{h^2}(1 - \cos\Delta\theta) \tag{2.65}$$

It is possible to write these Lagrange coefficients in terms of χ as

$$f = 1 - \frac{\chi^2}{r_1} C_2(z) \tag{2.66}$$

$$g = TOF - \frac{\chi^3}{\sqrt{\mu}} C_3(z) \tag{2.67}$$

$$\dot{f} = \frac{\sqrt{\mu}}{r_1 r_2} \chi \left[z C_3(z) - 1 \right] \tag{2.68}$$

$$\dot{g} = 1 - \frac{\chi^2}{r_2} C_2(z) \tag{2.69}$$

where $C_2(z)$ and $C_3(z)$ are the so-called *Stumpff functions*, which are defined by infinite series of the form

$$C_k(z) = \frac{1}{k!} - \frac{z}{(k+2)!} + \frac{z^2}{(k+4)!} - \cdots = \sum_{i=0}^{\infty} \frac{(-1)^i z^i}{(k+2i)!} \tag{2.70}$$

so that $C_2(z)$ becomes

$$C_2(z) = \begin{cases} \dfrac{1 - \cos\sqrt{z}}{z} & (z > 0) \\ \dfrac{1}{2} & (z = 0) \\ \dfrac{\cosh\sqrt{-z} - 1}{-z} & (z < 0) \end{cases} \tag{2.71}$$

while $C_3(z)$ becomes

$$C_3(z) = \begin{cases} \dfrac{\sqrt{z} - \sin\sqrt{z}}{\left(\sqrt{z}\right)^3} & (z > 0) \\ \dfrac{1}{6} & (z = 0) \\ \dfrac{\sinh\sqrt{-z} - \sqrt{-z}}{\left(\sqrt{-z}\right)^3} & (z < 0) \end{cases} \tag{2.72}$$

We have 4 equations, Eq.(2.66-2.69), and 3 unknowns, h, χ and z, but from the conservation of the angular momentum we also have that

$$f\dot{g} - \dot{f}g = 1 \tag{2.73}$$

so we have 3 linearly independent equations and 3 unknowns. If we equate Eq.(2.63) to Eq.(2.67), we obtaain

$$\frac{r_1 r_2}{h} \sin\Delta\theta = TOF - \frac{\chi^3}{\mu} C_3(z) \tag{2.74}$$

while if we equate Eq.(2.62) to Eq.(2.66), we obtain

$$1 - \frac{\mu r_2}{h^2}\left(1 - \cos\Delta\theta\right) = 1 - \frac{\chi^2}{r_1} C_2\left(z\right) \tag{2.75}$$

Solving for h we get

$$h = \sqrt{\frac{\mu r_1 r_2 \left(1 - \cos\Delta\theta\right)}{\chi^2 C_2\left(z\right)}} \tag{2.76}$$

which, when substituted into the Eq.(2.74), yields

$$\begin{aligned}\sqrt{\frac{r_1 r_2 \chi^2 C_2\left(z\right)}{\mu\left(1 - \cos\Delta\theta\right)}} \sin\Delta\theta &= TOF - \frac{\chi^3}{\sqrt{\mu}} C_3\left(z\right) \\ \chi\sqrt{C_2\left(z\right)}\sqrt{\frac{r_1 r_2}{\left(1 - \cos\Delta\theta\right)}} \sin\Delta\theta &= \sqrt{\mu} TOF - \chi^3 C_3\left(z\right)\end{aligned} \tag{2.77}$$

and rearranging to get $\sqrt{\mu}TOF$ on the left-hand side, we get

$$\sqrt{\mu} TOF = \chi\sqrt{C_2\left(z\right)} A + \chi^3 C_3\left(z\right) \tag{2.78}$$

where A is a constant given by

$$A = \sqrt{\frac{r_1 r_2}{\left(1 - \cos\Delta\theta\right)}} \sin\Delta\theta \tag{2.79}$$

Equating Eq.(2.64) to Eq.(2.68), we get

$$\frac{\mu}{h}\left(\frac{1 - \cos\Delta\theta}{\sin\Delta\theta}\right)\left[\frac{\mu}{h^2}\left(1 - \cos\Delta\theta\right) - \frac{1}{r_1} - \frac{1}{r_2}\right] = \frac{\sqrt{\mu}}{r_1 r_2}\chi\left[z C_3\left(z\right) - 1\right] \tag{2.80}$$

and substituting Eq.(2.76) in Eq.(2.80), we obtain

$$\begin{aligned}\sqrt{\frac{\chi^2 C_2\left(z\right)}{r_1 r_2\left(1 - \cos\Delta\theta\right)}}\left(\frac{1 - \cos\Delta\theta}{\sin\Delta\theta}\right)\left[\frac{\mu\chi^2 C_2\left(z\right)\left(1 - \cos\Delta\theta\right)}{\mu r_1 r_2\left(1 - \cos\Delta\theta\right)} - \frac{r_1 + r_2}{r_1 r_2}\right] = \\ = \frac{\chi}{r_1 r_2}\left[z C_3\left(z\right) - 1\right]\end{aligned} \tag{2.81}$$

Simplifying, we get

$$\frac{\sqrt{\chi^2 C_2\left(z\right)}}{A}\left(\chi^2 C_2\left(z\right) - r_1 - r_2\right) = \chi\left[z C_3\left(z\right) - 1\right] \tag{2.82}$$

Solving for χ, we obtain

$$\chi = \sqrt{\frac{y\left(z\right)}{C_2\left(z\right)}} \tag{2.83}$$

where

$$y(z) = r_1 + r_2 + A\frac{zC_3(z) - 1}{\sqrt{C_2(z)}} \tag{2.84}$$

If we replace Eq.(2.83) into Eq.(2.78), it is possible to write

$$\sqrt{\mu}TOF = \sqrt{y(z)}A + \left(\frac{y(z)}{C_2(z)}\right)^{\frac{3}{2}} C_3(z) \tag{2.85}$$

which is Lambert's equation in terms of the universal variable z.

2.3.1 Newton-Raphson Method

In this subsection we discuss how to solve Eq.(2.85). One of the most efficient numerical method for this case is the *Newton-Raphson method*, which states that to find the root, z, of a real-valued function, $F(z)$, we need to iterate using the following equation until a certain tolerance is reached

$$z_n = z_{n-1} - \frac{F(z_{n-1})}{F'(z_{n-1})} \tag{2.86}$$

where $F'(z)$ is the derivative of $F(z)$ with respect to z, n is the n^{th} iteration and $n-1$ is the $n-1^{th}$ iteration. Note that Eq.(2.86) is the Taylor series expansion of $F(z)$ truncated at the first term. In our case, the function is

$$F(z) = \sqrt{y(z)}A + \left(\frac{y(z)}{C_2(z)}\right)^{\frac{3}{2}} C_3(z) - \sqrt{\mu}TOF \tag{2.87}$$

so we need to compute $F'(z) = \frac{dF(z)}{dz}$, which is split in two cases: for $z \neq 0$ we have that

$$\begin{aligned} \left.\frac{dF(z)}{dz}\right|_{z\neq 0} = &\left(\frac{y(z)}{C_2(z)}\right)^{\frac{3}{2}} \left[\frac{1}{2z}\left(C_2(z) - \frac{3C_3(z)}{2C_2(z)}\right) + \frac{3C_3^2(z)}{4C_2(z)}\right] + \\ &+ \frac{A}{8}\left(\frac{3C_3(z)}{C_2(z)}\sqrt{y(z)} + A\sqrt{\frac{C_2(z)}{y(z)}}\right) \end{aligned} \tag{2.88}$$

and for $z = 0$ we need to take the limit as $z \to 0$, which yields

$$\left.\frac{dF(z)}{dz}\right|_{z=0} = \frac{\sqrt{2}}{40}y(0)^{\frac{3}{2}} + \frac{A}{8}\left(\sqrt{y(0)} + A\sqrt{\frac{1}{2y(0)}}\right) \tag{2.89}$$

Solving Eq.(2.87), and through backward substitution, we get the SMA, and consequently the other orbital parameters. Finally, it is possible to compute the

Lagrange coefficients which are used to calculate the velocities $\vec{v_1}$ and $\vec{v_2}$ using Eq.(2.61), which simplifies to as

$$\vec{v_1} = \frac{1}{g}\left(\vec{r_2} - f\vec{r_1}\right) \tag{2.90}$$

$$\vec{v_2} = \frac{1}{g}\left(\dot{g}\vec{r_2} - \vec{r_1}\right) \tag{2.91}$$

Compared to the classical method, the universal variable method is typically faster in terms of computational time. Additionally, it has the advantage of only needing a single initial guess (z_0) and does not require prior determination of the conic section.

The next chapter will explore heuristic algorithms. Specifically, we will focus on mathematical modeling of the particle swarm optimization technique, which will then be used in Chapters 5 and 6 to find the initial conditions of a periodic orbit in the CR3BP and a landing trajectory from that orbit to a candidate asteroid.

Chapter 3

Heuristic Algorithms

Broadly speaking, there are two types of numerical optimization methods: deterministic and stochastic. Deterministic, also known as gradient-based methods, assume that the objective function to be optimized is continuous and differentiable. In contrast, stochastic methods, also known as evolutionary algorithms, or heuristic algorithms, take inspiration from natural phenomena and employ a population of individuals to represent potential solutions. The optimal solution is then found through competition and cooperation among these individuals. The most widely used class of these methods is genetic algorithms, which simulate the evolution of a species based on the principle of survival of the fittest, as proposed by Darwin [10]. In this chapter, after an overview of some of the most used heuristic algorithms, *Particle Swarm Optimization*, which is then used in Chapters 5 and 6 to find the initial conditions of a periodic orbit in the CR3BP and a landing trajectory from that orbit to a candidate asteroid, will be discussed.

3.1 Computational Swarm Intelligence Introduction

Swarm Intelligence (SI) is a computational technique that is effective in adaptive systems. This approach combines genetic adaptation and social observation in problem-solving tools such as schools of fish, bird flocks, and insect colonies (e.g., ants, termites, and honeybees). In SI, a group of simple agents collectively solves problems through the installation of collective intelligence. Ethnologists conducted studies in the 1980s to model swarm behavior and observed that individual agents have stochastic behavior in response to their environment. The emergence of collective intelligence results from local rules that are independent of global rules, and interactions between self-organized agents. Swarms exhibit self-organization, and interactions on the local level lead to a global response. Trajectory tracking algorithms demonstrate how decentralized, self-organized patterns emerge in animal foraging behavior. The principles that express swarm intelligence as an intelligent behavior include the swarm's ability to process spatial and temporal data, adapt to changing conditions, allocate resources throughout the domain and adapting itself when necessary.

3.1.1 Artificial Bee Colony Algorithm

The Artificial Bee Colony (ABC) Algorithm, introduced by Karaboga [11] in 2005, is a swarm intelligence-based optimization algorithm that is inspired by the foraging behavior of honey bees. In this algorithm, the problem to be solved is formulated as an optimization problem, and a group of artificial bees are used to find the best solution. The ABC algorithm consists of three types of bees: employed bees, onlooker bees, and scout bees. Each employed bee is associated with a particular solution to the optimization problem. The employed bees search for new solutions by exploring the solution space in the vicinity of their current solution using local search strategies. Onlooker bees observe the employed bees and choose a solution to explore based on the quality of the associated solution. The onlooker bees also use local search strategies to explore the solution space around the chosen solution. Scout bees are responsible for randomly searching the solution space for new solutions. In each iteration of the ABC algorithm, the employed bees and onlooker bees generate new solutions by modifying their current solutions using local search strategies. The quality of the new solutions is evaluated using an objective function, and the best solution found so far is recorded. The scout bees randomly generate new solutions and replace any employed bee solution that has not been improved for a certain number of iterations. The ABC algorithm continues until a stopping criterion is met, such as reaching a maximum number of iterations or achieving a satisfactory solution quality. The final solution obtained by the algorithm is the best solution found during the optimization process.

3.1.2 Ant Colony Optimization

Ant Colony Optimization (ACO) is another heuristic algorithm that is inspired by the foraging behavior of ants. ACO is typically used to solve combinatorial optimization problems, such as the traveling salesman problem where the Traveling Salesman Problem (TSP) is a classic optimization problem that involves finding the shortest possible route that visits a set of cities and returns to the starting city, where each city is visited only once. The ACO algorithm works by simulating the behavior of ants as they search for food. Ants communicate with each other by leaving pheromone trails on the ground. The strength of the pheromone trail is proportional to the quality of the food source. Other ants follow the pheromone trails to find the food source. As more ants follow the trail, the pheromone concentration increases, making the trail more attractive to other ants. Eventually, the ants converge on the best food source, and the pheromone trail becomes very strong. In the ACO algorithm, a set of artificial ants is used to search for a good solution to the optimization problem. Each ant represents a candidate solution, and the ants build solutions by iteratively selecting components from the solution space. During the construction of a solution, each ant uses a probabilistic rule to select the next component to add to the solution. The probability of selecting a particular component is based on the pheromone trail associated with that component, as well as the heuristic information that guides the ant's search. As the ants build solutions, they update the pheromone trails associated with the components in the solution. The amount of pheromone deposited is proportional to the quality of the solution found by the ant. Stronger solutions lead to stronger pheromone trails, which makes those components more attractive to other ants. As the previous algorithm, the ACO algorithm iterates until it satisfies a termination condition, which could be either achieving a desirable level of solution quality or reaching the maximum number of iterations. The best solution is selected as the final solution evaluating an objective function. ACO algorithm is applied in the aerospace field, for example, to design the multiple gravity assist trajectory [12].

3.1.3 Fireworks Algorithm

In 2010, Ying Tan [13] proposed the Fireworks Algorithm (FWA), an optimization algorithm based on the behavior of fireworks. In the FWA, each firework represents a potential solution to the optimization problem. The firework's position in the search space corresponds to the parameters of the solution. The quality of the solution is evaluated by an objective function. The FWA uses two types of explosions: Gaussian explosions and uniform explosions. A Gaussian explosion occurs when a firework explodes at its current location, and the resulting sparks move away from the center according to a Gaussian distribution. A uniform explosion occurs when a firework explodes at a random location within a predefined range. After each explosion, the sparks evaluate their quality using the objective function. The sparks then compete for survival, with the weaker sparks being eliminated. The surviving sparks become the new population for the next iteration. The FWA also employs a mutation operator to introduce new solutions into the population. The mutation operator randomly selects a firework and perturbs its position in the search space. The resulting solution is then evaluated, and it replaces the weakest firework in the population if it is better. The FWA continues iterating until a stopping criterion is met, such as reaching a maximum number of iterations or achieving a satisfactory solution quality. FWA is applied, for example, to trajectory design for Earth to Lunar Halo Orbits [14].

3.2 Particle Swarm Optimization

Particle swarm optimization (PSO) is an iterative technique that was initially introduced in 1995 [15, 16]. PSO falls under the category of swarm intelligence methods, drawing inspiration from the unpredictable movement of bird flocks in their search for food. PSO leverages the concept of information sharing to influence the overall behavior of the swarm [17].
At the beginning of the optimization process, a randomly generated initial population of particles forms the swarm. Each particle in the swarm is associated with a position vector and a velocity vector at a particular iteration. The position vector contains the unknown parameter values, while the velocity vector determines the particle's position update after each iteration. During a single iteration, both the position and velocity vectors are updated. Each particle represents a potential solution to the problem and corresponds to a specific value of the cost function. By the end of the process, the best particle is selected and it represents the solution of the optimization problem.

3.2.1 PSO Mathematical Model

To minimize the cost (or objective) function, J, the task involves determining the optimal values for the n unknown parameters, denoted as $\varrho_1, ..., \varrho_n$. The dynamical system's time evolution is dependent on these parameters, which are subject to constraints within their respective ranges, such that

$$l_k \leqslant \varrho_k \leqslant u_k \quad for \quad k = 1, \ldots, n \tag{3.1}$$

where l_k and u_k are the lower and the upper bounds of the k^{th} unknown parameter respectively.
As mentioned earlier, the PSO technique is a population-based method, employing a swarm of N particles to represent the population. Each particle, indexed by i with $i = 1, \ldots, N$, is associated with a position vector $\vec{\varrho}(i)$ and a velocity vector $\vec{v}(i)$. It is important to note that in this context, the terms *position* and *velocity* refer to the search space of the unknown parameters and hold no physical interpretation. The position vector encompasses the values of the n unknown parameters for the problem at hand

$$\vec{\varrho}(i) = \left[\begin{array}{ccc} \varrho_1(i) & \ldots & \varrho_n(i) \end{array} \right]^T \tag{3.2}$$

The velocity vector, represented by the components $v_k(i)$ for $k = 1, \ldots, n$, governs the update of the particle's position. Since the position components are bounded, it is necessary to impose constraints on the velocity components to ensure they fall within appropriate ranges

$$-(u_k - l_k) \leqslant \varrho_k \leqslant (u_k - l_k) \quad for \quad k = 1, \ldots, n \tag{3.3}$$

The limitations presented in the Eq. (3.3) are imposed to not exceed position limits.
Every particle in the swarm represents a potential solution to the problem and is associated with a distinct value of the cost function. The formulas used for updating the position and velocity dictate the evolution of the swarm, driving it towards the globally optimal position. This optimal position corresponds to the best possible solution for the problem at hand. It is worth noting how PSO does not guarantee to find the global optimal solution for every problem. Instead, PSO tends to converge towards a local optimal solution, which is the best solution within a specific region of the search space.
To initialize the PSO algorithm, an initial population is randomly generated, consisting of N particles. The positions and velocities of these particles are distributed uniformly within the search space defined by the problem's constraints. In the first step, for each particle i (ranging from 1 to N), we evaluate the cost function associated with that particle to the current iteration j, denoted as $J^{(j)}(i)$. This cost function represents the quality of the particle's current position.
Next, we determine the best position ever visited by particle i up to the current iteration j. This position, denoted as $\vec{\Psi}^{(j)}(i)$, is obtained by selecting the position with the minimum cost function value among all iterations from 1 to j. It is important to note that this best position is specific to each particle and serves as a reference for comparison and improvement. Mathematically, we have

$$\vec{\Psi}^{(j)}(i) = \vec{\varrho}^{(l)}(i) \tag{3.4}$$

where l is defined as follows

$$l = \arg \min_{p=1,\dots,j} J^{(p)}(i) \tag{3.5}$$

Moving on to the second step, we calculate the global best position, denoted as $\vec{\Upsilon}(j)$, which represents the overall best position visited by any particle in the entire swarm. Therefore, we have

$$\vec{\Upsilon}^{(j)} = \vec{\Psi}^{(j)}(q) \tag{3.6}$$

where q is defined as follows

$$q = \arg \min_{i=1,\dots,N} \mathcal{F}^{(j)}(i) \tag{3.7}$$

$\mathcal{F}^{(j)}(i)$ denotes the cost function value associated with the best position ever explored by particle i up to iteration j. Expressing it mathematically, this yields

$$\mathcal{F}^{(j)}(i) = \min_{p=1,\dots,j} J^{(p)}(i) \tag{3.8}$$

Finally, we update the velocity vector for each particle. The velocity update equation consists of three terms: the inertial term, the cognitive term, and the social term. The inertial term is determined by multiplying the previous velocity vector of the kth unknown parameter, $v_k^{(j-1)}(i)$, by a constant weight factor c_I. The cognitive term is calculated by multiplying a cognitive weight factor c_C with the difference between the best position of the kth unknown parameter ever visited by particle i until the current iteration $\Psi_k^{(j)}(i)$ and the position of the kth unknown parameter of the particle i at the current iteration $\varrho_k^{(j)}(i)$. Similarly, the social term is obtained by multiplying a social weight factor c_S with the difference between the global best position of the kth unknown parameter until the current iteration $\Upsilon_k^{(j)}$ and and the position of the kth unknown parameter of the particle i at the current iteration $\varrho_k^{(j)}(i)$. In terms of mathematical formulation

$$v_k^{(j+1)}(i) = c_I \cdot v_k^{(j)}(i) + c_C \cdot \left(\Psi_k^{(j)}(i) - \varrho_k^{(j)}(i)\right) + c_S \cdot \left(\Upsilon_k^{(j)} - \varrho_k^{(j)}(i)\right) \tag{3.9}$$

The inertial, cognitive, and social weights have the following expressions [18]

$$\begin{cases} c_I = \frac{1+r_1(0,1)}{2} \\ c_C = 1.49445 \cdot r_2(0,1) \\ c_S = 1.49445 \cdot r_3(0,1) \end{cases} \tag{3.10}$$

where $r_1(0,1)$, $r_2(0,1)$, and $r_3(0,1)$ denote three separate random numbers chosen independently from a uniform distribution ranging from 0 to 1.
Successively, if the previous velocity component, $v_k^{(j+1)}(i)$, is less than a threshold value, $-(u_k - l_k)$, then the updated velocity component, $v_k^{(j+1)}(i)$, is set to $-(u_k - l_k)$. While if the previous velocity component, $-(u_k - l_k)$, is greater than $(u_k - l_k)$, then the updated velocity component, $v_k^{(j+1)}(i)$, is set to $(u_k - l_k)$. In a mathematical representation,

$$\begin{aligned} v_k^{(j+1)}(i) = -(u_k - l_k) \quad if \quad v_k^{(j+1)}(i) \leqslant -(u_k - l_k) \\ v_k^{(j+1)}(i) = (u_k - l_k) \quad if \quad v_k^{(j+1)}(i) \geqslant (u_k - l_k) \end{aligned} \tag{3.11}$$

To update the position vector for each particle i and each component $\varrho_k(i)$ with $k = 1, \ldots, n$ and $i = 1, \ldots, N$, at $j+1^{th}$ iteration we have

$$\varrho_k^{(j+1)}(i) = \varrho_k^{(j)}(i) + v_k^{(j)}(i) \tag{3.12}$$

If the previous position component, $\varrho_k^{(j)}(i)$, is less than a lower bound value l_k, then the updated position component, $\varrho_k^{(j+1)}(i)$, is set to l_k, and the corresponding velocity component, $v_k^{(j+1)}(i)$, is set to 0. If the previous position component, $\varrho_k^{(j)}(i)$, is greater than an upper bound value u_k, then the updated position component, $\varrho_k^{(j+1)}(i)$, is set to u_k, and the corresponding velocity component, $v_k^{(j+1)}(i)$, is set to 0. Mathematically,

$$\begin{aligned} \varrho_k^{(j+1)}(i) = l_k \quad and \quad v_k^{(j+1)}(i) = 0 \quad if \quad \varrho_k^{(j+1)}(i) \leqslant l_k \\ \varrho_k^{(j+1)}(i) = u_k \quad and \quad v_k^{(j+1)}(i) = 0 \quad if \quad \varrho_k^{(j+1)}(i) \geqslant u_k \end{aligned} \tag{3.13}$$

The algorithm continues iterating until the maximum number of iterations, $N_{it_{max}}$, is reached. The position vector of the global best particle, denoted as $\vec{\Upsilon}^{(N_{it_{max}})}$, is expected to contain the optimal values of the unknown parameters, corresponding to the global minimum of the objective function J. A sufficient number of iterations are used to ensure stability and achieve an optimal solution. To determine which N and $N_{it_{max}}$ to use, it is necessary to employ a process of trial and error.
The core concept of the method lies in the velocity updating, which incorporates three terms with stochastic weights. The first term, the inertial component, depends on the particle's velocity in the previous iteration. The second term, the cognitive component, directs the particle towards its personal best position. The third term, the social component, guides the particle towards the best position found by any particle in the swarm.
By following these steps in each iteration, the particle swarm optimization algorithm progresses towards finding a local optimal position, which corresponds to the best solution (within the search space) for the problem being considered.

The next chapter will analyze trajectories from Earth to a series of candidate asteroids and from them to Mars and there will be selected the asteroid that minimize ΔV from Earth to the asteroid and the total time of flight from Earth to Mars.

Chapter 4

Trajectory Design for Earth to Mars Missions

To minimize Earth-Mars total mission ΔV and consequently the overall cost of future Mars missions, a double arc trajectory is studied. The first arc will intercept one of the candidate asteroids studied in this section. Then, insertion into a Sun-asteroid Distant Retrograde Orbit (DRO) is performed, and, given a landing location on the asteroid surface, a potential landing trajectory onto the asteroid is studied similarly to what was proposed by Baraldi and Conte for Mars' moon, Phobos [19]. Since in-situ refueling is considered, the lift-off ΔV from the asteroid and the ΔV of the second arc trajectory to Mars are 'free'.
Missions to asteroids such as Itokawa demonstrated that near Earth asteroids with water in the form of hydrated mineral and ice exist and they are potentially convertible in propellant useful for spacecraft for the second arc trajectory from the asteroid to Mars [20]. Therefore, refueling with In-Situ Resource Utilization (ISRU) on asteroids can be highly cost-effective for a mission to Mars. ISRU refueling can help decrease the launch mass of the spacecraft as it wouldn't need to carry as much propellant from Earth, which in turn could minimize the size and cost of the rocket required for its launch.

4.1 Candidate Asteroid Selection

The number of known minor planets[1] has increased from less than 4000 in 1970 to over 1.2 million in 2022 [21]. Keeping track of these minor planets requires

[1] According to the International Astronomical Union (IAU), a minor planet is an astronomical object in direct orbit around the Sun that is exclusively classified as neither a planet nor a comet.

more effort from the organizations that maintain their catalogs. The process of discovering and designating minor planets involves collecting individual observations such as right ascension, declination, time, observatory location, and apparent magnitude and reporting them to the International Astronomical Union's Minor Planet Center (IAU MPC), which then publishes the observations for independent analysis. The MPC determines the heliocentric orbits of these minor planets based on their orbital elements such as semi-major axis, eccentricity, inclination, argument of perihelion, longitude of the ascending node, and mean anomaly, which are fitted to the observations. Similarly, catalogs of orbital elements are curated by various organizations including the Solar System Dynamics group at JPL, a consortium in Italy that began at the University of Pisa, and Lowell Observatory in Flagstaff, Arizona. Lowell's astorb catalog[2] has evolved into a modern relational database with associated web infrastructure.

For this study, the orbital parameters of all 1.2 million minor planets are taken from this catalogue. To reduce the number of minor planets/asteroids considered, we exclude all the objects with a SMA less than Earth's SMA and greater than Mars' SMA and all the objects with an inclination greater than 7°, considering that

$$\begin{aligned} a_{\oplus} &= 1.000001018\,[au] \\ a_{♂} &= 1.523662310\,[au] \\ i_{\oplus} &= 0.00^{\circ} \\ i_{♂} &= 1.85^{\circ} \end{aligned} \tag{4.1}$$

where $i_{\oplus}$ and $i_{♂}$ are calculated with respect to the plane of the ecliptic, $\oplus$ means "*Earth*" and ♂ means "*Mars*". A low inclination of the orbit asteroid is considered because the mission ΔV increases considerably if we make a change of plan with a great change of inclination Δi

$$\Delta V = \frac{2\sin\left(\frac{\Delta i}{2}\right)(1 + e\cos\theta)\,na}{\sqrt{1-e^2}\cos(\omega+\theta)} \tag{4.2}$$

where e is the orbital eccentricity, ω is the argument of periapsis, θ is the true anomaly, n is the mean motion and a is the semi-major axis. We can note as for low eccentricity orbit, the mean parameter we have to consider to minimize ΔV is Δi.

After this first selection, the candidate asteroids become 3434. To further reduce the number of asteroids, we solve Lambert's problem for finding the arc trajectory from Earth to an asteroid using the universal solution, as explained in Sec. 2.3. Lambert's problem is solved several times to obtain a porkchop plot, which is a

[2]`https://asteroid.lowell.edu/main/astorb/`

ΔV map with a 2-D domain composed by different TOF (y-axis) and different departure dates (x-axis). For computational speed, a coarse mesh is considered where TOF is equally split in 60 parts from 51 to 300 days and the departure dates changes every 30 days per 2 years starting on January 1, 2035. Once we have computed the total ΔV needed from Low Earth Orbit (LEO) at 400 km of altitude to each asteroid position for each different TOF and departure date, we select only the asteroids that have at least a total ΔV less than 4.5 km/s. How the total ΔV is computed is explained in the next section. After this selection, the candidate asteroids becomes 94. Tab. 4.1 summarizes their names and their orbital parameters.

Table 4.1: Candidate Asteroids and their Orbital Parameters with respect to the J2000 Ecliptic reference frame

Object	$a\,[au]$	e	$i\,[deg]$	$\Omega\,[deg]$	$\omega\,[deg]$	$M\,[deg]$
2000 EA14	1.1169	0.2026	3.5558	203.8305	206.0565	258.6195
1993 KA	1.2556	0.1978	6.0497	235.7651	342.0531	71.4521
1999 CG9	1.0618	0.0636	5.1553	138.4994	315.5890	37.8722
2005 ER95	1.2231	0.1591	3.3423	175.8631	8.4946	89.3191
2005 LC	1.1340	0.1027	2.7992	69.7928	147.0083	275.7425
2006 CL9	1.3462	0.2367	2.9376	139.2508	10.0614	321.4413
2006 DQ14	1.0277	0.0530	6.2957	155.3006	292.6021	176.4354
2006 UQ216	1.1039	0.1625	0.4738	217.6702	247.6721	336.2392
2007 HL4	1.1201	0.0907	6.5385	30.9718	139.3254	176.1519
2008 CM74	1.0889	0.1468	0.8537	321.4739	242.8326	36.1693
2008 HU4	1.0714	0.0556	1.3916	215.2683	350.5462	68.1344
2009 BD	1.0616	0.0518	1.2673	253.2008	316.4097	299.4390
2009 FH	1.4751	0.3394	0.6898	176.5157	24.2123	269.1949
2009 OS5	1.1481	0.0993	1.7107	144.3557	122.8071	64.5593
2009 SW171	1.3311	0.2333	3.0635	187.9849	150.2385	280.1851
2010 DJ	1.2064	0.1354	0.2327	3.2255	106.6390	323.4748
2010 RF12	1.0611	0.1882	0.8825	163.7123	267.3920	84.6385
2011 AA37	1.0959	0.0167	3.8169	275.6920	131.6060	268.3744
2011 CY7	1.2867	0.2137	3.9380	327.1000	164.8968	96.3243
2012 BB14	1.0637	0.0994	2.6444	316.8737	255.4661	315.9653
2012 VB37	1.4498	0.3127	1.9068	240.3259	153.9762	326.5411
2012 XM55	1.0976	0.1306	1.0810	66.4406	68.9951	274.9393
2013 HP11	1.1853	0.1259	4.1564	208.5827	9.6319	223.2356
2013 SP19	1.2849	0.2389	2.3260	0.7755	326.0269	189.0164
2013 UX2	1.1187	0.1493	4.1064	211.4071	228.0392	284.2737
2014 JR24	1.0665	0.1183	0.9298	48.8963	246.4457	301.3195

continued on next page...

...continued from previous page

Object	$a\,[au]$	e	$i\,[deg]$	$\Omega\,[deg]$	$\omega\,[deg]$	$M\,[deg]$
2014 LJ	1.0829	0.1413	0.9521	73.3514	95.1549	353.4160
2014 WX202	1.0356	0.0588	0.4128	243.9173	214.1195	267.0106
2014 WA366	1.0343	0.0716	1.5591	67.1066	287.6513	5.9672
2015 EZ6	1.2391	0.1945	3.1163	171.0002	6.4539	272.7066
2015 HC1	1.3543	0.2168	1.9762	228.1208	343.7456	351.6140
2015 VC2	1.0530	0.0744	0.8682	186.1494	288.2653	209.0057
2015 XX128	1.2664	0.2279	3.1299	77.4548	13.2059	13.2837
2015 XD169	1.0851	0.1212	3.7495	249.1294	137.7852	176.8251
2015 XA352	1.2694	0.1690	4.1123	236.5414	15.3890	195.7015
2016 CF137	1.0905	0.1000	2.4451	132.5417	301.5044	124.4844
2016 EP84	1.1904	0.1733	0.8190	287.4413	195.5128	163.0043
2016 GL222	1.1533	0.1368	3.5316	198.1055	303.3258	245.5768
2017 BF29	1.1812	0.1341	2.6128	302.3666	203.7956	251.7030
2017 BG30	1.0554	0.1071	1.6312	304.5028	250.4197	161.4550
2017 CP1	1.4166	0.2980	2.7992	330.5242	195.1257	196.4923
2017 FJ3	1.1334	0.1184	0.9633	167.2576	26.7249	319.8884
2017 FW90	1.0334	0.1460	3.1740	10.4163	85.8292	300.7627
2017 LD	1.3945	0.2778	0.0679	79.1456	195.8211	159.9548
2017 RL16	1.0175	0.1157	4.1178	16.5854	220.7477	216.1286
2017 UM52	1.0534	0.0525	3.3575	30.8950	53.1837	289.4977
2017 WM13	1.1319	0.1188	4.8496	230.7092	161.5628	153.4009
2017 YC1	1.2923	0.2610	2.6228	205.7536	169.4893	232.2218
2017 YW3	1.0947	0.1132	2.2001	273.7125	136.9870	218.4502
2018 LQ2	1.0911	0.0575	2.1262	178.3052	142.8374	351.7668
2018 RR1	1.0754	0.1413	0.6679	352.3493	277.1517	61.9671
2019 KJ2	1.0572	0.0265	3.1454	61.6680	252.4638	95.3290
2019 LV	1.0962	0.1495	4.9328	81.1664	47.5073	195.5807
2019 PY	1.0579	0.0575	6.8914	303.6425	109.2771	3.2759
2019 PO1	1.0360	0.0611	1.1203	328.2544	250.3860	222.5062
2019 SU3	1.1204	0.1085	1.2853	3.2505	332.3668	338.4469
2019 UO1	1.0984	0.0256	2.7706	218.9153	336.2423	158.6967
2019 UB4	1.0374	0.0963	0.9207	27.6592	286.5161	123.2244
2019 XV	1.1005	0.0976	0.3439	46.0513	356.4250	310.0650
2020 BK	1.2500	0.2201	3.4822	113.7524	32.5589	61.5776
2020 BV2	1.4253	0.2950	1.2474	135.6703	339.1188	298.2451
2020 CF2	1.1947	0.1900	1.1518	329.5924	141.7391	138.1247
2020 DE2	1.2712	0.2242	0.7483	228.1697	250.4966	57.3296
2020 HN	1.0563	0.1373	0.5865	217.9934	264.2954	297.2139

continued on next page...

...continued from previous page

Object	$a\,[au]$	e	$i\,[deg]$	$\Omega\,[deg]$	$\omega\,[deg]$	$M\,[deg]$
2020 HQ4	1.2499	0.2135	0.1407	251.7393	286.4554	34.0435
2020 HL6	1.2600	0.2319	0.2397	96.3950	169.7274	329.1604
2020 OE2	1.0796	0.0850	3.3913	301.1262	59.3533	60.4691
2020 OK5	1.0806	0.0837	1.0063	295.8379	108.1058	18.2104
2020 PP1	1.0026	0.0715	5.9441	140.0328	42.6179	322.8520
2020 RT3	1.3853	0.2488	2.5051	157.2788	187.7806	183.6656
2020 SM2	1.1954	0.2045	1.1506	358.5020	48.9329	275.8776
2020 SH6	1.1018	0.0731	1.6968	23.6197	276.4618	92.1913
2020 VV	1.1178	0.1187	0.3455	19.6803	332.6592	21.9319
2020 WY	1.0202	0.0286	1.7000	107.1036	180.3156	200.7350
2020 WQ3	1.2588	0.1922	3.0165	57.3089	16.6346	207.2667
2020 XJ4	1.2280	0.1750	3.0932	24.6187	30.8846	236.9143
2021 CE	1.4625	0.3031	0.9656	107.2257	11.5597	66.6887
2021 EN5	1.1529	0.0853	0.2830	46.1368	72.6451	255.1462
2021 GB8	1.0804	0.1775	1.9803	32.2510	88.9409	301.8775
2021 HF1	1.3025	0.2025	1.3916	47.0962	183.0440	74.9362
2021 JY5	1.0402	0.0884	2.1945	233.7615	79.1069	175.7563
2021 NV8	1.2375	0.2203	2.6848	98.6579	139.2184	100.8531
2021 RP2	1.1028	0.1764	0.0322	342.4884	72.8495	43.3287
2021 VZ8	1.1279	0.1714	1.9165	216.0648	133.4790	70.8031
2022 BT	1.1796	0.1830	3.9313	303.7319	149.1573	326.5947
2022 BX5	1.0788	0.0730	0.3867	6.1962	101.2866	3.0332
2022 KL6	1.2143	0.1754	1.4431	217.2650	354.2242	225.2985
2022 NX1	1.0219	0.0250	1.0667	274.7674	169.5831	65.0875
2022 RF1	1.2453	0.1260	4.2585	162.6316	181.1685	121.5854
2022 RS1	1.0201	0.0659	4.9525	160.4172	92.6020	246.9470
2022 SZ2	1.0858	0.1336	3.1691	180.9197	244.7806	82.1613
2022 SN21	1.2142	0.1602	3.9924	2.1186	353.9410	116.1647
2022 UA5	1.1326	0.1543	1.5597	23.7841	315.2201	140.0713
2022 WS8	1.1862	0.1774	1.2073	1.6289	0.4900	116.3800

4.2 Earth to Candidate Asteroids transfer

After importing the 94 candidate asteroids' orbital parameters, we set 3660 different departure dates from January 1, 2035 to January 7, 2045 (one per day) and 250 different TOFs from 51 to 300 days. To compute the first ΔV from a 400 km LEO to asteroid is necessary to know the Earth's velocity, $\vec{v}_{\oplus}$, at departure and the velocity required to initiate the transfer, which is given by Eq. (2.90), $\vec{v}_{tI_1}$, where we have to know the Earth's position on the departure day and the asteroid's position at arrival. Here, the subscript tI means "first transfer". Knowing the last two velocities, $\vec{v}_{tI_1}$ and $\vec{v}_{\oplus}$, we obtain the speed $v_{\infty\oplus}$ that the spacecraft should have at Earth's sphere of influence on a hyperbolic transfer.

$$v_{\infty\oplus} = \|\vec{v}_{tI_1} - \vec{v}_{\oplus}\| \tag{4.3}$$

Using the *vis viva* equation, Eq. (2.56), we can find the speed, $v_{hyp\oplus}$, that the spacecraft should have at $r_{LEO} = R_{\oplus} + h$ on a hyperbolic transfer, where $R_{\oplus}$ is the Earth's radius (equal to 6371 km) and h is the altitude equal to 400 km, and where the subscript hyp means "hyperbolic".

$$\epsilon = \frac{v_{hyp\oplus}^2}{2} - \frac{\mu_{\oplus}}{r_{LEO}} = \frac{v_{\infty\oplus}^2}{2} \tag{4.4}$$

where ϵ is the specific orbital energy and $\mu_{\oplus} = 398600\ km^3 s^{-2}$. Solving for $v_{hyp\oplus}$, we obtain

$$v_{hyp\oplus} = \sqrt{v_{\infty\oplus}^2 + 2\frac{\mu_{\oplus}}{r_{LEO}}} \tag{4.5}$$

Therefore the first ΔV for the Earth-Asteroid transfer, $\Delta V_{1_{\oplus\to A}}$, becomes

$$\Delta V_{1_{\oplus\to A}} = v_{hyp\oplus} - v_{LEO} \tag{4.6}$$

where

$$v_{LEO} = \sqrt{\frac{\mu_{\oplus}}{r_{LEO}}} \tag{4.7}$$

To compute the second ΔV from LEO to the asteroid, it is necessary to know the asteroid's velocity, $\vec{v}_A$, at arrival and the velocity computed from Eq. (2.91), $\vec{v}_{tI_2}$, where we have to know the Earth's position on the departure day and the asteroid's position on the arrival day.

$$\Delta V_{2_{\oplus\to A}} = \|\vec{v}_A - \vec{v}_{tI_2}\| \tag{4.8}$$

The total ΔV for the Earth-Asteroid transfer is computed as the sum of $\Delta V_{1_{\oplus\to A}}$ and $\Delta V_{2_{\oplus\to A}}$

$$\Delta V_{tot_{\oplus\to A}} = \Delta V_{1_{\oplus\to A}} + \Delta V_{2_{\oplus\to A}} \tag{4.9}$$

Solving Lambert's problem several times for each departure date and for each TOF, and computing $\Delta V_{tot_{\oplus\to A}}$, we obtain 94 different porkchop plots. In Fig. (4.1) a porkchop plot from Earth to asteroid 2009 OS5 is shown, while all the Earth-asteroid porkchop plots are shown in App. A.

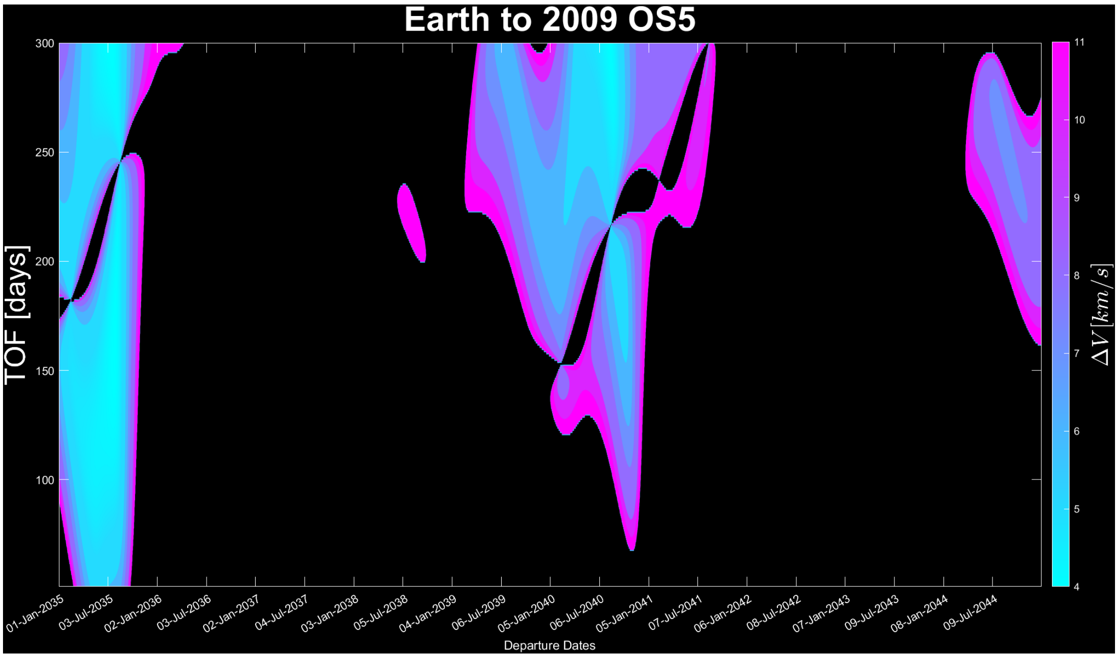

Figure 4.1: Porkchop Plot from Earth to Asteroid 2009 OS5

4.3 Candidate Asteroids for Mars transfers

Once the spacecraft arrives close enough to the asteroid, an insertion into a Sun-asteroid Distant Retrograde Orbit (DRO) is performed, and a landing trajectory is executed. The departure from the asteroid is set from 10 to 30 days after insertion into a DRO. As for the first case, 250 different TOFs, from 51 to 300 days are set. To compute the first ΔV from the asteroid to a 400 km Low Mars Orbit (LMO), it is necessary to know the asteroid's velocity, $\vec{v}_A$, at departure and the velocity computed from Eq. (2.90), $\vec{v}_{tII_1}$, where we have to know the asteroid's position at departure and Mars' position at arrival

$$\Delta V_{1_{A \to \mars}} = \|\vec{v}_{tII_1} - \vec{v}_A\| \tag{4.10}$$

where the subscript tII means "second transfer". To compute the second ΔV from the asteroid to a 400 km LMO, it is necessary to know Mars' velocity, $\vec{v}_{\mars}$, at arrival and the velocity computed from Eq. (2.91), $\vec{v}_{tII_2}$, where we have to know the asteroid's position at departure and Mars' position at arrival. Knowing the last two velocities, $\vec{v}_{\mars}$ and $\vec{v}_{tII_2}$ we obtain, $v_{\infty_{\mars}}$, which is the speed that the spacecraft has at the asteroid's sphere of influence.

$$v_{\infty_{\mars}} = \|\vec{v}_{\mars} - \vec{v}_{tII_2}\| \tag{4.11}$$

Using the *vis viva* equation, we can find the speed, $v_{hyp_♂}$, i.e. the speed that the spacecraft should have at $r_{LMO} = R_♂ + h$ in an hyperbolic transfer. Here, $R_♂$ is the Mars' radius equal to 3389.5 km and h is the altitude equal to 400 km and the subscript *hyp* means "hyperbolic"

$$\epsilon = \frac{v_{hyp_♂}^2}{2} - \frac{\mu_♂}{r_{LMO}} = \frac{v_{\infty_♂}^2}{2} \tag{4.12}$$

where $\mu_♂ = 42828\ km^3 s^{-2}$ is the gravitational parameter of Mars. Solving for $v_{hyp_♂}$, we obtain

$$v_{hyp_♂} = \sqrt{v_{\infty_♂}^2 + 2\frac{\mu_♂}{r_{LMO}}} \tag{4.13}$$

Therefore, the second ΔV for the Asteroid-Mars transfer, $\Delta V_{2_{A\to♂}}$, becomes

$$\Delta V_{2_{A\to♂}} = v_{hyp_♂} - v_{LMO} \tag{4.14}$$

where

$$v_{LMO} = \sqrt{\frac{\mu_♂}{r_{LMO}}} \tag{4.15}$$

is the circular orbit velocity corresponding to the targeted LMO. The total ΔV for the Asteroid-Mars transfer is computed as the sum of $\Delta V_{1_{A\to♂}}$ and $\Delta V_{2_{A\to♂}}$

$$\Delta V_{tot_{A\to♂}} = \Delta V_{1_{A\to♂}} + \Delta V_{2_{A\to♂}} \tag{4.16}$$

Every Asteroid-Mars transfer depends on all the possible Earth-Asteroid conics evaluated, i.e. 3,660 × 250 = 915,000 possible transfers. Considering that the possible Asteroid-Mars transfers are 21 × 250 = 5,250, the total transfers computed from Earth to Mars are 915,000 × 5,250 = 4,803,750,000 per asteroid possible mission scenarios. Assuming a computational time to solve Lambert's problem equal to 0.2 ms per solution, all cases for all 94 asteroids would take about 2 years and 10 months of continuous computation. Note that for this study a *MSI GE66 Raider* with a Intel(R) Core(TM) Processor i7-10875H CPU @ 2.30GHz, a 32 GB RAM and a 64 bit operating system, x-64-based processor was used. MATLAB R2022b was used as the programming software.
To avoid this problem, we find different local minima in the first Earth-Asteroid conics. Then, we divide the domain into 300 sub-domains. Departure dates are divided in 60 parts while TOFs are divided in 5 parts. Fig. 4.2 shows the subdivision of the domain considering only 60 sub-domains for simplicity for Earth to Asteroid 2017 RL16 porkchop plot.

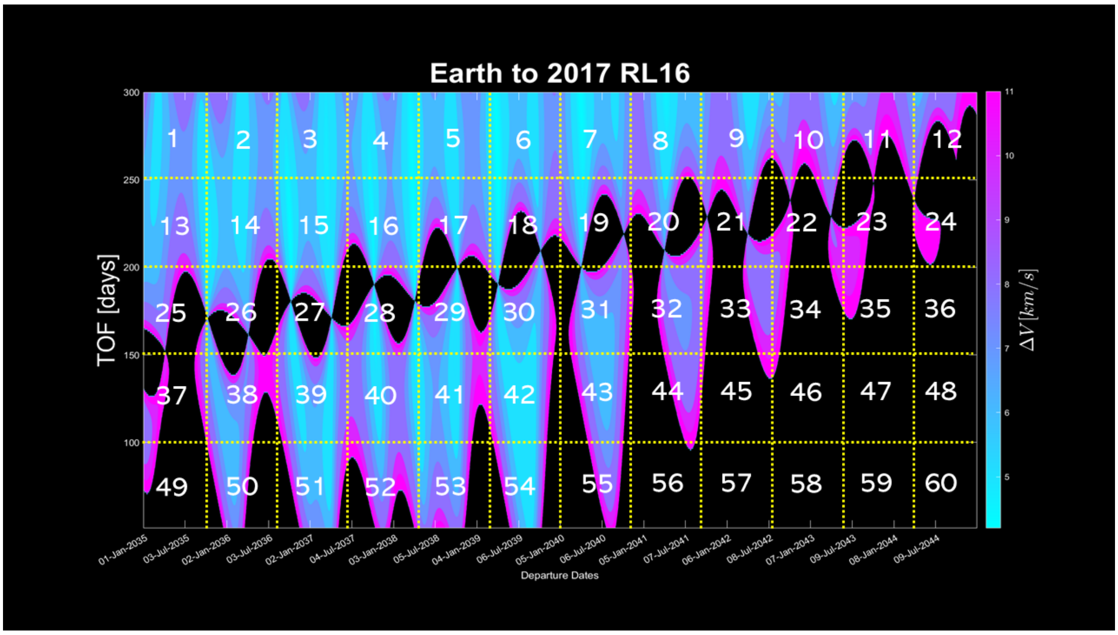

Figure 4.2: Porkchop Plot domain division

For each of these subdomains, we find the minimum ΔV. We start from each departure day and TOF, and look for the best case per asteroid using the following cost function, J_1, such that

$$J_1 = \begin{cases} \Delta V_{tot_{\oplus \to A}} & \text{if } \frac{\Delta V_{tot_{A \to \male}}}{\Delta V_{tot_{\oplus \to A}}} \leqslant 1.10 \\ \infty & \text{if } \frac{\Delta V_{tot_{A \to \male}}}{\Delta V_{tot_{\oplus \to A}}} > 1.10 \end{cases} \tag{4.17}$$

It should be noted that the propellant tanks are sized based on the largest mission ΔV (which could be the ΔV for Earth-asteroid or asteroid-Mars transfers) since the spacecraft refuels at the asteroid. Furthermore. we assume that the $\Delta V_{tot_{A \to \male}}$ may be at maximum 10% greater than $\Delta V_{tot_{\oplus \to A}}$ in order to not oversize the mass of the tanks structure since they would be more voluminous to contain more propellant or more massive (the thickness of the tank walls will be greater) to support a greater pressure (more propellant in the same volume). In this way the Asteroid-Mars transfers analyzed are $300 \times 21 \times 250 = 1{,}575{,}000$ per asteroid. Assuming the same computing time as before, all cases for all 94 asteroids were analyzed in about 8 h 13 min. The best ΔV case according to the cost function for each asteroid is summarized in Tab. 4.2.
Note that $\Delta V_{tot_{\oplus \to A}}$ is not the minimum ΔV possible for the first arc of the trajectory, but is the minimum ΔV such that $\Delta V_{tot_{A \to \male}} < 1.10 \cdot \Delta V_{tot_{\oplus \to A}}$. Thus, the best asteroid case (2022 SN21) results in a ΔV equal to 3.9079 km/s which is 36.7% lower than minimum ΔV (6.1696 km/s) for a direct Earth-Mars transfer in

the span of 10 years of departures starting from January 1, 2035. Fig. 4.3 shows an Earth-Mars porkchop plot where the departure dates are stopped at the first four years since the Earth-Mars synodic period is about 26 months.

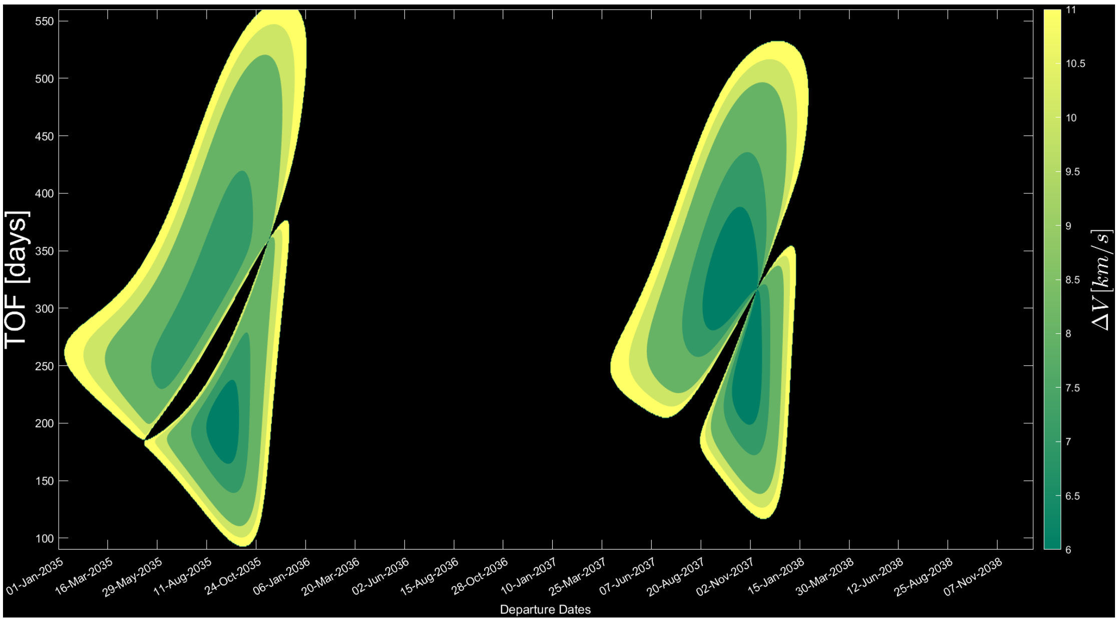

Figure 4.3: Earth-Mars Porkchop Plot

Tab. 4.3 shows combinations of departure days from Earth, arrival days on asteroid, departure days from the asteroid and arrival days on Mars. Tab. 4.2 shows that almost all TOFs exceed 1 year and more specifically they exceed the TOF for which we obtain the minimum ΔV in 10 years of possible Earth-Mars transfers. Also, $TOF_{\Delta V_{min,\oplus\rightarrow♂}}$ is equal to 252 days. Since total mission time is a critical parameter to minimize, e.g. for crewed missions, we give more importance to TOF and change the cost function J_2 as follows

$$J_2 = \begin{cases} \dfrac{\Delta V_{tot_{\oplus\rightarrow A}}}{\Delta V_{min,\oplus\rightarrow♂}} + \dfrac{TOF_{\oplus\rightarrow A\rightarrow♂}}{TOF_{\Delta V_{min,\oplus\rightarrow♂}}} & \text{if } \dfrac{\Delta V_{tot_{A\rightarrow♂}}}{\Delta V_{tot_{\oplus\rightarrow A}}} \leqslant 1.10 \\ \infty & \text{if } \dfrac{\Delta V_{tot_{A\rightarrow♂}}}{\Delta V_{tot_{\oplus\rightarrow A}}} > 1.10 \end{cases} \tag{4.18}$$

where

$$\begin{aligned} \Delta V_{min,\oplus\rightarrow♂} &= 6.1696 \text{ km/s} \\ TOF_{\Delta V_{min,\oplus\rightarrow♂}} &= 252 \text{ days} \end{aligned} \tag{4.19}$$

Using this new cost function, Tab. 4.2 and Tab. 4.3 become Tab. 4.4 and Tab. 4.5, respectively. Solving Lambert's problem several times for each departure date and for each TOF, we obtain 94 different porkchop plots. In Fig. (4.4) is shown a porkchop plot from asteroid 2021 C3 to Mars, while all the asteroid-Mars

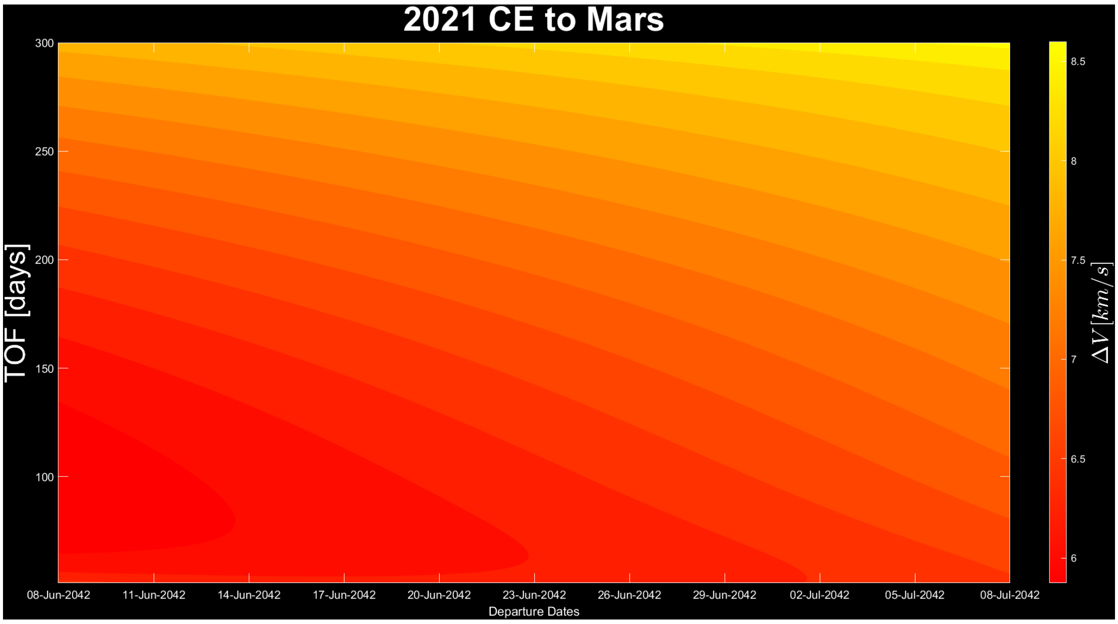

Figure 4.4: Porkchop Plot from asteroid 2021 C3 to Mars

porkchop plots are shown in App. B. Asteroid 2013 SP19 has best compromise from the minimum ΔV from the Earth to asteroid and the minimum total TOF from Earth to Mars (passing by the asteroid). So a spacecraft that leaves the Earth on September 12, 2035 will arrive on this asteroid on December 21, 2035 using a ΔV equal to 4.8673 km/s. After a stay on the asteroid of 10 days, until December 31, 2035 to complete the ISRU refueling, the spacecraft will reach Mars on March 5, 2036 using a "free" ΔV equal to 3.4714 km/s. In this way, 21.1% of ΔV is saved with respect to the best case of a direct Earth-Mars transfer (6.1696 km/s). This result is obtained spending 77 days less of mission time (175 days) respect to the best case of a direct Earth-Mars transfer (252 days). Therefore, we can think that when ISRU refueling missions will be consolidated, a human mission will prefer this second case, to reduce astronauts' risks linked to radiation exposure and to save on mass of consumables such as food and water brought from Earth. Fig. 4.5 and Fig. 4.7 show a double arc trajectory between Earth, asteroid and Mars for the two cases considered. Fig. 4.6 shows the first case from a different view. The cyan line represents Earth's orbit, the orange one depicts Mars' orbit, the red line shows the asteroid's orbit and finally the violet one represents the spacecraft trajectory. Note that the violet and red lines overlap for a short part (10 days) when the spacecraft is landed on the asteroid for ISRU. A double arc trajectory animation is provided for both cases scanning the QR code present in the Fig.4.8 and Fig. 4.9.

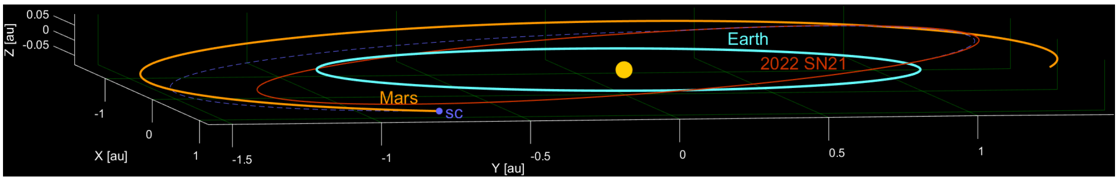

Figure 4.5: Double arc trajectory between Earth, asteroid 2022 SN21 and Mars

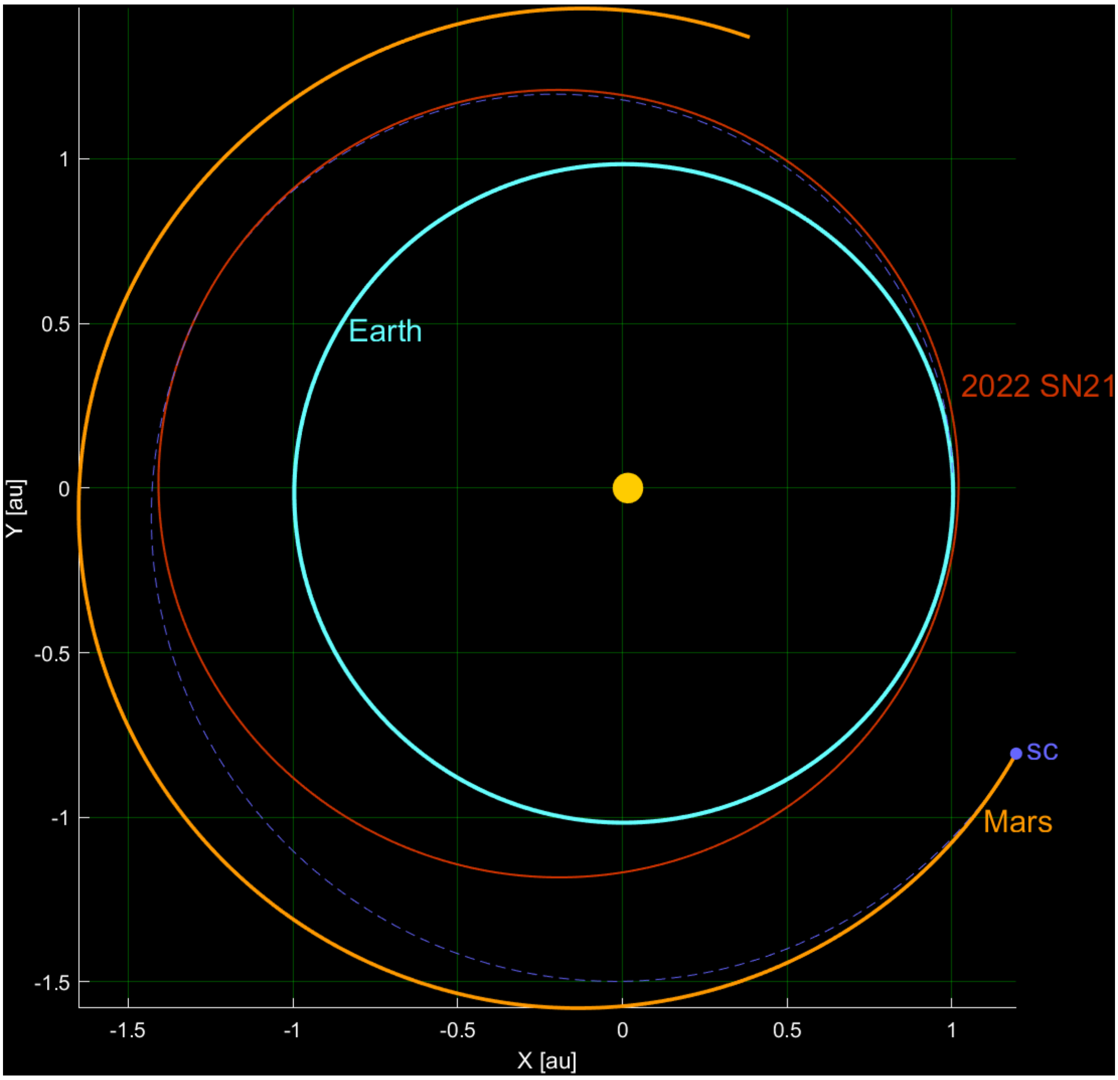

Figure 4.6: Double arc trajectory between Earth, asteroid 2022 SN21 and Mars up view

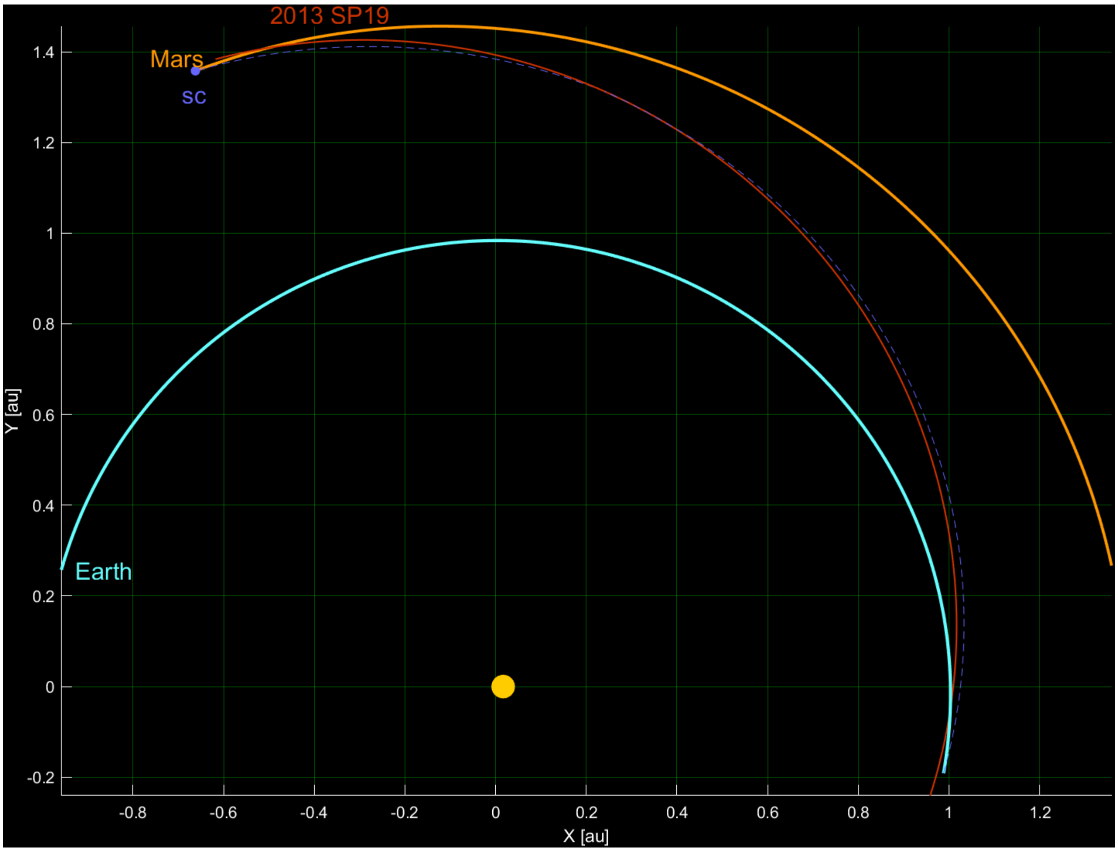

Figure 4.7: Double arc trajectory between Earth, asteroid 2013 SP19 and Mars

Figure 4.8: Link to double arc trajectory animation (case: asteroid 2022 SN21) `https://youtu.be/2reTw5fh3fw`

Figure 4.9: Link to double arc trajectory animation (case: asteroid 2013 SP19) `https://youtu.be/EujpPoFwCj4`

Table 4.2: Minimum ΔV $[km/s]$ and TOF [days] according to cost function J_1

Object	$\Delta V_{tot_{\oplus \to A}}$	$\Delta V_{tot_{A \to ♂}}$	$\frac{\Delta V_{tot_{A \to ♂}}}{\Delta V_{tot_{\oplus \to A}}}$	$\Delta V_{tot_{\oplus \to ♂}}$	TOF
2000 EA14	7.1792	7.2514	1.0101	14.4306	610
1993 KA	8.7925	8.6007	0.9782	17.3932	581
1999 CG9	6.2195	5.2220	0.8396	11.4415	477
2005 ER95	5.8374	5.3865	0.9228	11.2239	614
2005 LC	4.1310	3.9877	0.9653	8.1187	621
2006 CL9	6.9006	3.6433	0.5280	10.5439	630
2006 DQ14	6.7429	6.0021	0.8901	12.7450	477
2006 UQ216	6.1226	6.2058	1.0136	12.3284	509
2007 HL4	9.1215	7.2089	0.7903	16.3304	630
2008 CM74	6.6615	6.1845	0.9284	12.8461	563
2008 HU4	7.7178	8.2441	1.0682	15.9618	493
2009 BD	5.3838	5.3700	0.9974	10.7537	610
2009 FH	19.3465	21.0920	1.0902	40.4385	560
2009 OS5	4.1960	4.4742	1.0663	8.6702	400
2009 SW171	4.4733	4.1712	0.9325	8.6446	326
2010 DJ	8.2434	6.9209	0.8396	15.1643	531
2010 RF12	4.5960	4.9778	1.0831	9.5738	560
2011 AA37	6.5176	5.4685	0.8390	11.9860	396
2011 CY7	8.8709	8.0692	0.9096	16.9401	581
2012 BB14	5.2818	4.6725	0.8846	9.9543	377
2012 VB37	9.4828	9.7795	1.0313	19.2623	554
2012 XM55	6.5975	5.7957	0.8785	12.3932	610
2013 HP11	6.8970	7.5177	1.0900	14.4147	580
2013 SP19	4.4168	4.1874	0.9481	8.6042	522
2013 UX2	5.6104	5.4370	0.9691	11.0474	494
2014 JR24	6.5279	6.2608	0.9591	12.7887	494
2014 LJ	7.0773	7.4215	1.0486	14.4988	461
2014 WX202	6.4383	5.9849	0.9296	12.4232	530
2014 WA366	4.4867	4.6855	1.0443	9.1722	488
2015 EZ6	5.9032	6.4817	1.0980	12.3848	630
2015 HC1	6.8417	5.8701	0.8580	12.7118	630
2015 VC2	7.1580	5.7037	0.7968	12.8617	584
2015 XX128	7.6913	7.0279	0.9137	14.7192	525
2015 XD169	7.3484	4.6099	0.6273	11.9584	595
2015 XA352	10.0564	10.1552	1.0098	20.2116	526
2016 CF137	5.4005	4.7027	0.8708	10.1032	531
2016 EP84	4.6218	4.7910	1.0366	9.4128	630

continued on next page...

...continued from previous page

Object	$\Delta V_{tot_{\oplus \to A}}$	$\Delta V_{tot_{A \to \male}}$	$\frac{\Delta V_{tot_{A \to \male}}}{\Delta V_{tot_{\oplus \to A}}}$	$\Delta V_{tot_{\oplus \to \male}}$	TOF
2016 GL222	5.1578	5.1835	1.0050	10.3413	519
2017 BF29	6.7992	6.9312	1.0194	13.7305	495
2017 BG30	7.3813	5.2598	0.7126	12.6411	599
2017 CP1	10.7812	8.9085	0.8263	19.6896	603
2017 FJ3	5.7507	6.0302	1.0486	11.7809	560
2017 FW90	5.1874	5.2820	1.0182	10.4694	566
2017 LD	7.2928	7.6853	1.0538	14.9782	451
2017 RL16	5.7491	5.3656	0.9333	11.1147	630
2017 UM52	5.0144	5.1971	1.0364	10.2115	624
2017 WM13	7.4433	4.1106	0.5523	11.5539	590
2017 YC1	6.1692	5.7148	0.9263	11.8840	457
2017 YW3	5.9897	5.6480	0.9430	11.6377	548
2018 LQ2	5.2521	5.4897	1.0452	10.7418	492
2018 RR1	4.9588	4.8760	0.9833	9.8348	306
2019 KJ2	4.8080	5.1739	1.0761	9.9818	463
2019 LV	5.1132	4.6134	0.9023	9.7265	513
2019 PY	6.5645	6.7852	1.0336	13.3497	360
2019 PO1	5.4025	5.2993	0.9809	10.7017	630
2019 SU3	4.8097	4.2320	0.8799	9.0417	333
2019 UO1	5.5053	4.8423	0.8796	10.3476	627
2019 UB4	5.4233	4.5524	0.8394	9.9757	318
2019 XV	5.6671	5.5434	0.9782	11.2105	493
2020 BK	7.3098	7.1133	0.9731	14.4231	525
2020 BV2	11.6595	9.7429	0.8356	21.4024	630
2020 CF2	7.0719	7.3440	1.0385	14.4159	572
2020 DE2	5.3926	5.6864	1.0545	11.0790	610
2020 HN	6.2123	5.0681	0.8158	11.2804	520
2020 HQ4	7.3867	7.4138	1.0037	14.8006	510
2020 HL6	6.8797	6.9599	1.0117	13.8396	410
2020 OE2	5.2497	5.7200	1.0896	10.9697	393
2020 OK5	5.3845	5.5696	1.0344	10.9541	595
2020 PP1	5.2384	5.7346	1.0947	10.9731	626
2020 RT3	6.3195	6.7862	1.0738	13.1057	630
2020 SM2	11.8383	12.9408	1.0931	24.7791	554
2020 SH6	4.1919	4.5241	1.0793	8.7160	342
2020 VV	6.0688	6.3477	1.0460	12.4165	460
2020 WY	5.0434	5.1754	1.0262	10.2187	339
2020 WQ3	6.3347	6.7478	1.0652	13.0826	630

continued on next page...

...continued from previous page

Object	$\Delta V_{tot_{\oplus \to A}}$	$\Delta V_{tot_{A \to ♂}}$	$\frac{\Delta V_{tot_{A \to ♂}}}{\Delta V_{tot_{\oplus \to A}}}$	$\Delta V_{tot_{\oplus \to ♂}}$	TOF
2020 XJ4	5.7469	4.6529	0.8096	10.3998	524
2021 CE	7.0312	4.7125	0.6702	11.7436	558
2021 EN5	4.5182	4.3506	0.9629	8.8688	596
2021 GB8	6.7476	4.7015	0.6968	11.4490	630
2021 HF1	11.1259	10.0569	0.9039	21.1828	430
2021 JY5	5.7325	6.0855	1.0616	11.8180	303
2021 NV8	7.9323	8.4852	1.0697	16.4175	384
2021 RP2	4.0472	4.4004	1.0873	8.4476	431
2021 VZ8	6.7584	6.8244	1.0098	13.5829	365
2022 BT	10.1197	10.3357	1.0213	20.4555	454
2022 BX5	5.3645	5.7564	1.0731	11.1209	430
2022 KL6	6.6573	6.2360	0.9367	12.8933	581
2022 NX1	5.4890	5.9298	1.0803	11.4187	563
2022 RF1	5.3093	5.1348	0.9671	10.4441	356
2022 RS1	7.2044	7.2631	1.0081	14.4676	478
2022 SZ2	5.8386	6.0021	1.0280	11.8407	378
2022 SN21	3.9079	3.8458	0.9841	7.7537	512
2022 UA5	5.2942	4.6771	0.8834	9.9713	620
2022 WS8	5.4414	4.8754	0.8960	10.3169	490

Table 4.3: Transfer dates according to cost function J_1

Object	DD from $\oplus$	AD on A	DD from A	AD on ♂
2000 EA14	08-Nov-2043	03-Sep-2044	13-Sep-2044	10-Jul-2045
1993 KA	09-Jul-2043	16-Mar-2044	15-Apr-2044	09-Feb-2045
1999 CG9	05-Feb-2035	24-Aug-2035	03-Sep-2035	27-May-2036
2005 ER95	11-Jun-2043	06-Apr-2044	20-Apr-2044	14-Feb-2045
2005 LC	22-May-2041	18-Mar-2042	08-Apr-2042	02-Feb-2043
2006 CL9	22-May-2041	18-Mar-2042	17-Apr-2042	11-Feb-2043
2006 DQ14	07-Mar-2035	04-Aug-2035	31-Aug-2035	26-Jun-2036
2006 UQ216	01-Jan-2044	27-Oct-2044	06-Nov-2044	24-May-2045
2007 HL4	09-May-2043	04-Mar-2044	03-Apr-2044	28-Jan-2045
2008 CM74	15-May-2037	03-Jan-2038	02-Feb-2038	29-Nov-2038
2008 HU4	08-Mar-2043	13-Nov-2043	23-Nov-2043	13-Jul-2044
2009 BD	03-Mar-2037	28-Dec-2037	07-Jan-2038	03-Nov-2038
2009 FH	04-Sep-2038	12-May-2039	22-May-2039	17-Mar-2040
2009 OS5	02-Jul-2035	21-Nov-2035	01-Dec-2035	05-Aug-2036

continued on next page...

...continued from previous page

Object	DD from ⊕	AD on A	DD from A	AD on ♂
2009 SW171	14-Sep-2035	10-Feb-2036	20-Feb-2036	05-Aug-2036
2010 DJ	24-Mar-2043	28-Nov-2043	08-Dec-2043	05-Sep-2044
2010 RF12	07-Mar-2037	12-Nov-2037	22-Nov-2037	18-Sep-2038
2011 AA37	01-Jan-2035	20-Jul-2035	13-Aug-2035	01-Feb-2036
2011 CY7	06-May-2039	12-Jan-2040	11-Feb-2040	07-Dec-2040
2012 BB14	17-Jan-2035	05-Aug-2035	15-Aug-2035	29-Jan-2036
2012 VB37	03-Mar-2041	02-Nov-2041	12-Nov-2041	08-Sep-2042
2012 XM55	26-Dec-2042	22-Oct-2043	01-Nov-2043	27-Aug-2044
2013 HP11	02-Mar-2035	07-Nov-2035	07-Dec-2035	02-Oct-2036
2013 SP19	10-Sep-2035	20-Mar-2036	19-Apr-2036	13-Feb-2037
2013 UX2	06-Nov-2043	01-Sep-2044	11-Sep-2044	14-Mar-2045
2014 JR24	06-Aug-2037	22-Feb-2038	04-Mar-2038	13-Dec-2038
2014 LJ	04-Jul-2037	20-Jan-2038	30-Jan-2038	08-Oct-2038
2014 WX202	03-Mar-2035	19-Sep-2035	19-Oct-2035	14-Aug-2036
2014 WA366	01-Jan-2035	09-Sep-2035	19-Sep-2035	03-May-2036
2015 EZ6	23-Mar-2043	17-Jan-2044	16-Feb-2044	12-Dec-2044
2015 HC1	28-Jun-2041	24-Apr-2042	24-May-2042	20-Mar-2043
2015 VC2	11-Dec-2044	11-Sep-2045	21-Sep-2045	18-Jul-2046
2015 XX128	11-May-2043	04-Dec-2043	22-Dec-2043	17-Oct-2044
2015 XD169	04-Mar-2037	10-Dec-2037	24-Dec-2037	20-Oct-2038
2015 XA352	04-Jul-2038	11-Mar-2039	21-Mar-2039	12-Dec-2039
2016 CF137	03-Mar-2035	20-Sep-2035	20-Oct-2035	15-Aug-2036
2016 EP84	22-Mar-2041	16-Jan-2042	15-Feb-2042	12-Dec-2042
2016 GL222	03-May-2035	08-Nov-2035	08-Dec-2035	03-Oct-2036
2017 BF29	05-Jul-2039	05-Jan-2040	16-Jan-2040	11-Nov-2040
2017 BG30	07-Jan-2045	03-Oct-2045	02-Nov-2045	29-Aug-2046
2017 CP1	09-Jul-2043	07-Apr-2044	07-May-2044	03-Mar-2045
2017 FJ3	06-May-2041	11-Jan-2042	21-Jan-2042	17-Nov-2042
2017 FW90	27-Mar-2039	02-Dec-2039	18-Dec-2039	13-Oct-2040
2017 LD	01-Jan-2035	26-Jun-2035	06-Jul-2035	27-Mar-2036
2017 RL16	23-Apr-2043	17-Feb-2044	18-Mar-2044	12-Jan-2045
2017 UM52	02-Jan-2037	29-Oct-2037	22-Nov-2037	18-Sep-2038
2017 WM13	18-Nov-2040	22-Aug-2041	06-Sep-2041	01-Jul-2042
2017 YC1	01-Sep-2035	26-Jan-2036	05-Feb-2036	01-Dec-2036
2017 YW3	09-Nov-2043	04-Sep-2044	14-Sep-2044	10-May-2045
2018 LQ2	17-Mar-2037	04-Oct-2037	03-Nov-2037	22-Jul-2038
2018 RR1	02-Jul-2035	10-Oct-2035	03-Nov-2035	03-May-2036
2019 KJ2	01-Jan-2035	06-Sep-2035	16-Sep-2035	08-Apr-2036

continued on next page...

...continued from previous page

Object	DD from ⊕	AD on A	DD from A	AD on ♂
2019 LV	13-Jun-2043	03-Jan-2044	13-Jan-2044	07-Nov-2044
2019 PY	03-Mar-2035	19-Jul-2035	18-Aug-2035	26-Feb-2036
2019 PO1	05-Mar-2039	30-Dec-2039	29-Jan-2040	24-Nov-2040
2019 SU3	02-May-2035	27-Aug-2035	06-Sep-2035	30-Mar-2036
2019 UO1	09-Jul-2043	04-May-2044	31-May-2044	27-Mar-2045
2019 UB4	02-Mar-2035	10-Jun-2035	02-Jul-2035	14-Jan-2036
2019 XV	03-Mar-2035	13-Aug-2035	12-Sep-2035	08-Jul-2036
2020 BK	02-Jul-2039	02-Feb-2040	12-Feb-2040	08-Dec-2040
2020 BV2	07-Jan-2045	03-Nov-2045	03-Dec-2045	29-Sep-2046
2020 CF2	02-Mar-2043	10-Dec-2043	20-Dec-2043	24-Sep-2044
2020 DE2	15-Apr-2043	09-Feb-2044	19-Feb-2044	15-Dec-2044
2020 HN	04-May-2037	20-Nov-2037	10-Dec-2037	06-Oct-2038
2020 HQ4	29-Jul-2039	14-Feb-2040	24-Feb-2040	20-Dec-2040
2020 HL6	01-Jan-2035	07-Jun-2035	17-Jun-2035	15-Feb-2036
2020 OE2	24-Jan-2035	12-Aug-2035	22-Aug-2035	21-Feb-2036
2020 OK5	13-Jan-2043	15-Oct-2043	04-Nov-2043	30-Aug-2044
2020 PP1	09-Mar-2043	30-Dec-2043	29-Jan-2044	24-Nov-2044
2020 RT3	05-Sep-2041	02-Jul-2042	01-Aug-2042	28-May-2043
2020 SM2	25-Sep-2038	27-May-2039	06-Jun-2039	01-Apr-2040
2020 SH6	02-Jul-2035	15-Oct-2035	25-Oct-2035	08-Jun-2036
2020 VV	20-Sep-2037	17-Feb-2038	27-Feb-2038	24-Dec-2038
2020 WY	03-Mar-2035	15-Jul-2035	31-Jul-2035	05-Feb-2036
2020 WQ3	13-Jan-2039	09-Nov-2039	09-Dec-2039	04-Oct-2040
2020 XJ4	13-Apr-2039	13-Nov-2039	23-Nov-2039	18-Sep-2040
2021 CE	09-Apr-2041	03-Feb-2042	05-Mar-2042	19-Oct-2042
2021 EN5	03-Mar-2035	24-Nov-2035	24-Dec-2035	19-Oct-2036
2021 GB8	11-Nov-2042	07-Sep-2043	07-Oct-2043	02-Aug-2044
2021 HF1	23-Jul-2044	31-Oct-2044	30-Nov-2044	26-Sep-2045
2021 JY5	02-Mar-2035	07-Jul-2035	17-Jul-2035	30-Dec-2035
2021 NV8	01-Jan-2035	12-May-2035	22-May-2035	20-Jan-2036
2021 RP2	22-Sep-2043	09-Apr-2044	19-Apr-2044	26-Nov-2044
2021 VZ8	16-Nov-2041	24-Feb-2042	26-Mar-2042	16-Nov-2042
2022 BT	03-Jan-2039	10-Sep-2039	20-Sep-2039	01-Apr-2040
2022 BX5	29-May-2037	06-Sep-2037	06-Oct-2037	02-Aug-2038
2022 KL6	06-Jul-2039	13-Mar-2040	12-Apr-2040	06-Feb-2041
2022 NX1	04-Mar-2037	09-Nov-2037	22-Nov-2037	18-Sep-2038
2022 RF1	07-Sep-2035	16-Dec-2035	26-Dec-2035	28-Aug-2036
2022 RS1	02-Mar-2035	30-Jul-2035	27-Aug-2035	22-Jun-2036

continued on next page...

...continued from previous page

Object	DD from ⊕	AD on A	DD from A	AD on ♂
2022 SZ2	22-Sep-2043	19-Feb-2044	29-Feb-2044	04-Oct-2044
2022 SN21	26-Sep-2039	13-Apr-2040	25-Apr-2040	19-Feb-2041
2022 UA5	06-Jul-2041	02-May-2042	22-May-2042	18-Mar-2043
2022 WS8	01-Jan-2035	23-Sep-2035	03-Oct-2035	05-May-2036

Table 4.4: Minimum ΔV $[km/s]$ and TOF [days] according to cost function J_2

Object	$\Delta V_{tot_{\oplus \to A}}$	$\Delta V_{tot_{A \to ♂}}$	$\frac{\Delta V_{tot_{A \to ♂}}}{\Delta V_{tot_{\oplus \to A}}}$	$\Delta V_{tot_{\oplus \to ♂}}$	TOF
2000 EA14	7.1792	7.2514	1.0101	14.4306	610
1993 KA	9.6250	10.5276	1.0938	20.1526	396
1999 CG9	7.9294	6.1425	0.7747	14.0720	385
2005 ER95	6.9274	5.9813	0.8634	12.9087	480
2005 LC	5.7552	5.3828	0.9353	11.1380	540
2006 CL9	8.7572	5.1200	0.5847	13.8772	530
2006 DQ14	6.7429	6.0021	0.8901	12.7450	477
2006 UQ216	8.1518	8.8162	1.0815	16.9681	339
2007 HL4	9.1918	9.0776	0.9876	18.2694	479
2008 CM74	6.6615	6.1845	0.9284	12.8461	563
2008 HU4	7.7178	8.2441	1.0682	15.9618	493
2009 BD	6.8680	6.6815	0.9729	13.5495	419
2009 FH	19.3465	21.0920	1.0902	40.4385	560
2009 OS5	4.4800	4.6218	1.0316	9.1018	386
2009 SW171	4.5424	3.7633	0.8285	8.3057	289
2010 DJ	8.3379	6.2893	0.7543	14.6272	520
2010 RF12	5.7991	5.9989	1.0345	11.7980	480
2011 AA37	7.8285	7.0617	0.9021	14.8902	316
2011 CY7	8.8709	8.0692	0.9096	16.9401	581
2012 BB14	5.2818	4.6725	0.8846	9.9543	377
2012 VB37	10.4177	8.8125	0.8459	19.2302	510
2012 XM55	8.0595	8.0232	0.9955	16.0827	476
2013 HP11	9.9795	10.1917	1.0213	20.1712	325
2013 SP19	4.8673	3.4714	0.7132	8.3386	175
2013 UX2	5.6136	5.5184	0.9830	11.1320	493
2014 JR24	6.5279	6.2608	0.9591	12.7887	494
2014 LJ	7.0773	7.4215	1.0486	14.4988	461
2014 WX202	7.9827	6.4940	0.8135	14.4767	436
2014 WA366	6.5629	4.8550	0.7398	11.4179	401

continued on next page...

...continued from previous page

Object	$\Delta V_{tot_{\oplus \to A}}$	$\Delta V_{tot_{A \to ♂}}$	$\frac{\Delta V_{tot_{A \to ♂}}}{\Delta V_{tot_{\oplus \to A}}}$	$\Delta V_{tot_{\oplus \to ♂}}$	TOF
2015 EZ6	9.8934	9.9570	1.0064	19.8504	422
2015 HC1	7.9636	8.5970	1.0795	16.5606	510
2015 VC2	9.3318	6.3793	0.6836	15.7110	339
2015 XX128	7.6913	7.0279	0.9137	14.7192	525
2015 XD169	8.2444	5.6867	0.6898	13.9312	535
2015 XA352	13.7398	12.4198	0.9039	26.1596	369
2016 CF137	5.4005	4.7027	0.8708	10.1032	531
2016 EP84	5.9139	6.1560	1.0409	12.0699	547
2016 GL222	5.1578	5.1835	1.0050	10.3413	519
2017 BF29	8.3740	7.2544	0.8663	15.6285	405
2017 BG30	12.5428	7.3787	0.5883	19.9216	345
2017 CP1	10.9605	10.5579	0.9633	21.5184	574
2017 FJ3	5.9713	6.2517	1.0470	12.2230	460
2017 FW90	6.3206	6.3657	1.0071	12.6863	410
2017 LD	8.3711	6.4422	0.7696	14.8133	365
2017 RL16	8.7937	5.5630	0.6326	14.3568	306
2017 UM52	5.7730	5.6745	0.9829	11.4475	500
2017 WM13	8.7637	7.1691	0.8180	15.9328	457
2017 YC1	8.4034	8.2871	0.9862	16.6905	281
2017 YW3	6.9712	7.1040	1.0190	14.0752	430
2018 LQ2	6.3414	5.1472	0.8117	11.4886	348
2018 RR1	4.9588	4.8760	0.9833	9.8348	306
2019 KJ2	4.9554	4.6738	0.9432	9.6292	309
2019 LV	5.2364	5.6234	1.0739	10.8598	487
2019 PY	6.9847	6.5997	0.9449	13.5844	299
2019 PO1	10.8223	5.9753	0.5521	16.7976	393
2019 SU3	4.9401	3.8837	0.7861	8.8238	311
2019 UO1	7.0114	6.4745	0.9234	13.4859	345
2019 UB4	5.4233	4.5524	0.8394	9.9757	318
2019 XV	5.6849	5.9911	1.0539	11.6760	480
2020 BK	7.5331	6.7688	0.8985	14.3018	510
2020 BV2	11.6595	9.7429	0.8356	21.4024	630
2020 CF2	7.6096	8.0677	1.0602	15.6773	510
2020 DE2	6.0488	5.4075	0.8940	11.4563	560
2020 HN	6.9690	6.7300	0.9657	13.6990	480
2020 HQ4	7.3867	7.4138	1.0037	14.8006	510
2020 HL6	6.9472	6.5502	0.9428	13.4974	401
2020 OE2	6.1016	5.6127	0.9199	11.7143	293

continued on next page...

...continued from previous page

Object	$\Delta V_{tot_{\oplus \to A}}$	$\Delta V_{tot_{A \to ♂}}$	$\frac{\Delta V_{tot_{A \to ♂}}}{\Delta V_{tot_{\oplus \to A}}}$	$\Delta V_{tot_{\oplus \to ♂}}$	TOF
2020 OK5	5.5139	6.0050	1.0891	11.5189	337
2020 PP1	5.9938	6.4484	1.0758	12.4422	493
2020 RT3	8.2922	8.7540	1.0557	17.0462	530
2020 SM2	11.8383	12.9408	1.0931	24.7791	554
2020 SH6	4.1949	4.3826	1.0447	8.5775	328
2020 VV	7.4838	5.2993	0.7081	12.7831	348
2020 WY	5.0434	5.1754	1.0262	10.2187	339
2020 WQ3	7.5909	7.6041	1.0017	15.1951	530
2020 XJ4	6.2585	4.5080	0.7203	10.7665	489
2021 CE	10.4749	5.8739	0.5608	16.3488	252
2021 EN5	4.5182	4.3506	0.9629	8.8688	596
2021 GB8	8.3042	5.6839	0.6845	13.9881	410
2021 HF1	11.1259	10.0569	0.9039	21.1828	430
2021 JY5	5.7325	6.0855	1.0616	11.8180	303
2021 NV8	7.9323	8.4852	1.0697	16.4175	384
2021 RP2	4.1603	4.5150	1.0853	8.6753	406
2021 VZ8	6.7584	6.8244	1.0098	13.5829	365
2022 BT	10.1263	10.1478	1.0021	20.2741	294
2022 BX5	5.3645	5.7564	1.0731	11.1209	430
2022 KL6	6.6573	6.2360	0.9367	12.8933	581
2022 NX1	5.4890	5.9298	1.0803	11.4187	563
2022 RF1	5.3291	4.9446	0.9279	10.2737	355
2022 RS1	10.9451	7.2985	0.6668	18.2436	259
2022 SZ2	5.8386	6.0021	1.0280	11.8407	378
2022 SN21	6.4634	5.8872	0.9109	12.3506	382
2022 UA5	6.0829	3.7651	0.6190	9.8479	387
2022 WS8	6.1739	4.3038	0.6971	10.4777	356

Table 4.5: Transfer dates according to cost function J_2

Object	DD from $\oplus$	AD on A	DD from A	AD on ♂
2000 EA14	08-Nov-2043	03-Sep-2044	13-Sep-2044	10-Jul-2045
1993 KA	07-Sep-2039	08-Mar-2040	18-Mar-2040	07-Oct-2040
1999 CG9	02-May-2035	12-Sep-2035	22-Sep-2035	21-May-2036
2005 ER95	30-Sep-2043	27-Feb-2044	28-Mar-2044	22-Jan-2045
2005 LC	02-Mar-2035	07-Nov-2035	07-Dec-2035	23-Aug-2036
2006 CL9	13-Jul-2041	29-Jan-2042	28-Feb-2042	25-Dec-2042

continued on next page...

...continued from previous page

Object	DD from ⊕	AD on A	DD from A	AD on ♂
2006 DQ14	07-Mar-2035	04-Aug-2035	31-Aug-2035	26-Jun-2036
2006 UQ216	02-Jul-2035	10-Oct-2035	20-Oct-2035	05-Jun-2036
2007 HL4	06-Mar-2041	11-Nov-2041	21-Nov-2041	28-Jun-2042
2008 CM74	15-May-2037	03-Jan-2038	02-Feb-2038	29-Nov-2038
2008 HU4	08-Mar-2043	13-Nov-2043	23-Nov-2043	13-Jul-2044
2009 BD	01-Jan-2035	20-Jul-2035	30-Jul-2035	24-Feb-2036
2009 FH	04-Sep-2038	12-May-2039	22-May-2039	17-Mar-2040
2009 OS5	03-Jul-2035	11-Oct-2035	10-Nov-2035	23-Jul-2036
2009 SW171	05-Sep-2035	14-Dec-2035	24-Dec-2035	20-Jun-2036
2010 DJ	08-Mar-2043	13-Nov-2043	23-Nov-2043	09-Aug-2044
2010 RF12	24-Mar-2037	21-Aug-2037	20-Sep-2037	17-Jul-2038
2011 AA37	02-May-2035	19-Sep-2035	29-Sep-2035	13-Mar-2036
2011 CY7	06-May-2039	12-Jan-2040	11-Feb-2040	07-Dec-2040
2012 BB14	17-Jan-2035	05-Aug-2035	15-Aug-2035	29-Jan-2036
2012 VB37	08-Mar-2043	24-Sep-2043	04-Oct-2043	30-Jul-2044
2012 XM55	04-Jul-2037	20-Jan-2038	30-Jan-2038	23-Oct-2038
2013 HP11	07-Nov-2043	15-Feb-2044	16-Mar-2044	27-Sep-2044
2013 SP19	12-Sep-2035	21-Dec-2035	31-Dec-2035	05-Mar-2036
2013 UX2	08-Nov-2043	03-Sep-2044	13-Sep-2044	15-Mar-2045
2014 JR24	06-Aug-2037	22-Feb-2038	04-Mar-2038	13-Dec-2038
2014 LJ	04-Jul-2037	20-Jan-2038	30-Jan-2038	08-Oct-2038
2014 WX202	03-May-2035	19-Nov-2035	29-Nov-2035	12-Jul-2036
2014 WA366	03-Mar-2035	06-Aug-2035	05-Sep-2035	07-Apr-2036
2015 EZ6	05-Jul-2039	12-Jan-2040	05-Feb-2040	30-Aug-2040
2015 HC1	01-Jul-2044	17-Jan-2045	27-Jan-2045	23-Nov-2045
2015 VC2	03-Jul-2035	11-Oct-2035	30-Oct-2035	06-Jun-2036
2015 XX128	11-May-2043	04-Dec-2043	22-Dec-2043	17-Oct-2044
2015 XD169	03-May-2037	08-Jan-2038	18-Jan-2038	20-Oct-2038
2015 XA352	30-Sep-2039	08-Jan-2040	07-Feb-2040	03-Oct-2040
2016 CF137	03-Mar-2035	20-Sep-2035	20-Oct-2035	15-Aug-2036
2016 EP84	07-May-2041	10-Dec-2041	09-Jan-2042	05-Nov-2042
2016 GL222	03-May-2035	08-Nov-2035	08-Dec-2035	03-Oct-2036
2017 BF29	04-Sep-2039	13-Dec-2039	12-Jan-2040	13-Oct-2040
2017 BG30	02-Sep-2035	11-Dec-2035	21-Dec-2035	12-Aug-2036
2017 CP1	09-Jul-2043	15-Mar-2044	14-Apr-2044	02-Feb-2045
2017 FJ3	23-Aug-2041	20-Jan-2042	30-Jan-2042	26-Nov-2042
2017 FW90	25-Jun-2037	03-Oct-2037	13-Oct-2037	09-Aug-2038
2017 LD	02-Mar-2035	10-Jun-2035	20-Jun-2035	01-Mar-2036

continued on next page...

...continued from previous page

Object	DD from ⊕	AD on A	DD from A	AD on ♂
2017 RL16	01-Jan-2035	21-Apr-2035	21-May-2035	03-Nov-2035
2017 UM52	06-Apr-2037	12-Dec-2037	22-Dec-2037	19-Aug-2038
2017 WM13	18-Apr-2041	04-Nov-2041	14-Nov-2041	19-Jul-2042
2017 YC1	02-Jun-2035	10-Sep-2035	20-Sep-2035	09-Mar-2036
2017 YW3	17-Mar-2035	25-Jun-2035	25-Jul-2035	20-May-2036
2018 LQ2	03-Sep-2037	12-Dec-2037	22-Dec-2037	17-Aug-2038
2018 RR1	02-Jul-2035	10-Oct-2035	03-Nov-2035	03-May-2036
2019 KJ2	02-May-2035	10-Aug-2035	22-Aug-2035	06-Mar-2036
2019 LV	30-May-2043	05-Feb-2044	06-Mar-2044	28-Sep-2044
2019 PY	11-May-2035	19-Aug-2035	06-Sep-2035	05-Mar-2036
2019 PO1	01-Jan-2035	31-May-2035	10-Jun-2035	29-Jan-2036
2019 SU3	02-May-2035	10-Aug-2035	20-Aug-2035	08-Mar-2036
2019 UO1	02-May-2035	29-Sep-2035	09-Oct-2035	11-Apr-2036
2019 UB4	02-Mar-2035	10-Jun-2035	02-Jul-2035	14-Jan-2036
2019 XV	03-Mar-2035	31-Jul-2035	30-Aug-2035	25-Jun-2036
2020 BK	04-Jul-2039	20-Jan-2040	30-Jan-2040	25-Nov-2040
2020 BV2	07-Jan-2045	03-Nov-2045	03-Dec-2045	29-Sep-2046
2020 CF2	23-Jun-2043	09-Jan-2044	19-Jan-2044	14-Nov-2044
2020 DE2	13-May-2043	18-Jan-2044	28-Jan-2044	23-Nov-2044
2020 HN	04-May-2037	01-Oct-2037	31-Oct-2037	27-Aug-2038
2020 HQ4	29-Jul-2039	14-Feb-2040	24-Feb-2040	20-Dec-2040
2020 HL6	01-Jan-2035	31-May-2035	10-Jun-2035	06-Feb-2036
2020 OE2	02-May-2035	10-Aug-2035	20-Aug-2035	19-Feb-2036
2020 OK5	03-May-2035	13-Sep-2035	27-Sep-2035	04-Apr-2036
2020 PP1	14-Aug-2043	01-Mar-2044	11-Mar-2044	19-Dec-2044
2020 RT3	29-Oct-2041	17-May-2042	16-Jun-2042	12-Apr-2043
2020 SM2	25-Sep-2038	27-May-2039	06-Jun-2039	01-Apr-2040
2020 SH6	02-Jul-2035	10-Oct-2035	20-Oct-2035	25-May-2036
2020 VV	31-Dec-2043	09-Apr-2044	19-Apr-2044	13-Dec-2044
2020 WY	03-Mar-2035	15-Jul-2035	31-Jul-2035	05-Feb-2036
2020 WQ3	31-Mar-2039	17-Oct-2039	16-Nov-2039	11-Sep-2040
2020 XJ4	06-May-2039	30-Oct-2039	11-Nov-2039	06-Sep-2040
2021 CE	09-Jan-2042	08-Jun-2042	18-Jun-2042	18-Sep-2042
2021 EN5	03-Mar-2035	24-Nov-2035	24-Dec-2035	19-Oct-2036
2021 GB8	26-Jun-2035	04-Oct-2035	14-Oct-2035	09-Aug-2036
2021 HF1	23-Jul-2044	31-Oct-2044	30-Nov-2044	26-Sep-2045
2021 JY5	02-Mar-2035	07-Jul-2035	17-Jul-2035	30-Dec-2035
2021 NV8	01-Jan-2035	12-May-2035	22-May-2035	20-Jan-2036

continued on next page...

...continued from previous page

Object	DD from ⊕	AD on A	DD from A	AD on ♂
2021 RP2	27-Sep-2043	24-Feb-2044	25-Mar-2044	06-Nov-2044
2021 VZ8	16-Nov-2041	24-Feb-2042	26-Mar-2042	16-Nov-2042
2022 BT	02-Jul-2035	10-Oct-2035	20-Oct-2035	21-Apr-2036
2022 BX5	29-May-2037	06-Sep-2037	06-Oct-2037	02-Aug-2038
2022 KL6	06-Jul-2039	13-Mar-2040	12-Apr-2040	06-Feb-2041
2022 NX1	04-Mar-2037	09-Nov-2037	22-Nov-2037	18-Sep-2038
2022 RF1	01-Sep-2035	10-Dec-2035	20-Dec-2035	21-Aug-2036
2022 RS1	03-Mar-2035	11-Jun-2035	21-Jun-2035	17-Nov-2035
2022 SZ2	22-Sep-2043	19-Feb-2044	29-Feb-2044	04-Oct-2044
2022 SN21	02-Jul-2035	10-Oct-2035	20-Oct-2035	18-Jul-2036
2022 UA5	21-Feb-2035	21-Jul-2035	20-Aug-2035	14-Mar-2036
2022 WS8	29-Mar-2035	26-Aug-2035	05-Sep-2035	19-Mar-2036

Chapter 5

Sun-Asteroid Distant Retrograde Orbit Family

In this chapter, Sun-Asteroid Distant Retrograde Orbits family will be found. After the estimation of the asteroid mass and discussing about DROs importance, the guess for the initial conditions of the orbit will be obtained using Particle Swarm Optimization. Then, with the differential correction method, the exact initial conditions will be found. The procedure will be repeated for all DROs of the family of varying size. Finally the ΔV for orbit insertion will be calculated.

5.1 Sun-Asteroid Mass Ratio Estimation

Future missions using an asteroid for in situ refueling will need an initial reconnaissance mission. It will be useful to understand better the surface morphology and consequently the best landing site along with estimating the asteroid mass and other of its physical characteristics. Of course, the reconnaissance mission will have to search for resources and prove that there are enough supplies, for a given number (N) of resupplies.

In our case, we don't have the asteroid mass and consequently the gravitational parameter μ_A. For this reason we have selected[1] some minor planets (asteroids and comets) whose μ is known. To carry out a statistical investigation we need to know how μ varies as a function of another parameter. The parameter chosen is the diameter of the asteroid, intended as the mean diameter between the diameters along the x, y and z axes centered in the barycenter of the asteroid. Asteroids

[1] `https://ssd.jpl.nasa.gov/tools/sbdb_query.html`

considered are shown in Tab. 5.1. We interpolate the data with a cubic function

Table 5.1: Asteroid statistical investigation diameter vs μ

Object	Diameter $[km]$	μ $[km^3/s^2]$
16 Psyche (A852 FA)	226	1.53
22 Kalliope (A852 WA)	167.536	0.491
107 Camilla (A868 WA)	210.370	0.7475
243 Ida (A884 SB)	32	0.00275
253 Mathilde (A885 VA)	52.8	0.00689
433 Eros (A898 PA)	16.84	4.463e-04
704 Interamnia (A910 TC)	306.313	5.
25143 Itokawa (1998 SF36)	0.33	2.1e-9
101955 Bennu (1999 RQ36)	0.482	4.8904e-9
162173 Ryugu (1999 JU3)	0.896	3.00e-8
185851 (2000 DP107)	0.863	3.224e-8
67P/Churyumov-Gerasimenko	3.4	662.2e-9

like $f(x) = A \cdot x^3 + B \cdot x^2 + C \cdot x + D$, obtaining the blue line shown in Fig. 5.1. The reason why we have selected the function aforementioned is that we need to find a function like $\mu = f(d)$. Therefore, we have

$$\mu = G \cdot m = G \cdot \rho V = G \cdot \rho \frac{4}{3} \pi r^3 = G \cdot \rho \frac{1}{6} \pi d^3 \tag{5.1}$$

where m, ρ, V, r, d are respectively the mass, density, volume, mean radius and mean diameter of the asteroid, while G is the gravitational constant. Finally we have that the interpolating function is as the following

$$\mu = f(d) = a \cdot d^3 \tag{5.2}$$

We need to estimate the diameter of the asteroid to use in the interpolating function aforementioned. The estimation can be derived using the absolute magnitude H, representing the visual magnitude an observer would perceive if the asteroid were positioned 1 Astronomical Unit away from both the Sun and the observer, with a zero phase angle[2]. Additionally, the estimation can be based on the albedo a, which signifies the ratio of light received by a celestial body to the light it reflects. Albedo values span from 0 (complete darkness) to 1 (ideal reflector)[3]. As suggested by Harris [22], the diameter can be calculated as follow

$$d(H, a) = 10^{3.1236 - 0.5 \log(a) - 0.2H} \tag{5.3}$$

[2]`https://cneos.jpl.nasa.gov/glossary/h.html`

[3]`https://cneos.jpl.nasa.gov/glossary/albedo.html`

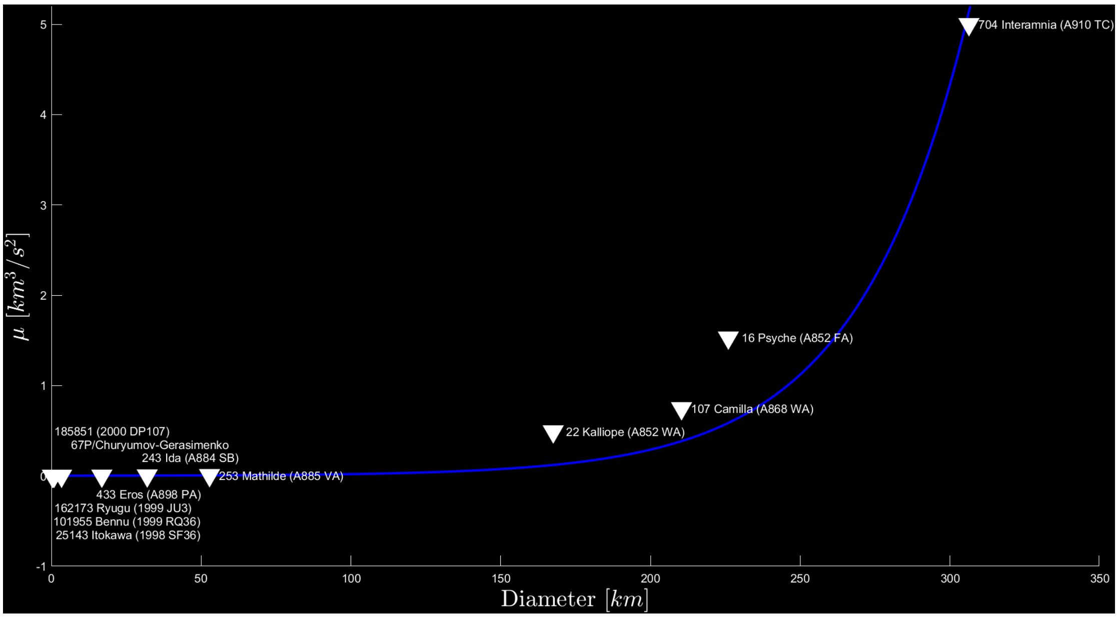

Figure 5.1: Diameter vs μ of some known asteroids

Considering that among all selected asteroids the only available physical parameter is the absolute magnitude H, for the diameter estimation we consider an albedo range between 0.01 and 0.9 and we calculate the mean diameter as follow:

$$d_{mean}(H) = \frac{d(H,0.01) + d(H,0.9)}{2} \tag{5.4}$$

If we consider the best asteroid shown in Tab. 4.4, the object 2013 SP19, we discover that using the Eq. (5.4) and the Eq. (5.3), the mean diameter is equal to 11 m. This means that there will be not enough resources for multiple resupplies. While if we consider the best asteroid shown in Tab. 4.2, the object 2022 SN21, the mean diameter is equal to 34 m, but at the same time we note that TOF in that case is almost two times bigger than a direct Earth-Mars transfer. Therefore we need a new cost function J_3 such as $J_3\left(\Delta V_{tot_{\oplus\to A}}, TOF, d_{mean}\right)$. For simplicity, we take into account a maximum excavation depth of approximately 20 meters. We can suppose to treat asteroids of *Type I* that, according the chemical-petrologic classification proposed by [23, 24], have a bulk water content equal to 20.08%. Conservatively, we assume that the mass percentage is equal to the volume percentage. Therefore we have that the extractable volume is equal to

$$V_{extractable} = \frac{4}{3}\pi r_{asteroid}^3 - \frac{4}{3}\pi\left(r_{asteroid} - h_{extractable}\right)^3 \tag{5.5}$$

where

$$\begin{aligned} r_{asteroid} &= \tfrac{d_{mean}}{2} \\ h_{extractable} &= 20 \quad m \end{aligned} \tag{5.6}$$

Considering that only the 20.08% can be used as propellant, we obtain

$$V_{ep} = 0.2008 V_{extractable} \tag{5.7}$$

where the subscript "ep" means *extractable propellant*. Note that we assume a perfectly spherical asteroid.
After the mission phase in which H_2O is split into LOX and LH_2 (not discussed in this study) the tanks are assumed to be filled to their maximum capacity. Therefore, it is necessary to estimate the volume capacity of the tanks. We assume to use a *SpaceX* spacecraft: *Starship*. The second stage of the *Starship system* has a propellant capacity equal to $1.2 \cdot 10^6$ kg[4]. To compute an approximation of the volume capacity of the tanks, we need to compute the propellant density ρ_p. To do it, we use the Eq. (5.8), function of the mixture ratio, MR, equal to 3.6[5], the liquid oxygen density, ρ_{LOX}, equal to 1141 kg/m^3 and the methane density, ρ_{CH_4}, equal to 430 kg/m^3.

$$\rho_p = \rho_{LOX} \rho_{CH_4} \frac{MR + 1}{\rho_{CH_4} MR + \rho_{LOX}} \tag{5.8}$$

With the aforementioned values, we obtain a capacity of the propellant tank, V_{tank}, equal to 1430 m^3. This way, by supposing that the *SpaceX Raptor*, the rocket engines used by *Starship*, could be converted from LOX/CH_4 propellant engines to LOX/LH_2 propellant engines and that the volume capacity of the propellant tank remains the same, we can compute the number of supplies, $N_{supplies}$, that an asteroid can guarantee as follows

$$N_{supplies} = V_{ep}/V_{tank} \tag{5.9}$$

Finally we can write the new function cost J_3 to select a new asteroid among those presented in Tab. 4.1 to maximize the number of supplies, minimize the ΔV_{tot} from Earth to the asteroid and minimize the TOF.

$$J_3 = \frac{\Delta V_{tot_{\oplus \to A}}}{\Delta V_{min, \oplus \to ♂}} + \frac{TOF_{\oplus \to A \to ♂}}{TOF_{\Delta V_{min, \oplus \to ♂}}} + \frac{N_{target}}{N_{supplies}} \tag{5.10}$$

[4] `https://www.spacex.com/vehicles/starship/`

[5] `https://www.faa.gov/space/stakeholder_engagement/spacex_starship/media/Appendix_G_Exhaust_Plume_Calculations.pdf`

where

$$\begin{aligned} &\Delta V_{min,\oplus\rightarrow\male} = 6.1696 \text{ km/s} \\ &TOF_{\Delta V_{min,\oplus\rightarrow\male}} = 252 \text{ days} \\ &N_{target} = 50 \text{ supplies} \end{aligned} \tag{5.11}$$

N_{target} is set as the number of supplies that an asteroid has to guarantee. Using the data from Tab. 4.2 and Tab. 4.4, and showing only the asteroids with $\Delta V_{tot_{\oplus\rightarrow A}} < 5$ km/s, we obtain Tab. 5.2. The speed given in the table is referred in km/s, the

Table 5.2: Candidate asteroids and critical parameters for the J_3 cost function

Object	$\Delta V_{tot_{\oplus\rightarrow A}}$	TOF	R_{mean_A}	$N_{supplies}$	J_3
2005 LC	4.1310	621	16.0	2	28.1
2009 OS5	4.1960	400	58.2	83	2.87
2009 SW171	4.4733	326	21.5	6	10.4
2010 RF12	4.5960	560	7.7	1	53.0
2013 SP19	4.4168	522	5.3	2	27.8
2014 WA366	4.4867	488	17.7	3	19.3
2016 EP84	4.6218	630	12.2	1	53.2
2018 RR1	4.9588	306	3.7	3	18.7
2019 KJ2	4.8080	463	13.6	2	27.6
2019 SU3	4.8097	333	12.8	1	52.1
2020 SH6	4.1919	342	38.1	29	3.76
2021 EN5	4.5182	596	17.9	3	19.8
2021 RP2	4.0472	431	3.3	3	19.0
2022 SN21	3.9079	512	17.1	3	19.3
2009 OS5	4.4800	386	58.2	83	2.86
2009 SW171	4.5424	289	21.5	6	10.2
2013 SP19	4.8673	175	5.3	2	26.5
2018 RR1	4.9588	306	3.7	3	18.7
2019 KJ2	4.9554	309	13.6	2	27.0
2019 SU3	4.9401	311	12.8	1	52.0
2020 SH6	4.1949	328	38.1	29	3.71
2021 EN5	4.5182	596	17.9	3	19.8
2021 RP2	4.1603	406	3.3	3	19.0

time of flight in *days* and the mean radius of the asteroid in m. Note that some asteroids are repeated in the table because different combinations of $\Delta V_{tot_{\oplus\rightarrow A}}$ and TOF are considered. Using the cost function J_3, asteroid 2009 OS5 has been selected. It is the best compromise from the minimum ΔV from the Earth to asteroid the minimum total TOF from Earth to Mars (passing by the asteroid) and

the maximum number of supplies possible (under the aforementioned assumptions). So a spacecraft that leaves the Earth on July 3, 2035 will arrive on asteroid 2009 OS5 on October 11, 2035 using ΔV of 4.4800 km/s, it will stay on it for 30 days, until November 10, 2035 to complete the ISRU refueling and it will reach Mars on July 23, 2036 with a "free" ΔV of 4.6218 km/s. In this way, 27.4% of ΔV is saved with respect to the best case of a direct Earth-Mars transfer. This result is obtained spending more than 134 days of mission time respect of the best case of a direct Earth-Mars transfer. The number of possible propellant resupplies on asteroid 2009 OS5 are fixed to 83.
Finally, we can estimate μ_A, interpolating data from Tab. 5.1 and using as reference diameter $2 \cdot 58.2\ m$. The interpolating function used is the following

$$\mu = f(d) = 1.598 \cdot 10^{-7} \cdot d^3 \tag{5.12}$$

Zooming into Fig. 5.1 , we obtain Fig. 5.2 where is shown a reference μ_A equal to $2.520204112512 \cdot 10^{-10}\ km^3/s^2$. As a result we can compute the mass ratio of

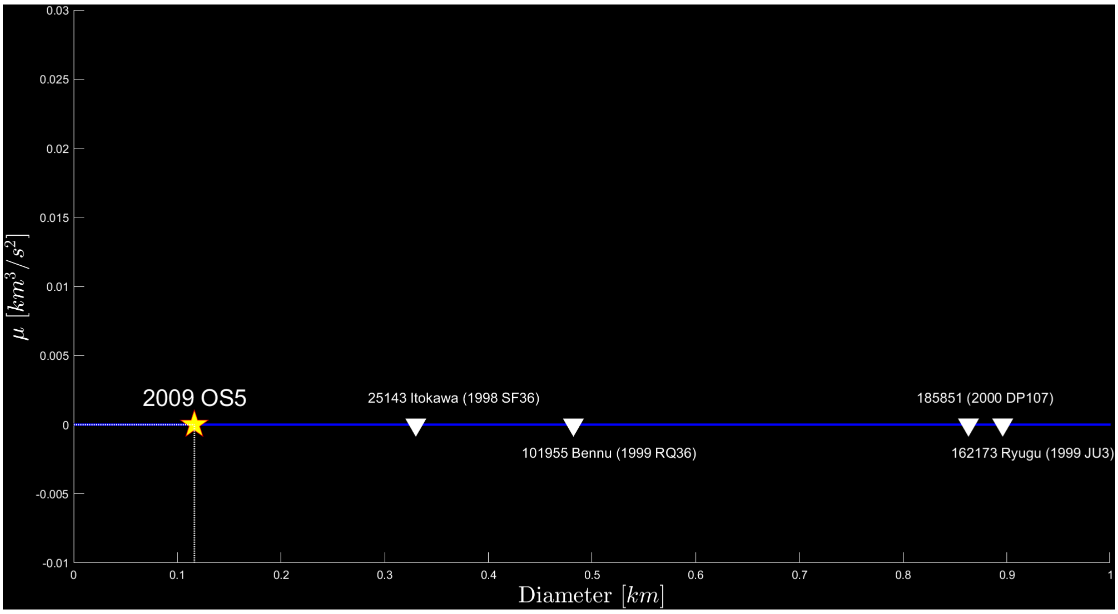

Figure 5.2: Zoom in of Fig. 5.1

the system Sun-asteroid 2009 0S5, $\mu_{A/\odot}$, as in Eq. 5.13, where $\odot$ means "Sun". Considering $\mu_\odot$ equal to 132,712,440,018 km^3/s^2 we obtain

$$\mu_{A/\odot} = \frac{\mu_A}{\mu_\odot + \mu_A} = 1.898996139450213 \cdot 10^{-21} \tag{5.13}$$

Since the gravitational parameter of the asteroid is very small, its gravitational influence is negligible compared to that of the Sun. However, in its vicinity, the gravity of the asteroid can generate significant perturbative effects.

5.2 Distant Retrograde Orbits

As shown in Sec. 1.5 Distant Retrograde Orbits (DROs) are large orbits encircling a smaller primary celestial body in the CR3BP. The word "distant" in the term "Distant Retrograde Orbit" indicates that the orbit is positioned at a certain distance from the celestial body, while the word "retrograde" means that the spacecraft moves in the opposite direction to the rotational motion of the celestial body. In the CR3BP, DROs can exhibit perfect periodicity, meaning their motion repeats exactly after a certain period. However, due to various factors such as the gravitational influence of other celestial bodies or non-spherical shape of the primary body, maintaining a perfectly periodic DRO can be challenging. Thus, in practice, slight perturbations in the in-plane velocity are often present, leading to quasi-periodic orbits. These quasi-periodic orbits closely resemble periodic motion, but exhibit small variations over time. Nevertheless, quasi-periodic DROs are still highly advantageous, especially for applications such as quarantine orbits, as their stability showcases their ability to withstand perturbations and maintain their intended purpose [25].
DROs are particularly favored for locating in-space infrastructures due to their outstanding stability and the ease of accessing them in terms of the gravitational potential energy. Their stability is characterized by their resistance to perturbations, making them reliable for long-duration missions and operations.

To find a periodic DRO, several parameters are used. One of these parameters is the ξ-amplitude, A_ξ, which represents the maximum distance from the smaller primary body in the positive ξ-axis direction, using a coordinate frame centered at the barycenter of the Sun-asteroid system as shown in Fig. 5.3. In this reference frame, the periapsis radius and its corresponding velocity V_η at the intersection of the $\xi\zeta$-plane (where $\eta = 0$) are crucial in creating a periodic orbit. The periapse radius determines the closest distance between the spacecraft and the smaller primary body, while the corresponding velocity ensures that the spacecraft follows a periodic orbit.

5.3 Obtaining DRO ICs with PSO

In this specific section, a Particle Swarm Optimization algorithm will be employed to determine a Sun-Asteroid DRO based on A_ξ and V_η. These serve as the starting point for optimizing the landing trajectory, which will be discussed in Chapter 6. Since DROs lie on the $\xi\eta$-plane, we can use the CR3BP equations of motion

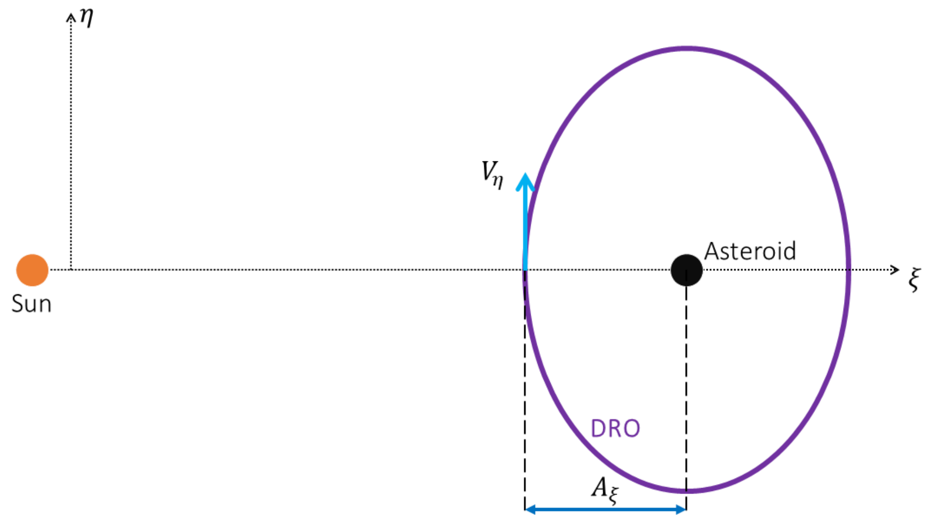

Figure 5.3: Geometric schematization of a Sun-asteroid DRO

neglecting the ζ-component. Therefore, the EOMs become

$$\begin{cases} \xi'' - 2\eta' - \xi = -\left(1 - \mu_{A/\odot}\right) \frac{\xi + \mu_{A/\odot}}{\rho_1^3} - \mu_{A/\odot} \frac{\xi - \left(1 - \mu_{A/\odot}\right)}{\rho_2^3} \\ \eta'' + 2\xi' - \eta = -\left(1 - \mu_{A/\odot}\right) \frac{\eta}{\rho_1^3} - \mu_{A/\odot} \frac{\eta}{\rho_2^3} \end{cases} \tag{5.14}$$

where

$$\begin{aligned} \rho_1 &= \sqrt{\left(\xi + \mu_{A/\odot}\right)^2 + \eta^2} \\ \rho_2 &= \sqrt{\left(\xi - \left(1 - \mu_{A/\odot}\right)\right)^2 + \eta^2} \end{aligned} \tag{5.15}$$

The PSO algorithm is used to research the ICs of the CR3BP EOMs ξ_0, η_0, $\dot{\xi}_0$ and $\dot{\eta}_0$, that lead to a periodic DRO. Starting by integrating the Eq.(5.14) at the point farthest from the sun on the ξ-axis, we obtain the following ICs

$$\begin{cases} \xi_0 = -A_\xi + 1 - \mu_{A/\odot} \\ \eta_0 = 0 \\ \dot{\xi}_0 = 0 \\ \dot{\eta}_0 = V_\eta \end{cases} \tag{5.16}$$

The velocity in $[\xi_0, \eta_0]$ has no ξ-component while the η-component is called V_η. In the CR3BP, when using the synodic coordinate system, an orbit is called periodic if it is indefinitely repeated. This implies that after a period of rotation denoted as

τ, the variables ξ, η, $\dot{\xi}$ and $\dot{\eta}$ return to their original values:

$$\begin{cases} \xi(\tau) = \xi(0) = \xi_0 \\ \eta(\tau) = \eta(0) = \eta_0 \\ \dot{\xi}(\tau) = \dot{\xi}(0) = \dot{\xi}_0 \\ \dot{\eta}(\tau) = \dot{\eta}(0) = \dot{\eta}_0 \end{cases} \tag{5.17}$$

Therefore PSO is performed using the following cost function J to minimize

$$J = |\xi(\tau) - \xi(0)| + |\eta(\tau) - \eta(0)| + |\dot{\xi}(\tau) - \dot{\xi}(0)| + |\dot{\eta}(\tau) - \dot{\eta}(0)| \tag{5.18}$$

which becomes

$$J = |\xi(\tau) + A_\xi - 1 + \mu_{A/\odot}| + |\eta(\tau)| + |\dot{\xi}(\tau)| + |\dot{\eta}(\tau) - V_\eta| \tag{5.19}$$

If we want to obtain a quasi-circular DRO, it's necessary that $\xi(\tau/2)$ is almost equal to $A_\xi + 1 - \mu_{A/\odot}$. Therefore, J changes as

$$\begin{aligned} J = |\xi(\tau) + A_\xi - 1 + \mu_{A/\odot}| + |\eta(\tau)| + |\dot{\xi}(\tau)| + |\dot{\eta}(\tau) - V_\eta| + \\ + |\xi(\tau/2) - A_\xi - 1 + \mu_{A/\odot}| \end{aligned} \tag{5.20}$$

In this way the number of decision variables become two: τ and V_η. By following the schematization of PSO shown in Fig. 5.4, we initialize the number of particles and the maximum number of iterations. In this study, for reasons of computational cost, we set up

$$\begin{aligned} N_{particles} &= 30 \\ N_{iterations_{max}} &= 200 \end{aligned} \tag{5.21}$$

To set the variables bounds, we need to reference values. In this case we can simplify the problem using the Keplerian Restricted 2 Body Problem (KR2BP). We suppose to have a circular orbit with asteroid 2000 OS5 as primary body. We consider a SMA equal to $A_\xi \cdot LU = 0.5\ km$. Where LU is the length unit used in the characterization of the physical properties of the system Sun-Asteroid in the CR3BP. LU represents the distance between the Sun and the asteroid 2009 OS5. From Tab. 4.1, we can use the 2009 OS5 SMA as LU. Subsequently will be useful the time unit TU of the system Sun-Asteroid in the CR3BP. It indicates the inverse of the relative angular frequency between the Sun and the asteroid 2009 OS5. Therefore, we obtain

$$\begin{aligned} LU = a_A &= 171{,}747{,}349 \quad km \\ TU = \frac{T_A}{2\pi} = \sqrt{\frac{a_A^3}{\mu_\odot}} &= 6{,}178{,}445 \quad s \end{aligned} \tag{5.22}$$

Finally we can compute the dimensionless speed, $\mathcal{V}_{sc}$, that a spacecraft would have if it orbited in a circular orbit around the asteroid 2009 OS5 and the dimensionless period, $\mathcal{T}$, of that orbit using the equations of KR2BP.

$$\begin{aligned} \mathcal{V}_{sc} &= \sqrt{\frac{\mu_A}{A_\xi \cdot LU}} \cdot \frac{TU}{LU} = 2.26 \cdot 10^{-2} \\ \mathcal{T} &= \sqrt{\frac{\left(A_\xi \cdot LU\right)^3}{\mu_A}} \cdot \frac{1}{TU} = 8.08 \cdot 10^{-7} \end{aligned} \tag{5.23}$$

We can set the variables bounds as follow After that we set up the inertial weight, c_I,

Table 5.3: Lower and Upper Bounds of the two decision variables

#	Variable	Lower Bound	Upper Bound
1	V_η	$0.9 \cdot \mathcal{V}_{sc}$	$1.1 \cdot \mathcal{V}_{sc}$
2	τ	$0.9 \cdot \mathcal{T}$	$1.1 \cdot \mathcal{T}$

the cognitive weight, c_C, and the social weight, c_S. The PSO Stochastic Parameters expressions [26] are

$$\begin{cases} c_I = \frac{1+r_1(0,1)}{2} \\ c_C = 1.49445 \cdot r_2(0,1) \\ c_S = 1.49445 \cdot r_3(0,1) \end{cases} \tag{5.24}$$

where $r_1(0,1)$, $r_2(0,1)$, and $r_3(0,1)$ denote three separate random numbers chosen independently from a uniform distribution ranging from 0 to 1. Finally, we set up the particles velocity limits as the difference between the upper bound and the lower bound of the each decision variables. By continuing to follow the flow chart shown in Fig. 5.4, we initialize the particles positions with the Matlab function *unifrnd* which returns an array of random numbers chosen from the continuous uniform distribution over the interval between the previously set bounds. After this step, we compute the best positions ever visited by particle i up to the current iteration j, $\Psi_k^{(j)}(i)$, where k indicates the k^{th} decision variable and we compute its respective minimum cost according the Eq. (5.20). Consequently the best global positions of the whole swarm until j^{th} iteration, $\Upsilon_k^{(j)}$, is calculated. If the cost of the positions $\Upsilon_k^{(j)}$ is less of a value called J_{min}, the main loop is stopped and the algorithm reports the best particles positions $\Upsilon_1^{(j)} = V_\eta$ and $\Upsilon_1^{(j)} = \tau$. In this algorithm, J_{min} is set equal to 10^{-15}. If the cost of the global best positions is more than J_{min} the main loop continues and updates the i^{th} particle velocities $v_k^{(j+1)}(i)$ at $j + 1^{th}$ iteration of the k^{th} decision variable as

$$v_k^{(j+1)}(i) = c_I \cdot v_k^{(j)}(i) + c_C \cdot \left(\Psi_k^{(j)}(i) - \varrho_k^{(j)}(i)\right) + c_S \cdot \left(\Upsilon_k^{(j)} - \varrho_k^{(j)}(i)\right) \tag{5.25}$$

where $\varrho_k^{(j)}(i)$ indicates the position of the i^{th} particle at the j^{th} iteration of the k^{th} decision variable. After this we apply the velocities limits and compute the new

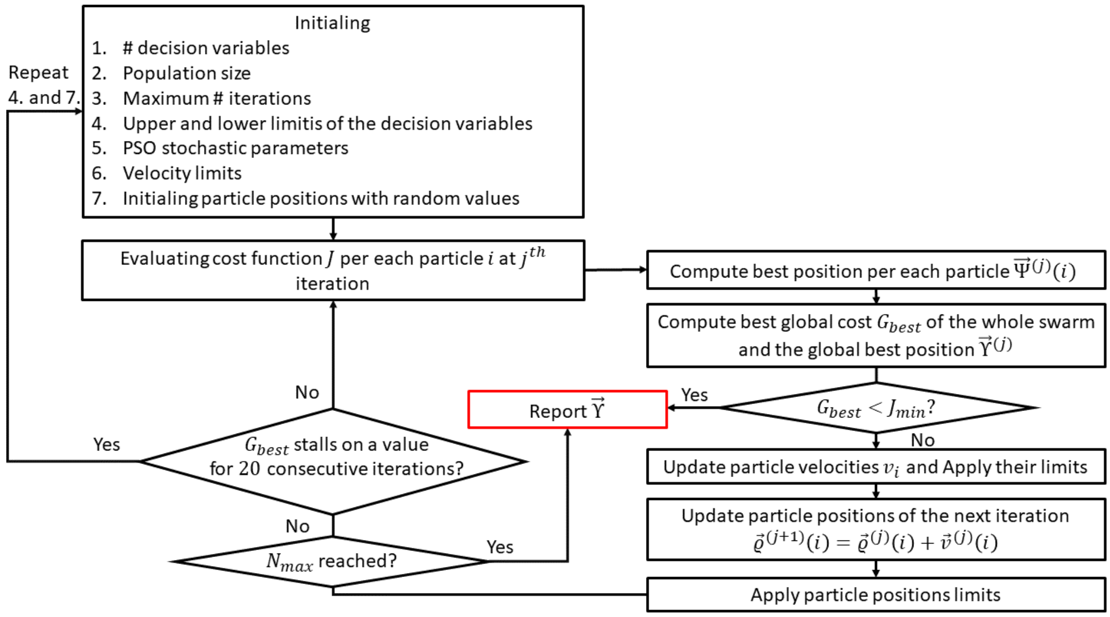

Figure 5.4: Schematization of PSO algorithm

particle positions as in Eq. (3.12).
We apply position limits in the event that the particle positions exceeds the limits imposed. At this point we re-evaluate the new position and the main loop restarts. The main loop ends when the the iteration j^{th} reaches the number maximum of the iterations or when, as aforementioned, the cost of the global best positions, G_{best}, is more than J_{min}.
If the global best doesn't change for 20 iterations consecutively, a re-initialization is performed. The position bounds are re-set as follows

$$\begin{aligned} l_k &= (1 - 10^{-s-5}) \cdot \Upsilon_k^{(j)} \\ u_k &= (1 + 10^{-s-5}) \cdot \Upsilon_k^{(j)} \end{aligned} \tag{5.26}$$

Where l_k and u_k are the lower and upper bounds of the k^{th} decision variable respectively. s indicates the s^{th} re-initialization.

Fig. 5.2 shows the Global Best Cost evolution until the number of the j^{th}-iteration reached $N_{iterations_{max}}$. We can note that as the first best particle position already has a low cost $(2 \cdot 10^{-8})$. This means that the bounds are consistent. After less than 9 iterations the Global Best Cost decreases by an order of magnitude. After the 9^{th} iteration, the Global Best Cost is reduced by 18% from the last iteration, which results to $2.23 \cdot 10^{-9}$. If we zoom into Fig. 5.2, we obtain Fig. 5.5, which shows 20 iterations in which the Global Best Cost is not updated, so the algorithm

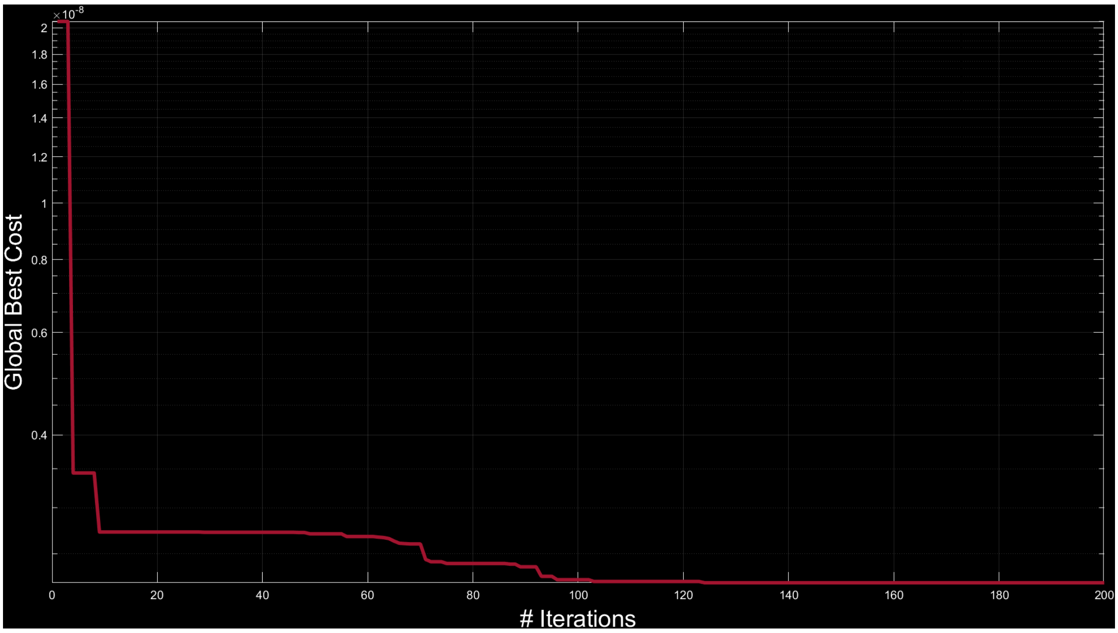

Figure 5.5: Global Best Cost evolution

re-initialize the particle positions obtaining the end of the "stall".

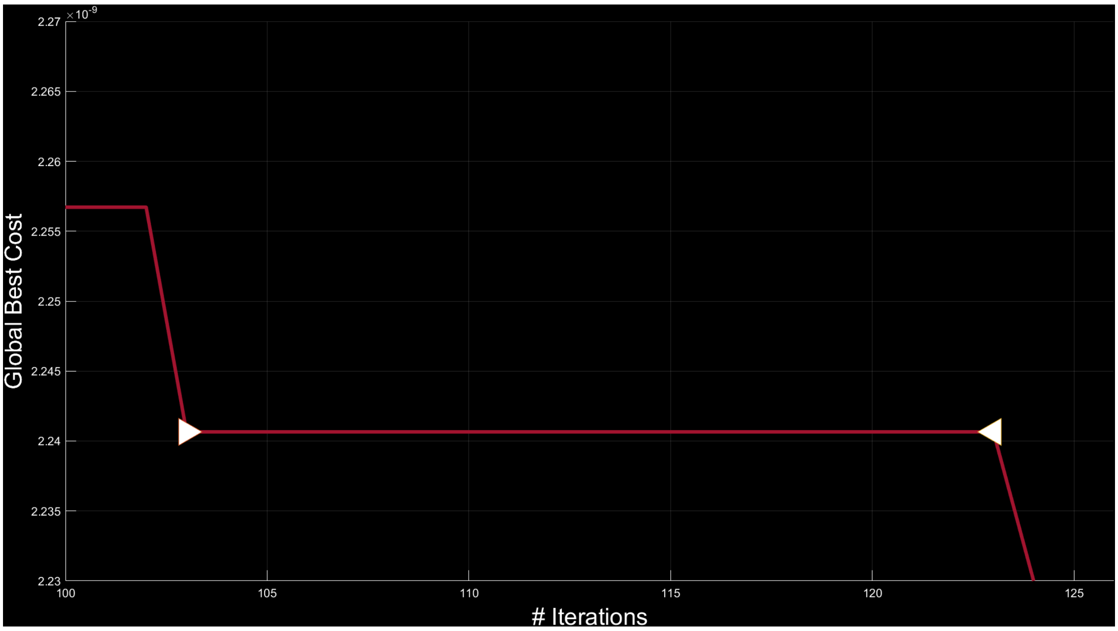

Figure 5.6: Zoom in of Fig. 5.5

The values obtained from the PSO are

$$\begin{cases} V_\eta = 8.357933214810436 \cdot 10^{-7} \\ \tau = 2.4891604948189 \cdot 10^{-2} \end{cases} \tag{5.27}$$

The values units become

$$\begin{cases} V_y = V_\eta \cdot \frac{LU}{TU} = 0.0232 \quad m/s \\ T = \tau \cdot TU = 42.7198 \quad h \end{cases} \tag{5.28}$$

5.4 Sun-2009 OS5 DRO design with Differential Corrections method

By starting from the values presented in 5.27, we apply the Differential Corrections method to design the right DRO. We will confront the results between DC method and PSO and we will evaluate if it is opportune to use only PSO to find the entire Sun-2009 OS5 DRO family. Using the Eq. (1.79), and adapting it to our case, we have

$$\begin{Bmatrix} \delta\xi_f \\ \delta\eta_f \\ \delta\zeta_f \\ \delta\dot{\xi}_f \\ \delta\dot{\eta}_f \\ \delta\dot{\zeta}_f \end{Bmatrix} = \begin{bmatrix} \Phi_{11} & \Phi_{12} & \Phi_{13} & \Phi_{14} & \Phi_{15} & \Phi_{16} \\ \Phi_{21} & \Phi_{22} & \Phi_{23} & \Phi_{24} & \Phi_{25} & \Phi_{26} \\ \Phi_{31} & \Phi_{32} & \Phi_{33} & \Phi_{34} & \Phi_{35} & \Phi_{36} \\ \Phi_{41} & \Phi_{42} & \Phi_{43} & \Phi_{44} & \Phi_{45} & \Phi_{46} \\ \Phi_{51} & \Phi_{52} & \Phi_{53} & \Phi_{54} & \Phi_{55} & \Phi_{56} \\ \Phi_{61} & \Phi_{62} & \Phi_{63} & \Phi_{64} & \Phi_{65} & \Phi_{66} \end{bmatrix} \begin{Bmatrix} \delta\xi_0 \\ \delta\eta_0 \\ \delta\zeta_0 \\ \delta\dot{\xi}_0 \\ \delta\dot{\eta}_0 \\ \delta\dot{\zeta}_0 \end{Bmatrix} + \begin{Bmatrix} \dot{\xi}_f \\ \dot{\eta}_f \\ \dot{\zeta}_f \\ \ddot{\xi}_f \\ \ddot{\eta}_f \\ \ddot{\zeta}_f \end{Bmatrix} \delta\tau \tag{5.29}$$

Indeed, in this case, compared with the halo design explained in Sec. 1.4.3, $\delta\xi_0$ can be neglected, as well as all the ζ-components because DROs lie on the $\xi\eta$-plane. Recalling Eq. (1.81), and inserting it in the Eq.(5.29), we obtain

$$\delta\dot{\xi}_f = \Phi_{45}\delta\dot{\eta}_0 - \ddot{\xi}_f \frac{\Phi_{25}\delta\dot{\eta}_0}{\delta\dot{\eta}_f} \tag{5.30}$$

Solving for $\delta\dot{\eta}_0$, we have

$$\delta\dot{\eta}_0 = \frac{\delta\dot{\xi}_f}{\Phi_{45} - \Phi_{25}\frac{\ddot{\xi}_f}{\delta\dot{\eta}_f}} \tag{5.31}$$

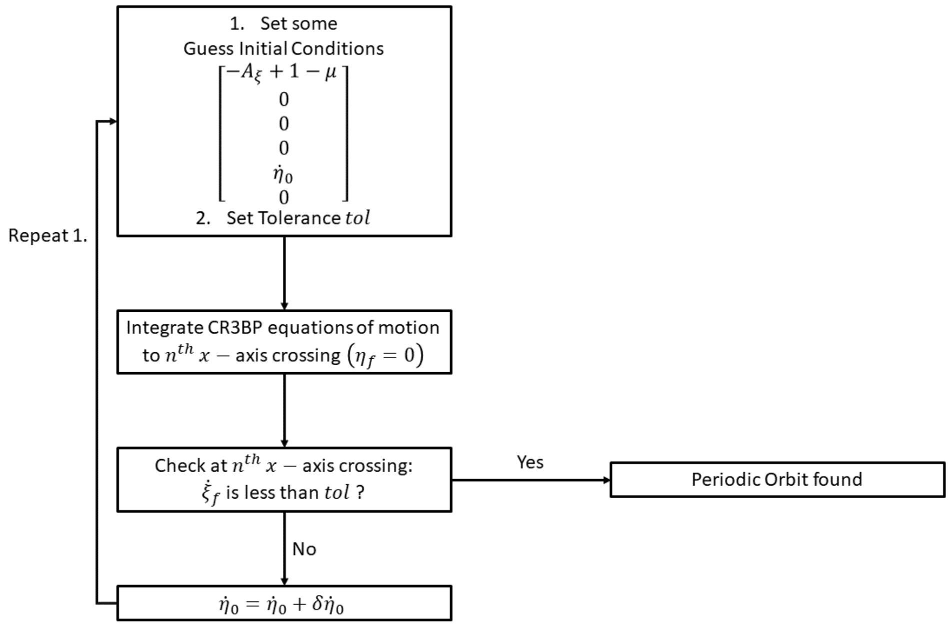

Figure 5.7: DC flow chart

The revised initial condition $\dot{\eta}_0 + \delta\dot{\eta}_0$ is used to begin the next iteration and this process is continued until $\dot{\xi}_f$ stays within some acceptable tolerance, set equal to $1 \cdot 10^{-10}$ or until a maximum number of iterations, set equal to 40, is achieved. In Fig. 5.7 a flowchart of the differential correction algorithm to find DRO orbit with fixed A_ξ, is shown. The dimensionless half period, $\tau/2$, is found, using the symmetry of DRO with respect to ξ-axis. Indeed the integration of the CR3BP equations of motion are stopped when the orbit reaches the value $\eta = 0$.

We can note from the Fig. 5.8 as $\dot{\eta}_0$, changes only its 13^{th} decimal place. At the same time, Fig. 5.9 shows us as $\tau/2$ changes only its 7^{th} decimal place. It means that we are computationally close to the solution. The relative error between the solution proposed by PSO and the solution proposed by DC method is $1.4769 \cdot 10^{-5}$ for V_η and $6.0876 \cdot 10^{-4}$ for τ. The DC method does not falls below the set tolerance in 40 iterations as we can see from the Fig. 5.10. Finally, Fig. 5.11 shows the DRO obtained from using the differential corrector method. We can note that the reference frame is shifted of a value equal to $1 - \mu$, in the center of the asteroid. The plots have been reported in dimensional form for ease of reading. In addition it is to be noted that the asteroid shown in the figure is not 2009 OS5, but Psyche 16 with the diameter of 2009 OS5.
Psyche 16 is a fascinating asteroid that has garnered significant attention in the field of astronomy. Discovered in 1852 by the Italian astronomer Annibale de Gasparis, Psyche 16 is located in the main asteroid belt between Mars and Jupiter.

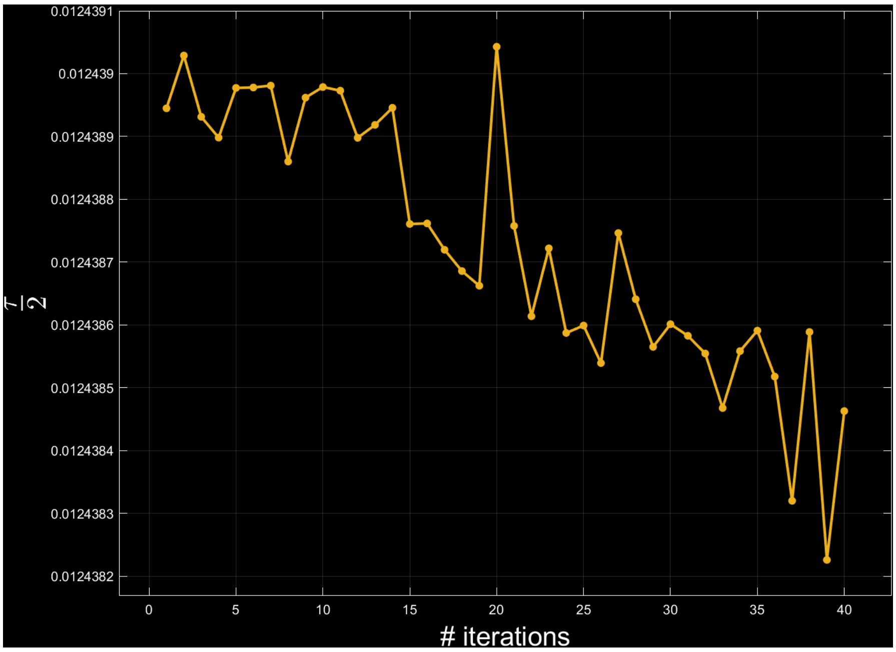

Figure 5.8: $\dot{\eta}_0$ evolution

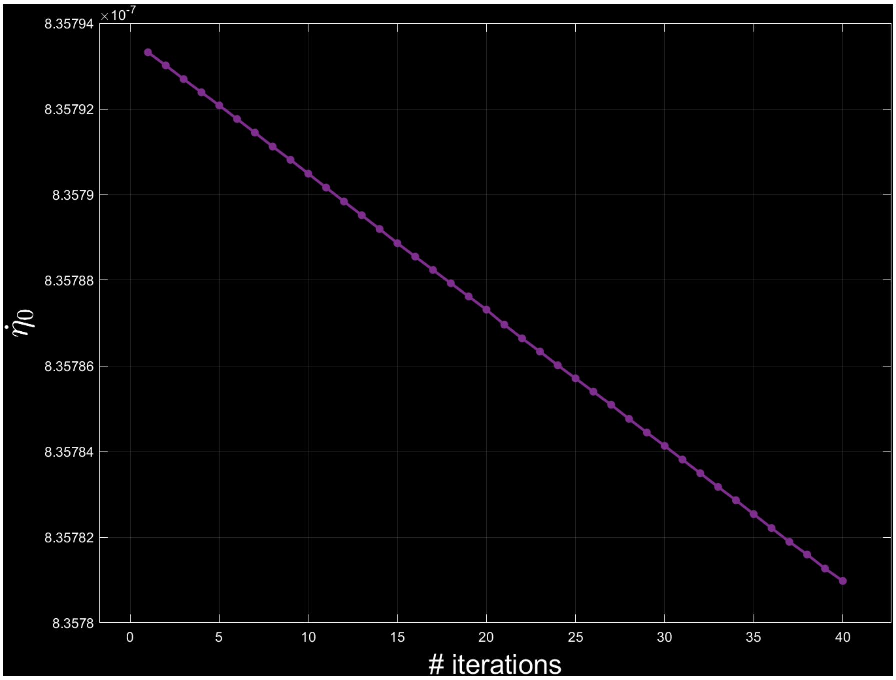

Figure 5.9: $\tau/2$ evolution

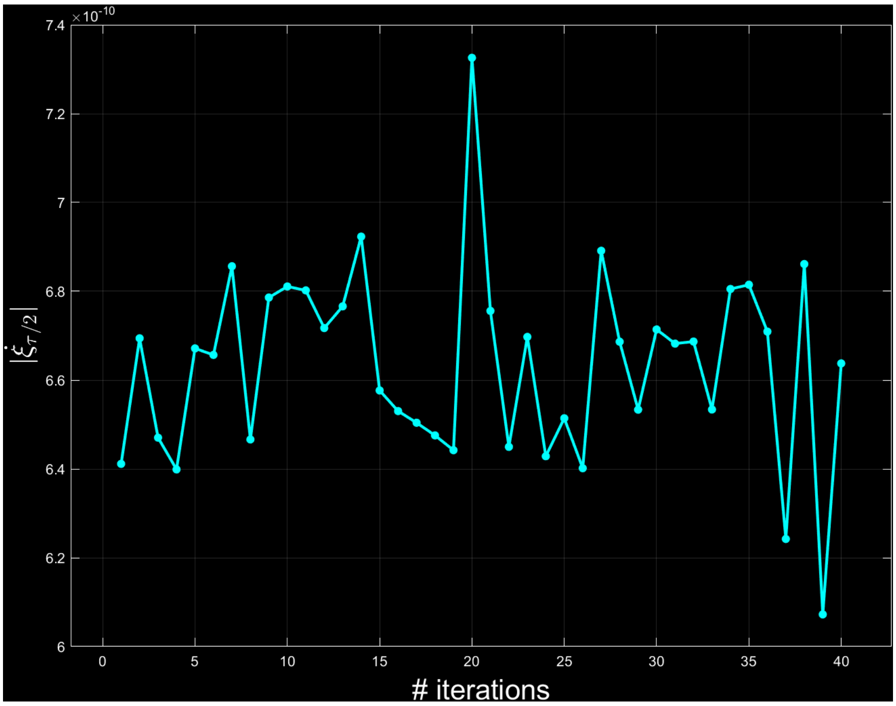

Figure 5.10: $|\dot{\xi}_f|$ evolution

What makes Psyche 16 particularly intriguing is its composition, as it is believed to be primarily made of metal, primarily nickel and iron. In fact, it is estimated that Psyche 16 could contain more metal than all the known asteroids in the asteroid belt combined. NASA is planning a mission called *Psyche*, set to launch on October 10, 2023, which aims to explore this intriguing asteroid up close[6].

5.5 Sun-2009 OS5 DROs Family

Since the results obtained from the two different methods explained above are quite similar to each other, the Sun-2009 OS5 DROs family will be obtained using only the PSO.
The Sun-2009 OS5 DROs family is obtained with different $A_\xi \cdot LU$. They vary from 500 m to 2500 m every 250 m. In Tab. 5.4 are summarized all the main parameters linked with DROs family such as A_ξ, V_η and τ and with the PSO algorithm such as the Best Global Cost of Eq.(5.20). While in Fig. 5.12 are shown all the DROs obtained from PSO.

[6]`https://www.nasa.gov/mission_pages/psyche/overview/index.html`

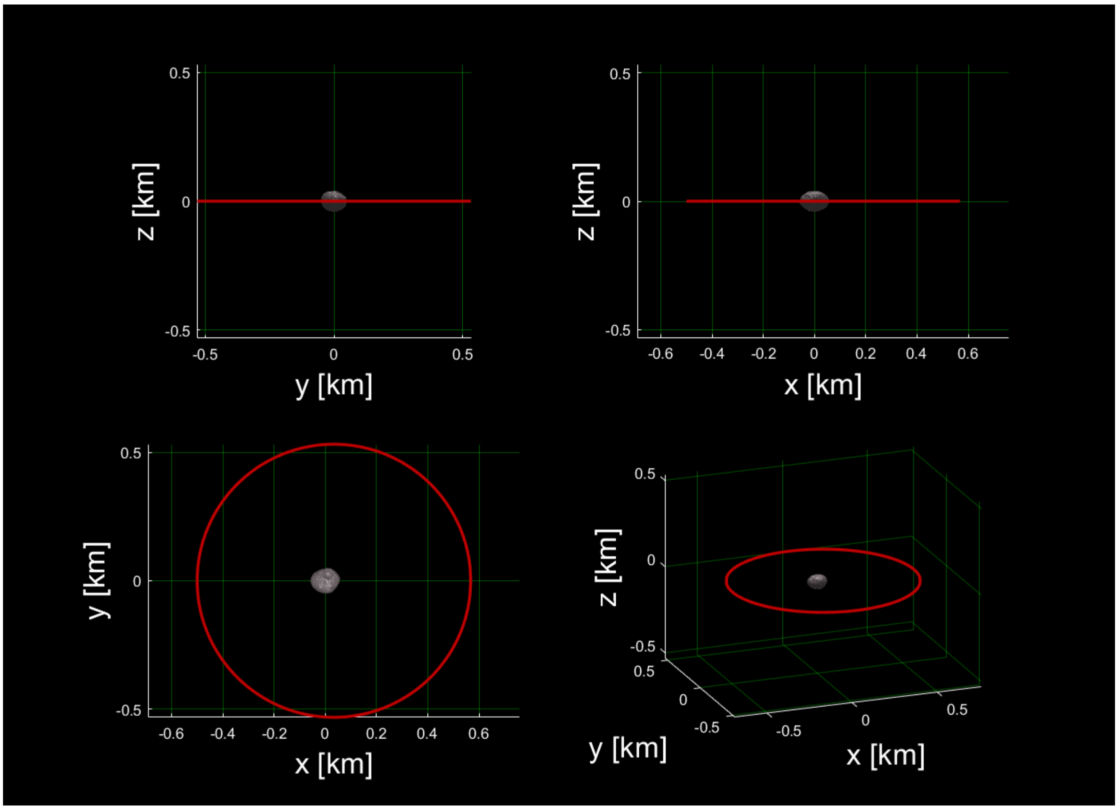

Figure 5.11: Sun-2009 OS5 DRO from different views

Table 5.4: DROs Family main parameters and PSO Best Global Cost

A_ξ	V_η	τ	G_{best}
2.91e-09	8.13891358563799e-07	0.022854256836790	2.38e-09
4.37e-09	6.61020059810958e-07	0.040855665395517	3.87e-09
5.82e-09	5.79476336590143e-07	0.064311562605193	5.35e-09
7.28e-09	5.15967840571650e-07	0.087341829308445	7.07e-09
8.73e-09	4.75350601136578e-07	0.115831098076684	7.19e-09
1.02e-08	4.43528953094944e-07	0.146573698802440	9.17e-09
1.16e-08	4.15041954569664e-07	0.175706672013026	9.32e-09
1.31e-08	3.93213223717243e-07	0.208111182644281	1.02e-08
1.46e-08	3.77522018290711e-07	0.247002715276282	1.08e-08

It is necessary to update the ΔV from the Earth to the asteroid 2009 OS5, $\Delta V_{\oplus \rightarrow A}$, because the velocity that the spacecraft should equalize is no more equal to $\vec{V}_{2009-OS5}$. Considering that the asteroid's velocity, $\vec{V}_{2009-OS5}$, is computed respect to the J2000 Ecliptic reference frame, $V_\eta \cdot \frac{LU}{TU}$ has been rotated according to that

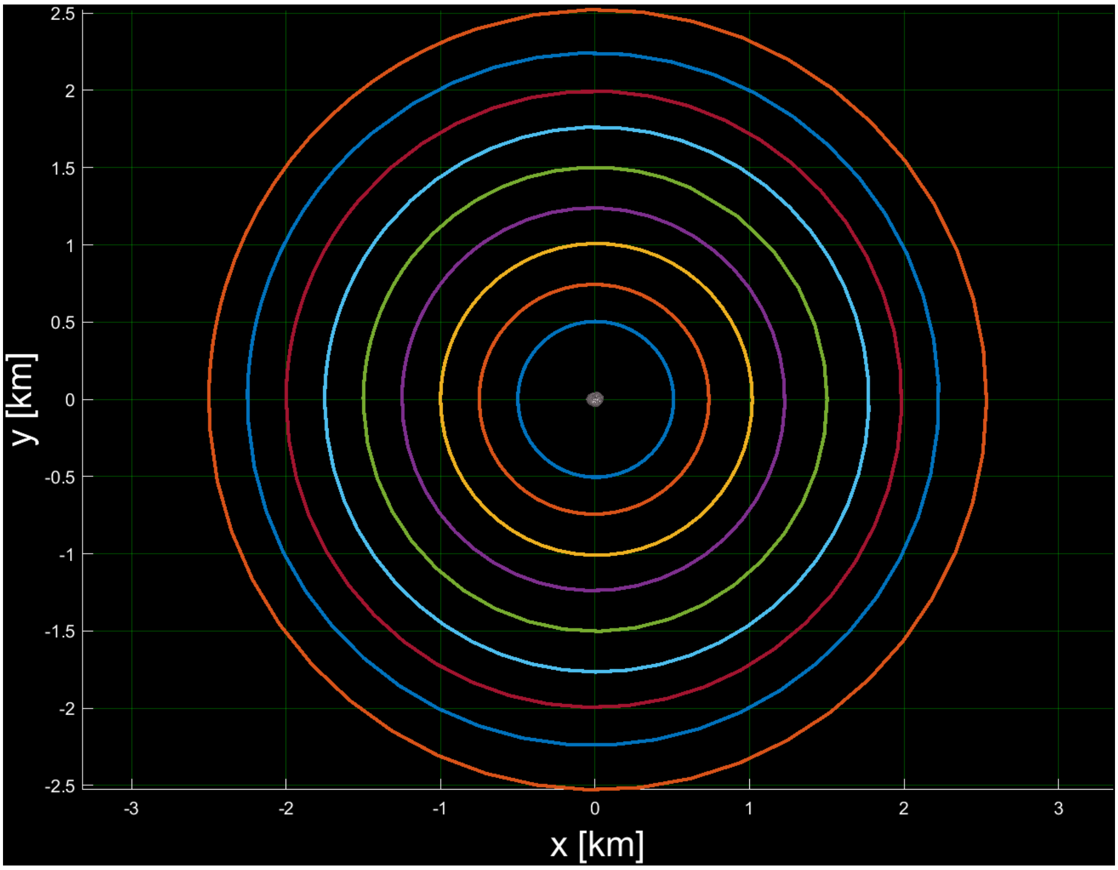

Figure 5.12: Sun-2009 OS5 DRO Family

reference system. Recalling the concepts discussed in Sec. 4.2, the velocity that the spacecraft should have in J2000 Ecliptic reference frame for DRO insertion, here called $\vec{V}_{DRO}$, is equal to

$$\vec{V}_{DRO} = \vec{V}_{2009-OS5} + \vec{V}_{\eta|_{ERF}} \cdot \frac{LU}{TU} \tag{5.32}$$

$\Delta V_{2_{\oplus \to A}}$ is computed, as norm of the vector difference between $\vec{V}_{DRO}$ and the velocity, $\vec{v}_{tI_2}$, at which the spacecraft arrives from a transfer orbit, started from a 400 km LEO and ended in a Sun-2009 OS5 DRO.

$$\Delta V_{2_{\oplus \to A}} = \left\| \vec{V}_{DRO} - \vec{v}_{tI_2} \right\| \tag{5.33}$$

We note that for this analysis we have considered that the arrival position is the center of the asteroid and not the correct DRO position, since we are talking of hundreds of meters of difference on a scale of hundreds of billions of meters. All velocities aforementioned are shown in Fig. 5.13.

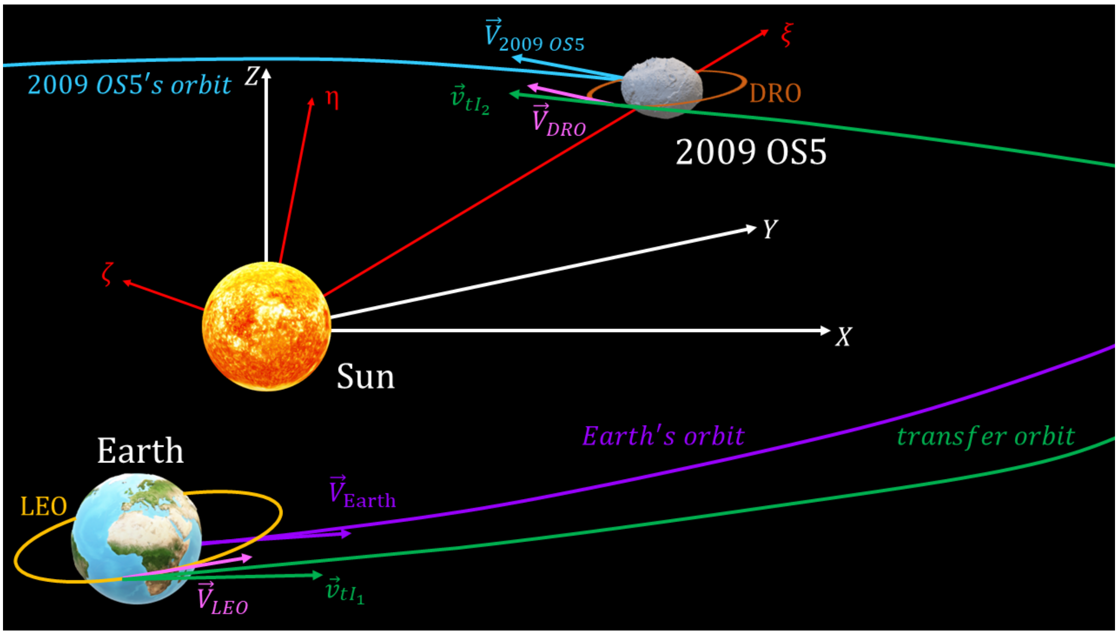

Figure 5.13: Main velocities of the first trajectory arc schematization

Applying Eq.(5.32) and Eq.(5.33) and considering $\Delta V_{1_{\oplus\to A}}$ equal to 3.4051 km/s, we obtain new $\Delta V_{tot_{\oplus\to A}}$ similar to the previous computed, which was equal to 4.4800 km/s. They changes from each other in the order of mm/s, for this reason we have not reported the results, but we still conducted the study for completeness.

Chapter 6

Landing Trajectories Optimization on Asteroid

This chapter examines the process of optimizing landing trajectories from a Sun-asteroid DRO using one impulsive maneuver. The spacecraft starts on a marginally stable parking orbit around the asteroid 2009-OS5, and the goal is to determine the required ΔV to achieve a specified landing location. Given the limited size and gravitational influence of the asteroid, the challenge lies in determining the optimal approach to safely land a spacecraft on its surface. To accomplish this, various factors need to be considered, such as the asteroid's shape, rotation, surface, gravitational field, and terrain characteristics. These elements greatly impact the planning and execution of a successful landing. Since this problem is extremely complex, we restrict our study to achieving a point on an imaginary sphere which contains the asteroid. After reaching that point, other accurate models can be considered. These models will consider all disturbance, and a three dimensional model of the spacecraft which will need multiple continuous impulses to landing safe on the asteroid.

6.1 PSO applied to landing trajectories on 2009-OS5

Particle Swarm Optimization has been employed to iteratively refine the landing trajectories as proposed by Baraldi and Conte for Mars' moon, Phobos [19]. Choosing the parameters to optimize is a complex task, and there are various approaches to tackling the optimization. In the subsequent analysis, the parameters selected are: ΔV, α, $\vec{X}_{DRO}$ and TOF. The first one indicates the magnitude of the ΔV needed to achieve the given landing location, the second parameter (α) gives the

ΔV's direction; the parameter $\vec{X}_{DRO}$ indicates a point on the parking orbit where the landing maneuver starts, while TOF indicates the landing trajectory time of flight. As shown in Fig. 6.1, α is the angle with respect the ξ-axis (which is collinear with the Sun-asteroid line) at which the ΔV is applied, while $\vec{X}_{DRO}$ are the coordinates (ξ, η) given from one of the DRO of the family analyzed in the previous chapter.

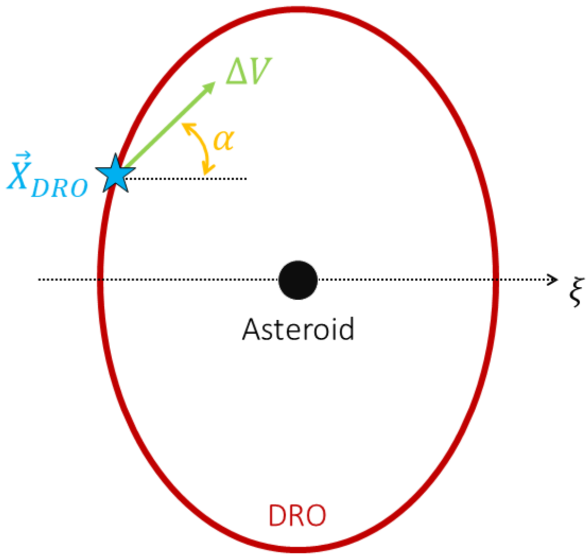

Figure 6.1: Main PSO parameters schematization

We can set the variables bounds as shown in Tab. 6.1, where V_η and τ are the values found in Chapter 5, for the specific parking DRO here considered ($A_\xi \cdot LU = 2.5\ km$). Since the DRO has been discretized in p points, the lower bound of $\vec{X}_{DRO}$ is the first point ($\vec{X}_{DRO}(1)$), while the upper bound is the last point ($\vec{X}_{DRO}(p)$). For the reasons stated above, we decided not to reach directly the

Table 6.1: Lower and Upper Bounds of the four decision variables

#	Variable	Lower Bound	Upper Bound
1	ΔV	0	V_η
2	α	0	2π
3	$\vec{X}_{DRO}$	$\vec{X}_{DRO}(1)$	$\vec{X}_{DRO}(p)$
4	TOF	$0.15 \cdot \tau$	$0.8 \cdot \tau$

surface of the asteroid, but a point on an imaginary sphere of radius 3 times that of the asteroid. The positions are placed on the $\xi\eta$-plane and they are distributed each 45° as shown in Fig. 6.2.

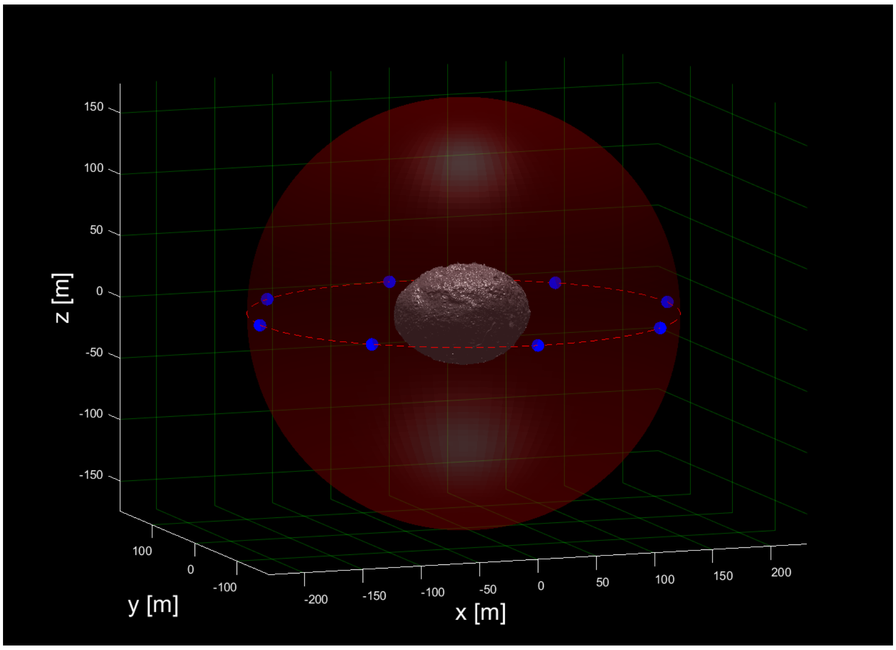

Figure 6.2: Landing Positions

As explained in the previous chapter, we initialize the particle positions with the Matlab function *unifrnd*, which returns an array of random numbers chosen from the continuous uniform distribution over the interval between the set bounds. Therefore the first iteration begins and the new initial conditions for the Eq. (5.14) and Eq. (5.15) become

$$\begin{cases} \xi_0 = \xi_{DRO}(i) \\ \eta_0 = \eta_{DRO}(i) \\ \dot{\xi}_0 = \dot{\xi}_{DRO}(i) + \Delta V \cdot \cos\alpha \\ \dot{\eta}_0 = \dot{\eta}_{DRO}(i) + \Delta V \cdot \sin\alpha \end{cases} \tag{6.1}$$

where i indicates the ith discretization point of DRO with $1 < i < N$.

The cost function, J, to minimize is modeled as follows

$$J = \frac{||\vec{r}_{final} - \vec{r}_{landing}|| \cdot LU}{0.005} + \frac{\Delta V}{V_\eta} \tag{6.2}$$

where $\vec{r}_{final}$ indicates the final coordinates $(\xi_f \ \eta_f)$ at which the integration is stopped, while $\vec{r}_{landing}$ indicates the landing coordinates set previously. The latter are transformed into kilometers and divided for 0.005, because we want to have an error close to 5 m. In the last term we have the ΔV used for the landing maneuver compared with V_η. We want to minimize also the ΔV, but we have to remember that the order of magnitude is $cm/s - mm/s$, so it does not influence the mission ΔV-budget significantly. The cost function is built to approach infinity if the trajectory enters into the sphere shown in Fig. 6.2.

To optimize computational cost, the number of particles and the maximum number of iterations are set up as follows

$$\begin{aligned} N_{particles} &= 50 \\ N_{iterations_{max}} &= 200 \end{aligned} \tag{6.3}$$

The procedure follows the procedures explained in Chapters 3 and 5. Therefore, after updating particles' positions, velocities and global best cost, we obtain the 8 landing trajectories with their respective ΔV vectors shown in Fig. 6.3 and Fig. 6.4. The white orbit is the parking DRO from which ΔVs are applied.

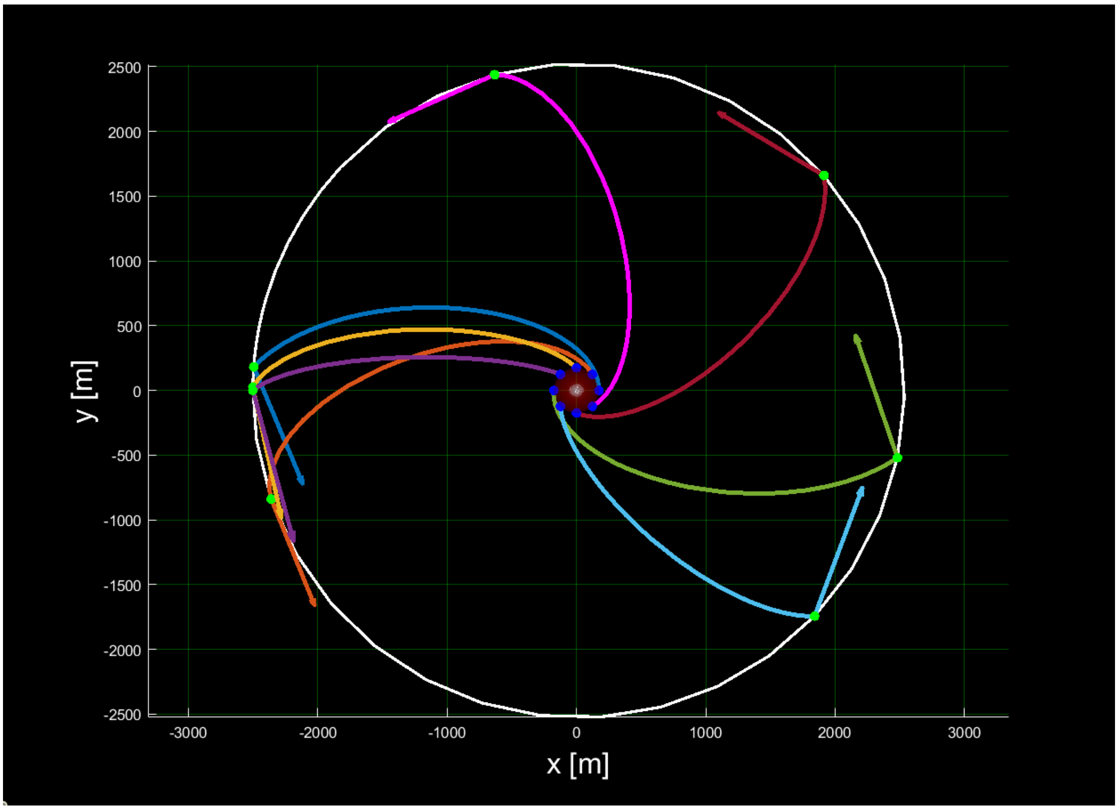

Figure 6.3: Landing Trajectories and ΔV Vectors

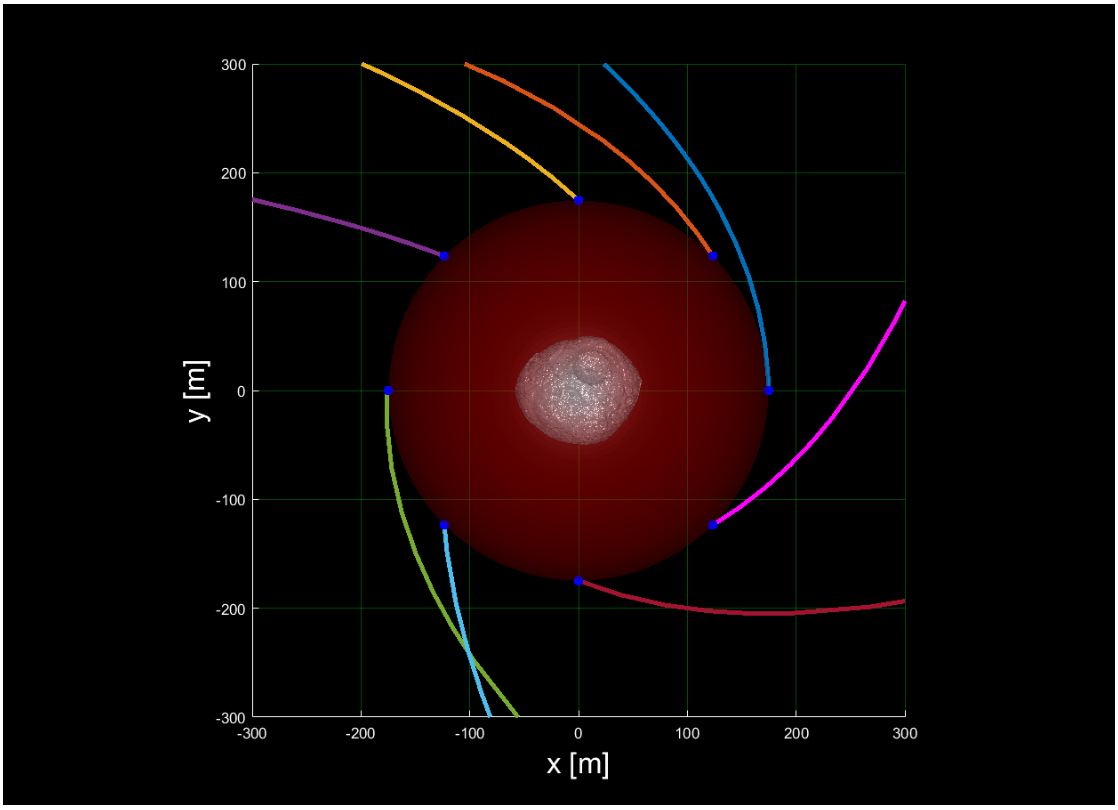

Figure 6.4: Zoomed version of Fig. 6.3

Fig. 6.5 summarizes the evolutions of the global best bost as iterations change for each landing location. Note that 0° indicates the point placed at the maximum x, and the other points are obtained by rotating it counterclockwise by 45°. In addition, the color of each case of the plot of the Global Best Cost evolution is the same as the landing trajectory. We can see as in all cases, J reaches a value less than or about equal to 1. It means that the final point of the landing trajectory is closer than 5 m respect of the arrival location and that the ΔV is less than V_η. Tab. 6.2 summarizes all the main parameters useful for finding the landing trajectory. In this case, the angle θ indicates the arrival point on the imaginary sphere. As we expected, ΔVs are on the order of a few mm/s. $\vec{X}_{DRO}$ indicates the starting position in meter in a reference frame shifted to the center of the asteroid. The landing trajectory TOF is between 2 and 4 day, which are acceptable times, because the total *waiting time* from the insertion into parking DRO to departure for Mars is equal to 30 days for the asteroid 2009-OS5. This means that a spacecraft would have up to 20 days to perform all necessary ISRU operations while at the asteroids.

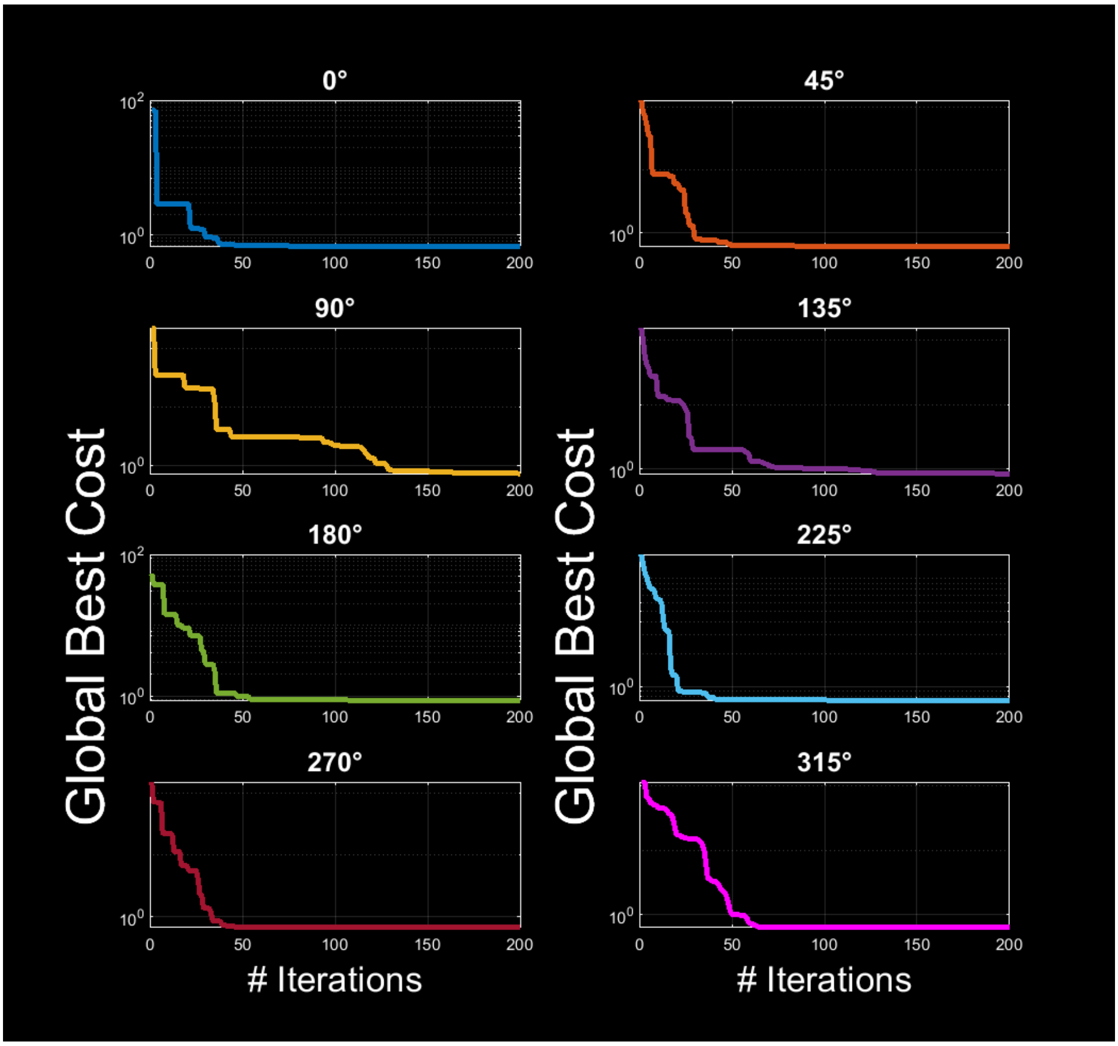

Figure 6.5: Global Best Cost evolution

Table 6.2: Landing maneuver main parameters and PSO Best Global Cost (J)

θ	ΔV $[mm/s]$	α	$\vec{X}_{DRO}$ $[m, m]$	TOF $[day]$	J
0°	7.23	292.78°	[-2493.50, 181.25]	2.70	0.69
45°	6.55	292.22°	[-2358.89, -839.35]	3.40	0.62
90°	7.63	282.29°	[-2500.34, 25.31]	2.88	0.73
135°	8.93	285.13°	[-2500.00, 0]	2.65	0.85
180°	7.38	108.97°	[2481.19, -5193.30]	2.65	1.08
225°	7.84	69.52°	[1840.60, -1743.62]	2.65	0.75
270°	6.99	149.16°	[1912.03, 1660.23]	2.92	0.67
315°	6.59	203.94°	[-632.32, 2438.09]	3.23	0.63

To successfully land on an asteroid, an autonomous landing navigation and guidance scheme could be considered [27]. It involves planning desired descent landing trajectories while considering initial and terminal constraints, and designing guidance control laws to track the reference descent trajectory [28].

Conclusions

This thesis has explored the potential of utilizing asteroids as refueling points for Earth-Mars missions to minimize the ΔV requirements and overall cost. By implementing In-Situ Resource Utilization (ISRU) techniques, the spacecraft can extract and utilize resources from asteroids, such as water for propellant production or direct consumption (e.g. drinking).

The study focused on trajectories from Earth to candidate asteroids and from there to Mars. The objective was to minimize the total ΔV from Earth to the asteroid and the time of flight from Earth to Mars, while maximizing the number of resupplies on the asteroid. A double arc trajectory was investigated, involving the interception of a candidate asteroid, insertion into a Sun-asteroid Distant Retrograde Orbit (DRO), a landing trajectory on the asteroid, and then departure towards Mars using the propellant obtained from the asteroid.

The dynamics of Sun-asteroid systems were modeled using the Circular Restricted Three-Body Problem, enabling the computation of periodic orbits such as DROs. Particle Swarm Optimization was employed to determine the initial conditions of the proposed DRO, and PSO was also used to compute optimal landing trajectories on the asteroid.

The results indicate that utilizing the asteroid 2009-OS5 for refueling can lead to a 27% reduction in Earth-Asteroid ΔV (4.4800 km/s) compared to the minimum direct Earth-Mars ΔV possible (6.1696 km/s). The estimated number of refueling opportunities on this asteroid is approximately 83 times, making it a promising candidate for future missions. Consider that in the case of the asteroid 2009 OS5, the 83 refueling opportunities should not be seen as 83 distinct missions, but rather as a few missions where fleets of spacecraft refuel on the asteroid. This is because the alignment of Earth-Asteroid-Mars, which allows for significant ΔV savings, may occur only once every decade, making the planning of Earth-Mars missions complex. However, there might be asteroids with periodic alignments that incur slightly higher ΔV costs, which need to be taken into consideration. In any case, the study suggests the existence of numerous asteroids with potential ΔV savings. As a result, one possible solution for future Earth-Mars missions could involve utilizing all the available resources on a single asteroid over a short series of missions, and subsequently shifting to another asteroid for future missions.

Furthermore, this research delved into the optimization of landing trajectories on the asteroid's surface using impulsive maneuvers. While the study focused on reaching a point on an imaginary sphere encompassing the asteroid, future work can explore more accurate models considering disturbances, three-dimensional spacecraft model, the asteroid's shape, rotation, surface, gravitational field, and terrain characteristics, which would require multiple continuous impulses for a safe landing.

Overall, this thesis demonstrates the feasibility and potential benefits of utilizing asteroids as refueling points for Earth-Mars missions. By leveraging in-situ resources and optimizing trajectories, significant reductions in launch mass and mission costs can be achieved, bringing us closer to the realization of human colonization of Mars.

To estimate the reduction of mission costs, we introduce some concepts from fondamental rocketry. In the chemical propulsion, the relevant masses are: the payload mass, m_u, the propellant mass, m_p, and the structural mass, m_s. So we have the initial mass of the rocket as follows

$$m_0 = m_u + m_p + m_s \tag{6.4}$$

where m_0 is the total initial mass. Considering that all the propellant is used, the final mass, m_f, becomes

$$m_f = m_0 - m_p = m_u + m_s \tag{6.5}$$

We introduce the payload fraction, λ

$$\lambda = \frac{m_u}{m_0} \tag{6.6}$$

and the structural fraction

$$\epsilon = \frac{m_s}{m_s + m_p} \tag{6.7}$$

Recalling Tsiolkovsky's rocket equation, we have

$$\Delta V = c \cdot \ln\left(\frac{m_0}{m_f}\right) = c \cdot \ln\left(\frac{m_u + m_p + m_s}{m_u + m_s}\right) = -c \cdot \ln\left[\lambda + \epsilon\left(1 - \lambda\right)\right] \tag{6.8}$$

where c is the effective exhaust velocity. Solving for λ, we have

$$\lambda = \frac{e^{-\frac{\Delta V}{c}} - \epsilon}{1 - \epsilon} \tag{6.9}$$

In multistage rocket with N stages, and with the same c and ϵ for each stage, Eq. (6.9) becomes

$$\lambda_{tot} = \left[\frac{e^{-\frac{\Delta V_{tot}}{Nc}} - \epsilon}{1 - \epsilon} \right]^N \tag{6.10}$$

where $\lambda_{tot} = \frac{(m_u)_N}{(m_0)_1}$.

Considering a rocket with $N = 3$ stages, ΔV to reach a 400 km LEO equal to 10 km/s, the structural fraction $\epsilon = 0.1$ and the effective exhaust velocity $c = 4.5$ km/s we have that in case of direct Earth-Mars transfer ($\Delta V_{min,\oplus\rightarrow\male} = 6.1696$ km/s)

$$\lambda_{tot} = 0.0113 \tag{6.11}$$

It means that the payload mass is 1.13% of the structural and propellant mass of the first stage.

In case of Earth-Mars transfers via asteroid 2009-OS5 ($\Delta V_{min,\oplus\rightarrow\male} = 4.4800$ km/s) we have

$$\lambda_{tot} = 0.0195 \tag{6.12}$$

It means that the payload mass is 1.95% of the structural and propellant mass of the first stage. Therefore, we can send the same rocket configuration to Mars with 1.73 times the payload mass than in direct Earth-Mars transfer case, with obvious economic advantages related to launch costs. On the other hand, it is necessary to establish an ISRU station on the asteroid, or to develop technology that will allow the spacecraft to do resource extraction on its own.

By further exploring and refining these concepts, we can pave the way for successful and cost-effective human missions to Mars, opening up new possibilities for space exploration and colonization.

6.2 Future Developments

Building upon the findings and methodologies presented in this thesis, there are several areas of research that hold promise for further exploration and advancement in utilizing asteroids as refueling points for Earth-Mars missions.

To gain a more comprehensive understanding of the dynamics involved in utilizing asteroids as refueling points, future studies should consider the influence of perturbations, such as gravitational interactions with other celestial bodies, solar radiation pressure, and non-uniform mass distributions. By incorporating these factors into modeling frameworks, more accurate and realistic models can be developed to analyze long-term dynamics, stability, and trajectory planning under complex celestial interactions.

Further improvement in mission planning and resource utilization can be achieved through advanced asteroid characterization. Thorough investigations of shape, rotation, surface properties, gravitational fields, and terrain characteristics will enable precise landing trajectory planning, landing site selection, and resource extraction operations. Utilizing high-resolution imaging, radar mapping, and in-situ measurements will provide valuable insights into the geological composition, topography, and subsurface structures of asteroids.

Future research should explore the development and optimization of techniques for extracting water, metals, minerals, gases, and other valuable substances from asteroids. Advancements in mining technologies, refining processes, and resource utilization strategies tailored to the unique properties of different asteroids will enhance the self-sustainability of space missions.

In-situ manufacturing and utilization of materials obtained from asteroids offer significant benefits. Future work should focus on developing technologies for producing components, structures, and consumables directly in space. Additive manufacturing, 3D printing, and regenerative life support systems can reduce reliance on Earth-based resupply missions and enhance mission sustainability.

Advancements in guidance, navigation, and control (GNC) are crucial for safe and precise operations in proximity to asteroids. Future efforts should explore advanced algorithms for autonomous navigation, hazard avoidance, and spacecraft rendezvous and docking with asteroids. Incorporating machine learning, computer vision, and sensor fusion approaches can improve the reliability and adaptability of GNC systems in challenging and dynamic environments.

By addressing these future research directions, we can unlock the full potential of utilizing asteroids as refueling points for Earth-Mars missions. Advancements in modeling accuracy, resource extraction techniques, in-situ manufacturing, and GNC systems will contribute to reducing mission costs, enhancing mission sustainability, and paving the way for long-term human presence and colonization of Mars and beyond. The journey towards a new era of space exploration and settlement is filled with opportunities for innovation and collaboration among space agencies, research institutions, and commercial entities. Together, we can explore and leverage the vast resources available in our solar system, driving humanity towards a future of interplanetary exploration and habitation.

Fig. 6.6 shows a visual concept of ISRU on asteroids product by *Aitubo*, an artificial intelligence art generator. To generate the figure we use the prompt "Extracting minerals on an asteroid to refuel spacecraft in human space missions".

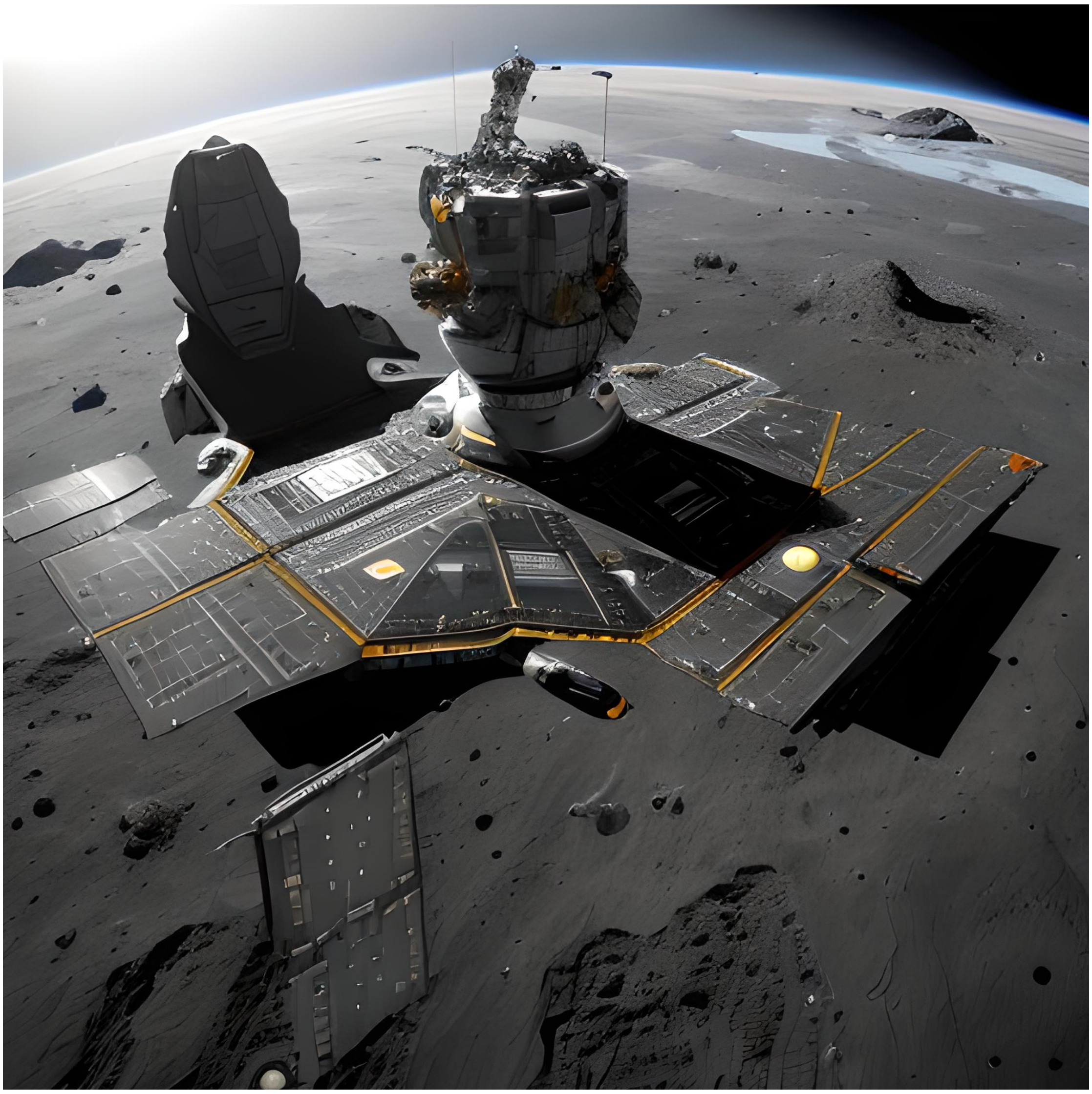

Figure 6.6: ISRU on asteroid

Appendix A

Porkchop Plots for Earth to each Candidate Asteroids

This appendix presents a compilation of all 94 Porkchop Plots Earth-asteroid missions within a specific range of time of flight and departure dates. The catalog encompasses a period of 10 years, starting from January 1st, 2035, and includes Earth-asteroid trajectories with TOF ranging from 51 to 300 days.

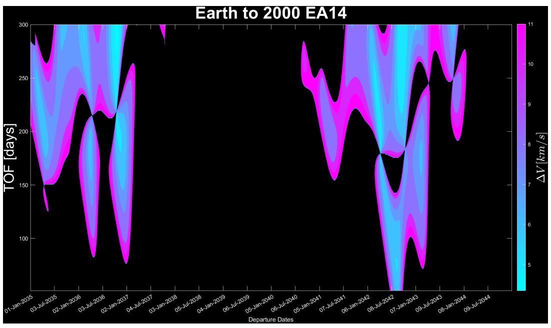

Figure A.1: Porkchop Plot from Earth to Asteroid 2000 EA14

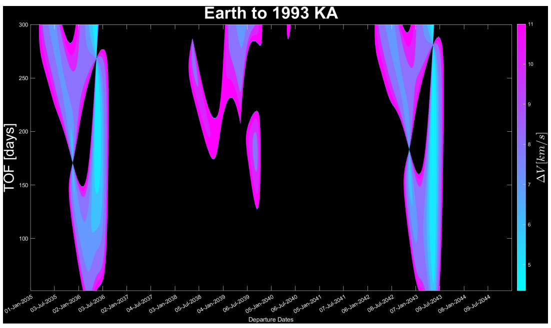

Figure A.2: Porkchop Plot from Earth to Asteroid 1993 KA

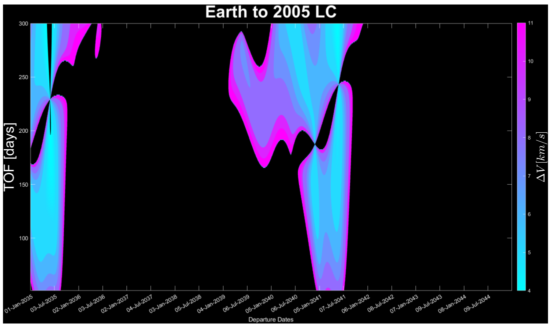

Figure A.3: Porkchop Plot from Earth to Asteroid 2005 LC

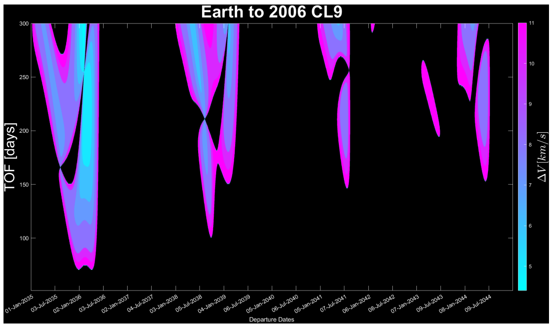

Figure A.4: Porkchop Plot from Earth to Asteroid 2006 CL9

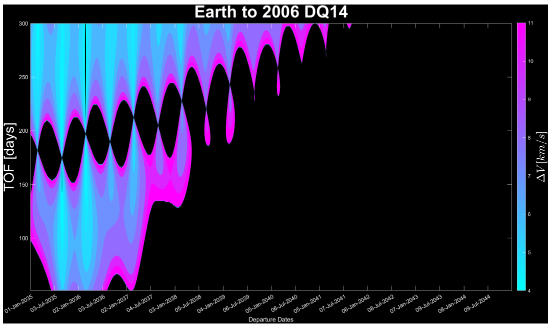

Figure A.5: Porkchop Plot from Earth to Asteroid 2006 DQ14

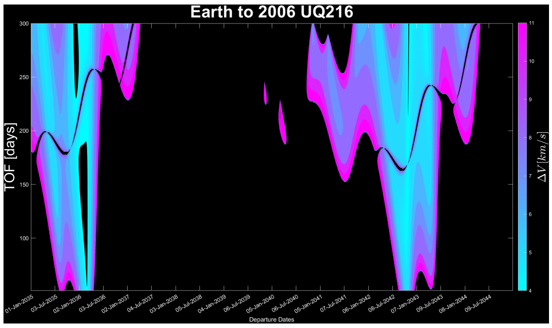

Figure A.6: Porkchop Plot from Earth to Asteroid 2006 UQ216

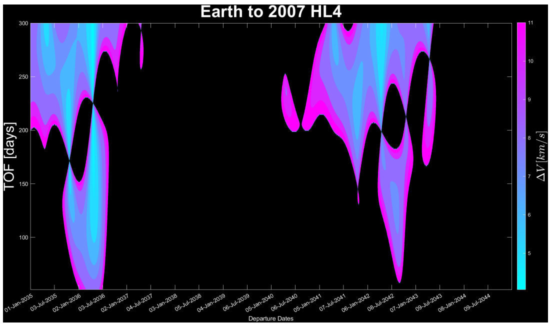

Figure A.7: Porkchop Plot from Earth to Asteroid 2007 HL4

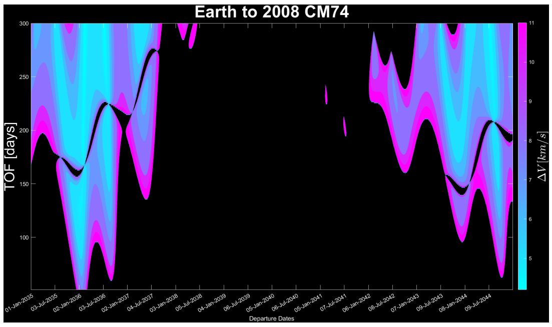

Figure A.8: Porkchop Plot from Earth to Asteroid 2008 CM74

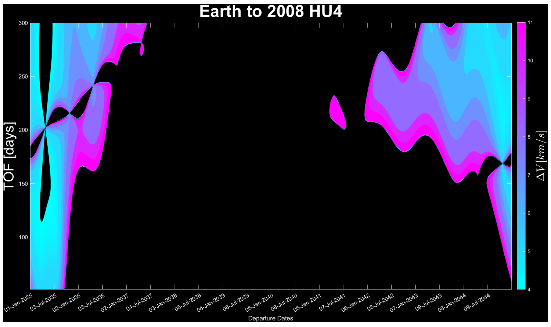

Figure A.9: Porkchop Plot from Earth to Asteroid 2008 HU4

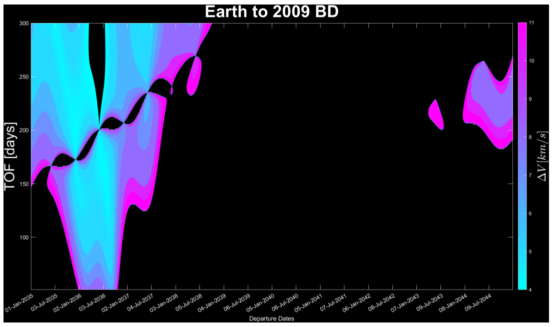

Figure A.10: Porkchop Plot from Earth to Asteroid 2009 BD

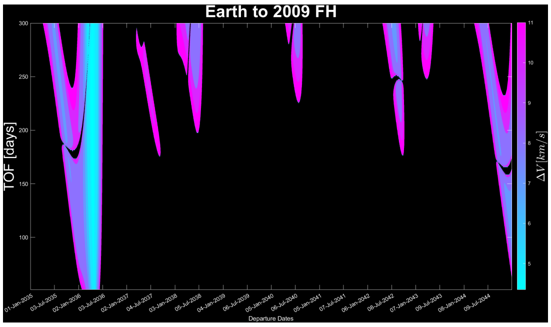

Figure A.11: Porkchop Plot from Earth to Asteroid 2009 FH

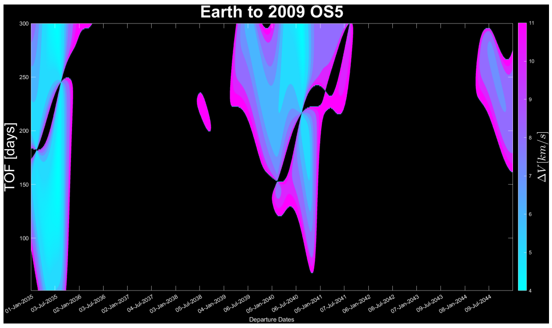

Figure A.12: Porkchop Plot from Earth to Asteroid 2009 OS5

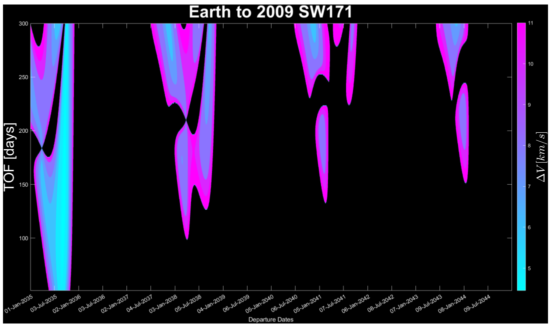

Figure A.13: Porkchop Plot from Earth to Asteroid 2009 SW171

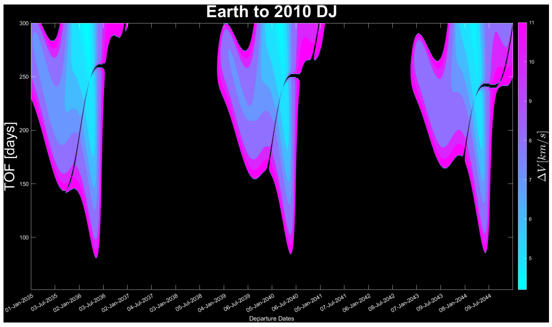

Figure A.14: Porkchop Plot from Earth to Asteroid 2010 DJ

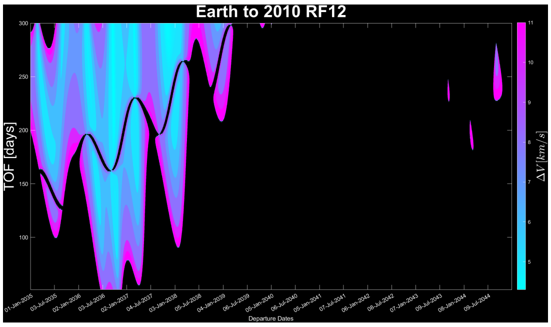

Figure A.15: Porkchop Plot from Earth to Asteroid 2010 RF12

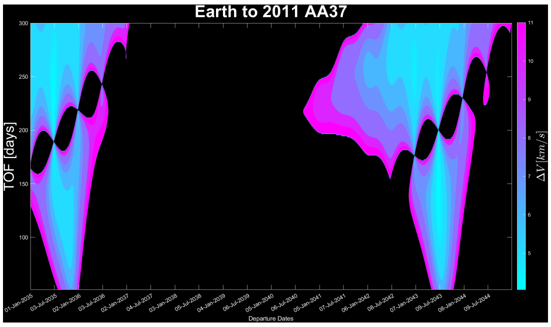

Figure A.16: Porkchop Plot from Earth to Asteroid 2011 AA37

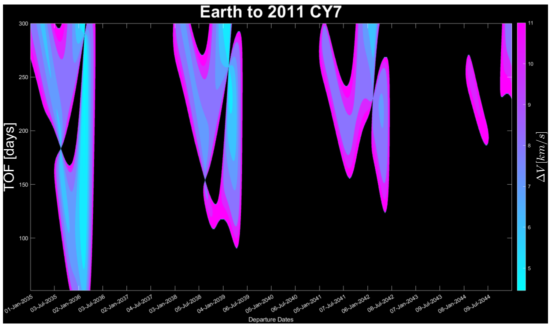

Figure A.17: Porkchop Plot from Earth to Asteroid 2011 CY7

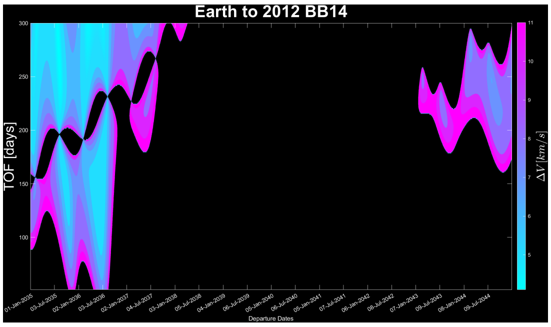

Figure A.18: Porkchop Plot from Earth to Asteroid 2012 BB14

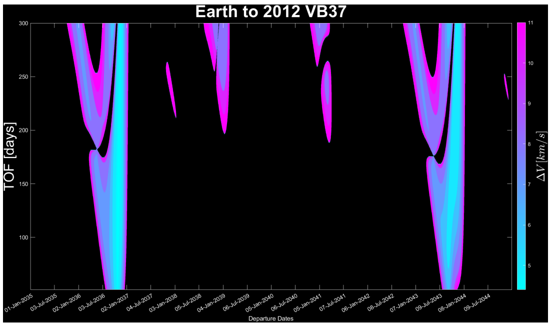

Figure A.19: Porkchop Plot from Earth to Asteroid 2012 VB37

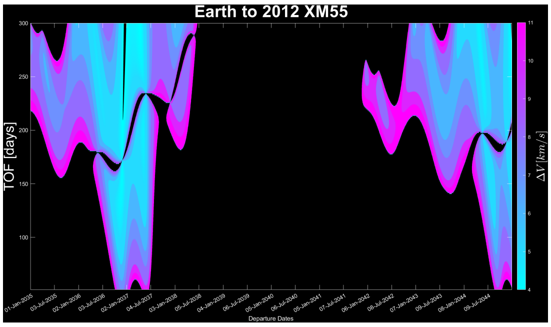

Figure A.20: Porkchop Plot from Earth to Asteroid 2012 XM55

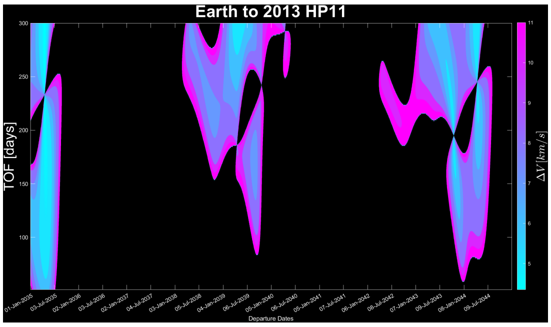

Figure A.21: Porkchop Plot from Earth to Asteroid 2013 HP11

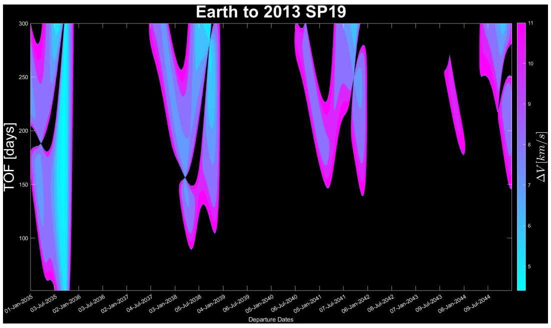

Figure A.22: Porkchop Plot from Earth to Asteroid 2013 SP19

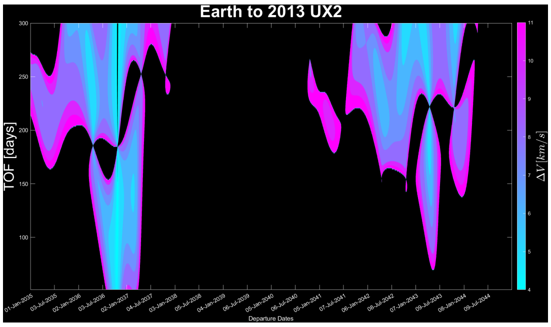

Figure A.23: Porkchop Plot from Earth to Asteroid 2013 UX2

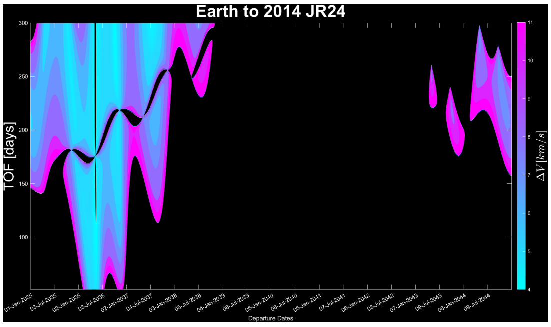

Figure A.24: Porkchop Plot from Earth to Asteroid 2014 JR24

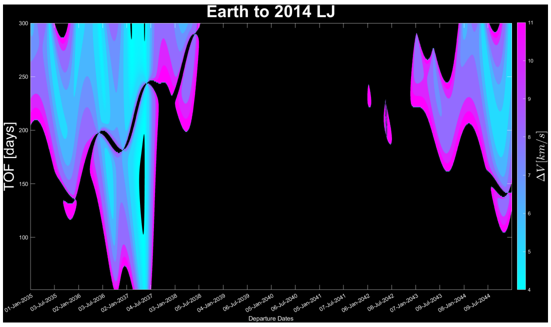

Figure A.25: Porkchop Plot from Earth to Asteroid 2014 LJ

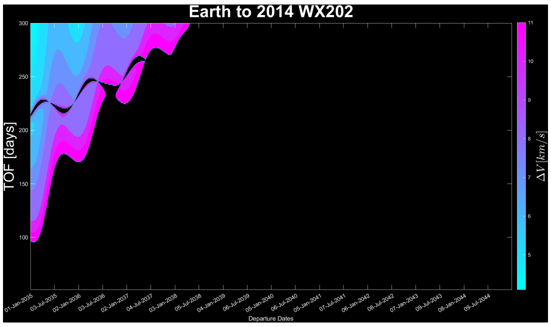

Figure A.26: Porkchop Plot from Earth to Asteroid 2014 WX202

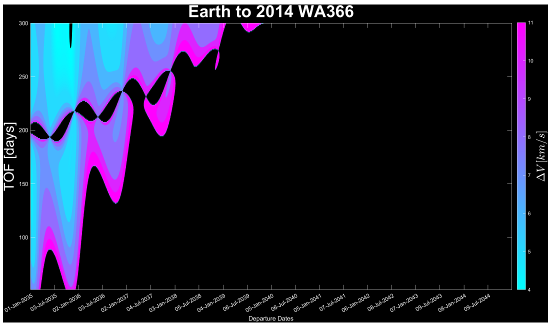

Figure A.27: Porkchop Plot from Earth to Asteroid 2014 WA366

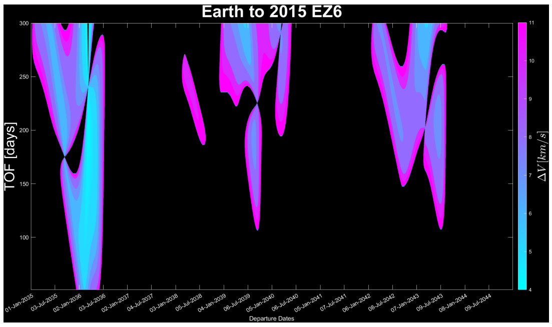

Figure A.28: Porkchop Plot from Earth to Asteroid 2015 EZ6

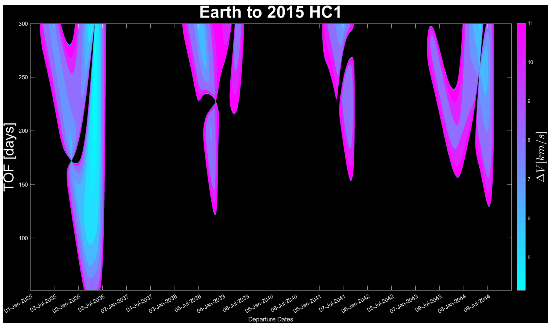

Figure A.29: Porkchop Plot from Earth to Asteroid 2015 HC1

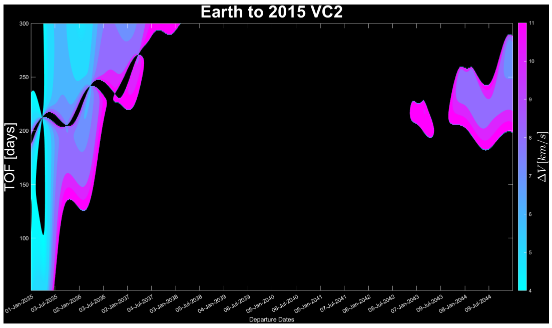

Figure A.30: Porkchop Plot from Earth to Asteroid 2015 VC2

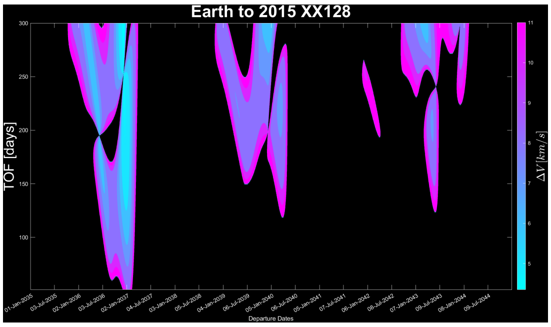

Figure A.31: Porkchop Plot from Earth to Asteroid 2015 XX128

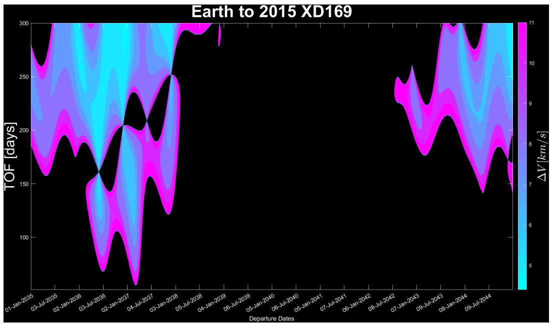

Figure A.32: Porkchop Plot from Earth to Asteroid 2015 XD169

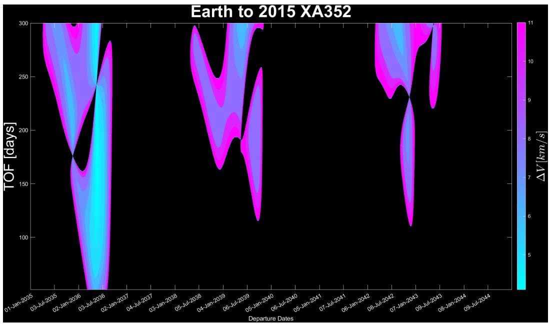

Figure A.33: Porkchop Plot from Earth to Asteroid 2015 XA352

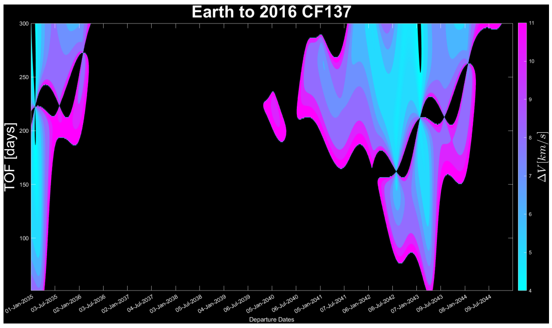

Figure A.34: Porkchop Plot from Earth to Asteroid 2016 CF137

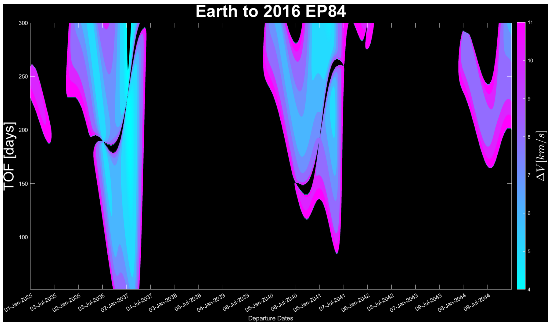

Figure A.35: Porkchop Plot from Earth to Asteroid 2016 EP84

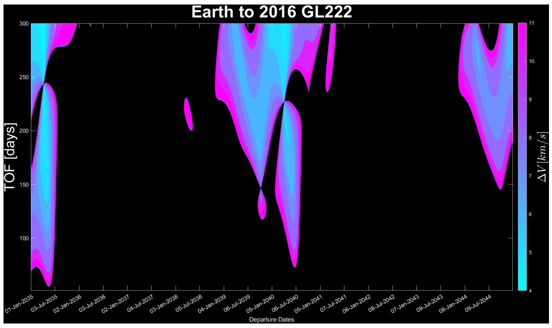

Figure A.36: Porkchop Plot from Earth to Asteroid 2016 GL222

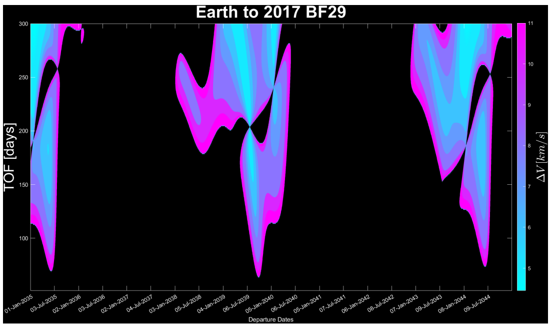

Figure A.37: Porkchop Plot from Earth to Asteroid 2017 BF29

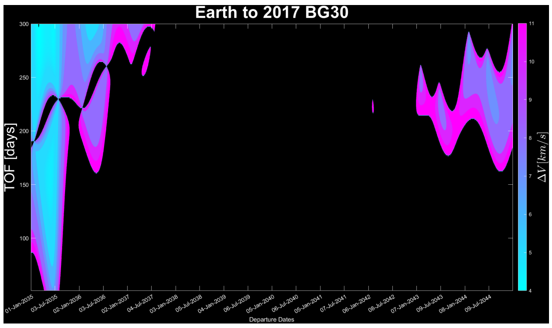

Figure A.38: Porkchop Plot from Earth to Asteroid 2017 BG30

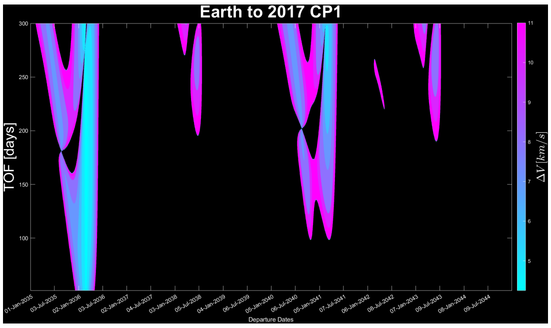

Figure A.39: Porkchop Plot from Earth to Asteroid 2017 CP1

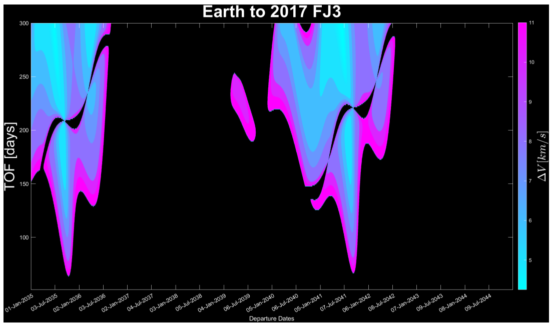

Figure A.40: Porkchop Plot from Earth to Asteroid 2017 FJ3

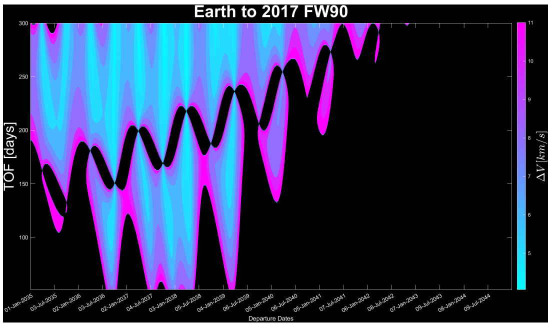

Figure A.41: Porkchop Plot from Earth to Asteroid 2017 FW90

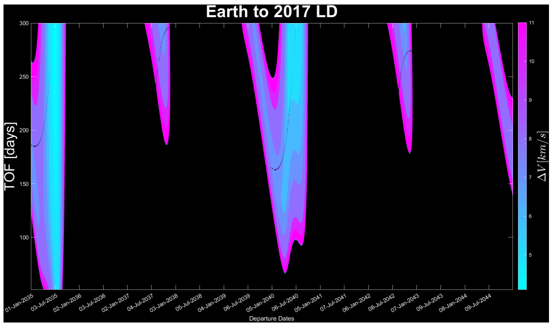

Figure A.42: Porkchop Plot from Earth to Asteroid 2017 LD

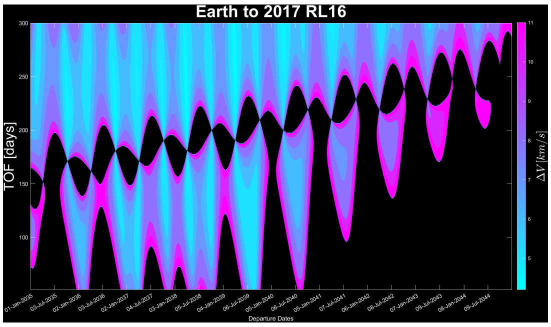

Figure A.43: Porkchop Plot from Earth to Asteroid 2017 RL16

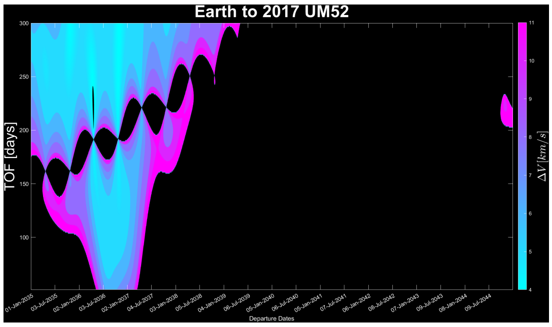

Figure A.44: Porkchop Plot from Earth to Asteroid 2017 UM52

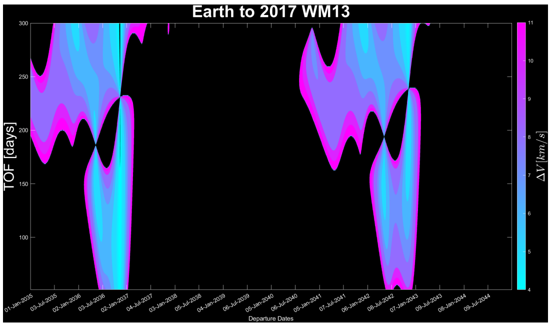

Figure A.45: Porkchop Plot from Earth to Asteroid 2017 WM13

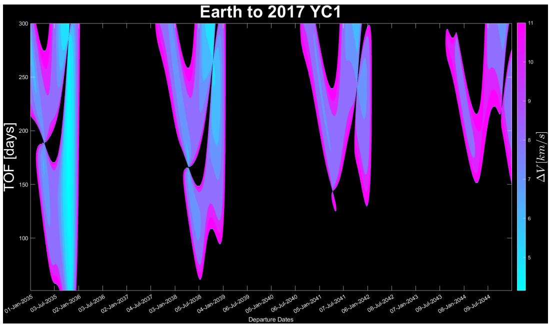

Figure A.46: Porkchop Plot from Earth to Asteroid 2017 YC1

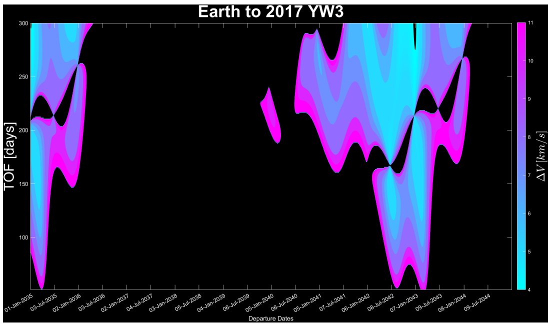

Figure A.47: Porkchop Plot from Earth to Asteroid 2017 YW3

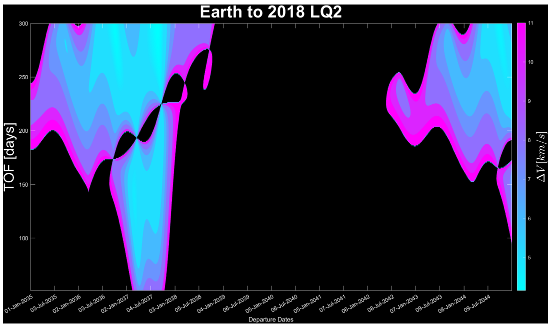

Figure A.48: Porkchop Plot from Earth to Asteroid 2018 LQ2

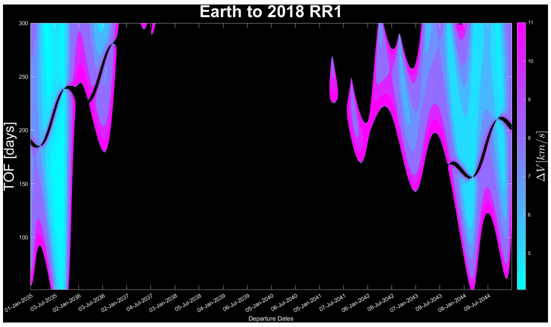

Figure A.49: Porkchop Plot from Earth to Asteroid 2018 RR1

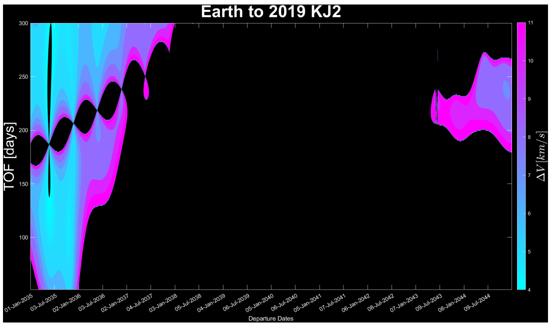

Figure A.50: Porkchop Plot from Earth to Asteroid 2019 KJ2

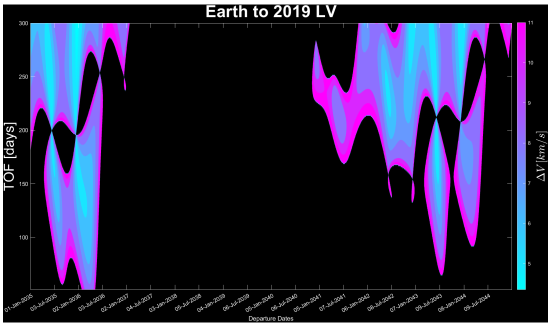

Figure A.51: Porkchop Plot from Earth to Asteroid 2019 LV

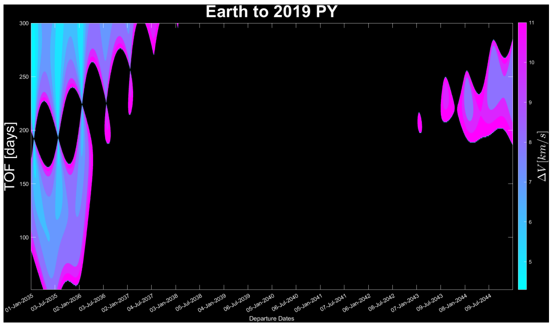

Figure A.52: Porkchop Plot from Earth to Asteroid 2019 PY

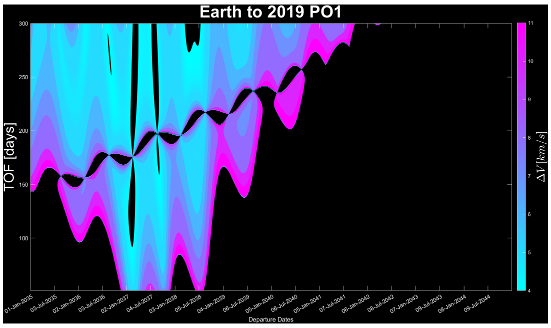

Figure A.53: Porkchop Plot from Earth to Asteroid 2019 PO1

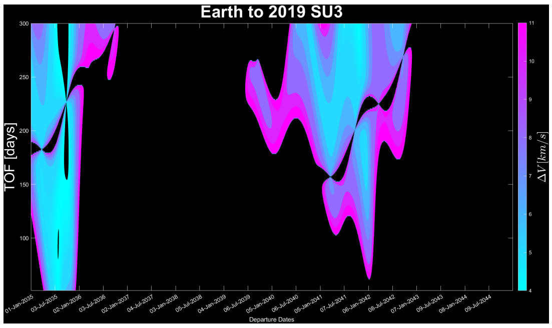

Figure A.54: Porkchop Plot from Earth to Asteroid 2019 SU3

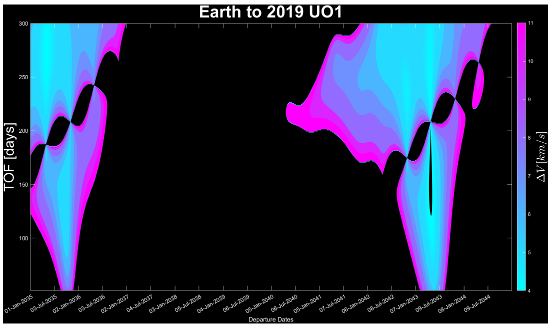

Figure A.55: Porkchop Plot from Earth to Asteroid 2019 UO1

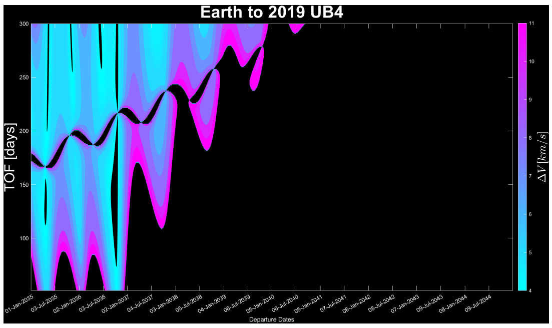

Figure A.56: Porkchop Plot from Earth to Asteroid 2019 UB4

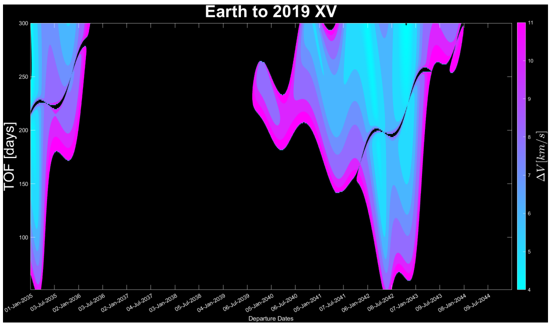

Figure A.57: Porkchop Plot from Earth to Asteroid 2019 XV

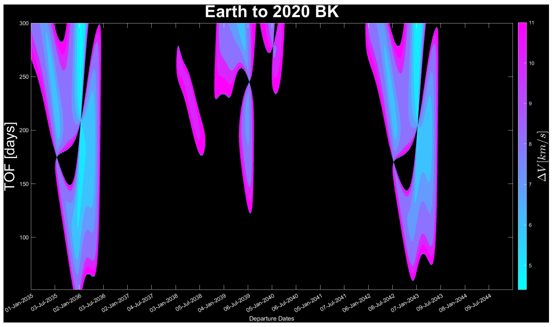

Figure A.58: Porkchop Plot from Earth to Asteroid 2020 BK

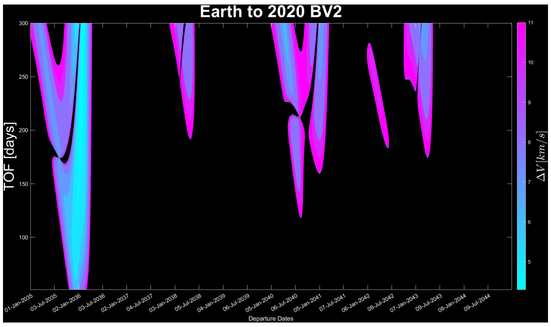

Figure A.59: Porkchop Plot from Earth to Asteroid 2020 BV2

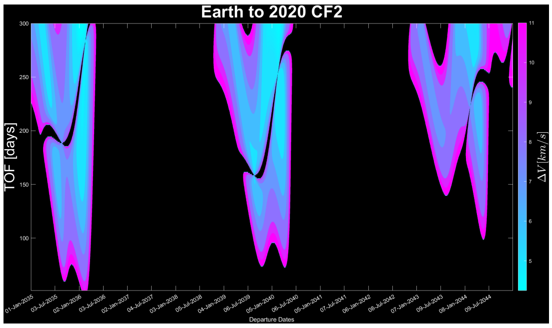

Figure A.60: Porkchop Plot from Earth to Asteroid 2020 CF2

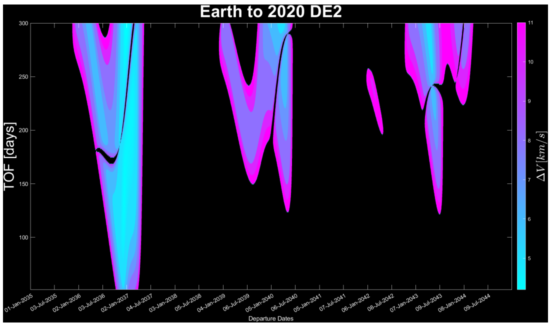

Figure A.61: Porkchop Plot from Earth to Asteroid 2020 DE2

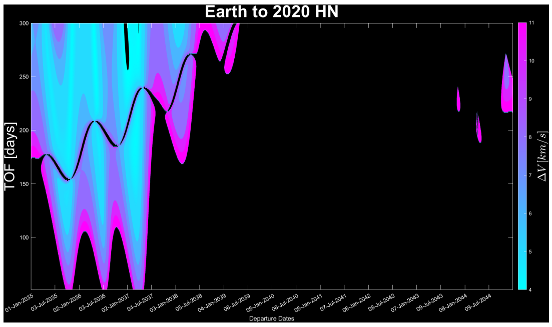

Figure A.62: Porkchop Plot from Earth to Asteroid 2020 HN

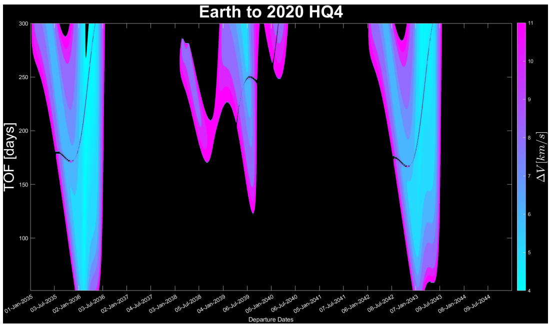

Figure A.63: Porkchop Plot from Earth to Asteroid 2020 HQ4

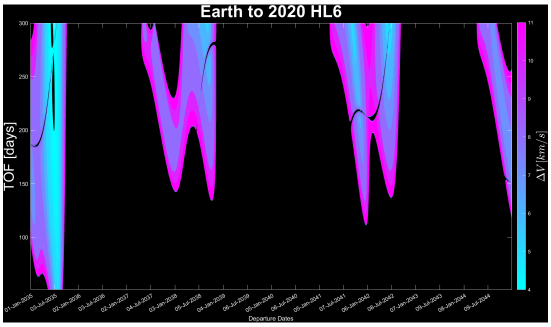

Figure A.64: Porkchop Plot from Earth to Asteroid 2020 HL6

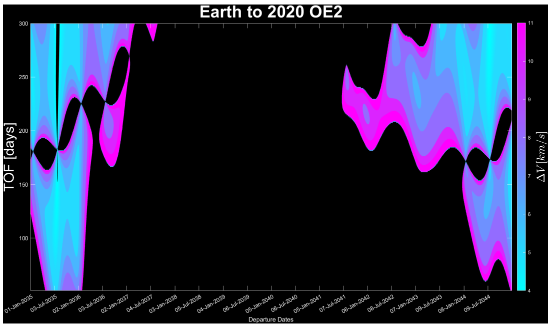

Figure A.65: Porkchop Plot from Earth to Asteroid 2020 OE2

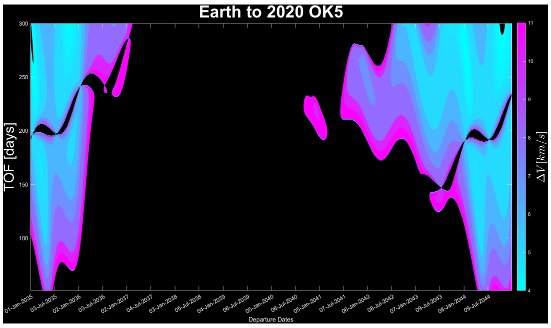

Figure A.66: Porkchop Plot from Earth to Asteroid 2020 OK5

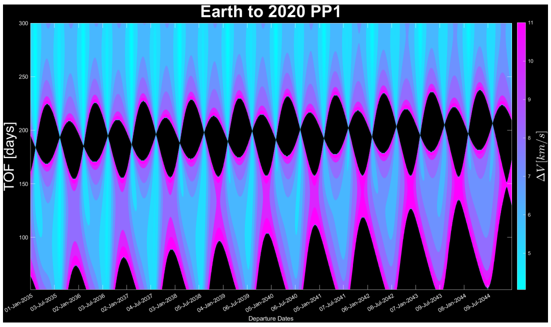

Figure A.67: Porkchop Plot from Earth to Asteroid 2020 PP1

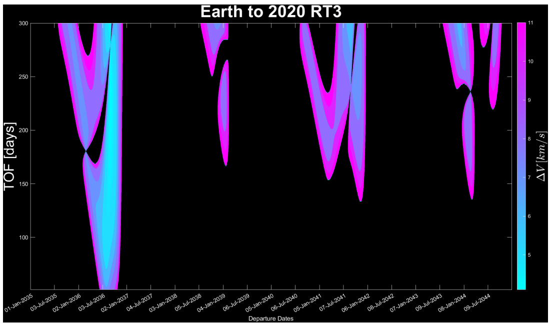

Figure A.68: Porkchop Plot from Earth to Asteroid 2020 RT3

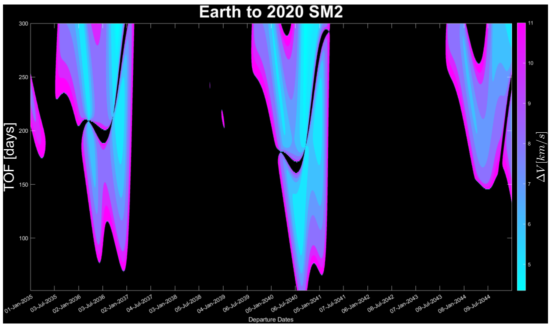

Figure A.69: Porkchop Plot from Earth to Asteroid 2020 SM2

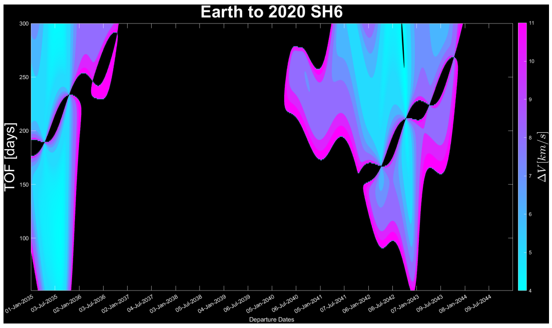

Figure A.70: Porkchop Plot from Earth to Asteroid 2020 SH6

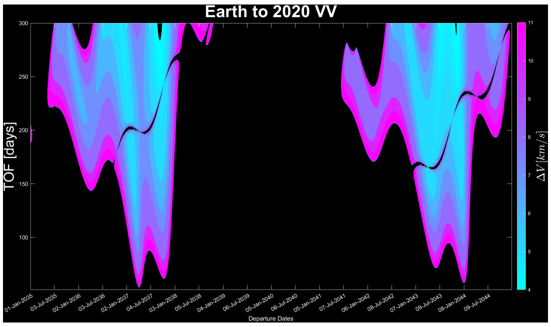

Figure A.71: Porkchop Plot from Earth to Asteroid 2020 VV

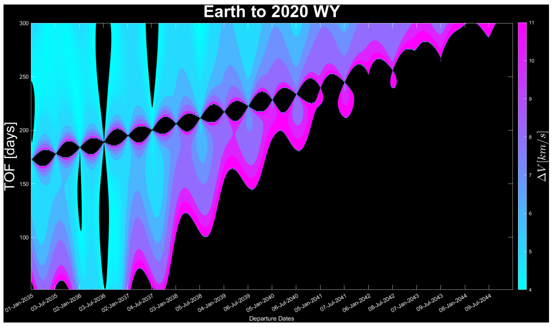

Figure A.72: Porkchop Plot from Earth to Asteroid 2020 WY

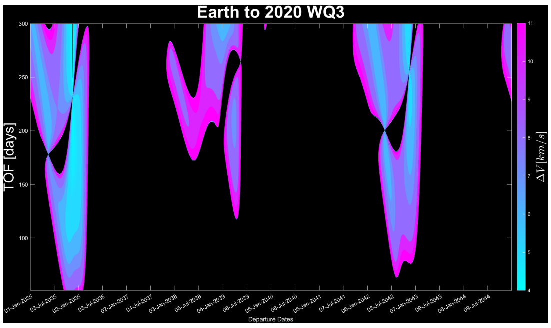

Figure A.73: Porkchop Plot from Earth to Asteroid 2020 WQ3

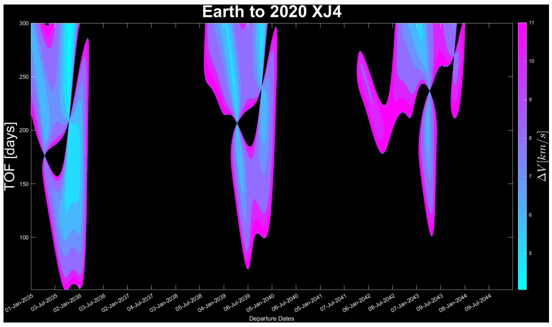

Figure A.74: Porkchop Plot from Earth to Asteroid 2020 XJ4

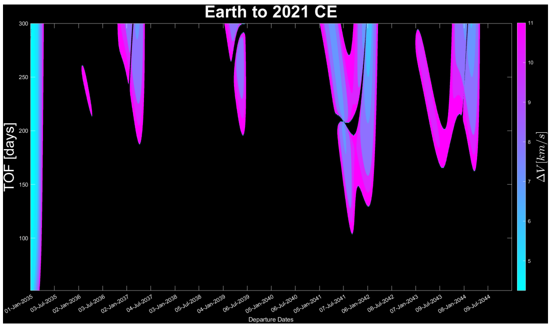

Figure A.75: Porkchop Plot from Earth to Asteroid 2021 CE

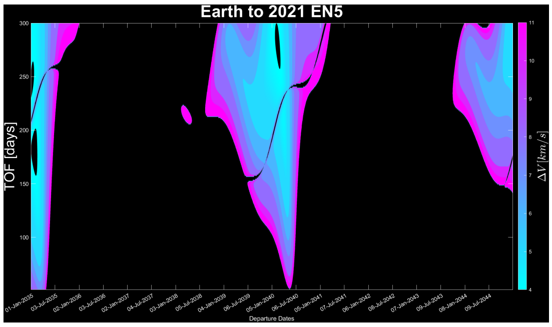

Figure A.76: Porkchop Plot from Earth to Asteroid 2021 EN5

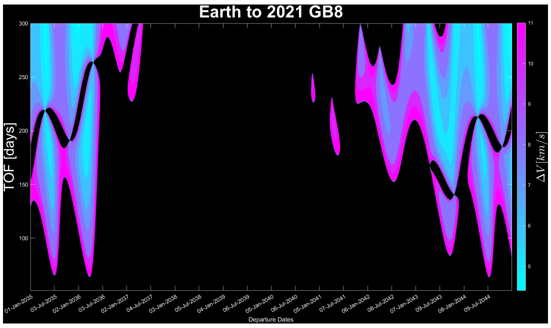

Figure A.77: Porkchop Plot from Earth to Asteroid 2021 GB8

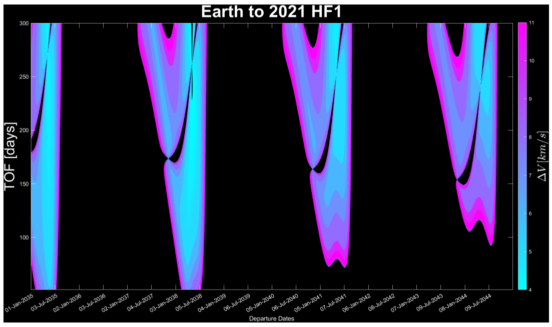

Figure A.78: Porkchop Plot from Earth to Asteroid 2021 HF1

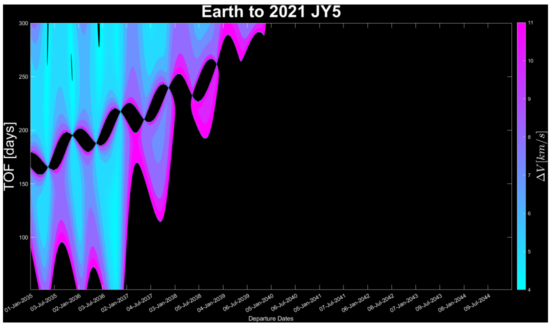

Figure A.79: Porkchop Plot from Earth to Asteroid 2021 JY5

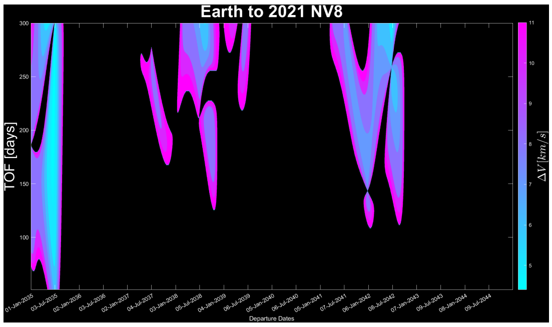

Figure A.80: Porkchop Plot from Earth to Asteroid 2021 NV8

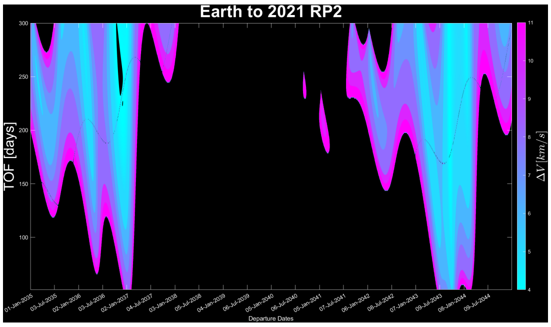

Figure A.81: Porkchop Plot from Earth to Asteroid 2021 RP2

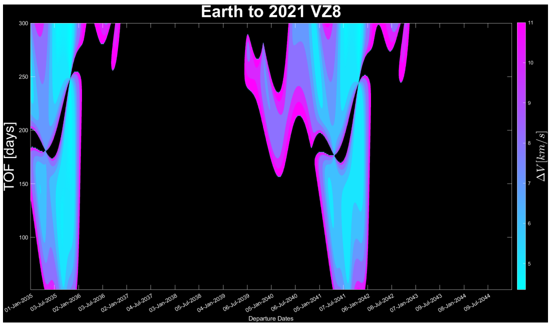

Figure A.82: Porkchop Plot from Earth to Asteroid 2021 VZ8

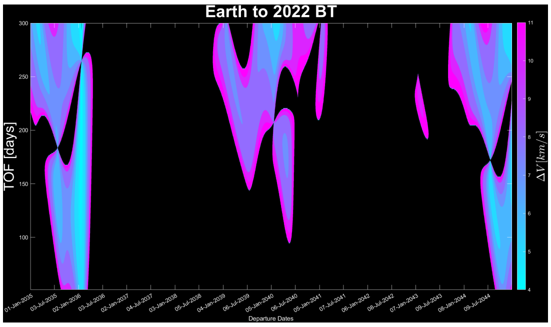

Figure A.83: Porkchop Plot from Earth to Asteroid 2022 BT

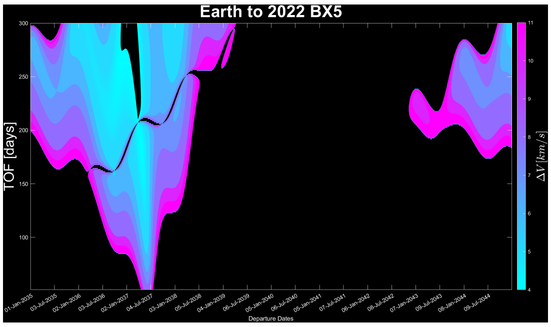

Figure A.84: Porkchop Plot from Earth to Asteroid 2022 BX5

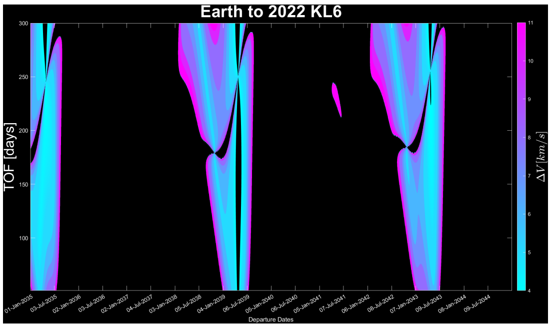

Figure A.85: Porkchop Plot from Earth to Asteroid 2022 KL6

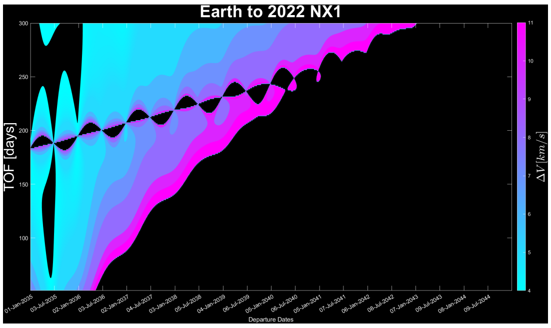

Figure A.86: Porkchop Plot from Earth to Asteroid 2022 NX1

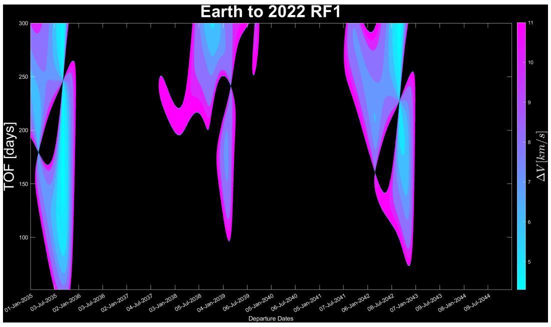

Figure A.87: Porkchop Plot from Earth to Asteroid 2022 RF1

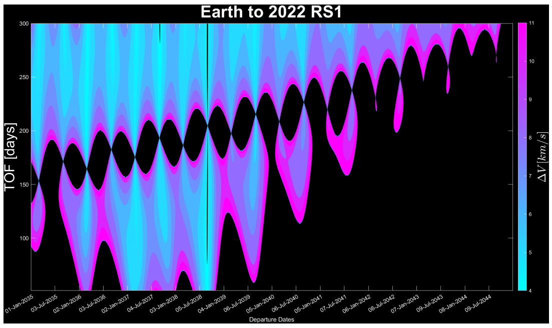

Figure A.88: Porkchop Plot from Earth to Asteroid 2022 RS1

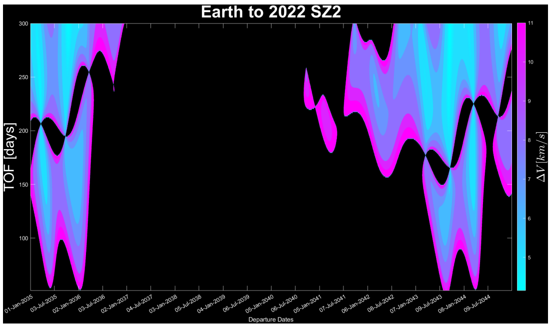

Figure A.89: Porkchop Plot from Earth to Asteroid 2022 SZ2

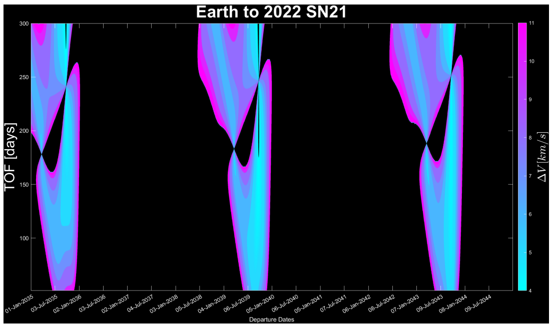

Figure A.90: Porkchop Plot from Earth to Asteroid 2022 SN21

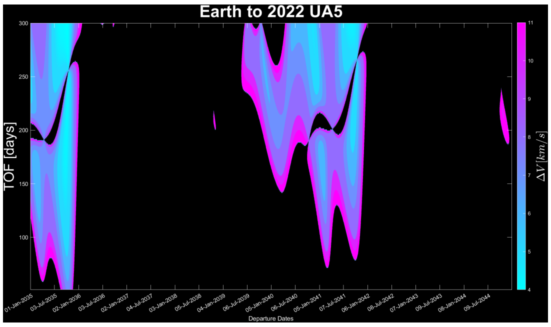

Figure A.91: Porkchop Plot from Earth to Asteroid 2022 UA5

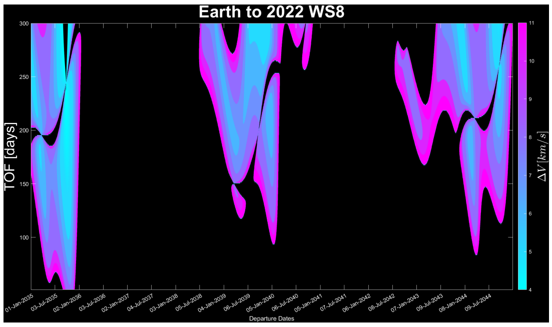

Figure A.92: Porkchop Plot from Earth to Asteroid 2022 WS8

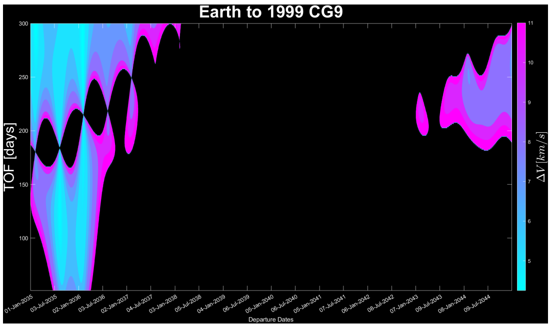

Figure A.93: Porkchop Plot from Earth to Asteroid 1999 CG9

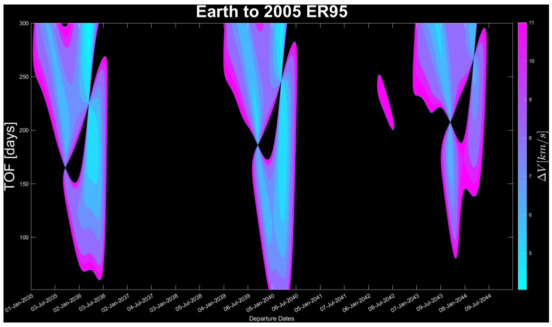

Figure A.94: Porkchop Plot from Earth to Asteroid 2005 ER95

If some porkchop plots are completely black, it means that no solutions with a ΔV less than 11 km/s was found.

Appendix B

Porkchop Plots for each Candidate Asteroids to Mars

This appendix presents a collection of all 94 Porkchop Plots asteroid-Mars trajectories within a specific range of flight time and departure dates. The catalog covers a 30-day period, starting from the day of arrival on the asteroid, and includes asteroid-Mars trajectories with TOFs between 51 and 300 days.

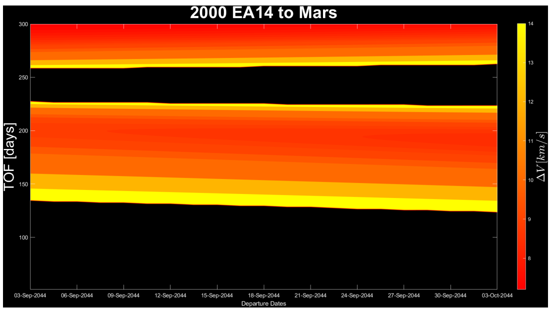

Figure B.1: Porkchop Plot from Asteroid 2000 EA14 to Mars

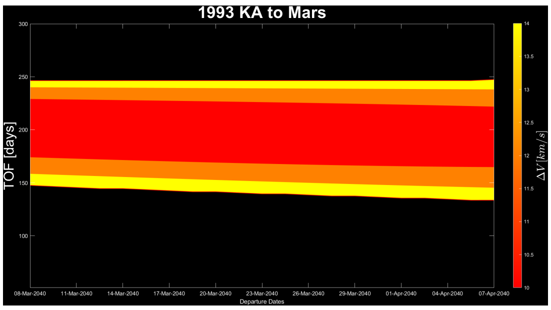

Figure B.2: Porkchop Plot from Asteroid 1993 KA to Mars

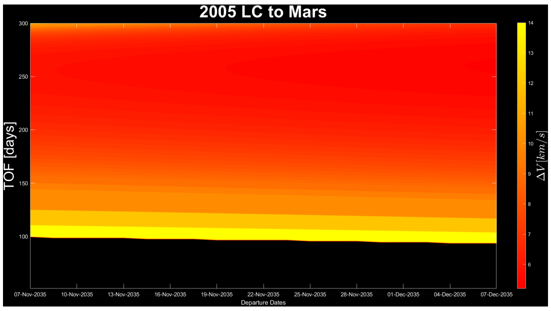

Figure B.3: Porkchop Plot from Asteroid 2005 LC to Mars

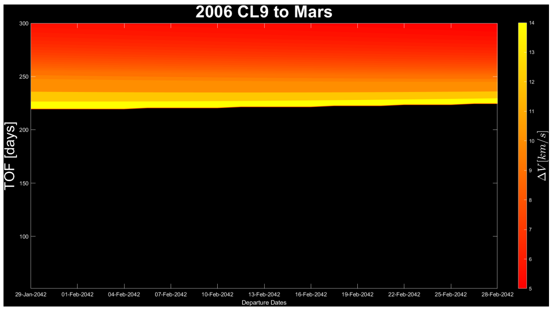

Figure B.4: Porkchop Plot from Asteroid 2006 CL9 to Mars

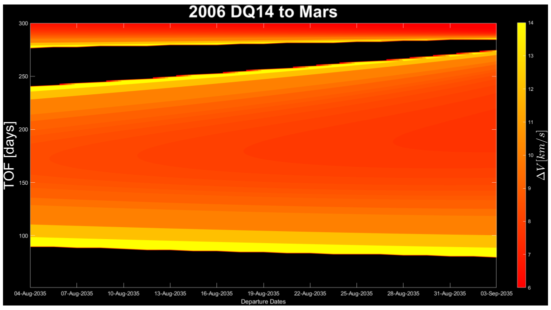

Figure B.5: Porkchop Plot from Asteroid 2006 DQ14 to Mars

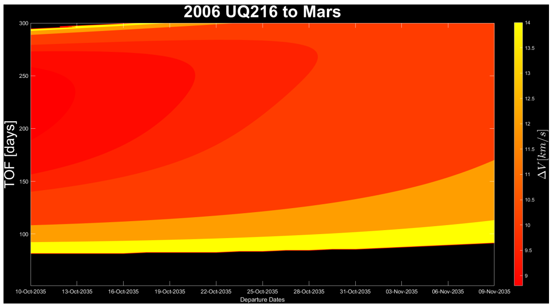

Figure B.6: Porkchop Plot from Asteroid 2006 UQ216 to Mars

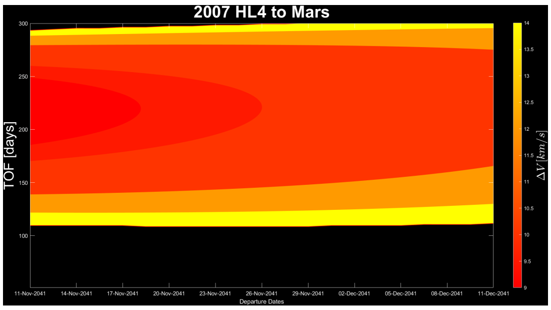

Figure B.7: Porkchop Plot from Asteroid 2007 HL4 to Mars

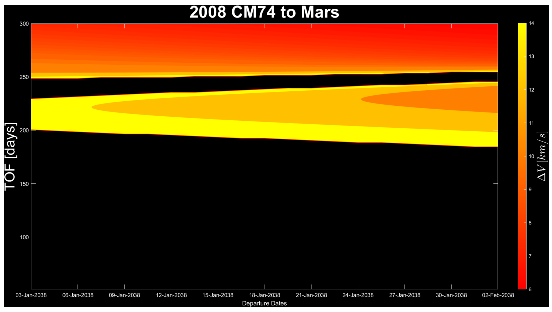

Figure B.8: Porkchop Plot from Asteroid 2008 CM74 to Mars

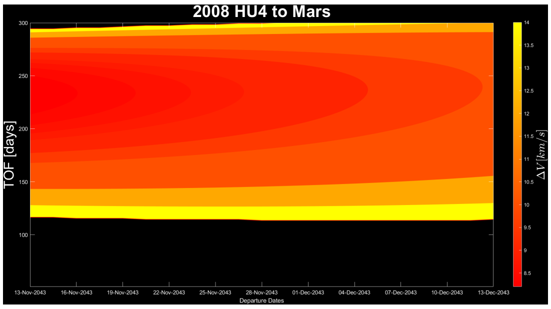

Figure B.9: Porkchop Plot from Asteroid 2008 HU4 to Mars

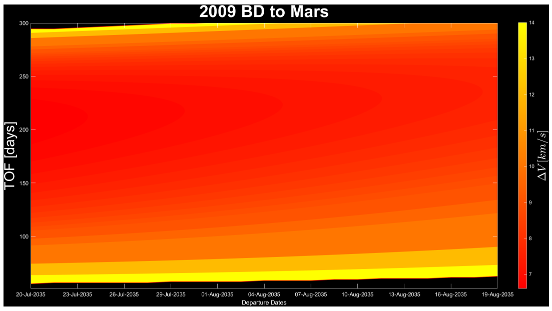

Figure B.10: Porkchop Plot from Asteroid 2009 BD to Mars

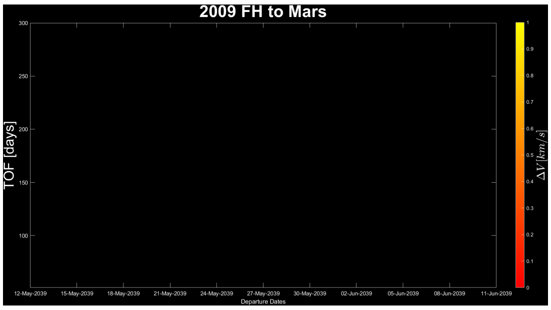

Figure B.11: Porkchop Plot from Asteroid 2009 FH to Mars

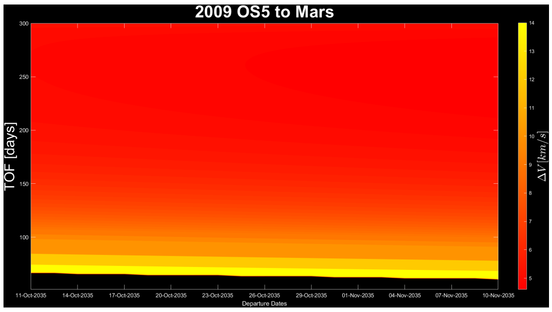

Figure B.12: Porkchop Plot from Asteroid 2009 OS5 to Mars

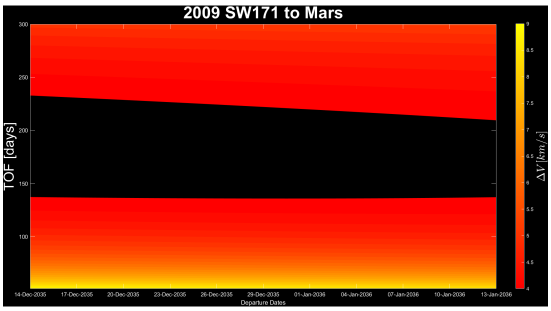

Figure B.13: Porkchop Plot from Asteroid 2009 SW171 to Mars

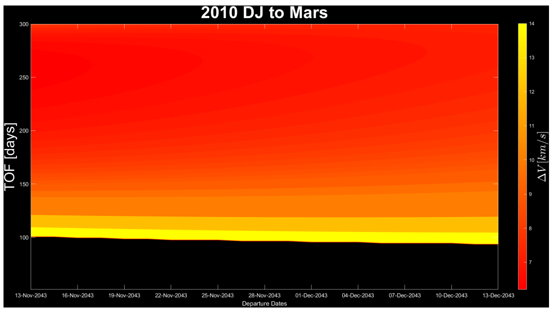

Figure B.14: Porkchop Plot from Asteroid 2010 DJ to Mars

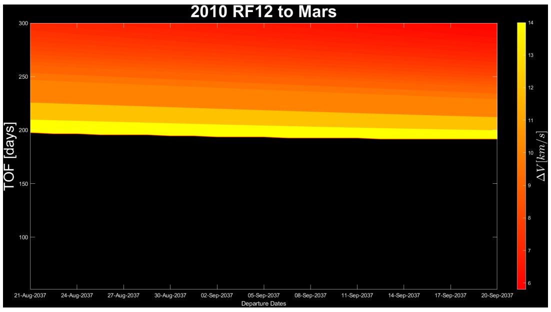

Figure B.15: Porkchop Plot from Asteroid 2010 RF12 to Mars

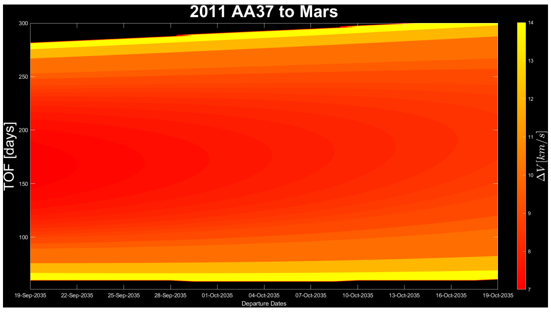

Figure B.16: Porkchop Plot from Asteroid 2011 AA37 to Mars

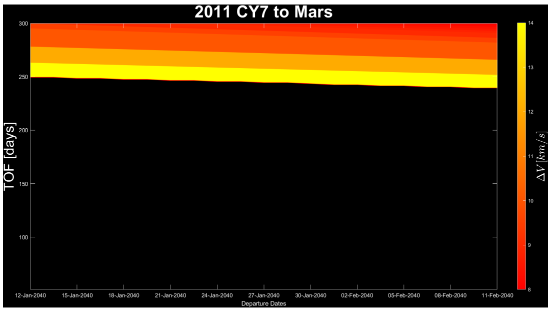

Figure B.17: Porkchop Plot from Asteroid 2011 CY7 to Mars

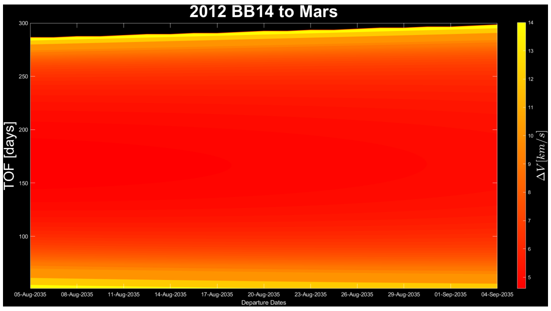

Figure B.18: Porkchop Plot from Asteroid 2012 BB14 to Mars

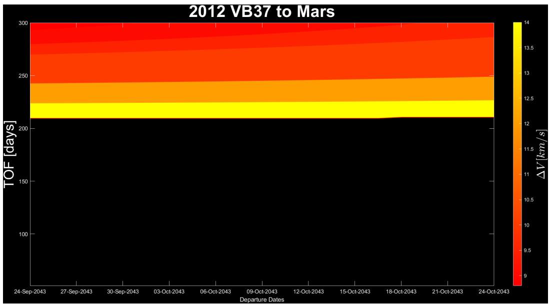

Figure B.19: Porkchop Plot from Asteroid 2012 VB37 to Mars

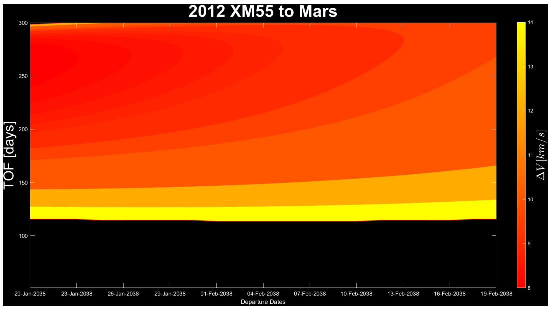

Figure B.20: Porkchop Plot from Asteroid 2012 XM55 to Mars

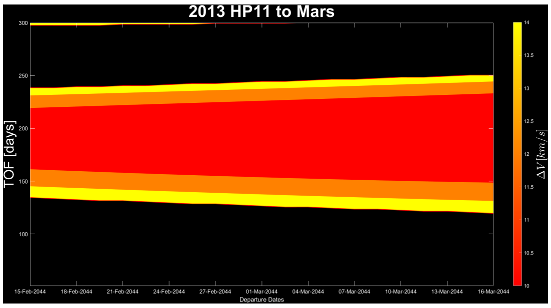

Figure B.21: Porkchop Plot from Asteroid 2013 HP11 to Mars

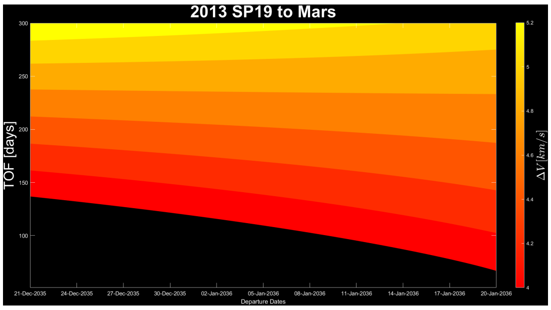

Figure B.22: Porkchop Plot from Asteroid 2013 SP19 to Mars

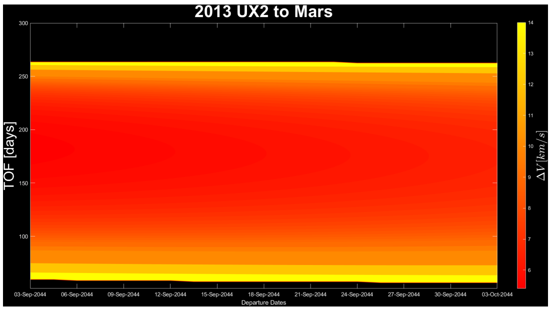

Figure B.23: Porkchop Plot from Asteroid 2013 UX2 to Mars

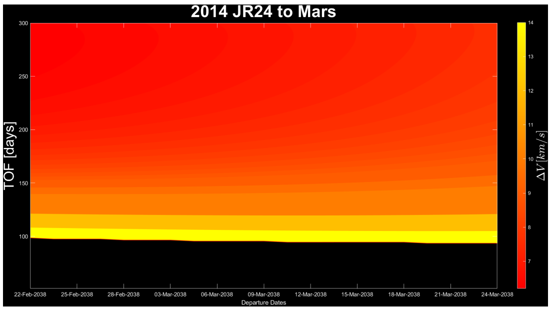

Figure B.24: Porkchop Plot from Asteroid 2014 JR24 to Mars

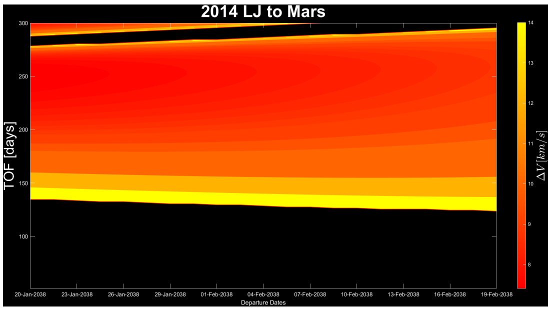

Figure B.25: Porkchop Plot from Asteroid 2014 LJ to Mars

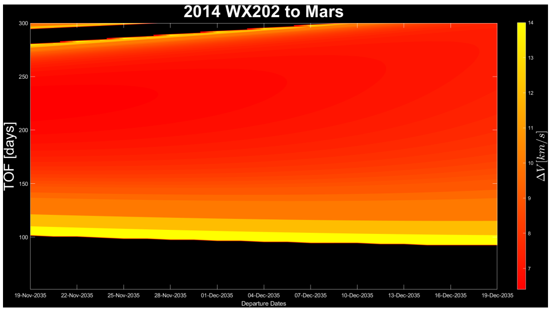

Figure B.26: Porkchop Plot from Asteroid 2014 WX202 to Mars

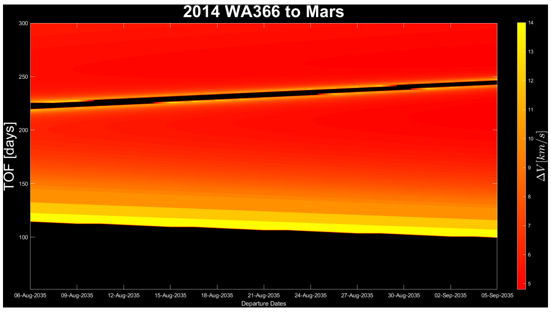

Figure B.27: Porkchop Plot from Asteroid 2014 WA366 to Mars

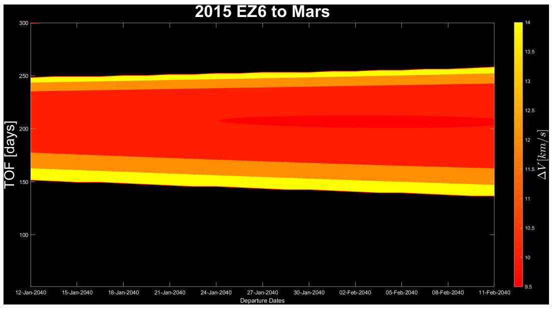

Figure B.28: Porkchop Plot from Asteroid 2015 EZ6 to Mars

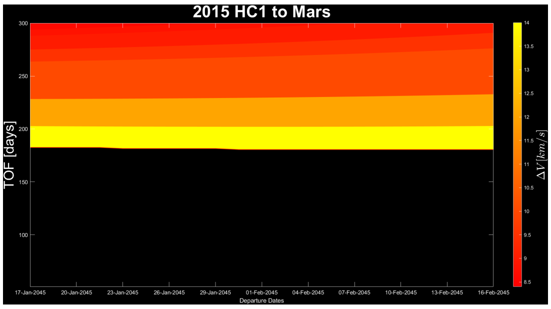

Figure B.29: Porkchop Plot from Asteroid 2015 HC1 to Mars

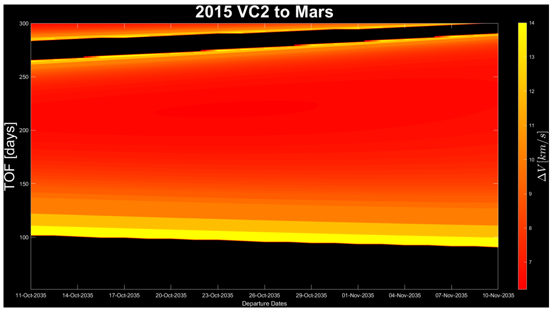

Figure B.30: Porkchop Plot from Asteroid 2015 VC2 to Mars

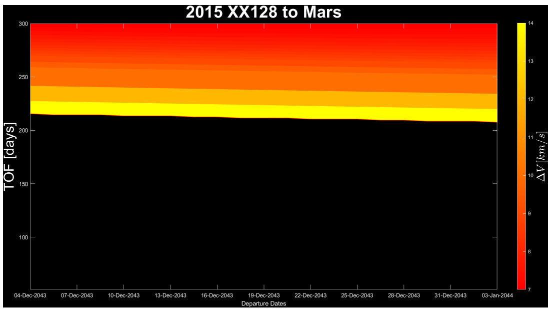

Figure B.31: Porkchop Plot from Asteroid 2015 XX128 to Mars

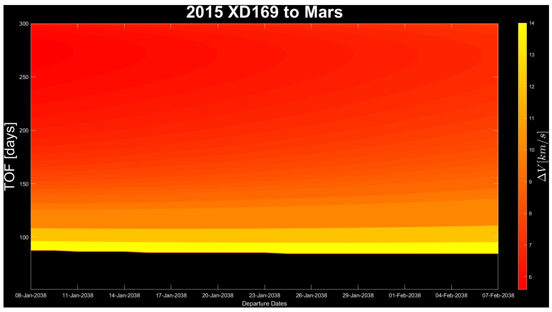

Figure B.32: Porkchop Plot from Asteroid 2015 XD169 to Mars

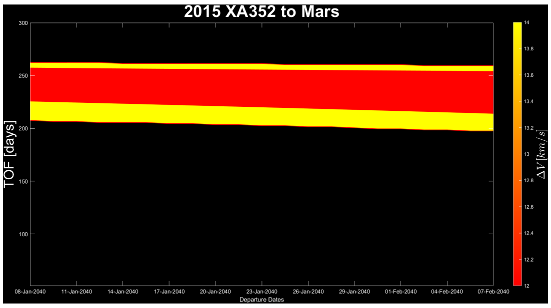

Figure B.33: Porkchop Plot from Asteroid 2015 XA352 to Mars

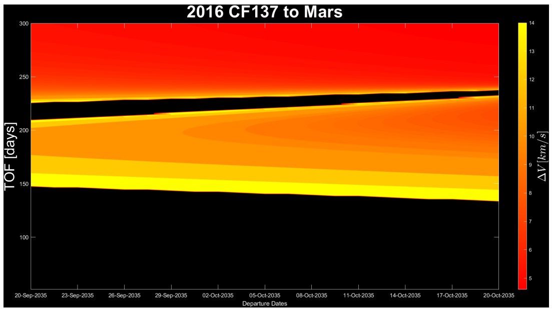

Figure B.34: Porkchop Plot from Asteroid 2016 CF137 to Mars

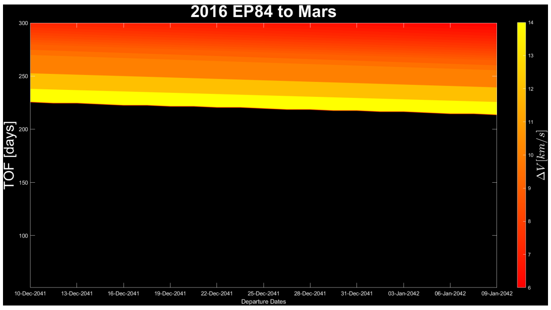

Figure B.35: Porkchop Plot from Asteroid 2016 EP84 to Mars

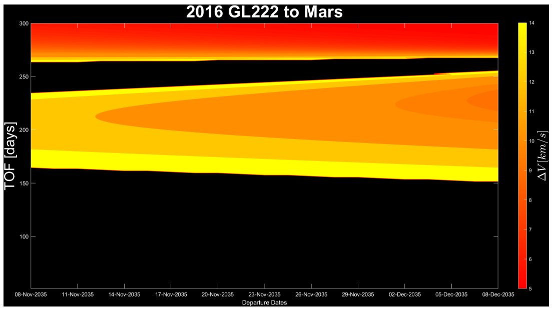

Figure B.36: Porkchop Plot from Asteroid 2016 GL222 to Mars

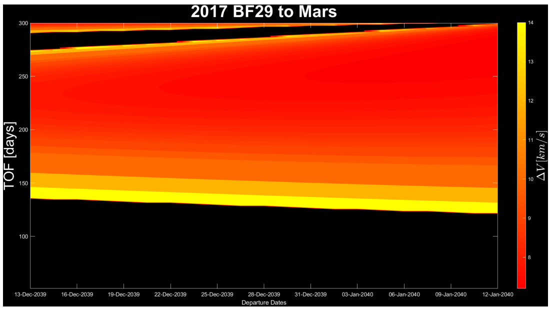

Figure B.37: Porkchop Plot from Asteroid 2017 BF29 to Mars

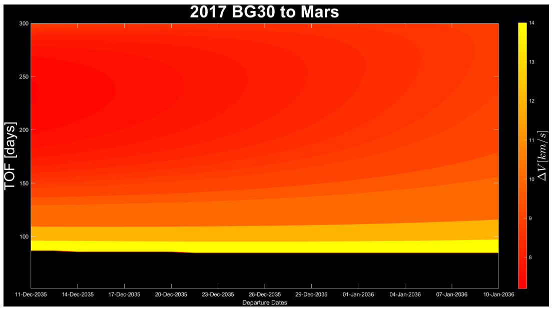

Figure B.38: Porkchop Plot from Asteroid 2017 BG30 to Mars

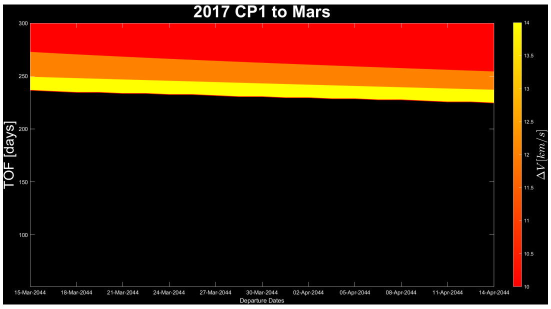

Figure B.39: Porkchop Plot from Asteroid 2017 CP1 to Mars

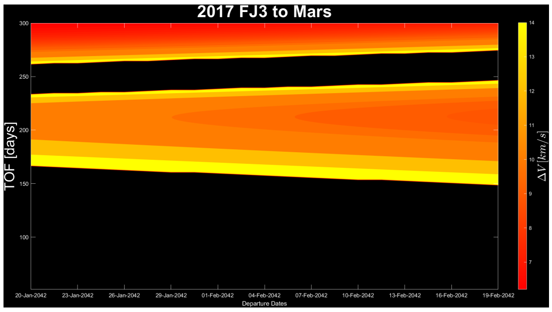

Figure B.40: Porkchop Plot from Asteroid 2017 FJ3 to Mars

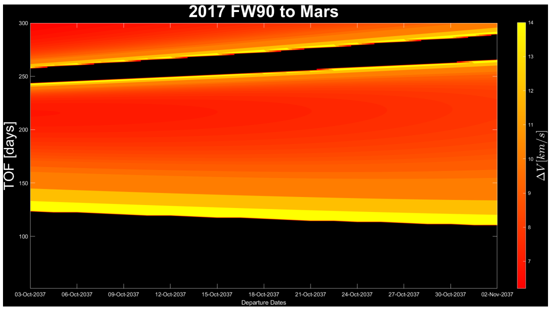

Figure B.41: Porkchop Plot from Asteroid 2017 FW90 to Mars

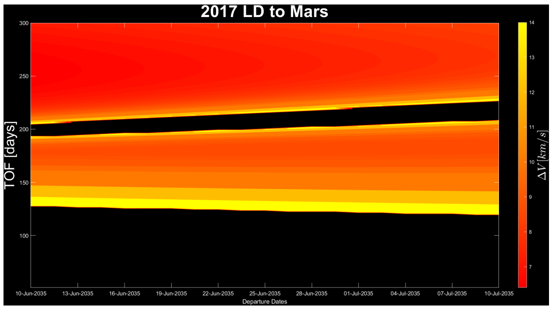

Figure B.42: Porkchop Plot from Asteroid 2017 LD to Mars

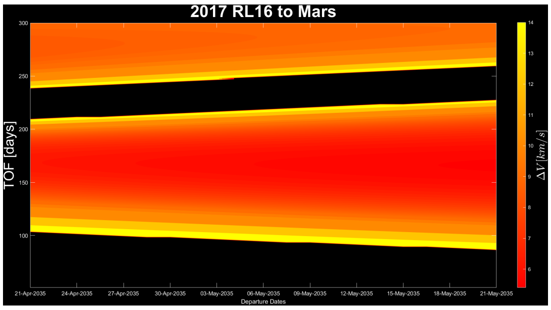

Figure B.43: Porkchop Plot from Asteroid 2017 RL16 to Mars

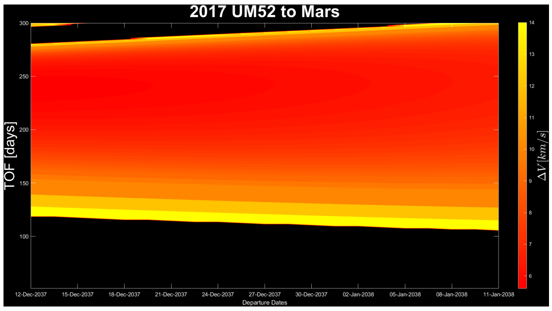

Figure B.44: Porkchop Plot from Asteroid 2017 UM52 to Mars

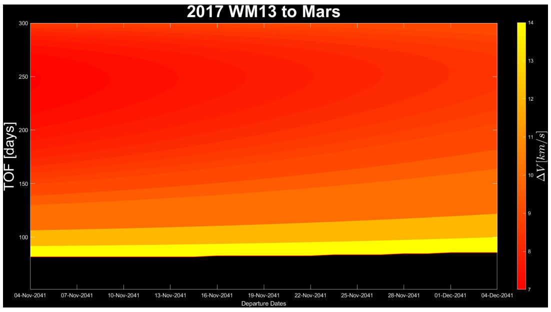

Figure B.45: Porkchop Plot from Asteroid 2017 WM13 to Mars

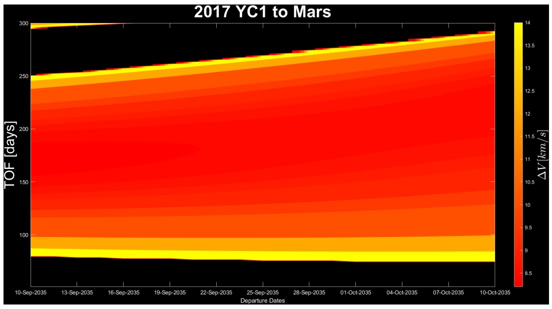

Figure B.46: Porkchop Plot from Asteroid 2017 YC1 to Mars

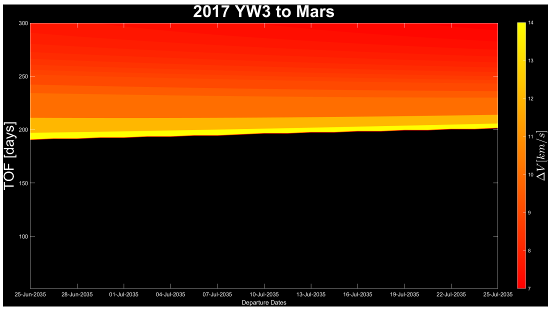

Figure B.47: Porkchop Plot from Asteroid 2017 YW3 to Mars

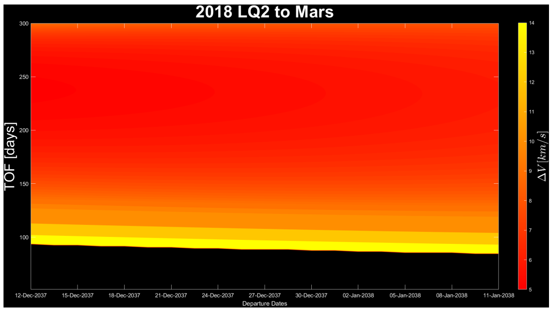

Figure B.48: Porkchop Plot from Asteroid 2018 LQ2 to Mars

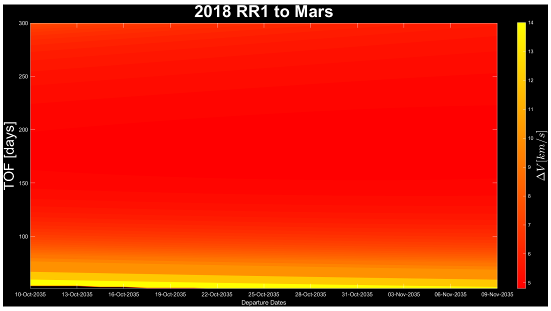

Figure B.49: Porkchop Plot from Asteroid 2018 RR1 to Mars

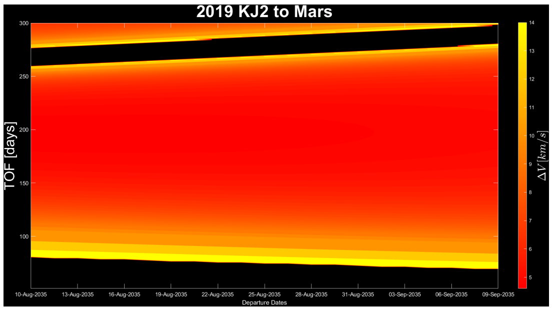

Figure B.50: Porkchop Plot from Asteroid 2019 KJ2 to Mars

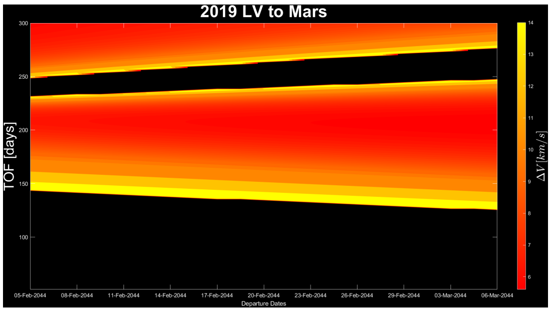

Figure B.51: Porkchop Plot from Asteroid 2019 LV to Mars

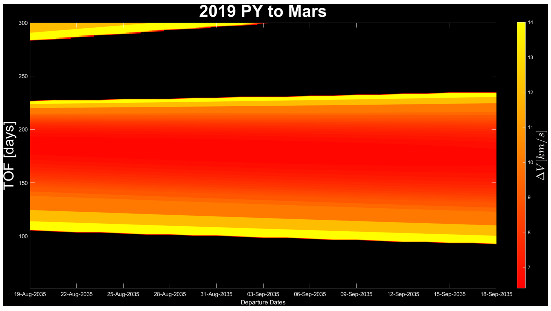

Figure B.52: Porkchop Plot from Asteroid 2019 PY to Mars

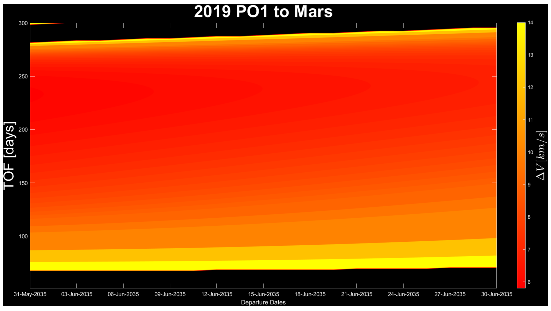

Figure B.53: Porkchop Plot from Asteroid 2019 PO1 to Mars

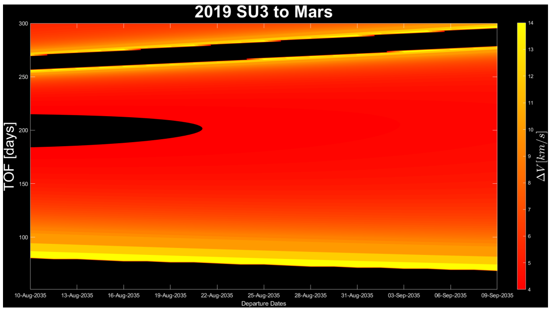

Figure B.54: Porkchop Plot from Asteroid 2019 SU3 to Mars

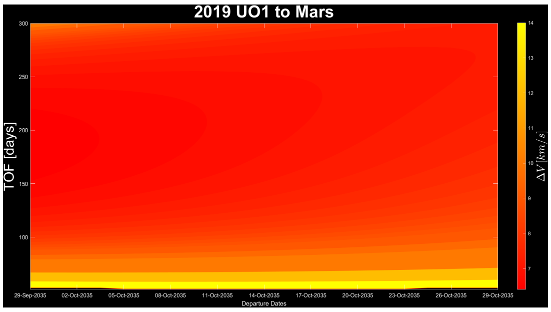

Figure B.55: Porkchop Plot from Asteroid 2019 UO1 to Mars

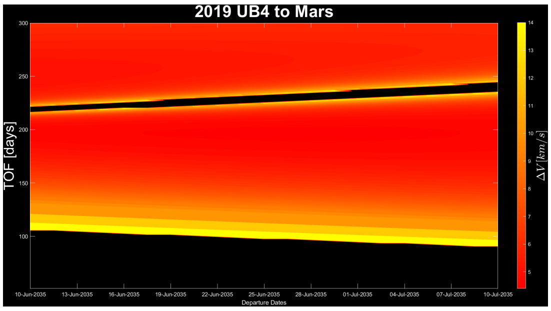

Figure B.56: Porkchop Plot from Asteroid 2019 UB4 to Mars

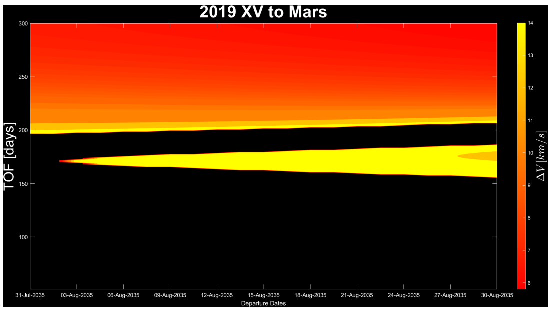

Figure B.57: Porkchop Plot from Asteroid 2019 XV to Mars

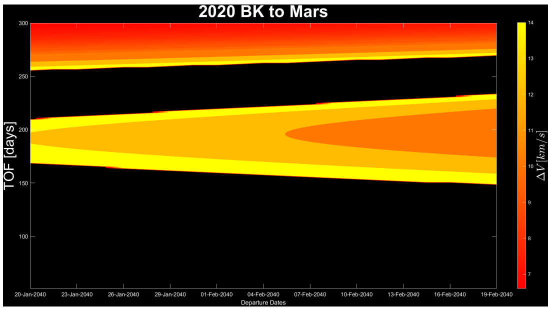

Figure B.58: Porkchop Plot from Asteroid 2020 BK to Mars

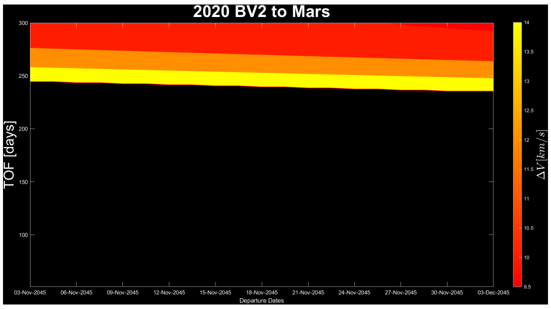

Figure B.59: Porkchop Plot from Asteroid 2020 BV2 to Mars

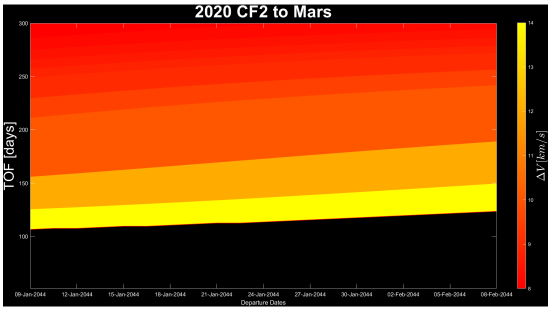

Figure B.60: Porkchop Plot from Asteroid 2020 CF2 to Mars

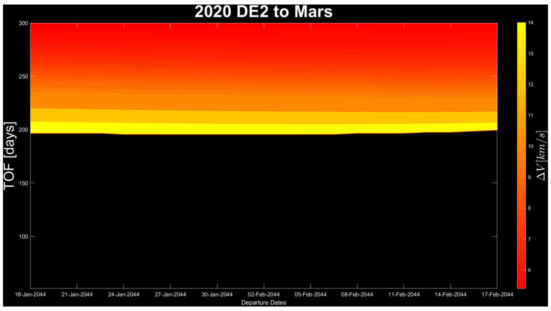

Figure B.61: Porkchop Plot from Asteroid 2020 DE2 to Mars

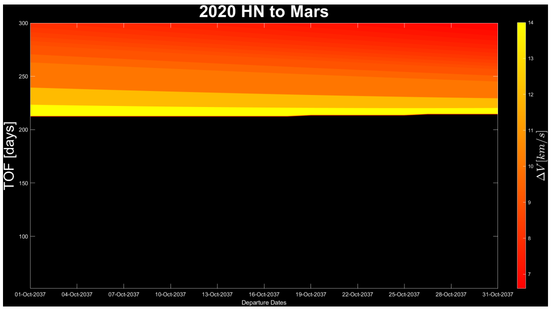

Figure B.62: Porkchop Plot from Asteroid 2020 HN to Mars

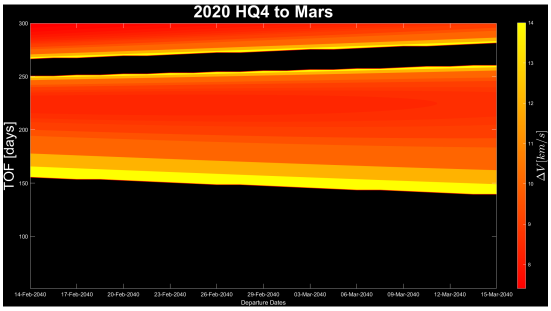

Figure B.63: Porkchop Plot from Asteroid 2020 HQ4 to Mars

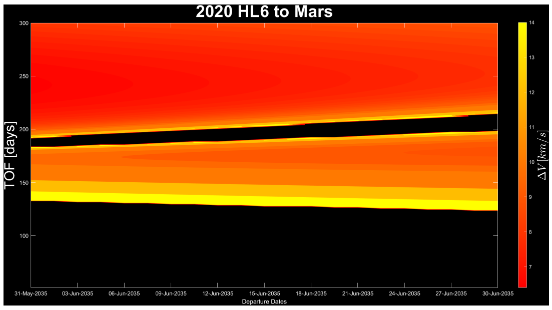

Figure B.64: Porkchop Plot from Asteroid 2020 HL6 to Mars

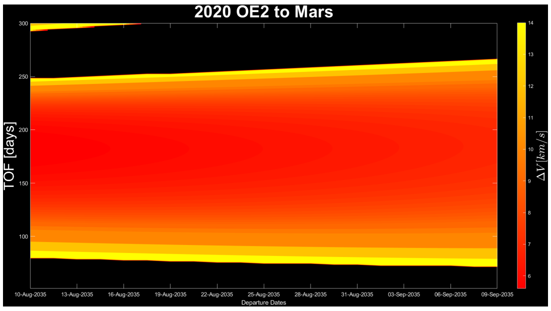

Figure B.65: Porkchop Plot from Asteroid 2020 OE2 to Mars

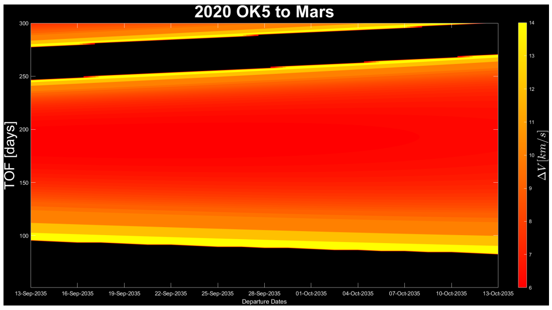

Figure B.66: Porkchop Plot from Asteroid 2020 OK5 to Mars

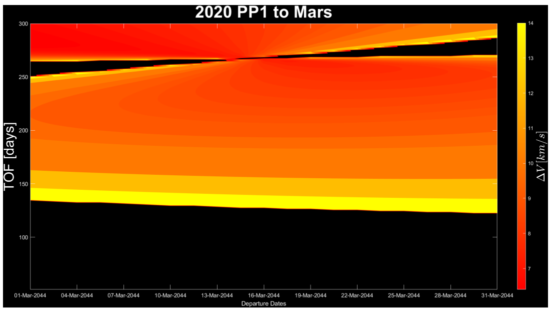

Figure B.67: Porkchop Plot from Asteroid 2020 PP1 to Mars

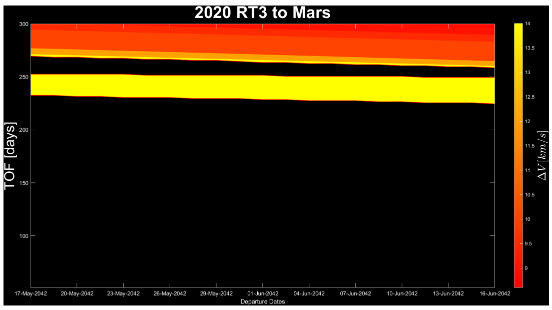

Figure B.68: Porkchop Plot from Asteroid 2020 RT3 to Mars

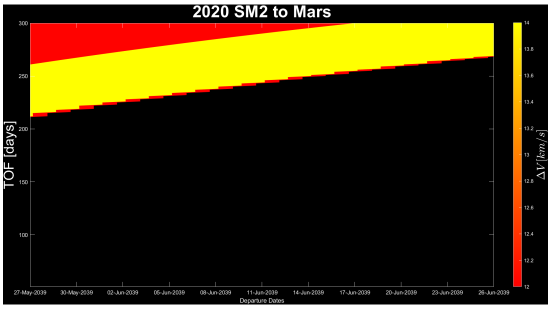

Figure B.69: Porkchop Plot from Asteroid 2020 SM2 to Mars

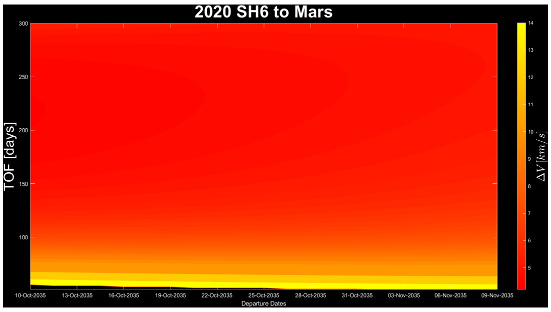

Figure B.70: Porkchop Plot from Asteroid 2020 SH6 to Mars

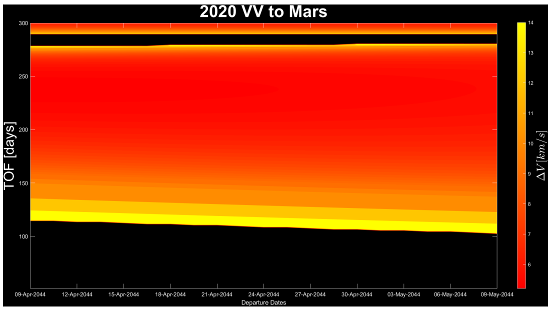

Figure B.71: Porkchop Plot from Asteroid 2020 VV to Mars

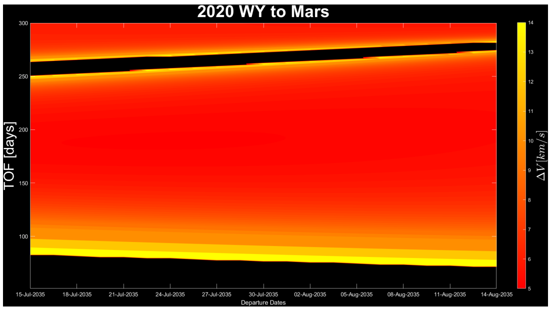

Figure B.72: Porkchop Plot from Asteroid 2020 WY to Mars

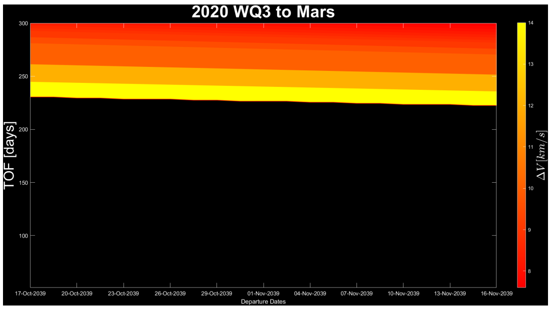

Figure B.73: Porkchop Plot from Asteroid 2020 WQ3 to Mars

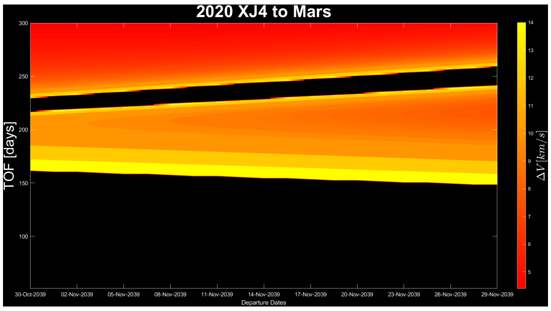

Figure B.74: Porkchop Plot from Asteroid 2020 XJ4 to Mars

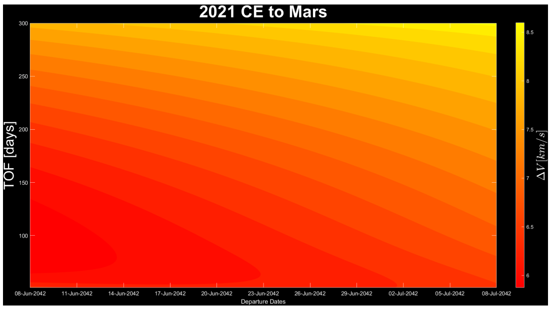

Figure B.75: Porkchop Plot from Asteroid 2021 CE to Mars

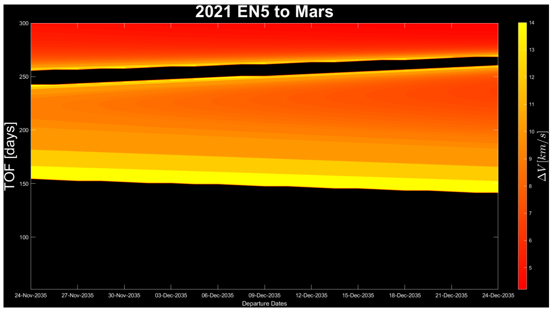

Figure B.76: Porkchop Plot from Asteroid 2021 EN5 to Mars

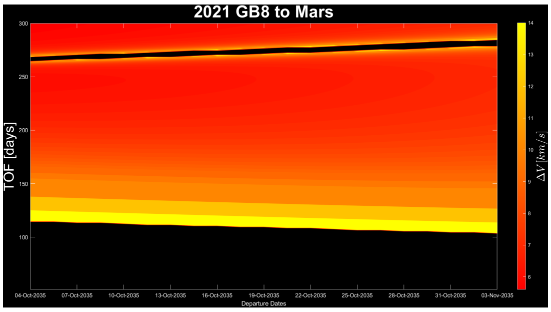

Figure B.77: Porkchop Plot from Asteroid 2021 GB8 to Mars

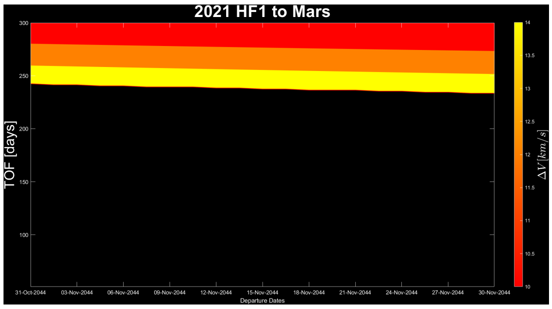

Figure B.78: Porkchop Plot from Asteroid 2021 HF1 to Mars

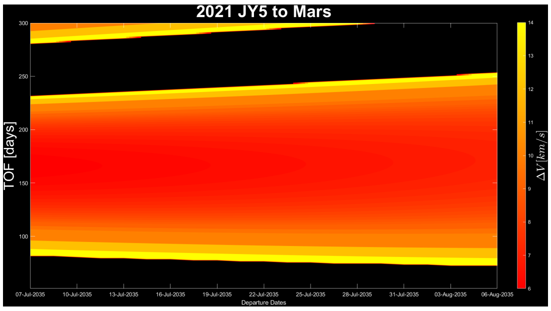

Figure B.79: Porkchop Plot from Asteroid 2021 JY5 to Mars

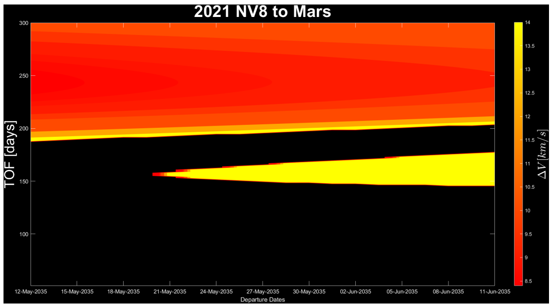

Figure B.80: Porkchop Plot from Asteroid 2021 NV8 to Mars

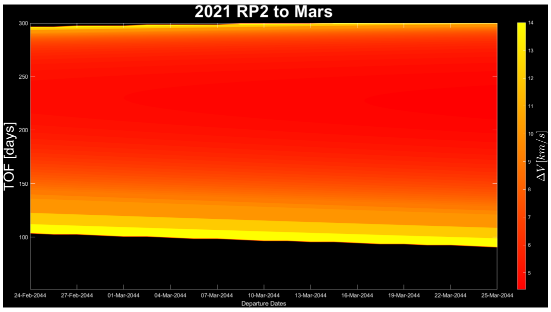

Figure B.81: Porkchop Plot from Asteroid 2021 RP2 to Mars

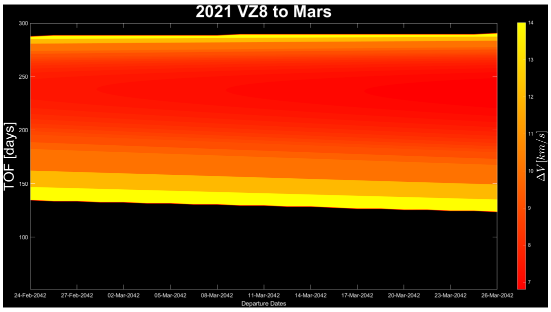

Figure B.82: Porkchop Plot from Asteroid 2021 VZ8 to Mars

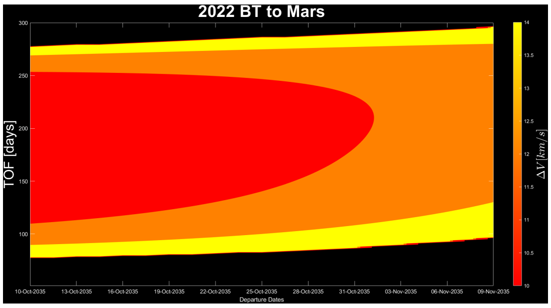

Figure B.83: Porkchop Plot from Asteroid 2022 BT to Mars

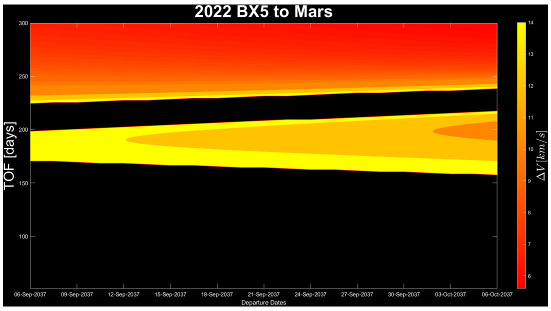

Figure B.84: Porkchop Plot from Asteroid 2022 BX5 to Mars

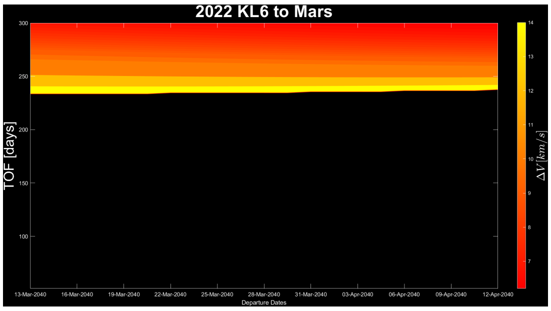

Figure B.85: Porkchop Plot from Asteroid 2022 KL6 to Mars

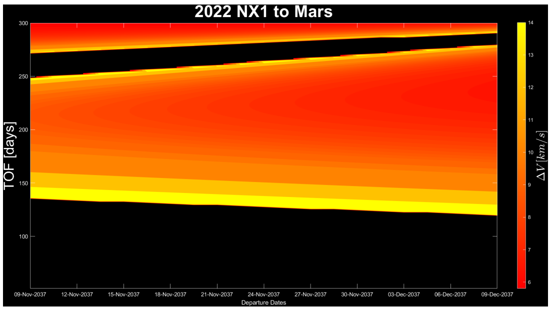

Figure B.86: Porkchop Plot from Asteroid 2022 NX1 to Mars

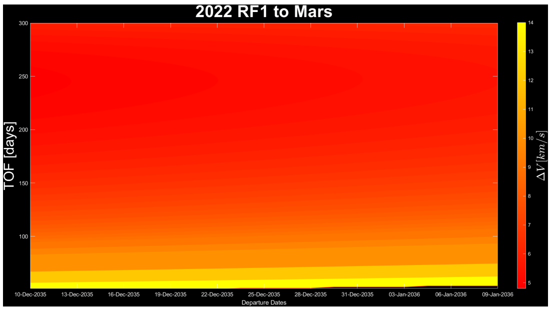

Figure B.87: Porkchop Plot from Asteroid 2022 RF1 to Mars

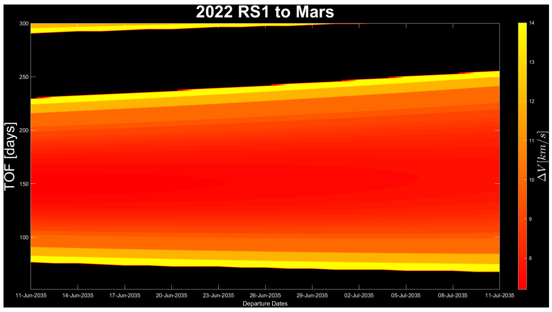

Figure B.88: Porkchop Plot from Asteroid 2022 RS1 to Mars

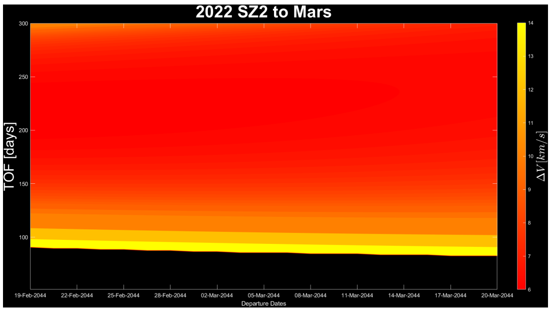

Figure B.89: Porkchop Plot from Asteroid 2022 SZ2 to Mars

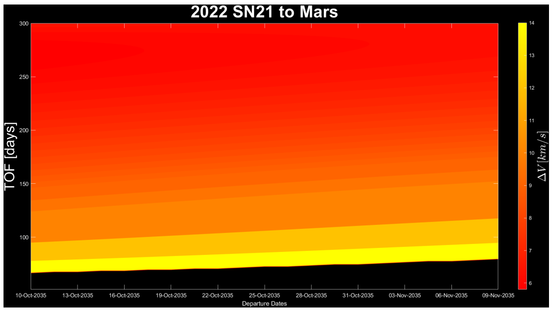

Figure B.90: Porkchop Plot from Asteroid 2022 SN21 to Mars

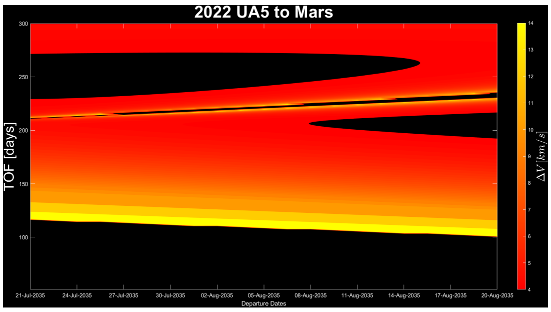

Figure B.91: Porkchop Plot from Asteroid 2022 UA5 to Mars

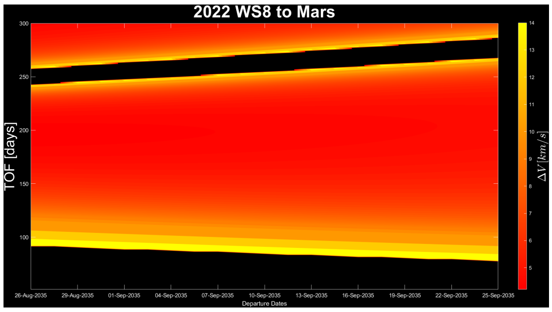

Figure B.92: Porkchop Plot from Asteroid 2022 WS8 to Mars

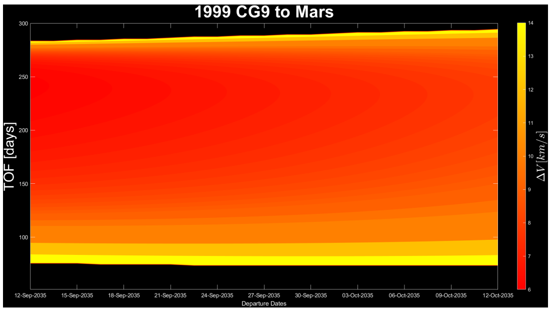

Figure B.93: Porkchop Plot from Asteroid 1999 CG9 to Mars

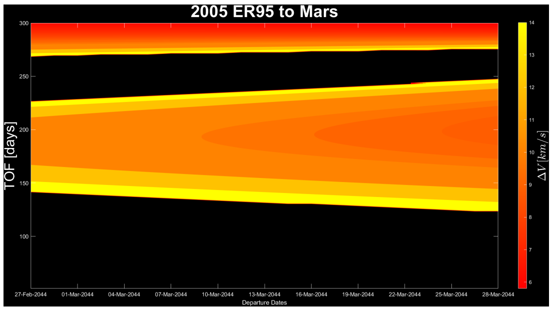

Figure B.94: Porkchop Plot from Asteroid 2005 ER95 to Mars

If some porkchop plots are completely black, it means that no solutions with a ΔV less than 14 km/s was found.

Bibliography

[1] Isaac Newton, Daniel Bernoulli, Colin MacLaurin, and Leonhard Euler. *Philosophiae naturalis principia mathematica*. excudit G. Brookman; impensis TT et J. Tegg, Londini, 1833 (cit. on p. 2).

[2] Victor G. Szebehely and F. T. Geyling. «Theory of Orbits: The Restricted Problem of Three Bodies». In: 1967 (cit. on p. 13).

[3] Julia L Bell, Martin W Lo, and Roby S Wilson. «Genesis Trajectory Design». In: (2000) (cit. on p. 13).

[4] Davide Conte. *Semi-Analytical Solutions for Proximity Operations in the Circular Restricted Three-Body Problem*. The Pennsylvania State University, 2019 (cit. on p. 16).

[5] D. L Richardson. «Analytic construction of periodic orbits about the collinear points». In: *Celestial Mechanics* (1980) (cit. on p. 17).

[6] David B. Spencer and Davide Conte. *Interplanetary Astrodynamics*. CRC Press, 2023 (cit. on p. 23).

[7] J.L Lagrange. *Sur le mouvement des noeuds des orbites planétaires*. Nouveaux mémoires de l'Académie royale des sciences et belles-lettres de Berlin, 1778 (cit. on pp. 32, 37).

[8] Richard H. Battin. «An introduction to the mathematics and methods of astrodynamics». In: 1987 (cit. on pp. 32, 42).

[9] Johann Heinrich Lambert. *Mémoire sur quelques propriétés remarquables des quantités transcendentes circulaires et logarithmiques*. Histoire de l'Académie Royale des Sciences et des Belles-Lettres de Berlin, 1761, pp. 265–322 (cit. on p. 32).

[10] Charles Darwin. *On the origin of species, 1859*. Routledge, 2004 (cit. on p. 48).

[11] D. Karaboga. «Artificial bee colony algorithm». In: *Scholarpedia* 5.3 (2010). revision #91003, p. 6915. DOI: `10.4249/scholarpedia.6915` (cit. on p. 49).

[12] Matteo Ceriotti and Massimiliano Vasile. «MGA trajectory planning with an ACO-inspired algorithm». In: *Acta Astronautica* 67.9 (2010), pp. 1202–1217. ISSN: 0094-5765. DOI: https://doi.org/10.1016/j.actaastro.2010.07.001. URL: https://www.sciencedirect.com/science/article/pii/S0094576510002468 (cit. on p. 50).

[13] Ying Tan and Yuanchun Zhu. «Fireworks algorithm for optimization». In: *Advances in Swarm Intelligence: First International Conference, ICSI 2010, Beijing, China, June 12-15, 2010, Proceedings, Part I 1*. Springer. 2010, pp. 355–364 (cit. on p. 50).

[14] Guanwei He, Davide Conte, Robert Melton, and David Spencer. «Fireworks Algorithm Applied to Trajectory Design for Earth to Lunar Halo Orbits». In: *Journal of Spacecraft and Rockets* 57 (Jan. 2020), pp. 1–12. DOI: 10.2514/1.A34469 (cit. on p. 50).

[15] Russell Eberhart and James Kennedy. «A new optimizer using particle swarm theory». In: *MHS'95. Proceedings of the sixth international symposium on micro machine and human science*. Ieee. 1995, pp. 39–43 (cit. on p. 51).

[16] J. Kennedy and R. Eberhart. «Particle swarm optimization». In: *Proceedings of ICNN'95 - International Conference on Neural Networks*. Vol. 4. 1995, 1942–1948 vol.4. DOI: 10.1109/ICNN.1995.488968 (cit. on p. 51).

[17] R. Mendes, J. Kennedy, and J. Neves. «The fully informed particle swarm: simpler, maybe better». In: *IEEE Transactions on Evolutionary Computation* 8.3 (2004), pp. 204–210. DOI: 10.1109/TEVC.2004.826074 (cit. on p. 51).

[18] Tetsuyuki Takahama and Setsuko Sakai. «Solving Difficult Constrained Optimization Problems by the ϵ Constrained Differential Evolution with Gradient-Based Mutation». In: *Constraint-Handling in Evolutionary Optimization*. Ed. by Efrén Mezura-Montes. Berlin, Heidelberg: Springer Berlin Heidelberg, 2009, pp. 51–72. ISBN: 978-3-642-00619-7. DOI: 10.1007/978-3-642-00619-7_3. URL: https://doi.org/10.1007/978-3-642-00619-7_3 (cit. on p. 53).

[19] Vittorio Baraldi and Davide Conte. «Trajectory Optimization and Control Applied to Landing Maneuvers on Phobos from Mars-Phobos Distant Retrograde Orbits». In: *AAS/AIAA Astrodynamics Specialist Conference* (2021) (cit. on pp. 56, 100).

[20] Ziliang Jin and Maitrayee Bose. «New clues to ancient water on Itokawa». In: *Science Advances* 5.5 (2019), eaav8106. DOI: 10.1126/sciadv.aav8106. eprint: https://www.science.org/doi/pdf/10.1126/sciadv.aav8106. URL: https://www.science.org/doi/abs/10.1126/sciadv.aav8106 (cit. on p. 56).

[21] N.A. Moskovitz, L. Wasserman, B. Burt, R. Schottland, E. Bowell, M. Bailen, and M. Granvik. «The astorb database at Lowell Observatory». In: *Astronomy and Computing* 41 (2022), p. 100661. ISSN: 2213-1337. DOI: `https://doi.org/10.1016/j.ascom.2022.100661`. URL: `https://www.sciencedirect.com/science/article/pii/S2213133722000750` (cit. on p. 56).

[22] Alan W. Harris and Alan W. Harris. «On the Revision of Radiometric Albedos and Diameters of Asteroids». In: *Icarus* 126.2 (1997), pp. 450–454. ISSN: 0019-1035. DOI: `https://doi.org/10.1006/icar.1996.5664`. URL: `https://www.sciencedirect.com/science/article/pii/S001910359695664X` (cit. on p. 81).

[23] W.R. Van Schmus and J.A. Wood. «A chemical-petrologic classification for the chondritic meteorites». In: *Geochimica et Cosmochimica Acta* 31.5 (1967), pp. 747–765. ISSN: 0016-7037. DOI: `https://doi.org/10.1016/S0016-7037(67)80030-9`. URL: `https://www.sciencedirect.com/science/article/pii/S0016703767800309` (cit. on p. 82).

[24] H.B. Wiik. «The chemical composition of some stony meteorites». In: *Geochimica et Cosmochimica Acta* 9.5 (1956), pp. 279–289. ISSN: 0016-7037. DOI: `https://doi.org/10.1016/0016-7037(56)90028-X`. URL: `https://www.sciencedirect.com/science/article/pii/001670375690028X` (cit. on p. 82).

[25] Collin J. Bezrouk and Jeffery Parker. «Long Duration Stability of Distant Retrograde Orbits». In: *AIAA/AAS Astrodynamics Specialist Conference*. DOI: `10.2514/6.2014-4424`. eprint: `https://arc.aiaa.org/doi/pdf/10.2514/6.2014-4424`. URL: `https://arc.aiaa.org/doi/abs/10.2514/6.2014-4424` (cit. on p. 86).

[26] Xiaohui Hu, Russell Eberhart, et al. «Solving constrained nonlinear optimization problems with particle swarm optimization». In: *Proceedings of the sixth world multiconference on systemics, cybernetics and informatics*. Vol. 5. Citeseer. 2002, pp. 203–206 (cit. on p. 89).

[27] Shuang Li, Pingyuan Cui, and Hutao Cui. «Autonomous navigation and guidance for landing on asteroids». In: *Aerospace Science and Technology* 10.3 (2006), pp. 239–247. ISSN: 1270-9638. DOI: `https://doi.org/10.1016/j.ast.2005.12.003`. URL: `https://www.sciencedirect.com/science/article/pii/S1270963805001690` (cit. on p. 106).

[28] Huang Xiangyu, Cui Hutao, and Cui Pingyuan. «An autonomous optical navigation and guidance for soft landing on asteroids». In: *Acta Astronautica* 54.10 (2004), pp. 763–771. ISSN: 0094-5765. DOI: `https://doi.org/10.1016/j.actaastro.2003.09.001`. URL: `https://www.sciencedirect.com/science/article/pii/S0094576503003187` (cit. on p. 106).